

Generating Small Molecule Fuels: (Photo)Electrochemical Catalysts

A thesis submitted to the University of East Anglia

For the degree of Doctor of Philosophy

Submitted April 2014

Lee Webster

Energy Materials Laboratory

School of Chemistry, UEA

Norwich

This copy of the thesis has been supplied on condition that anyone who consults it is understood to recognise that its copyright rests with the author and that use of any information derived therefrom must be in accordance with current UK Copyright Law. In addition, any quotation or extract must include full attribution.

Abstract

The work contained in this thesis focuses on the synthesis and electrochemistry of certain metal complexes that are involved in either catalysing production of a renewable fuel, hydrogen, or are capable of mediating the reduction of molecular nitrogen to ammonia, nitrogen fixation. Electrochemical analysis is used to measure the kinetic and mechanistic properties of the molecular catalysts used in this work. Semiconducting silicon electrodes have been explored as a means of coupling these hydrogen evolving and nitrogen fixation systems to the harvesting of visible light – solar fuels and solar synthesis respectively.

Chapter 1 gives a general overview of the world demand for energy and how it is currently produced. The current methods of renewable energy conversion are discussed with solar energy capture offering the greatest potential. Conversion of solar to chemical energy is described to be best attained by a solar producer cell which employs metal catalysts.

Chapter 2 outlines the major techniques used throughout the course of the work with light harvesting solar cells and electrocatalysts as described in this thesis, including the theory behind them.

Chapter 3 expands the study of hydrogen evolution by cationic hydrido- complexes of molybdenum and tungsten. The understanding of the basic electrochemistry of the systems is extended and electrocatalytic hydrogen evolution is optimised.

Chapter 4 is concerned with an enzyme related to the formate dehydrogenases which has been shown to exhibit hydrogen metabolising chemistry (Sawers *et al.*). Molybdenum and tungsten dithiolene complexes are analysed for catalysis of hydrogen evolution and/or oxidation by (spectro)electrochemical methods as potential models for this pterin enzyme.

Chapter 5 extends the studies of electrochemical nitrogen fixation by a tungsten hydrazido- complex at the synthetic and mechanistic levels. Photofixation of dinitrogen at a p-type silicon electrode *via* this hydrazide system is explored and limitations discussed.

Acknowledgements

First, I would like to thank my supervisor, Professor Chris Pickett, for his enthusiastic and kind supervision during my Ph.D. I greatly appreciate the extensive knowledge and numerous ideas (maybe too many!) he has generously imparted to me during my studies.

I would like to acknowledge Professor Guo-Xin Jin for giving me the opportunity to work in the Laboratory of Advanced Materials in the School of Chemistry at Fudan University. His friendly and patient supervision was greatly welcomed.

Sincere gratitude must go to Dr. Saad Ibrahim and Dr. Joseph Wright for their assistance during this Ph.D. Saad's lab skills in electrochemistry and organometallic synthesis are invaluable. Joseph's knowledge of seemingly everything that anybody would ever need to know about chemistry and computing (and many other topics!) proved to be excellent help.

I would also like to acknowledge past and present colleagues in the Energy Materials Laboratory: Jamie, Tim, Peiyi, Trevor, Pei-Meng, Peter, Khalaf, Amanda, James and Ahmed. I am sure that everyone has helped me at some point in the past three years, be it in the lab or simply through friendship and general support.

Special thanks goes to my family for their love, support and interest in whatever it is that I have done for the past three years. My grandparents, parents and brother have all helped me as much as they possibly could.

Last, but definitely not least, the upmost love and thanks goes to my colleague and now beautiful girlfriend Aušra. You have helped with so many things in and out of the lab that I cannot list them all here for the threat of making this thesis any longer! All I can say is, the moon of my life, I thank you for all the help you have given me and I hope that I can be as much help to you... Xxx

‘Any unsaved data will be lost’

– Nintendo quit game screen

‘Use a picture. It's worth a thousand words’*

– Arthur Brisbane

* ‘The thousand words have been included for clarity’

– Author

Contents

1 Energy: past, present and future	1
1.1 The world's energy demand	1
1.1.1 Energy requirements	1
1.1.2 Current energy sources/vectors	2
1.1.3 Environmental effects of fossil fuels	3
1.1.4 Renewable energy sources	4
1.1.4.1 Solar energy	5
1.2 Renewable energy vectors	7
1.2.1 Artificial photosynthesis – solar producer cell	7
1.2.2 Hydrogen production	9
1.2.3 Products of carbon dioxide reduction	11
1.2.4 Nitrogen fixation	13
1.3 Inorganic catalysis of small molecule reactions	14
1.3.1 Electrocatalysis of hydrogen evolution	16
1.3.2 Catalytic reduction of carbon dioxide	17
1.3.3 Nitrogen fixation	19
1.4 Scope of the work	20
1.5 References	22
2 Instrumentation and techniques	25
2.1 Electrochemical techniques	25
2.1.1 Cyclic voltammetry	25
2.1.1.1 Non-reversible systems	32
2.1.1.2 Experimental problems with cyclic voltammetry	39
2.1.2 Controlled potential electrolysis (CPE)	39
2.1.3 Calculation of efficiencies and yields	42
2.1.3.1 Chemical yield	42
2.1.3.2 Current efficiency	42
2.1.3.3 Turnover number (TON) and turnover frequency (TOF)	43
2.1.4 Electrocatalysis	44
2.1.5 Semiconductor electrochemistry	44
2.1.5.1 Background to semiconductor electrochemistry	44
2.1.5.2 Theory behind semiconductor electrochemistry	45
2.1.5.3 Limitations of semiconductor electrochemistry	48
2.1.5.4 Measures of photoelectrochemical efficiency	49
2.1.6 Design of electrochemical cells	50
2.1.7 Electrodes	51
2.1.7.1 Working Electrodes	51
2.1.7.2 Secondary electrodes	53
2.1.7.3 Reference electrodes	54
2.2 Digital simulation	54
2.3 Spectroelectrochemistry	56
2.4 References	61
3 Photoelectrocatalysis of hydrogen production at p-type silicon by molybdenum hydride systems	62
3.1 Introduction	62
3.1.1 Overview	62
3.1.2 The hydride complexes: synthesis and background chemistry	63

3.1.3 Early studies of the electrochemistry of cationic hydrido-carboxylato- complexes of molybdenum and tungsten	64
3.1.3.1 Basic electron-transfer chemistry: primary and secondary reduction steps	64
3.1.3.2 Binding of substrates at Mo ^{II} and W ^{II} centres	67
3.1.3.3 Bioinorganic context: carboxylate as a leaving group at the active site of the MoFe-protein of nitrogenase	67
3.1.4 Early studies of the photoelectrocatalytic systems at p-type silicon	69
3.1.4.1 Photoelectrocatalysis of proton and CO ₂ reduction on p-type Si	69
3.1.4.2 Photoelectrocatalysis at other semiconducting materials	70
3.1.5 Scope of the Chapter	72
3.2 Results and Discussion	73
3.2.1 Basic electrochemistry of [MH ₂ (η^2 -O ₂ CR)(dppe) ₂] ⁺ systems	73
3.2.1.1 The primary electron-transfer step	73
3.2.1.2 EPR detection of the primary Mo ^{III} reduction product	75
3.2.1.3 DFT calculations on the parent and one electron reduced species	77
3.2.1.4 Influence of the metal and the carboxylate ligand on the primary electron transfer	81
3.2.1.5 Determination of heterogenous rate constants for the primary electron transfer step	82
3.2.1.6 Effect of electrode material on electron transfer kinetics	85
3.2.2 Electrocatalysis of Hydrogen Evolution	86
3.2.2.1 Effect of addition of acid on the cyclic voltammetry of [MoH ₂ (η^2 -O ₂ CCH ₃)(dppe) ₂] ⁺	86
3.2.2.2 Bulk electrolysis and detection of dihydrogen	89
3.2.2.3 Cyclic voltammetry of the catholyte at the termination of electrolysis: detection of a molybdenum product	91
3.2.2.4 The nature of the electrolysis product A and relationship to A ⁺ ,B ⁺ and B	96
3.2.3 Global scheme for electrocatatlysis of hydrogen evolution	99
3.2.4 Photoelectrochemistry of [MoH ₂ (η^2 -O ₂ CCH ₃)(dppe) ₂] ⁺ at p-type silicon	101
3.2.4.1 Light and dark cyclic voltammetric studies	101
3.2.4.2 Photoelectrocatalysis of hydrogen evolution	105
3.2.4.3 Comparison between bulk electrolysis on illuminated p-type silicon and on vitreous carbon electrodes	108
3.2.4.4 Photoelectrochemical efficiency	109
3.3 Conclusions	110
3.4 Future avenues of research	111
3.5 References	115
4 Electrochemistry of molybdenum and tungsten dithiolenes	116
4.1 Introduction	116
4.1.1 Overview and biological significance	116
4.1.2 Established hydrogenases	117
4.1.3 Molybdenum and tungsten enzymes containing pyranopterin	118
4.1.3.1 Formate dehydrogenase enzymes	120
4.1.4 Current studies of Mo/W bis(dithiolene) active site analogues	121

4.1.5 Catalysis involving metal dithiolene systems	122
4.1.6 The ‘non-innocent’ dithiolene ligand	125
4.2 Scope of the chapter	126
4.3 Results and discussion	127
4.3.1 Basic redox properties of $[M(CO)_2(S_2C_2Ph_2)_2]$	127
4.3.1.1 Reductive cyclic voltammetry	127
4.3.1.2 Spectroelectrochemistry	130
4.3.1.3 DFT calculations	136
4.3.2 Hydrogen evolution	142
4.3.2.1 Cyclic voltammetry	142
4.3.2.2 Controlled potential electrolysis	149
4.3.2.3 Spectroelectrochemistry	153
4.3.2.4 Possible mechanism of electrocatalysis	155
4.3.3 Oxidative electrochemistry	156
4.3.3.1 Hydrogen oxidation	157
4.4 Conclusions	159
4.5 Future avenues of research	160
4.6 References	161
5 (Photo)electrosynthesis of ammonia	163
5.1 Introduction	163
5.1.1 Biological nitrogen fixation	163
5.1.2 Lowe-Thorneley (LT) model	165
5.1.3 Studies of the site of dinitrogen binding within FeMo-co	166
5.1.4 Obligatory dihydrogen evolution and suggested mechanism	167
5.1.5 Studies of synthetic systems related to nitrogenase activity	168
5.1.6 Background chemistry of Mo and W tertiary phosphine systems	169
5.1.6.1 Synthesis of dinitrogen complexes	169
5.1.6.2 Manner of dinitrogen binding	170
5.1.6.3 Protonation of coordinated dinitrogen	171
5.1.6.4 Kinetics of protonation	172
5.1.6.5 Tetrakis monotertiary phosphine dinitrogen complexes: formation of ammonia	173
5.1.6.6 Bis(ditertiary)phosphine complexes: formation of diazenides and hydrazides and related organohydrazides	174
5.1.6.7 The updated Chatt cycle	174
5.1.8 Related Schrock Chemistry	175
5.1.9 Cyclic and catalytic systems	177
5.1.9.1 Schrock chemistry	177
5.1.9.2 Electrosynthesis of ammonia via W hydrazides	178
5.1.10 Photofixation of ammonia	179
5.2 Scope of this chapter	180
5.3 Results and discussion	181
5.3.1 Electrosynthesis of ammonia	181
5.3.1.1 Electrosynthesis of ammonia at a Hg electrode	181
5.3.1.2 Initial stage of electrolysis: ammonia forming phase	182
5.3.1.3 Second phase of electrolysis: detection of intermediates	185
5.3.1.4 The nature of the intermediates I^1 and I^2	191
5.3.1.5 FTIR Spectroelectrochemistry of $trans-[W(N_2H_2)(TsO)(dppe)_2]^+$	192

5.3.2 Electrosynthesis of ammonia from a two phase system	195
5.3.3 Photoelectrosynthesis of ammonia	198
5.3.4 Photoelectrosynthesis of ammonia: a diurnal approach	204
5.4 Conclusions	205
5.5 Future avenues of research	206
5.6 References	208
6 Experimental	211
6.1 General materials and techniques	211
6.2 Experimental techniques	212
6.2.1 Electrochemical experiments and materials	212
6.2.2 Photoelectrochemistry	213
6.2.3 Spectroelectrochemistry	214
6.2.4 Indolphenol test	214
6.2.5 Electron paramagnetic resonance (EPR)	215
6.3 Computational techniques	215
6.3.1 Digital simulation	215
6.3.2 Density functional theory (DFT)	215
6.4 References	217

Chapter 1

Energy: past, present and future

1.1 The world's energy demand

1.1.1 Energy requirements

Year after year the global demand for energy increases. This is attributable to economic growth and the ever increasing world population. Every extra person needs to be supplied with energy, in addition to rising demand from the existing population.

As a result, the demand for energy is growing exponentially, Figure 1.¹

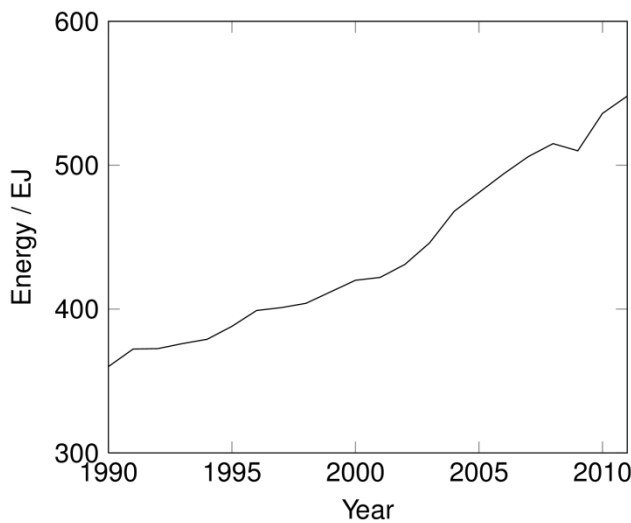


Figure 1 Worldwide total energy consumption (EJ, exajoules = 1×10^{18} J).

The Figure shows a rise in energy of 50 EJ over the period 1990-2000 and a 130 EJ rise to 550 EJ in 2010, consistent with an approximate exponential increase in energy demand. In fact, the world power consumption is approximated to double from 13.5 TW in 2001 to 27 TW by 2050 and to triple to 43 TW by 2100.²

Therefore the world's energy requirements are escalating very quickly and current methods of energy production are under scrutiny as described below.

1.1.2 Current energy sources/vectors

The vast majority of the world's energy is still derived from fossil fuels as shown in Table 1.

Type	Share / %
Oil	32.4
Coal / peat	27.3
Natural gas	21.4
Biofuels and waste	10.0
Nuclear	5.70
Hydro	2.30
Other	0.90

Table 1 Distribution of today's energy supply (other includes geothermal, wind, heat etc.).³

Over 80 % of energy is currently derived from coal, oil and natural gas; fossil fuels. The low level of contribution of non-fossil energy sources to the present day global energy demand reflects the readily available resources of oil, gas and coal. Even when oil reserves become limiting, there will remain large reservoirs of gas and coal to utilise. It is also believed that there are ample fossil energy reserves, in one form or another, to supply energy at a reasonable cost.⁴ However, these fuels are becoming more difficult to extract, with the latest method of hydraulic fracturing ('fracking') creating controversy over their environmental impact. The concerns have included ground water contamination and risks to air quality by migration of gases and chemicals used in the process to the surface.⁵⁻⁷

Fossil fuels as energy vectors are excellent; they can store and transport impressive amounts of energy for their mass. Their energy densities are up to 31.4 MJ kg⁻¹ for

coal, 41.9 MJ kg^{-1} for oil and 47.2 MJ kg^{-1} for natural gas. This means that energy losses, in terms of transportation of the fuel, are kept to a minimum which in turn helps keep the cost of energy low. The energy vector replacement would have to have a similarly high energy density. Hydrogen, in the gaseous form, has an energy density of 142 MJ kg^{-1} .⁸ A method for the safe storage and transportation of dihydrogen needs to be sought due to constraints about the safety of gaseous hydrogen (dihydrogen). Current methods cannot achieve the energy densities required to compete with fossil fuels, so the possibility of using hydrogen as a fuel is still some way off.

1.1.3 Environmental effects of fossil fuels

The energy stored in fossil fuels is contained in the form of carbon-carbon and carbon-hydrogen bonds; once the fuels are burned to release energy, by-products such as carbon dioxide and water vapour are released. These are known to be greenhouse gases and so the problem for the immediate future is not a limitation of fossil fuel reserves but the consequences of fuel combustion.

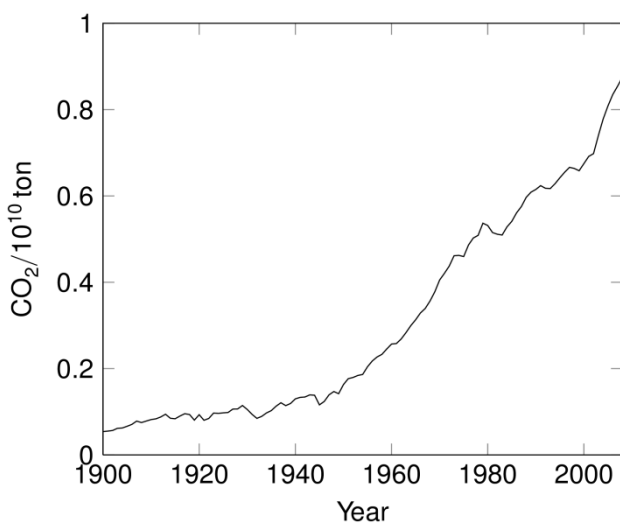


Figure 2 Estimated carbon dioxide released to the atmosphere.⁹

Figure 2 shows the estimated amounts of carbon dioxide released to the atmosphere; levels of CO_2 have been rising exponentially throughout the 20th century. In fact, the atmospheric concentration of CO_2 has risen from 280 ppm (parts per million) before the industrial revolution to a value of 400 ppm today.⁹

Greenhouse gases absorb radiation from the earth's surface within the thermal infrared region and then re-radiate this energy in all directions. This process is the fundamental cause of the greenhouse effect whereby heat struggles to escape from the earth's atmosphere. It has been reported that there has been a rise in the average temperature of earth's atmosphere and oceans since the late 19th century and it is projected to continue. Since the early 20th century, the earth's mean surface temperature has increased by about 0.8 °C, with about two-thirds of the increase occurring since 1980.¹⁰

There are no natural destruction mechanisms of CO₂ in the atmosphere, so the long term removal of atmospheric CO₂ must occur by dissolution and mineralisation in the oceans.¹¹ However, the mixing time between the near-surface ocean layer and the deep oceans is between 400 and several thousand years.^{12, 13} Hence, without any type of human intervention to change levels of CO₂, whatever effects the increased levels of CO₂ has on the environment over the next 40-50 year period will persist globally for the next 500-2000 years or even more.¹¹ Increasing the CO₂ burden of seawater increases the acidity with consequential detrimental environmental effects.¹⁴

1.1.4 Renewable energy sources

Renewable energy is obtained from resources that are naturally replenished such as sunlight, wind, rain, waves and geothermal heat. Currently about 17% of global energy consumption comes from renewable sources. The distribution of the use of available renewable energy sources is shown in Table 2.¹⁵

Type	Share / %
Biomass heat	68.7
Hydropower	20.0
Wind power	3.06
Bioethanol	3.00
Biomass electricity	1.68
Biodiesel	1.02
Solar hotwater	1.02
Geothermal heat	0.72
Geothermal electricity	0.42
Solar PV power	0.36
Solar capture/storage	0.01
Ocean power	0.01

Table 2 Distribution of available renewable energy sources.¹⁵

Biomass heating is by far the most common renewable energy source used today. This involves using agricultural, forest, urban and industrial residues and waste to produce heat and electricity. On large scales, the use of biomass takes agricultural land out of food production, reduces the carbon sequestration capacity of forests, and extracts nutrients from the soil, so carries environmental concerns. Combustion of biomass creates air pollutants and adds significant quantities of carbon to the atmosphere that may not be returned to the soil for many decades. It is therefore much more desirable to move away from energy sources that involve burning, whether it is renewable or otherwise. Sources that take up essential agricultural land where food could be grown should also be reduced, leaving solar, wind and water as the most environmentally viable energy sources.

1.1.4.1 Solar energy

Although hydro and wind power presently produce more renewable energy, solar energy has by far the most potential. The amount of energy received by the earth from the sun in one hour is sufficient to power the whole world for one year if it could all be harnessed.^{16, 17} This is around 174 PW (petawatts). The most common way that solar energy is used is by conversion to electricity by PV (photovoltaic) cells. These work

using semiconductor technology of alternating n-type (phosphorus doped) and p-type (boron doped) silicon wafers. Upon illumination, electrons in the electron rich p-type material are promoted to higher energy where they can migrate across the overall silicon lattice until they recombine with a hole in the electron-deficient n-type silicon. The movement of electrons creates electricity. The efficiency of these cells is increasing all the time as the technology is updated, at the moment the market average is an efficiency of 12–18% solar to electric conversion.¹⁸ The most efficient solar cell so far is a multi-junction concentrator solar cell with an efficiency of 43.5 % produced by the US company Solar Junction in April 2011.¹⁹

Solar energy can also be harnessed and used much more directly, especially in the developing world. Solar hot water systems use sunlight to heat water. In low geographical latitudes (below 40 degrees), 60 to 70% of the domestic hot water use of temperatures up to 60 °C can be provided by solar heating systems.²⁰

Solar distillation can be used to make disinfected water. Solar water disinfection involves exposing water-filled PET (poly(ethylene terephthalate)) bottles to sunlight for several hours. Exposure times vary depending on weather and climate from a minimum of six hours to two days during fully overcast conditions.²¹ It is recommended by the World Health Organization as a viable method for household water treatment and safe storage.²²

Solar cookers use sunlight for cooking, drying and pasteurization. A basic solar cooker consists of an insulated container with a transparent lid and can reach temperatures of 85-135 °C.²³

Solar chemical processes use solar energy to drive chemical reactions. These processes offset energy that would otherwise come from a fossil fuel source and can also convert solar energy into storable and transportable fuels. Solar-induced chemical reactions can be divided into thermochemical or photochemical, depending on whether it is heat or light derived energy that is required to power the reaction.

1.2 Renewable energy vectors

All the renewable energy sources mentioned above can create usable energy but the energy must be used directly or it will be lost. For example, heated water or solar cookers will cool once the sun goes down. Even PV cells which produce electricity from sunlight need to be coupled to a storage system to prevent the captured energy from being lost. The current electrical storage method of batteries loses a lot of the energy captured; a simple lead-acid battery has efficiencies in the range 60-90 % depending upon percentage charge²⁴ and a lifetime of 200-300 cycles.²⁵ Therefore, materials are required that can store as much energy as possible, while losing as little as achievable and the energy must be readily released when it is needed. By looking for inspiration from the existing fossil fuel system, a good way to store the energy is in chemical bonds, so a way of converting sunlight directly to a chemical fuel is required.

1.2.1 Artificial photosynthesis – solar producer cell

Nature already has a way of converting sunlight directly into chemical fuels. This is photosynthesis and it uses sunlight to convert carbon dioxide and water to sugars and oxygen, Equation 1.1.



(Equation 1.1)

The average rate of energy capture by photosynthesis globally is approximately 130 terawatts,²⁶ which is about six times larger than the power consumption of human civilization. As well as energy, photosynthesis is also a major source of fixed carbon; approximately 258 billion tons of carbon dioxide is converted to fixed carbon by photosynthesis annually.²⁷ In all, photosynthetic organisms convert around 100-115 thousand million metric tons of carbon into biomass per year.²⁸ For the 45 % of light that is viable for conversion by photosynthesis, an efficiency of solar to chemical energy of 3-6 % is achievable.²⁹

Artificial replication of the conversion of sunlight straight through to chemical fuels is possible using a solar producer cell.

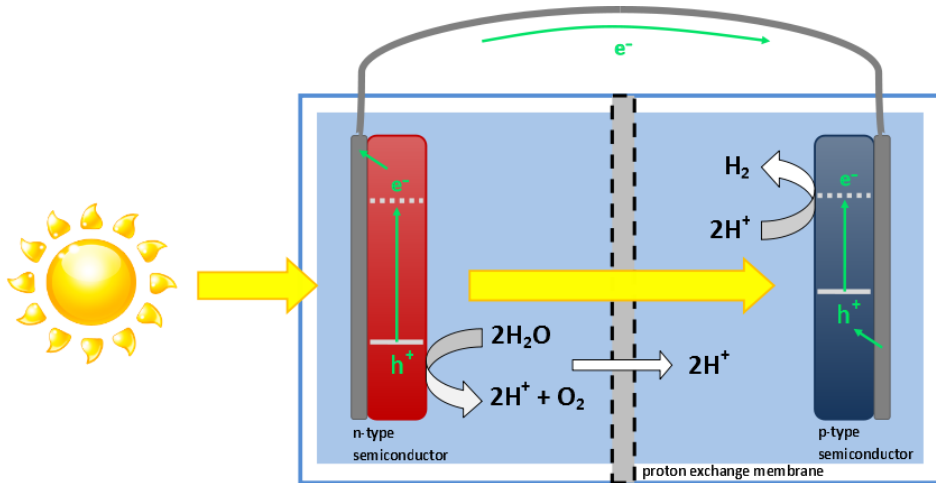


Figure 3 Typical solar producer cell setup.³⁰

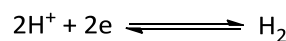
Figure 3 shows the design for one potential solar producer cell. It is divided into two halves; an oxidation reaction on the left and a reduction reaction on the right. In this case the cell produces hydrogen as the energy vector, so splitting water into protons and oxygen is the oxidation reaction. Once the protons are passed through a proton exchange membrane to the reduction side, they are reduced to hydrogen by the electrons generated from the splitting of water. Each side requires a semiconductor to harness the light and an electrocatalyst to perform the chemical reaction. For the cell to turnover hydrogen with no external bias the two electrocatalysts have to run at low voltages as well as being very efficient at their respective chemical reactions. They are therefore required to have a high turnover number and low degradation.

One complete solar producer cell has been fabricated by the Toyota Central Research and Development Laboratories for the reduction of CO_2 to formate with an overall conversion efficiency of solar to chemical energy of 0.03-0.04 % with no external bias.³⁰ The cell employs TiO_2 as the n-type semiconductor for water oxidation and zinc-doped indium phosphide surface modified with a Ru(bipy) type catalyst that has been previously reported³¹ as the p-type semiconductor/metal-complex hybrid photoelectrocatalyst for CO_2 reduction. Although the overall percentage energy conversion of the cell is low when compared to photosynthesis, this proves that the technology is viable. The majority of research groups working in this area focus on one half of the cell, striving to engineer semiconductor and electrocatalyst systems with

the best efficiency possible for their specific reaction. This will improve the overall solar to chemical energy conversion efficiency once implemented within a completed solar cell. The possible renewable fuel cell vectors that are being researched into are mainly hydrogen, products of carbon dioxide reduction and also, less related to an energy vector, but more of a chemical feedstock is the reduction of nitrogen to ammonia.

1.2.2 Hydrogen production

Hydrogen is seen as a clean energy carrier for the future,³² as a substantial amount of energy can be stored in the simplest of chemical bonds and produced from one of the most straightforward chemical reactions, Equation 1.2.

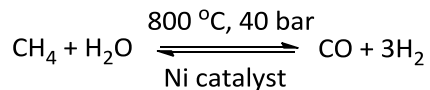


(Equation 1.2)

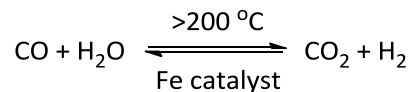
The idea of a hydrogen economy is not new: suggestions of using this more renewable energy source were made long before the first energy crisis of the 1970s.³³ In the 1930s Erren suggested that hydrogen produced from electrical water splitting could be used as a transportation fuel.³⁴

Currently, hydrogen is produced by reformation of fossil fuels and this is a relatively energy intensive process. Alternatives are nickel-catalysed methane steam reforming and the water-gas shift reaction, which are outlined in Scheme 1. These methods could provide an initial venture into the hydrogen economy, but would only signify a small improvement as they are still not sustainable. They are non-renewable methods of hydrogen production because they still rely on oxidation of carbon: fossil fuels.

Methane steam reforming



Water-gas shift reaction



Scheme 1 Hydrogen formation reactions.

Biomass is another possibility, as it can easily be converted into a number of fuels including methanol, ethanol, biodiesel and pyrolysis oil, which could be used to generate hydrogen *in situ*. However, even if biomass is collected sustainably, there are drawbacks. Firstly, the conversions of the carbon-based fuels extracted from biomass into hydrogen will rely on methods that are similar to those outlined above, so are liable to produce significant amounts of greenhouse gases. In addition, it would be difficult to achieve the scales of biomass needed to support a hydrogen economy. The final and possibly the most important argument against biomass, as previously stated, is that precious land space is required where food could be grown and this is desperately needed in a world that is food-limited.

A different method looks at the possibility of reducing the temperature necessary for the thermal splitting of water and a number of thermal chemical cycles have been proposed. Direct thermal splitting requires temperatures of over 2000 °C³⁵ and produces a rapidly recombining mixture of hydrogen and oxygen. This method requires great care as large mixtures of hydrogen and oxygen are potentially extremely explosive so the evolution of the two gases would need to be segregated not only from each other, but also the temperature of the reactor.

A completely different approach is to look to nature for inspiration. Enzymes found in many bacteria and other organisms can produce hydrogen with extremely high turnovers, so a lot of research is going into understanding the mechanisms by which these enzymes work. These enzymes are the [NiFe]- and the [FeFe]-hydrogenases.

A device based upon enzymes would ultimately not be suitable to run a hydrogen economy due to low current densities achieved from large protein-supported enzymic

structures. It is also very difficult to extract sufficient amounts to adapt for commercial applications and their stability is often limited outside of their natural environment.³⁶

As the large enzymes are difficult to work with, research has been undertaken to try to understand the mechanism from closely related synthetic active site mimics.^{37, 38} At present, these active site mimics are much less effective than the enzymes in terms of air stability, overpotential and turnover rates, but can be easily synthesised in the lab and improvements are made on a relatively short timescale.

1.2.3 Products of carbon dioxide reduction

The use of carbon dioxide as a renewable and environmentally friendly source of carbon, a fuel and a C₁ building block is highly attractive. Unfortunately, carbon dioxide is a highly oxidised and thermodynamically stable compound, and is consequently not very reactive. As a result of the stability of carbon dioxide and the rising levels of CO₂ in the atmosphere, one proposal to reduce the amount of CO₂ is Carbon Capture and Storage (CCS). Here, carbon dioxide is captured from large point sources, such as fossil fuel power plants. It is then transported to a storage site and deposited where it will not re-enter the atmosphere, normally an underground geological formation. Although CO₂ has been injected into geological formations for several decades for various purposes, including for enhanced oil recovery, the long term storage of CO₂ is a relatively new concept. The first commercial example was in Weyburn in 2000³⁹ and another 75 other large scale integrated projects are mentioned in the 2012 Global Status of CCS report.⁴⁰ A major concern with CCS is whether leakage of stored CO₂ will compromise the method as a climate change mitigation option. If leakage occurs in a small area, highly concentrated CO₂ can prove fatal. This has been the case on occasions such as the extreme carbon dioxide outburst at the Menzengraben potash mine 7 July 1953.⁴¹ Other concerns are the cost in terms of both money and energy, and latest research argues that there is a high probability that earthquakes will be triggered by injection of large volumes of CO₂ into the brittle rocks commonly found in continental interiors.⁴²

Carbon dioxide sequestration, whereby CO₂ is reused by electrochemical reduction to some form of useable fuel is a challenging task, but a much more attractive and

practical solution to reducing atmospheric levels of CO₂ than CCS. The reaction is much more complex than simple proton reduction for hydrogen evolution, as it is affected by outside stimuli, such as the influence of pH on the reduction potential, Figure 4.⁴³

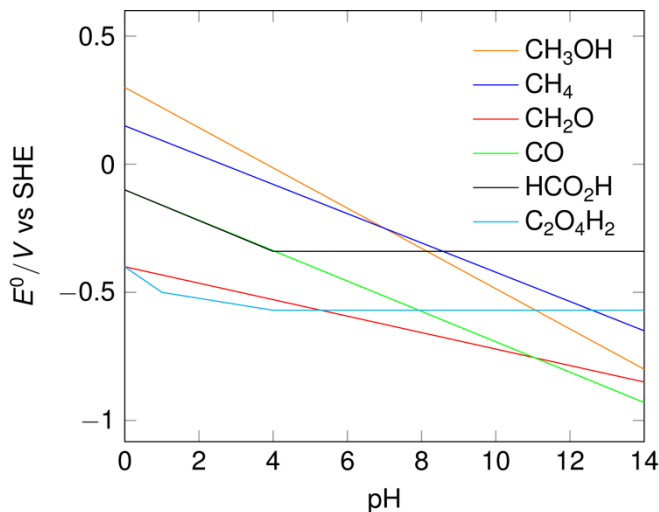
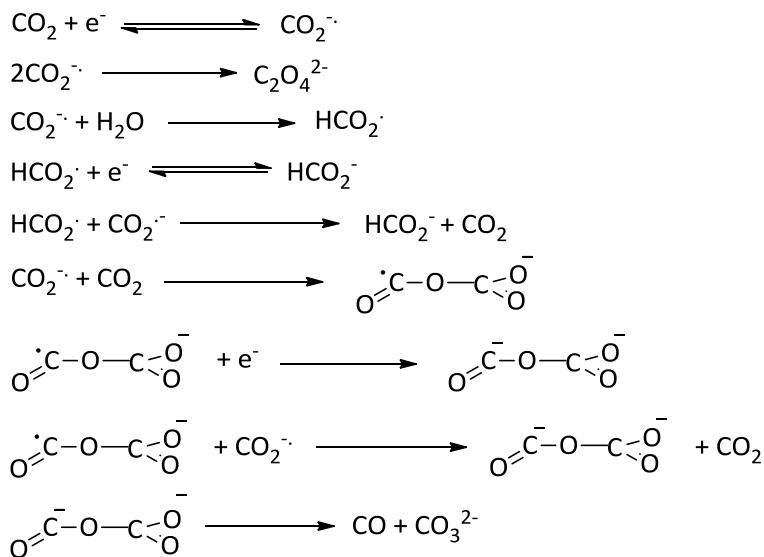


Figure 4 Plot showing influence of pH on the standard reduction potential of CO₂ and the product formed.⁴³

Radical reactions can also be triggered, which can propagate lots of different reactions, shown in Scheme 2.⁴³



Scheme 2 Possible radical reactions of carbon dioxide.⁴³

The figure and scheme above illustrates the diverse products that can be formed from direct CO₂ reduction. This broad range encompasses both liquids and gases, so carbon feed stocks could be synthesised for specific uses. However, there is enormous

difficulty in producing a single carbon feedstock from the direct reduction of CO₂ as only small changes in either reduction potential or pH can alter the product. Therefore, research into control and tunability of carbon dioxide reduction is just as important and ultimately associated with improving catalytic efficiency. The introduction of CO₂ reduction catalysts should offer more selective control over the carbon based products formed and improve the turnover of the desired product's formation. If CO₂ reduction can be controlled in such a way that CO is the major product, there is the possibility of following Fischer-Tropsch chemistry, whereby CO and H₂ can produce hydrocarbon fuels. This is advantageous if liquid fuels can be produced as a move to this 'renewable' fuel would cause less social disruption.

Consequently, designing CO₂ reduction catalysts is a widely studied, yet challenging topic in chemistry.

1.2.4 Nitrogen fixation

Molecular nitrogen is the major component of the earth's atmosphere. The molecule is non-polar and possesses a triple bond that is extremely resistant towards dissociation, as shown by the bond dissociation energy of 945 kJ mol⁻¹.⁴⁴ Due to the extreme inert nature of the gas, it is difficult to convert dinitrogen into reduced forms such as ammonia, or other nitrogen-containing compounds.

Ammonia is an industrial necessity as a chemical feedstock for use in fertiliser and necessary for all life on earth, because nitrogen atoms are required in the biosynthesis of nucleotides for DNA, RNA and amino acids. The vast scale use of nitrogen, along with other anthropogenic effects such as the release of NO_x emissions from fossil fuel combustion, has led to drastic modifications in the natural nitrogen cycle. This has culminated in unfavourable transformations to many ecosystems, for example nitrogen saturation in grassland and acidification of freshwater sources.⁴⁵

Three large scale processes have been developed for the conversion of dinitrogen gas into useable nitrogen containing feedstocks. Ammonia produced from such processes currently exceed contributions from natural nitrogen fixation.⁴⁶ The Birkeland-Eyde arc method generated nitric acid via an electrical discharge into an oxygen-nitrogen

mixture.⁴⁷ However, the high temperatures needed in the furnace to overcome the activation energy barrier for this reaction rendered this process obsolete. The Frank-Caro cyanamide procedure reacted calcium carbide with nitrogen at temperatures in excess of 1000 °C to generate CaNCN. The reaction is exothermic and self-sustaining once the reaction temperature was reached. The third and most commercially successful route to synthetic nitrogen is the Haber-Bosch procedure.⁴⁸ In this process, hydrogen gas produced by steam reformation or partial oxidation of hydrocarbons is reacted with dinitrogen gas over an iron catalyst at temperatures greater than 150 °C and 150 bar of pressure.⁴⁹ The reaction of H₂ with N₂ to form NH₃ is exothermic, but because of the considerable activation barrier due to slow reaction kinetics, high temperatures are needed to sustain an increased rate of ammonia formation. Conversely, as the temperature is increased the equilibrium of the reaction shifts towards the reactant gases. Thus, increased pressure is needed to shift the equilibrium in favour of ammonia production. Although this procedure is energy intensive, the process is actually reasonably energy efficient, with state of the art Haber-Bosch plants reaching efficiencies approaching the theoretical limit.⁵⁰ The Haber process is now used to produce 150 million tons of ammonia from nitrogen per year,⁵¹ consuming up to 5 % of world's natural gas supplies and around 2 % of the world's total energy supply annually. Since nature can accomplish this reaction at ambient temperature and pressure,⁵² there is significant room for improvement in artificial nitrogen fixation. The temperature and pressure required for effective nitrogen reduction catalysis could be reduced by searching for a more efficient method, possibly by designing a superior catalyst.

1.3 Inorganic catalysis of small molecule reactions

As mentioned above, direct catalysis of production of small molecules for fuels requires a significant energy input for the reaction to proceed at a substantial rate. This could necessitate high temperature and/or pressure, or if the reaction is electrochemically driven; a large overpotential. This is in contrast to the thermodynamic potential for these types of reactions, which are in most cases of modest values. For example, the combination of dihydrogen and dinitrogen to give

ammonia is thermodynamically favoured at room temperature. The reaction has a very high activation energy barrier but can be driven at a practical rate with an iron/rhenium catalyst. In the same way, reduction potentials for electrochemical reactions can be dramatically reduced to close to their thermodynamic reduction potentials by employing noble metal electrodes. The reduction of protons to dihydrogen (or the converse reaction) is slow at conventional electrodes (vitreous carbon, mercury). However, if the electrode is replaced by a catalytic material, such as platinum, the reaction can then proceed at a reasonable rate at a low overpotential. Overpotential is the difference between the thermodynamic potential and the applied potential at which a reaction takes place. The thermodynamic potential of the H^+/H_2 couple is usually quoted as 0.00 V vs NHE (normal hydrogen electrode) and this is what is used for the purpose of this thesis.

The scarcity and high costs of precious metals such as platinum pose serious limitations to the widespread use. Therefore, if these reactions are to be utilised on the large scales required to solve the future energy demand, then these reactions will need to be catalysed with more abundant metals. Examples of abundant transition metals are iron, manganese and copper as shown in Figure 5.⁵³

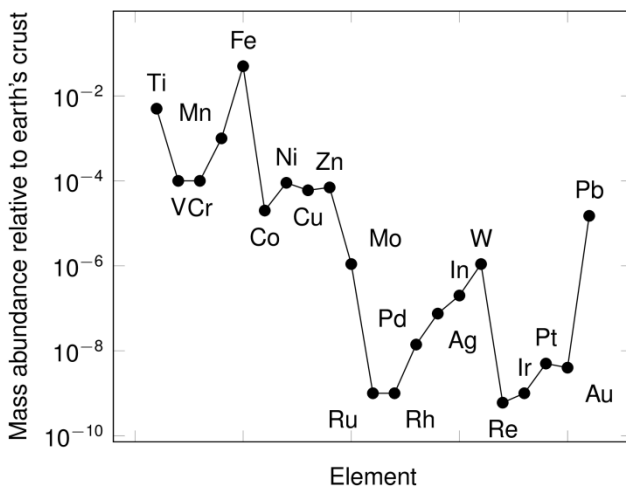


Figure 5 Mass fraction abundance of transition metals in the earth's crust.⁵³

Thus, the design and analysis of abundant transition metal electrocatalysts are required to establish molecular catalysts for these reactions that can transferred to large scales. Some recent developments in this field are mentioned below.

1.3.1 Electrocatalysis of hydrogen evolution

Recent electrocatalysts developed for hydrogen production have been based on many abundant transition metals, including complexes of nickel^{54, 55} cobalt,^{56, 57} iron,^{58, 59} and molybdenum^{60, 61}. Two of the most active hydrogen evolution catalysts reported are the dicobaloxime systems detailed by Gray⁶² in terms of low reduction potential, and the DuBois synthetic nickel electrocatalyst which has an extremely high turnover.⁶³

Catalytic hydrogen evolution described by Gray used two monomeric cobalt complexes ligated by an octamethylene linked bis(glyoxime) structure as the electrocatalyst. The two cobalt centres are far enough removed from each other that there is no electronic communication between them as confirmed by the linear plot of cathodic peak current *versus* square root of the scan rate for the Co^{II/III} couple. Upon addition of *p*-toluenesulfonic acid monohydrate ($\text{TsOH}\cdot\text{H}_2\text{O}$) as the acid source, catalytic waves were observed at a potential slightly negative of the formal reduction potential for the Co^{II/III} couple (-0.37 V *vs* SCE). This is a very modest potential for hydrogen evolution, but because the acid used is relatively strong, this corresponds to an overpotential of approximately 100 mV when compared to the standard potential for hydrogen evolution of $\text{TsOH}\cdot\text{H}_2\text{O}$ in acetonitrile. ($E^0(\text{HA}/\text{H}_2) = -0.27 \text{ V vs SCE}$).⁶⁴ The overall rate constant for hydrogen evolution, k_{cat} , was estimated from the height of the catalytic plateau current to be *ca* 1000 M⁻¹ s⁻¹. The lack of an increase in the catalytic rate constant for the mononuclear Co complex suggested that hydrogen evolution was likely to proceed through reductive generation of Co^{II}H, rather than the homolysis of two Co^{III}H units. As of yet, no bulk electrosynthesis of dihydrogen formation by these complexes has been reported, so the turnover and Faradaic efficiencies are unknown.

The synthetic nickel catalyst detailed by DuBois is believed to have some biological relevance to the [FeFe]-hydrogenase in that both catalytic sites contain pendant amines on the ligands that function as proton relays. The amine positioned near the iron centre in the active site of the diiron hydrogenase subsite has been proposed to facilitate formation or cleavage of the H-H bond.⁶⁵ Proposed transition states demonstrate how the doubly protonated Ni⁰ intermediate contorts to make use of these amine proton relays, Figure 6.

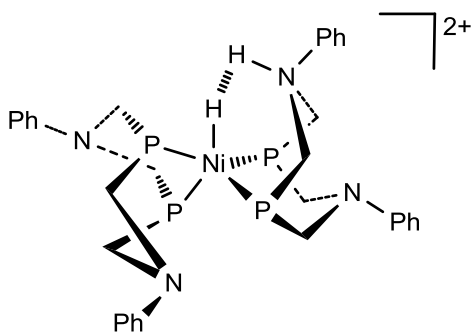


Figure 6 Pendant amines of $[\text{Ni}(\text{P}^{\text{Ph}}_2\text{N}^{\text{Ph}}_2)_2]^{2+}$ function as proton relay.⁶⁴

The catalytic conditions of H₂ production from protonated dimethylformamide [(DMF)H]OTf as the proton source in dry acetonitrile achieved good turnover rates and a current efficiency of 99 % at a potential of -1.13 V vs Fc⁺/Fc. However, this corresponds to a large overpotential of *ca* 625 mV when compared to the standard reduction potential for hydrogen evolution from this acid. The rate of catalysis was enhanced dramatically when the solvent media was altered to contain up to 1.2 M of water, giving a turnover frequency of over 100 000 s⁻¹. The catalytic rate constant was calculated, in addition to turnover rates, from cyclic voltammetric data of the cathodic peaks currents before and during maximum catalysis, giving $k_{\text{cat}} = 6.5 \times 10^4 \text{ M}^{-1} \text{ s}^{-1}$ based upon the concentration of acid and water added. The rate constant also indicates fast catalysis and is attributed to the relay properties of the pendant amines. It is defined by ultraviolet-visible spectroscopy that up to 5 % of the catalyst is decomposed during the 0.5 hours needed for catalysis and much more is lost at higher acid concentrations, so this would need to be improved for industrial use. The proton relaying ligand is also being applied to other metals such as cobalt.⁶⁶

1.3.2 Catalytic reduction of carbon dioxide

The latest research on homogeneous reduction of carbon dioxide using inorganic catalysts still relies heavily on complexes based upon noble metals such as rhenium⁶⁷ and palladium.⁶⁸ However, these complexes do provide the most efficient catalysis.

Research into carbon dioxide reduction using more abundant transition metals is most notably performed using the iron porphyrin systems of Saveant. This dates back to 1991 where iron⁰ porphyrins were reported to reduce CO₂ to CO at -1.8 V vs SCE in

DMF.⁶⁹ Regrettably, these porphyrins were unstable and degraded after a few catalytic cycles. Over the years, the stability and reductions potential of the porphyrin systems has been improved by modifications to the basic haem ligand.⁷⁰ This has resulted in relocation of the reduction potential for CO₂ to CO conversion to -1.5 V vs SCE in the presence of weak Brønsted acids. Recent functionalisation of the porphyrins with a phenolic group to provide an internal weak acid source created initial catalytic turnover frequencies (TOF) of 15000 s⁻¹, resulting in 50 million turnovers in four hours at an overpotential of 0.466 V.⁷¹

Another recent example of homogenous CO₂ reduction is a report of Ni(cyclam) systems at a glassy carbon electrode.⁷² Although these systems have previously been reported for CO₂ reduction in the 1980s for having remarkably low overpotentials in aqueous solutions,^{73, 74} the catalytic activity was proven to be attributed to a Ni(cyclam) species absorbed onto a mercury electrode.^{74, 75} The behaviour was verified by a plateau in catalytic turnover even with increasing concentrations of catalyst, so was attributed to the limited area of adsorbed species on the mercury electrode and the homogeneous catalytic ability of the Ni(cyclam) was thought to be negligible. No studies of note were undertaken of Ni(cyclam) catalysed CO₂ reduction at other electrode materials than mercury, resulting in this useful study of the catalysis at a glassy carbon electrode and establishing that homogeneous CO₂ reduction using Ni(cyclam) complexes was achievable with turnover frequencies of up to 90 s⁻¹ and turnover numbers of 4 for a long term controlled potential electrolysis.

Akin to hydrogen evolution, biological systems have also developed enzymes for efficient and selective conversion of carbon dioxide to carbon containing compounds used for energy. These enzymes reversibly catalyse the interconversion of carbon monoxide with water to form carbon dioxide, protons and electrons. These are the Ni-Fe-S⁷⁶ and Mo-S-Cu⁷⁷ enzymes and are collectively known as carbon monoxide dehydrogenases.

Although most of the work in trying to mimic active sites of proteins has focused on the hydrogenases, some work has been done on ‘bio-inspired’ reduction of carbon dioxide. Tezuka and co-workers first reported the reduction of CO₂ by using a Fe₄S₄(SR₄)²⁻ cluster in DMF.⁷⁸ Although iron-sulfur clusters are more commonly known

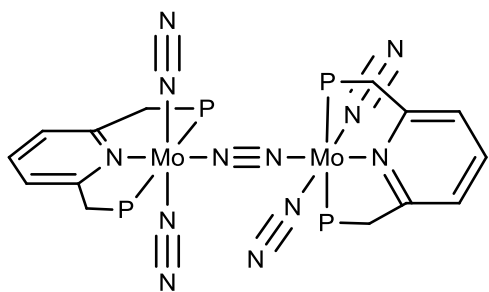
in biology as electron transfer units, they are known to have multiplicity of function.⁷⁹ This cluster was shown to be able to reduce CO₂ to formate at a potential of -1.7 V vs SCE.

More recently, the Tatsumi group detailed the synthesis of sulphide-bridged molybdenum copper complexes related to the active site of the CO dehydrogenase enzyme.⁸⁰ Several compounds were synthesised with a good resemblance to the active site, yet none exhibited reactivity towards carbon monoxide. This emphasises the difficulty in constructing a working mimic of biological systems.

1.3.3 Nitrogen fixation

Research into electrocatalysis of fixing nitrogen into ammonia has proceeded a long way since the discovery of dinitrogen binding to transition metal complexes.⁸¹ The latest results rely on well-protected iron or molybdenum cavities described by Schrock, discussed in detail later, and molybdenum complexes including PNP-type pincer ligands synthesised by Nishibayashi.

The molybdenum system reported by Nishibayashi gives almost triple the turnover rates over the systems described by Schrock, as 23 equivalents of ammonia are produced with respect to the catalyst.⁸² The formation of ammonia from this system relied on a bimetallic structure of two molybdenum centres bearing tridentate PNP type pincer ligands, bridged by dinitrogen, Figure 7.



in an ammonia yield of only 2 equivalents based on available nitrogen atoms present. These ligands can also be carbon monoxide; however this dramatically reduced the yield of ammonia so the dinitrogen ligands must be of some importance. The reaction also required a vast excess of reducing cobaltocene equivalents, 216 equivalents based on the catalyst where 23 counterparts of ammonia were produced, yielding only 32 % current efficiency.

The Holland group based their approach to reduction and hydrogenation of nitrogen to ammonia based on iron-potassium molecular catalysts taking inspiration from the current Haber-Bosch method. The Haber-Bosch process uses an iron surface promoted with potassium cations to catalyse the reaction. This is manipulated by Holland and co-workers to form a molecular iron complex that reacts with N₂ and a potassium reductant to give a complex with two nitrides, which are bound to iron and potassium cations.⁸³ The nitride complex reacted with acid and/or H₂ to give substantial, although not yet catalytic yields of ammonia. These reactions, however, provided structural and spectroscopic insight into N₂ cleavage and N-H bond forming reactions of iron. So far, only molybdenum and tungsten complexes have been shown to do this chemistry.

1.4 Scope of the work

The aims of this work was to develop molecular catalysts for reactions related to the formation of possible renewable energy vectors with the prospect of also harnessing solar energy. This was achieved by exploring (photo)electrocatalytic reactions at both conventional and semiconductor electrodes using electrochemical methods. The catalysts synthesised and used here all have at least some biological relevance to the active site of an enzyme, so any mechanisms for the catalytic behaviour seen could help to understand the mechanisms for the enzyme itself. The reductive catalytic reactions were studied using mainly electrochemical methods, as the idea was to implement them as part of a producer cell type set up. Only the reductive half of the cell was explored, so the finished cell would require an oxidative reaction to complete the circuit. However, to simplify the understanding of these types of producer cell reactions, studying them individually using an external bias from a potentiostat removes the complications of observing both half cells simultaneously.

Semiconductor electrodes based on p-type silicon were explored as a means of harvesting light energy to provide a photovoltage at the semiconductor-electrolyte interface, thus enabling hydrogen evolution and nitrogen fixation reactions to be driven at lower applied potentials.

1.5 References

1. IEA Key World Energy Statistics, **2010**
2. M. I. Hoffert, K. Caldeira, A. K. Jain, E. F. Haites, L. D. Harvey, S. D. Potter, M. E. Schlesinger, T. M. L. Wigley, D. J. Wuebbles, *Nature*, **1998**, 395, 881
3. IEA Key World Energy Statistics, **2012**
4. United Nations Development Program, **2003**, World Energy Assessment Report
5. Industry Issues: Putting the Heat on Gas- Environmental Health Perspectives (US National Institute of Environmental Health Sciences)
6. Modern Shale Gas Development in the United States: A Primer- DOE Office of Fossil Energy and National Energy Technology Laboratory
7. Chemicals Used in Hydraulic Fracturing- Committee on Energy and Commerce U.S. House of Representatives
8. Adapted from C. Ronneau, Energie, pollution de l'air et developpement durable, Louvain-la-Neuve: Presses Universitaires de Louvain, **2004**
9. National Oceanic and Atmospheric Administration (Noaa)
10. America's Climate Choices, Washington, D.C.: The National Academies Press, **2011**, p. 15
11. N. S. Lewis, D. G. Nocera, *Proc. Natl. Acad. Sci.* **2006**, 103, 15729
12. T. M. L. Wigley, R. Richels, J. A. Edmonds, *Nature*, **1996**, 379, 240
13. E. Maier-Reimer, K. Hasselmann, *Climate Dyn.* **1987**, 2, 63
14. K. Caldeira, M. E. Wickett, *Nature*, **2003**, 425, 365
15. REN21 Renewables **2012** Global Status Report
16. O. Morton, *Nature*, **2006**, 443, 19
17. N. S. Lewis, *Science*, **2007**, 315, 798
18. SunPower™ 318 Solar Panel Data Sheet, **2010**
19. Solar Junction Breaking CPV Efficiency Records, Greentech Media, **2011**
20. Renewables for Heating and Cooling, International Energy Agency, **2008**
21. How does it work? SODIS, **2011** (http://www.sodis.ch/methode/anwendung/index_EN)
22. Household water treatment and safe storage, World Health Organization, **2014** (http://www.who.int/household_water/research/technologies_intro/en/)
23. Solar Cookers International, **2010** (<http://www.solarcookers.org/basics/how.html>)
24. Solar-facts.com, **2014** (<http://www.solar-facts.com/batteries/battery-charging.php>)
25. Battery University, **2014** (http://batteryuniversity.com/learn/article/alternate_battery_systems)
26. H. Nealson, P. G. Conrad, *Biol. Sci.* **1999**, 354, 1923
27. R. J. Geider *et al.*, *Global Change Biol.* **2001**, 7, 849
28. C. B. Field, M. J. Behrenfeld, J. T. Randerson, P. Falkowski, *Science*, **1998**, 281, 237
29. Renewable biological systems for alternative sustainable energy production, Agricultural Services Bulletins, **1997**

30. Adapted from S. Sato, T. Arai, T. Morikawa, K. Uemura, T. M. Suzuki, H. Tanaka, T. Kajino, *J. Am. Chem. Soc.* **2011**, *133*, 15240
31. T. Arai, S. Sato, K. Uemura, T. Morikawa, T. Kajino, T. Motohiro, *Chem. Commun.* **2010**, *46*, 6944
32. J. A. Turner, *Science*, **2004**, *305*, 972
33. The energy "crisis" and British coal: The economics of the fuel market in the 1970s and beyond, C. Robinson, **1974**
34. P. Hoffmann, The Forever Fuel: The Story of Hydrogen, Westview Press, **1981**
35. A. Weimer, Development of Solar-powered Thermochemical Production of Hydrogen from Water, **2005**
36. J. A. Cracknell, K. A. Vincent, F. A. Armstrong, *Chem. Rev.* **2007**, *107*, 4206
37. J. C. Fontecilla-Camps, A. Volbeda, C. Cavazza, Y. Nicolet, *Chem. Rev.* **2007**, *107*, 4273
38. C. Pickett, C. Tard, *Chem. Rev.* **2009**, *109*, 2245
39. Burying the problem, Canadian Geographic Magazine, **2008**
40. The Global Status of CCS, The Global CCS Institute, **2012**
41. F. H. Hedlund, *Safety Science*, **2012**, *50*, 537
42. M. D. Zoback, S. M. Gorelick, *Proc. Natl. Acad. Sci.* doi:10.1073/pnas.1202473109
43. C. Amatore, J. M. Savéant, *J. Am. Chem. Soc.* **1981**, *103*, 5021
44. N. Hazari, *Chem. Soc. Rev.* **2010**, *39*, 4044
45. Nitrogen: Multiple and Regional Impacts, United States Environmental Protection Agency, **2002**
46. J. N. Galloway, J. D. Aber, J. W. Erisman, S. P. Seitzinger, R. W. Howarth, E. B. Cowling, B. J. Cosby, *Bioscience*, **2003**, *53*, 341
47. A. J. Ihde, *The development of modern chemistry*, Courier Dover Publications, **1984**
48. J. R. Jennings, *Catalytic Ammonia Synthesis*, Plenum Press, **1991**
49. Max. Appl. Ammonia, *Ullmann's Encyclopedia of Industrial Chemistry*, **2006**, Wiley-VCH, Weinheim, doi:10.1002/14356007.a02_143.pub2
50. United Nations Industrial Development Organisation (UNIDO), I.F.D.C.I. Fertiliser Manual, 3rd Ed. Kluwer Academic Publishers, **1998**
51. L. Forni, *Chem. Ind.* **2009**, *91*, 108
52. L. C. Seefeldt, B. M. Hoffman, D. R. Dean, *Annu. Rev. Biochem.* **2009**, *78*, 701
53. Adapted from R. M. Pasquarelli, D. S. Ginley, R. O'Hare, *Chem. Soc. Rev.* **2011**, *40*, 5406
54. A. D. Wilson *et. al.* *Proc. Natl. Acad. Sci.* **2007**, *104*, 6951
55. U. J. Kilgore *et. al.* *J. Am. Chem. Soc.* **2011**, *133*, 5861
56. P.-A. Jacques, V. Artero, J. Pecaut, M. Fontecave, *Proc. Natl. Acad. Sci.* **2009**, *106*, 20627
57. J. L. Dempsey, B. S. Brunschwig, J. R. Winkler, H. B. Gray, *Acc. Chem. Res.* **2009**, *42*, 1995
58. T. Liu, M. Y. Darensbourg, *J. Am. Chem. Soc.* **2007**, *129*, 7008
59. F. Gloaguen, T. B. Rauchfuss, *Chem. Soc. Rev.* **2009**, *38*, 100
60. A. M. Appel, D. L. DuBois, M. R. DuBois, *J. Am. Chem. Soc.* **2005**, *127*, 12717

61. H. I. Karunadasa, C. J. Chang, J. R. Long, *Nature*, **2010**, *464*, 1329
62. C. N. Valdez, J. L. Dempsey, B. S. Brunschwig, J. R. Winkler, H. B. Gray, *Proc. Natl. Acad. Sci.* **2012**, *109*, 15589
63. M. L. Helm, M. P. Stewart, R. M. Bullock, M. R. DuBois, D. L. DuBois, *Science*, **2012**, *333*, 863
64. A. Kutt, I. Leito, I. Kaljurand, L. Soovali, V. M. Vlasov, L. M. Yagupolskii, I. A. Koppel, *J. Org. Chem.* **2006**, *71*, 2829
65. B. E. Barton, M. T. Olsen, T. B. Rauchfuss, *J. Am. Chem. Soc.* **2008**, *130*, 16834
66. E. S. Wiedner, A. M. Appel, D. L. DuBois, and R. M. Bullock, *Inorg. Chem.* **2013**, *52*, 14391
67. J. M. Smieja, C. P. Kubiak, *Inorg. Chem.* **2010**, *49*, 9283
68. J. W. Raebiger, J. W. Turner, B. C. Noll, C. J. Curtis, A. Miedaner, B. Cox, D. L. DuBois, *Organometallics*, **2006**, *25*, 3345
69. M. Hammouche, D. Lexa, M. Momenteau, J. M. Savéant, *J. Am. Chem. Soc.* **1991**, *113*, 8455
70. I. Bhugun, D. Lexa, J. M. Savéant, *J. Am. Chem. Soc.* **1996**, *118*, 1769
71. C. Costentin, S. Drouet, M. Robert, J. M. Savéant, *Science*, **2012**, *338*, 90
72. J. D. Froelich, C. P. Kubiak, *Inorg. Chem.* **2012**, *51*, 3932
73. M. Beley, J. P. Collin, R. Ruppert, J. P. Sauvage, *J. Chem. Soc. Chem. Commun.* **1984**, 1315
74. M. Beley, J. P. Collin, R. Ruppert, J. P. Sauvage, *J. Am. Chem. Soc.* **1986**, *108*, 7461
75. G. B. Balazs, F. C. Anson, *J. Electroanal. Chem.* **1992**, *322*, 235
76. S. W. Ragsdale, J. E. Clark, L. G. Ljungdahl, L. L. Lundie, H. L. Drake, *J. Biol. Chem.* **1983**, *258*, 2364
77. M. Gnida, R. Ferner, L. Gremer, O. Meyer, W. Meyer-Klaucke, *Biochem.* **2003**, *42*, 222
78. M. Tezuka, T. Yajima, A. Tsuchiya, Y. Matsumoto, Y. Uchida, M. Hidai, *J. Am. Chem. Soc.* **1982**, *104*, 6834
79. H. Beinert, R. H. Holm, E. Munck, *Science*, **1997**, *277*, 653
80. M. Takuma, Y. Ohki, K. Tatsumi, *Inorg. Chem.* **2005**, *44*, 6034
81. A. D. Allen, C. V. Senoff, *Chem. Commun.* **1965**, 621
82. Y. Nishibayashi, *Dalton Trans.* **2012**, *41*, 7447
83. M. M. Rodriguez, E. Eckhard, W. W. Brennessel, P. L. Holland, *Science*, **2011**, *334*, 780

Chapter 2

Instrumentation and techniques

2.1 Electrochemical techniques

Electrochemistry can be a very powerful technique for analysing the behaviour of electroactive systems. There are many types of electrochemical techniques that can be used to study the mechanisms of the electroactive species and these include linear sweep voltammetry, cyclic voltammetry, potential step experiments, rotating disc electrode experiments. Electrochemistry can also be used to synthesise material on a bulk scale by a technique called controlled potential electrolysis or coulometry.

2.1.1 Cyclic voltammetry

Cyclic voltammetry (CV) is a very popular analytical technique due to the non-destructive nature of the procedure. The non-destructive nature comes from the use of a small electrode (area in the order of 10^{-1} cm^2 or less), so only a small amount of the electroactive species is altered at one time, leaving the bulk solution untouched. CV is being applied to an ever increasing range of systems and can provide useful information about redox behaviour of electrochemically active processes, over a wide potential range. This technique is very useful for preliminary mechanistic investigations, indicating the type of mechanism undertaken and the potential at which the process occurs.

During normal cyclic voltammetry with an inert working electrode, most commonly a vitreous carbon electrode, the electrode material does not participate in the electrochemical reaction. In other words, the electrode plays the role of a heterogeneous outer sphere electron donor (or acceptor). The direct reduction (or oxidation) of the substrate by the electrode requires a sizable overpotential to give rise to a significant current. An overpotential is subsequently required for the reaction to proceed at a substantial rate. This is particularly true when the reaction does not merely consist of an outer sphere electron transfer between the electrode and a reactant, but gives rise to bond breaking and bond formation. These further chemical reactions can simply be investigated by varying the sweep/scan rate.

CV works by applying a potential sweep to an electroactive substance in solution and measuring the current changes as the compound is oxidised, O , or reduced, R . The potential sweep involves selecting an initial start potential, E_1 , then sweeping to a second potential and halting, the vertex potential, E_2 , over a certain time; termed the scan rate. The potential is then swept backwards, usually back to the start potential, and typically at the same scan rate. This is defined as the end potential, E_3 and is explained pictorially in Figure 1..

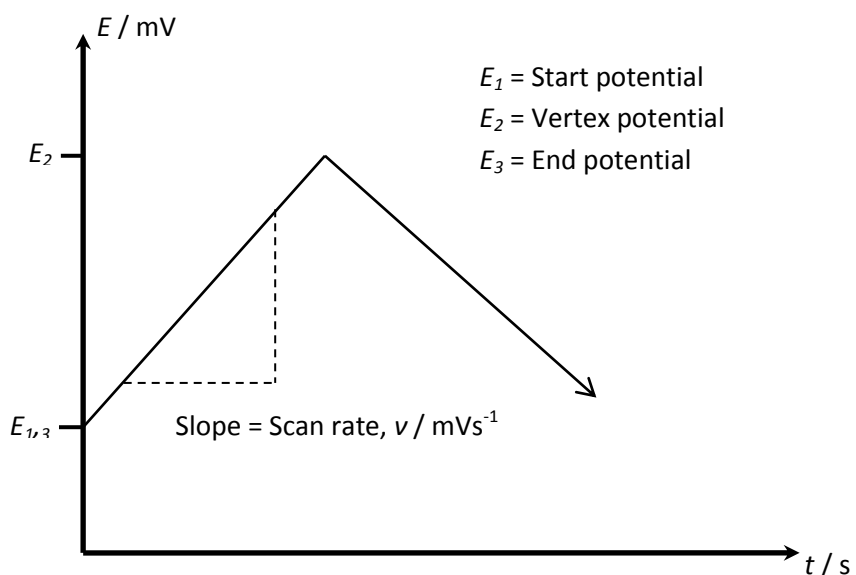


Figure 1 Potential vs time graph to show triangular sweep used in cyclic voltammetry.

As with any chemical or electrochemical procedure, the thermodynamics and kinetics of the electron transfer process must both be considered. This is achieved using the following mathematical methods.

If an electrochemical cell is left with no current flowing, eventually the potential of the working electrode will reach a steady state value indicating the cell is in equilibrium. The potential of the working electrode is then given by the Nernst equation, Equation 2.1.

$$E_e = E_e^\theta + \frac{RT}{nF} \ln \frac{c_O^\sigma}{c_R^\sigma}$$

(Equation 2.1)

The equilibrium potential is now related to the standard potential of the couple O/R , E_e^θ , and the surface concentrations, σ , of O and R (F = Faraday constant, 96485 C mol^{-1} ; n = no. of electrons).

If no current has flowed through the cell then no chemical reaction can have occurred, so the surface concentrations, c_O^σ and c_R^σ , must therefore be equal to the bulk concentrations, c_O^∞ and c_R^∞ . Consequently, the Nernst equation can be altered, Equation 2.2.

$$E_{cell} = E_e^\theta + \frac{RT}{nF} \ln \frac{c_O^\infty}{c_R^\infty}$$

(Equation 2.2)

Now the cell potential can be calculated from the bulk concentrations of the analyte constituents in solution.

If the potential of the working electrode is adjusted from the equilibrium potential, gauged by the bulk concentrations of O and R , equilibrium can only be reinstated when the surface concentrations of O and R have taken up new values as stipulated by the Nernst equation. For this to occur, a current is required to flow through the electrode/solution interface. If the working electrode is made more negative, O is converted to R by the passage of a cathodic current. The reverse is observed if the working electrode potential is made more positive.

These straightforward predictions of $I-E$ behaviour of the cell only cover the thermodynamics of the system. The kinetics of electron transfer at any potential will modify the magnitude of the current density flowing. However, the applied electrode

potential alters the rate constants for the electron transfer. To account for all these changes, the current density is calculated by the Butler-Volmer equation, Equation 2.3.

$$I = I_0 \left[\exp\left(\frac{\alpha_A nF}{RT} \eta\right) - \exp\left(\frac{\alpha_C nF}{RT} \eta\right) \right]$$

(Equation 2.3)

This fundamental equation of electrode kinetics illustrates the way in which current density varies with exchange current density (background current), I_0 , overpotential, η , and the transfer coefficients, α_A and α_C . The electron transfer coefficient usually takes the unitless value of 0.5 and the component signifies the fraction of the interfacial potential at the electrode/electrolyte interface that does electrostatic work on the electroactive material in solution to take it to the top of the free energy barrier.

Cyclic voltammetric measurements are concerned with looking at only a very small portion of the bulk solution at one time, the fraction at the electrode surface known as the Nernst diffusion layer. As a result of this, mass transport becomes a very important factor. There are three methods of mass transport.

Diffusion – the movement of a species down a concentration gradient which must occur whenever there is a chemical reaction at the electrode surface. If O is converted to R , the concentration of O is lower at the surface than in the bulk, while this is the opposite for R , hence O will diffuse towards and R away from the electrode surface.

Migration – the movement of charged species due to a potential gradient. It is the method by which charge passes through the electrolyte. The forces leading to migration are solely electrostatic; therefore any ionic species in solution can become charge carriers. With this in mind, the electrolyte is required in large excess to prevent the electroactive species becoming the charge carrier.

Convection – the movement of a species by mechanical forces.

In an unstirred solution with an excess of electrolyte as in cyclic voltammetry, diffusion is the only type of mass transport that the electroactive species can undergo. The simplest diffusion model assumes that the working electrode is perfectly flat and of infinite dimensions. Using these assumptions, the concentration deviations can only take place perpendicular to the electrode surface and diffusion can then be

characterised according to Fick's laws of diffusion. Fick's first law states that the flux of a species, i , through a plane parallel to the electrode is given by Equation 2.4.

$$\text{Flux, } J = -D_i \frac{dc_i}{dx}$$

(Equation 2.4)

D_i is the diffusion coefficient which typically has values in the region of $10^{-5} \text{ cm}^2 \text{ s}^{-1}$. The second law portrays the change in concentration of i with time attributable to the diffusion, Equation 2.5.

$$\frac{\delta c_i}{\delta t} = D_i \frac{d^2 c_i}{dx^2}$$

(Equation 2.5)

The flux of O or R can be equated with the flux of electrons by Equation 2.6,

$$\frac{I}{nF} = -D_o \left(\frac{\delta c_0}{\delta x} \right)_{x=0}$$

(Equation 2.6)

or Equation 2.7.

$$\frac{I}{nF} = -D_R \left(\frac{\delta c_R}{\delta x} \right)_{x=0}$$

(Equation 2.7)

This diffusion controlled process leads to the shape of the CV, a typical example is shown in Figure 2.

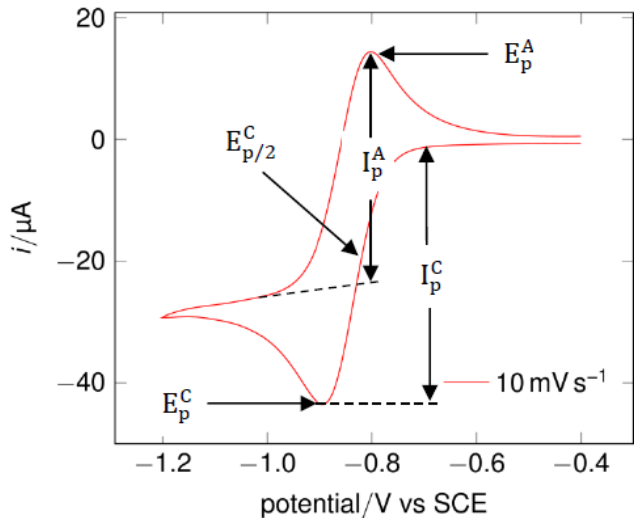


Figure 2 Cyclic voltammetry of cobaltocenium reduction in 0.1 M $[\text{NBu}_4][\text{BF}_4]$ -MeCN at a scan rate of 10 mV s^{-1} .

The exact form of the cyclic voltammogram can be determined mathematically by again solving Fick's second law for O and R to obtain Equation 2.8.

$$I_p = -0.4463 nF \left(\frac{nF}{RT} \right)^{\frac{1}{2}} c_0^{\infty} D^{\frac{1}{2}} \nu^{\frac{1}{2}}$$

(Equation 2.8)

This is called the Randles-Sevcik equation and can be reduced to the form shown in Equation 2.9 if standard temperature is 25 °C (298 K).

$$I_p = -(2.69 \times 10^5) n^{\frac{3}{2}} c_0^{\infty} D^{\frac{1}{2}} \nu^{\frac{1}{2}}$$

(Equation 2.9)

Here, I_p , the peak current density is in A cm^{-2} , D is in $\text{cm}^2 \text{s}^{-1}$, ν is in V s^{-1} and c_0^{∞} is in mol cm^{-3} . From this equation we can see that the peak current density is proportional to the concentration of electroactive species and to the square roots of the scan rate and diffusion coefficient. Adherence to this relationship can be used to establish the diffusion-controlled nature of the electrode process, and to determine either n or D if one of these is known independently.

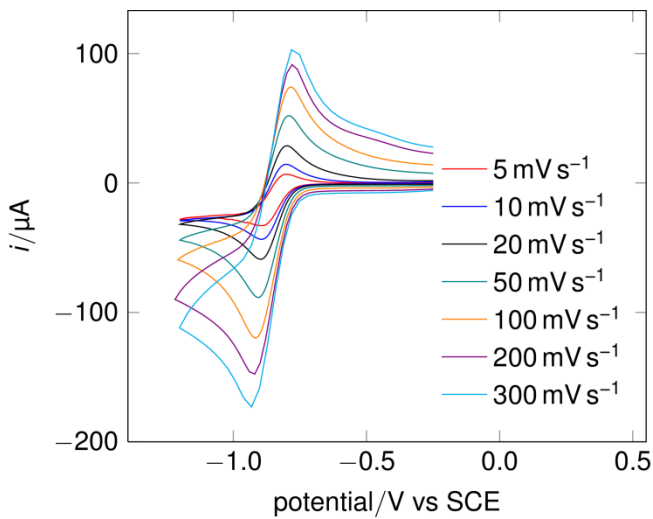


Figure 3 Cyclic voltammetry of cobaltocenium reduction in 0.1 M $[\text{NBu}_4]\text{[BF}_4]$ -MeCN at various scan rates.

Once data for a compound has been collected at various scan rates there are numerous methods for testing whether the system is reversible, as listed below.

1. $\Delta E_P = E_P^A - E_P^C = 59/n \text{ mV}$

2. $|E_P - E_{P/2}| = 59/n \text{ mV}$

3. $|I_P^A/I_P^C| = 1$

4. $I_P \propto \nu^{1/2}$

5. E_P is independent of ν

If the system does not comply with one or more of the above conditions then it is implied that the electron transfer of the system is not reversible on the timescale of the experiment and the experiment is more complicated.

In certain cases, a redox active species may adsorb on the electrode surface. Where both partners of a reversible couple remain bound then the cyclic voltammogram has a symmetric shape with:

7. $\Delta E_P = E_P^A - E_P^C = 0 \text{ mV}$

8. $|I_P^A/I_P^C| = 1$

9. Peak width at half height = $90/n \text{ mV}$

$$10. I_P \propto \nu$$

The latter relationship provides a ready means of distinguishing solution and surface confined redox processes.

2.1.1.1 Non-reversible systems

For reversible systems, the rate of electron transfer at any potential is always considerably greater than the rate of mass transport. This implies that a Nernstian equilibrium is always maintained at the electrode surface. When the rate of the electron transfer cannot maintain this equilibrium, the shape of the cyclic voltammogram changes and the system is said to be irreversible. At low scan rates, the rate of electron transfer can still be larger than that of mass transfer, so a reversible voltammogram is recorded. Conversely, as the scan rate is increased, the rate of mass transfer increases and becomes comparable to the rate of electron transfer. This most notably effects the peak separation which becomes larger as the scan rate is increased. However, the most prominent trait of an irreversible system seen in a cyclic voltammogram is the lack of a reverse peak.

There are two possible explanations for a redox active system to operate irreversibly in a cyclic voltammetric experiment. These are either slow electron transfer or coupled chemical reactions. An example of an electrochemical process that exhibits slow electron transfer is where a spin-state change occurs, as in $\text{Co}^{\text{III}}/\text{Co}^{\text{II}}$ redox couples.¹ There are many examples of electrochemistry with coupled chemical reactions and this will be covered later.

If a system demonstrates slow electron transfer, it is common for the cyclic voltammogram to show reversibility at slow scan rates and irreversibility at fast scan rates. In the transitional region between these two states is a region where the voltammogram is partially reversible. Here the system is said to exhibit quasi-reversibility. This changeover from reversibility arises from the rate of electron transfer becoming insufficient in comparison to the rate of mass transport and therefore the Nernstian equilibrium at the electrode surface cannot be maintained. In the quasi-

reversible region both, the forward and back reactions contribute to the observed current. The region is usually confined to the region defined by Equation 2.10,

$$0.3 v^{1/2} \geq k_s \geq 2 \times 10^{-5} v^{1/2} \text{cm s}^{-1}$$

(Equation 2.10)

where k_s is the rate constant for the electron transfer.

Values for the electron transfer rate constant, k_s , can be obtained from ΔE_P values by virtue of working curves that have already been constructed.² Working curves are a plot of Equation 2.11.

$$n\Delta E_P \text{ vs } \log \Psi \quad \text{where } \Psi = (RT/nFD\pi v)^{1/2} k_s$$

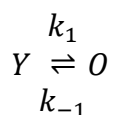
(Equation 2.11)

Rate constants of up to 1 cm s^{-1} can be calculated from this method. Alternatively, digital simulation of experimental data can be used to calculate the electron transfer rate constant and this will be discussed later.

In the case of coupled chemical reactions the scan rate has the opposite effect in that voltammograms become more reversible at higher scan rates. This is due to the reduced amount of time available for the chemical reaction to take place on the electrolysed species at the electrode surface.

There are many types of coupled homogeneous chemical reactions that are characterised by their mechanism.

The first is a CE mechanism which can be represented by Equations 2.12 and 2.13.



(Equation 2.12)



(Equation 2.13)

These types of reactions typically include reduction of weak acids whereby the proton is reduced once it has been dissociated.

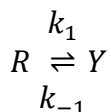
Tests for a CE mechanism are:

1. $I_P^C/v^{1/2}$ decreases as v increases
2. $|I_P^A/I_P^C|$ increases with v and is always ≥ 1

The second is an EC mechanism is a very common mechanism in organic electrochemistry and is described by Equations 2.14 and 2.15.



(Equation 2.14)



(Equation 2.15)

The cyclic voltammogram observed varies depending on the rates of the two steps. The simplest case is where the electron transfer is entirely irreversible. Here no kinetic data can be obtained as the chemical reaction has no effect on the voltammogram.

The effect of a following chemical reaction is most easily noticed by the effect on the reverse scan, where R is oxidised. For a fast chemical reaction, R is rapidly removed from the region near the electrode by diffusion. Consequently, at low scan rates no reverse peak is witnessed. As the scan rate is increased the reverse peak becomes increasingly visible because the time for diffusion of R away from the electrode surface is diminished.

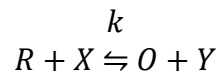
EC reactions can be diagnosed by:

1. $|I_P^A/I_P^C|$ is always less than 1 but tends to 1 as v increases
2. $I_P^C/v^{1/2}$ decreases slightly as v increases

The catalytic mechanism is a specific type of following chemical reaction whereby the reactant, O , is regenerated chemically, Equations 2.16 and 2.17.



(Equation 2.16)



(Equation 2.17)

Analysing these types of reaction mechanisms is difficult as they behave according to second order conditions. Therefore, systems are usually conditioned in such a way that $c_X^\infty \gg c_O^\infty$. In this way, the concentration of X remains in essence constant during the experiment and the reaction mechanism can be treated as *pseudo* first order. Under these *pseudo* first order conditions, where k is small or ν is large then the chemical reaction has no effect and a reversible voltammogram is recorded. However, if k is faster or ν is reduced then catalysis inevitably will occur, so more reactant, O , is regenerated and consequently more current, $|I_p^C|$, is produced. This value will subsequently exceed the value predicted by the Randles-Sevcik equation. The values of $|I_p^C/\nu^{1/2}|$ increase with slower scan rates and the voltammogram peak becomes less defined as the limit of catalysis is approached. When the limit is attained, the peak disappears and is replaced by a scan rate independent plateau. The current density of the plateau is given by Equation 2.18.

$$I_{cat} = -nFc_O^\infty \sqrt{D(kc_X^\infty)}$$

(Equation 2.18)

Therefore, values of k can easily be obtained from the experimental value of I_{cat} .

Catalytic turnover frequencies were recently determined for a hydrogen evolution catalyst by DuBois *et al.* from Equation 2.19.³

$$\frac{i_{cat}}{i_p} = \frac{n}{0.4463} \sqrt{\frac{RT(k[c_X^\infty])}{F\nu}}$$

(Equation 2.19)

This is ultimately derived from the same method as above, as Equation 2.19 is derived from the division of the formula for I_{cat} , Equation 2.18, by the formula for I_p , Equation 2.8. This method requires an accurate measure of the one electron I_p for the catalyst in the absence of substrate and the value of I_{cat} that is achieved at a plateau in catalysis. For hydrogen evolution catalysis, where the substrate is H^+ , the equation can be further simplified by assuming that two electrons are passed for each molecule of H_2 produced and that the acid concentration does not change in the course of the measurement as it is in a large excess. This yields Equation 2.20 to calculate the catalytic turnover frequency.

$$k_{obs} = \nu \left(\frac{i_{cat}/i_p}{0.72} \right)^2$$

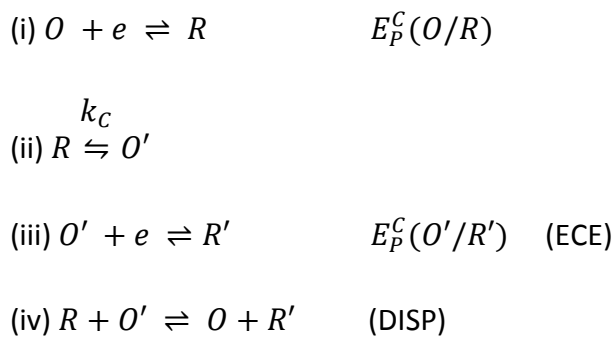
(Equation 2.20)

In a substrate independent regime, where an increase in acid concentration will not affect the peak current as there is another limiting factor in the catalytic cycle, k_{obs} is equal to k_{cat} . In a substrate dependent regime, the catalytic rate constant, k_{cat} , is achieved by dividing by the concentration of substrate.

A catalytic mechanism can be recognised by:

1. $|I_P^C/\nu^{1/2}|$ increases with decreasing ν
2. I_P^C may reach a limiting value at low scan rates
3. $|I_P^C|$ values are greater than predicted by the Randles-Sevcik equation
4. $|I_P^A/I_P^C| \ll 1$

The ECE mechanism follows a pathway where the initial reaction product reacts chemically to yield a species O' , which itself is not as readily reduced as O .



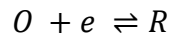
Scheme 1 ECE mechanism.

These multi-electron transfer processes are most common in organic electrochemistry, but are also possible in inorganic electrochemistry. However, even for relatively simple experimental schemes there are many variables than can affect the CV response. These are not only the first order rate constant, k_c , the timescale and the scan rate employed, but also the thermodynamics of the two redox couples involved, O/R and O'/R' and their electrode kinetics (*i.e.* whether the couples are electrochemically reversible or not). For the forward peak, when k_c is large compared to the rate of mass transport, the electrode reaction will appear to be an $(n_1 + n_2)$ electron process as R will rapidly convert to O' , which reduces further. Conversely, if k_c is low it will behave like an n_1 electron process since R will not react to produce significant quantities of O' within the timescale of the experiment, as the kinetics are slow compared to the scan rate. Thus for a given system, the apparent number of electrons involved, n_{APP} , will decrease from $(n_1 + n_2)$ towards n_1 as the scan rate increases. If O' is as readily reduced as O , then the forward peak will increase from a one electron process at fast scan rates to a two electron process at slow scan rates where response profiles Equation 2.21.

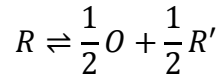


There can be difficulty discriminating between an ECE mechanism and a mechanism involving disproportionation.⁴ This arises in a number of electrode reactions that behave as if multiple electrons are simultaneously transferred. For example, a first electron is transferred in a reduction reaction mechanism which is followed by a chemical reaction, with the product being more or as easily reduced as the starting material, thus producing an overall two-electron process as shown in Scheme 1. The

second electron transfer may occur either heterogeneously at the electrode via reaction (iii) or homogeneously in the bulk solution via disproportionation reaction (DISP mechanism) with electron transfer from the primary reduced species as in equation (iv). This discrimination becomes important when the DISP mechanism is more complicated, for instance when other reactions such as H atom transfer or dimerisation compete with the two electron process. These two mechanistic ambiguities can be distinguished by performing a double potential step chronoamperometry experiment.⁵ Assuming a reductive process as described above, the potential is started at a value positive of both the $E_P^C(O/R)$ and $E_P^C(O'/R')$ redox couples. It is then stepped to a value negative of these two couples, then the second step is to a potential midway between $E_P^C(O/R)$ and $E_P^C(O'/R')$ so that the reduction of O' to R' can be driven but also the oxidation of R to O . If a DISP mechanism takes place, the resultant current is oxidative due to the reconversion of R to O and negligible O' is present. The mechanism is outlined in Equations 2.22 and 2.23.



(Equation 2.22)



(Equation 2.23)

If an ECE mechanism takes place, in the second step, there will be contributions to the current from both the oxidation of R and also the reduction of O' so there should principally be some distinction. In favourable cases, a characteristic ‘hump’ appears during the second step in an ECE mechanism and not in a DISP one.

Tests for these two similar mechanisms include:

1. $|I_P^C/v^{1/2}|$ varies with scan rate but may reach limiting values at high and low scan rates, Equation 2.24.

$$|I_P^C/v^{1/2}| \text{ (low } v) > |I_P^C/v^{1/2}| \text{ (high } v)$$

(Equation 2.24)

2. $|I_P^A/I_P^C|$ increases with scan rate and tends to one at high scan rates.

2.1.1.2 Experimental problems with cyclic voltammetry

All transient electrochemical techniques carry an additional double layer charging current attributed to the supporting electrolyte. This contributes to the total current along with the faradaic current of the system under analysis. It is described Equations 2.25 and 2.26.

$$I_{dl} = C_{dl}\nu$$

(Equation 2.25)

$$I_{total} = I_{faradaic} + I_{dl}$$

(Equation 2.26)

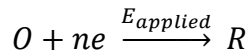
From this you can see that the charging current, I_{dl} , is proportional to ν , whereas $I_{faradaic}$ is proportional to $\nu^{1/2}$. This is not a problem at moderate scan rates of 100 mV s⁻¹, I_{dl} will take very small values of between 2 and 4 μA cm⁻². However, if high scan rates such as 100 V s⁻¹ are required, then the double layer charging current is no longer insignificant and cyclic voltammograms may become distorted or hidden beneath the charging current.

The problem of iR drop (potential drop) changes the applied voltage from the necessary value, $E_{obs} = E_{app} - iR$. This has the effect of decreasing peak heights and increasing peak separations. This behaviour is very similar to that expected for a slow electron transfer step, so the two must not be confused. Therefore, when interpreting whether a system has slow electron transfer or suffering from iR drop, it is best to check the behaviour of a well known reversible electrochemical couple such as ferrocene.

2.1.2 Controlled potential electrolysis (CPE)

Coulometric experiments are used to electrochemically synthesise products, whereby the charge consumed by the oxidation or reduction of the starting material is measured at an electrode under potentiostatic control. If only the oxidised species is initially present, then the working electrode potential is set at a constant value

sufficiently negative to cause rapid reduction of the analyte, Equation 2.27. The potential is maintained at this value until only the reduced species is present in solution.



(Equation 2.27)

As the oxidised species is consumed the current decreases, reaching a plateau at a value close or equal to zero when the conversion is completed. A residual current usually remains that is attributed to the charging current or background impurities (charging current is dynamic so tends to zero when the potential is fixed). The experimental results are recorded by a current-time curve, usually in the shape of an exponential decay, Figure 4.

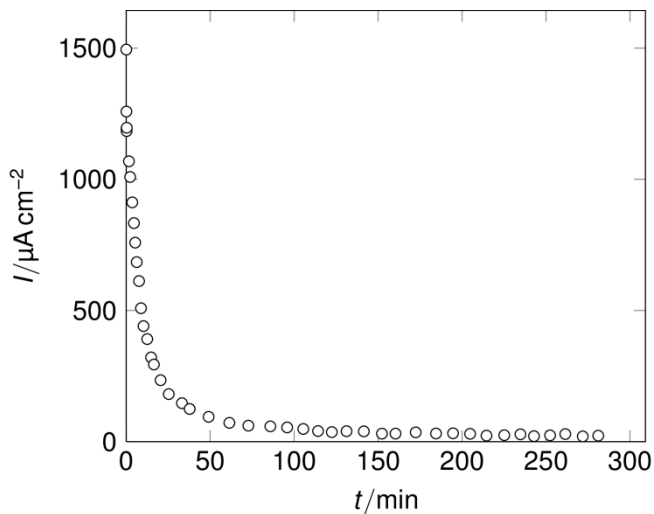


Figure 4 Current-time curve.

The charge consumed during the experiment, measured in coulombs (C), can be obtained from the area beneath the current-time curve by integrating the current over the time of the experiment, Equation 2.28.

$$Q(t) = \int_0^t i(t) \cdot dt$$

(Equation 2.28)

The number of electrons, n , required for the reduction of starting material, O , to a product, R , at the applied potential can then be calculated through Faraday's law, Equation 2.29.

$$Q = nFN$$

(Equation 2.29)

Here, N represents the total number of moles of starting material present at the beginning of the electrolysis and F is Faraday's constant (96485 C mol^{-1}).

The rate of electrolysis (the cell current) for a given volume in the working electrode compartment is governed by two variables; the electrode area and the rate of stirring of the solution. The rate of stirring of the solution will determine the thickness, δ , of the diffusion layer, which then determines the flux of the electroactive material to the electrode surface and therefore the magnitude of the current.

At the surface of the electrode, the concentration of the starting material, O , can be approximately considered as zero, $c_O^0 = 0$, because it is reduced immediately on arrival. At a distance corresponding to the diffusion layer, δ , the concentration of O attains that of the bulk solution, c_O^∞ . Using Fick's first law of diffusion (the flux of a material to the concentration gradient across a planar boundary, where D is the diffusion coefficient of the species concerned), if the electrochemical reaction rate is limited by diffusion not electron transfer kinetics, the current density I ($I = i / \text{electrode area, } A$) can be calculated, Equations 2.30 and 2.31.

$$\text{Flux, } -J = D \frac{dc}{dx}$$

(Equation 2.30)

$$I = nFD_0 \frac{c_{bulk}^0}{c_{surface}^0} = nFD_0 \frac{c_{bulk}^0}{\delta} = \frac{i}{A}$$

(Equation 2.31)

From this direct relationship, it can be seen that if the diffusion layer thickness is halved by increasing the stirring rate, the cell current will double and the electrolysis completion time will half.

2.1.3 Calculation of efficiencies and yields

After exhaustive controlled potential electrolysis experiments where an electrocatalyst has been employed, various values are taken which give a measure of the efficiency of the catalyst.

2.1.3.1 Chemical yield

The chemical yield is a measure of the percentage of the product achieved experimentally based upon the maximum amount of product that is theoretically possible, Equation 2.32.

$$\text{Chemical Yield} = \frac{\text{Product produced}}{\text{Product expected}} \times 100 \%$$

(Equation 2.32)

This value is easily calculated for hydrogen evolution electrocatalysis experiments where a known number of equivalents of acid (H^+) is added. The theoretical maximum amount of hydrogen can be calculated from the redox equation, Equation 2.33.



(Equation 2.33)

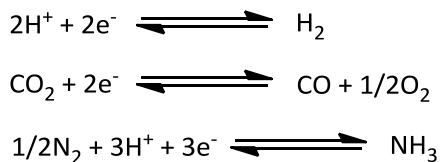
2.1.3.2 Current efficiency

The current efficiency is a measure of the electrochemical efficiency of the catalyst. It is the theoretical amount of charge required to produce a fixed number of moles of product divided by the experimental quantity of charge consumed to produce the same amount and is expressed as a percentage, Equation 2.34.

$$\text{Current Efficiency} = \frac{\text{Theoretical charge(C)}}{\text{Actual charge consumed (C)}} \times 100 \%$$

(Equation 2.34)

For example, the theoretical charge required to convert one mmol of protons to dihydrogen is determined by the stoichiometry in Scheme 2 and is $10^{-3} F = 96.49 \text{ C}$.



Scheme 2 Redox reactions encountered in this thesis.

If this process is found to produce 0.5 mmol of H_2 after the passage of 100 C then the current efficiency is 96.49 %.

2.1.3.3 Turnover number (TON) and turnover frequency (TOF)

The definition of turnover number can be ambiguous. Originally defined by biochemists as the number of turnovers an enzyme can undergo before total loss of activity, it has been used by chemists (and electrochemists) using the definition shown in Equation 2.35.

$$\text{TON} = \frac{\text{No. mols product}}{\text{No. mols catalyst}}$$

(Equation 2.35)

Whereas this definition of TON is convenient for conventional homogeneous catalysis, in an electrochemical experiment where only a fractional quantity of the catalyst is engaged in turnover, in the reaction layer adjacent to the electrode, its use is limited. Moreover, within the biochemical definition, electrocatalyst depleted in the reaction layer is replaced by that in bulk solution. The derived parameter, turnover frequency TOF, *i.e.* TON h^{-1} is similarly limited as it will depend on the ratio of electrode area to cell volume and the stirring rate. Saveant has discussed these definitions in electrochemical and chemical contexts.⁶ Nevertheless, within the context of comparison of a set of experimental results undertaken under the same conditions, rather than as absolute figures of merit, TON and TOF are of some value.

2.1.4 Electrocatalysis

Catalysts are required for some chemical processes to enable the reactions to occur at convenient rates, even if the reaction is thermodynamically favourable. This is the same for electrode reactions as they may only occur at high overpotentials due to poor kinetics. The aim of electrocatalysis is consequently to unearth alternative routes that require lower activation energies and hence allow such electrode reactions to occur at high current density, closer to the thermodynamic potential of the reaction. Electrocatalysis is important to many applications of electrochemistry since the energy efficiency of any cell is determined by the overpotentials involved at the anode and cathode. The efficiency of a cell is particularly important when the electrochemistry will be applied to fuel cell technology, as any overpotential will result in less energy or fuel created by the cell. The overpotential is given by the Tafel equation, Equation 2.36.

$$\eta = \frac{2.3RT}{\alpha_c nF} [\log I - \log I_0]$$

(Equation 2.36)

Catalysts for reducing overpotential of electrode reactions can be by either species attached to the electrode surface or dissolved in the electrolyte.

Currently, the reactions of the greatest importance of electrocatalysis are those that are required for use in producer cells, such as for hydrogen and oxygen evolution.

2.1.5 Semiconductor electrochemistry

2.1.5.1 Background to semiconductor electrochemistry

The widespread interest in the use of semiconductor materials for electrochemical studies was initiated by the oil crisis back in the early 1970s. This was when the first search for renewable energy suddenly became apparent. Work by Fujishima and Honda who reported the photoelectrochemical splitting of water using a titanium dioxide electrode in 1972 gave the semiconductor research area a greater awareness.⁷

This premise of being able to generate hydrogen using sunlight encouraged a wave of scientists to involve themselves in semiconductor electrochemistry.⁸⁻¹³

The main underlying problem with the semiconductor solar cell setup is that reactions related to the production of fuel rely on successive rapid electron transfer to and from the solution redox species. This is because production of fuels such as hydrogen from protons and carbon monoxide from carbon dioxide require electrochemical reductions needing more than one electron. In semiconductors, side reactions such as electron-hole recombination limit the supply of electrons to the electrocatalyst and therefore the semiconductor electrode often limits the reaction rate.

The field then saw a remarkable resurgence of activity following a paper by Oregan and Gratzel reporting that a stable photoelectrochemical cell could be made using nanocrystalline titanium dioxide coated with a ruthenium-based sensitising dye.¹⁴ This not only reintroduced semiconductors as viable materials, but also created a new area of research in dye sensitised solar cells (DSSCs).

2.1.5.2 Theory behind semiconductor electrochemistry

Semiconductors can reduce the potential required for a redox couple upon visible illumination. Wrighton showed that p-type silicon photoelectrodes could be used to effect uphill reactions by around 500 mV.⁹ It was shown that the conversion of water to hydrogen catalysed by a bipyridine derivative can be shifted from -1.23 V at a reversible platinum electrode, to -0.73 V at an illuminated p-type silicon electrode as shown by cyclic voltammetry. This phenomenon is rationalised by the promotion of electrons from the valence band to the conduction band upon illumination with light of the correct wavelength, Figure 5.

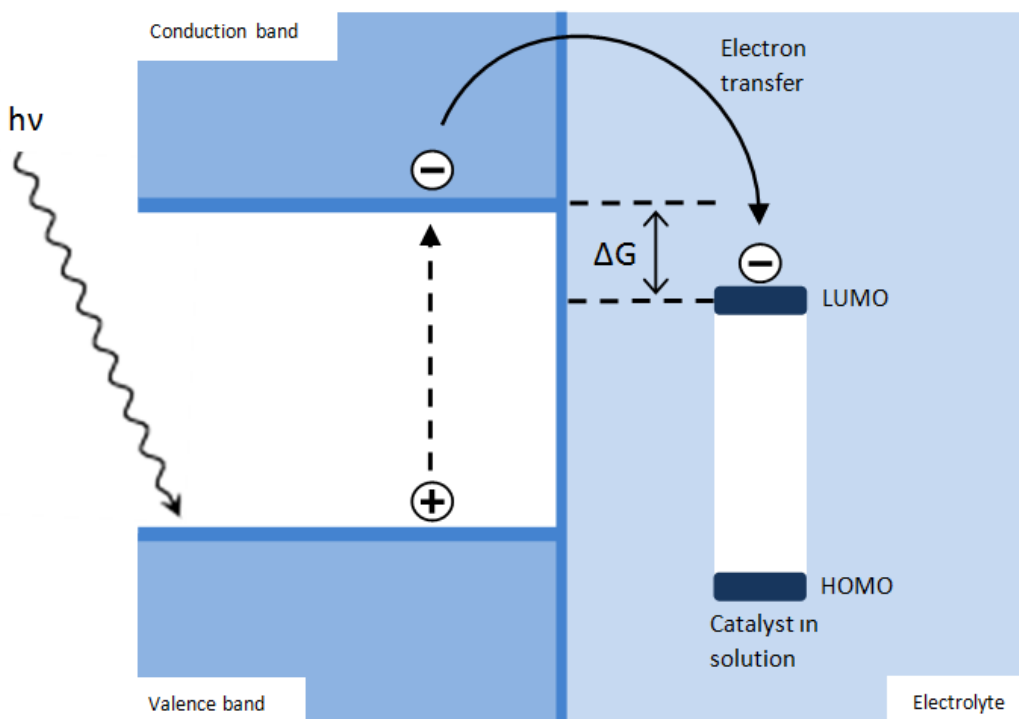


Figure 5 Promotion of electrons to conduction band in illuminated p-type silicon and movement across semiconductor/electrolyte interface.

The most effective wavelength of light for this process in semiconducting silicon can be measured in terms of quantum efficiency (QE), the efficiency with which the light is converted to electrons. Using this method it was found that the most effectual wavelength of light was 400-800 nm. Above 800 nm QE drops off and reaches zero at 1100 nm, consistent with the 1.1 eV band gap of silicon. The position of the silicon band gap in two different electrolytes was measured as +0.05 V to -0.85 V vs SCE.¹³

Also noted was that redox couples could be seen outside the 1.1 eV bandgap of silicon. The ability to observe redox couple outside the bandgap of silicon is attributed to the fact that ‘both bands’ (valence band and conduction band) move with applied potential. The unpinning of the semiconductor band edges at the semiconductor/electrolyte interface is suggested to be the reason for this. If the unpinned band edges move with applied potential then the semiconductor behaves like a metal, in that changes in applied potential occur across the Helmholtz layer rather than across the space charge layer of the semiconductor.

The actual mechanism for electron transfer at a semiconductor/electrolyte interface is more complicated. The movement of the majority carriers create a charge separation.

In a p-type semiconductor, a negative surface charge is accomplished by a depletion of the valence band holes (positive charges) as shown in Figure 6.¹⁵

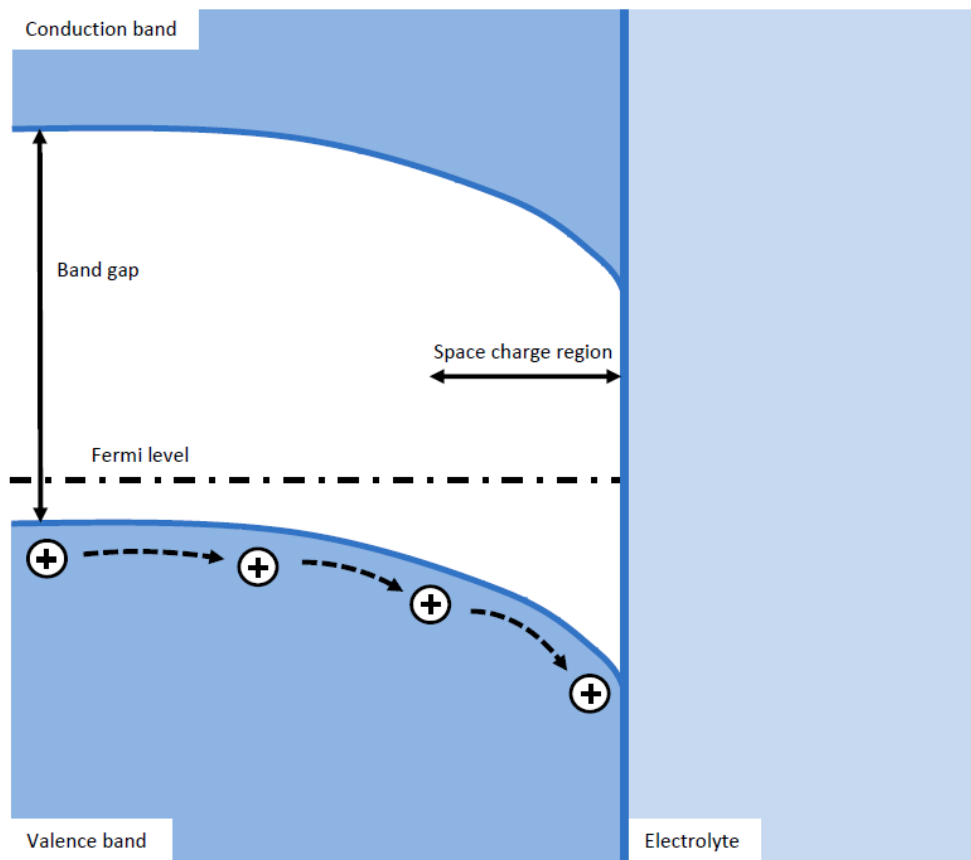


Figure 6 Representation of the mechanism of electron transfer at a p-type semiconductor/electrolyte interface.¹⁵

The valence band holes migrate towards the semiconductor/electrolyte interface where they are removed by the flow of the current. The electric fields associated with these charge distributions result in the curvature of the valence and conduction bands. The section where this curvature takes place is known as the space charge region and the depth is related to the doping density, the electrical properties of the material and the magnitude of the electric field. In the dark, the high concentration of majority carriers compared to minority carriers (valence band holes in the case of a p-type semiconductor) dominate the current, concluding that electron transfer is from the valence band. Upon illumination, photocurrent responses reflect a combination of electron transfer processes involving both minority and majority carriers.

2.1.5.3 Limitations of semiconductor electrochemistry

The efficiency of a solar cell is ultimately determined by the quantum yield of minority carriers available in the electrolyte, so the limiting factors leading to this need to be thoroughly understood. The main limiting factor is recombination: the union of the two opposing energy carriers, an electron and a hole. Electron hole recombination can occur in two regions within a semiconductor as shown Figure 7, either coming together in energy levels in the space charge region, R_1 , or at the surface via surface states, R_2 .

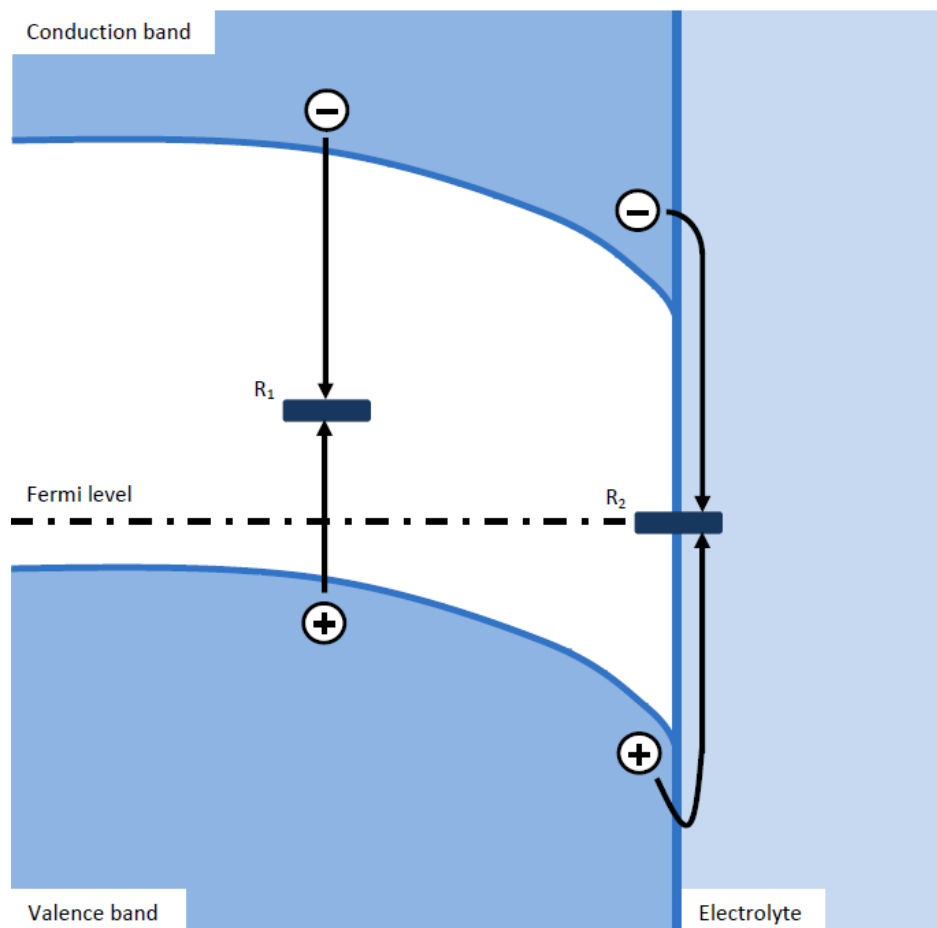


Figure 7 Possible recombination pathways in n p-type semiconductor.¹⁶

The largest effects of recombination are apparent at low band bending, *i.e.* at potentials close to the flatband potential, since the recombination rate depends on the density of minority carriers.¹⁶

2.1.5.4 Measures of photoelectrochemical efficiency

There are three important electrical output quantities for a semiconductor/electrolyte junction incorporated within a solar cell type arrangement.¹⁷ The first is the short-circuit photocurrent density, I_{SC} . This quantity is the obtainable current density when photogenerated charges are free to flow through the external circuit. This provides information on the net quantum yield for charge separation and as a measure of the yield of minority carriers that survive to cross the semiconductor/electrolyte interface. At short circuit, no net power is produced by the completed cell because the voltage across the cell is zero. Therefore, the short-circuit current is the largest current which may be drawn from the solar cell. The second parameter is the open-circuit voltage, V_{OC} . This is the maximum voltage produced from a solar cell and occurs when the net current through the cell is zero, so again the cell will produce no power. This value reflects the Gibbs free energy that can be produced by the photogenerated carriers. As described at both the short-circuit current and the open-circuit voltage, the power from the solar cell is zero. Therefore, the third parameter, the ‘fill factor’ is the key quantity. In conjunction with V_{OC} and I_{SC} , it determines the maximum power from a solar cell. The fill factor is defined as the ratio of the maximum power (P_J) from the solar cell to the product of V_{OC} and I_{SC} . Graphically, the fill factor is a measure of the ‘squareness’ of the solar cell, Figure 8.

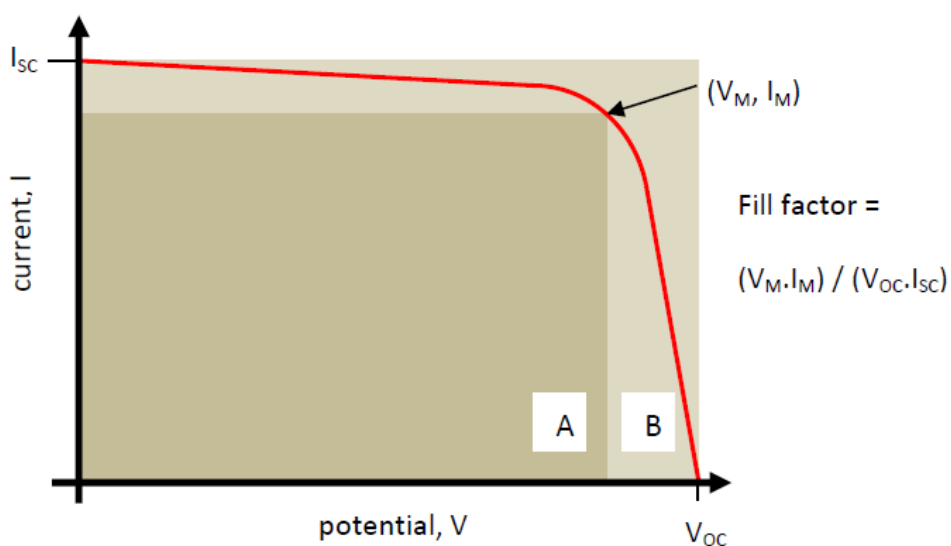


Figure 8 Fill factor diagram for a solar cell.¹⁸

2.1.6 Design of electrochemical cells

Electrochemical cells consist of the electrodes and electrolyte in glass compartments that are commonly separated by glass frits. Three electrodes are regularly employed: a working electrode which is used to probe the material under investigation, a reference electrode that maintains a constant reference potential, and a secondary (or counter) electrode to supply the current, Figure 7. The cell must be designed so that the data collected is characteristic of the properties of the reaction at the working electrode.

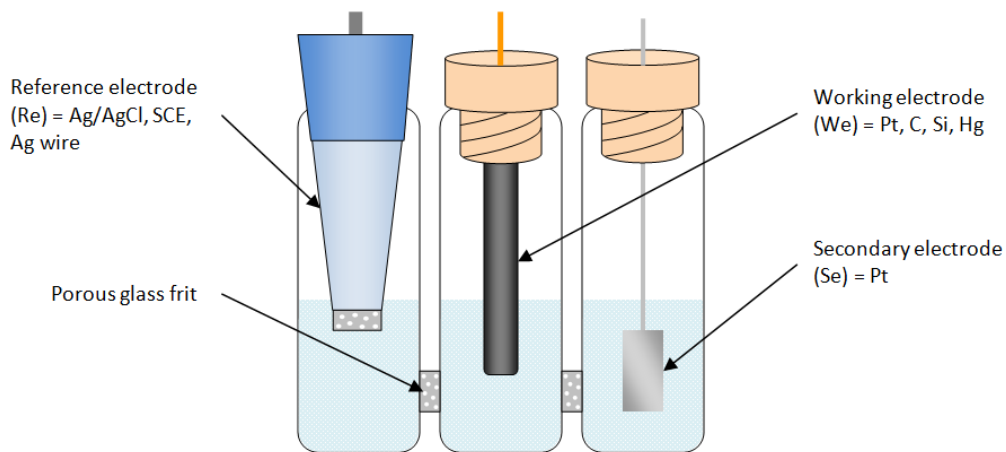


Figure 9 Diagram of 3 compartment electrochemical cell containing electrodes.

For cyclic voltammetry, the separation of the 3 electrodes into individual compartments is not always necessary. A simple CV experiment can be done in a single compartment, if the reference electrode does not offer any interference to the analyte, as such a small amount of the bulk concentration is oxidised or reduced at one time. For experimental accuracy and reproducibility it is best to use a three compartment cell. However, separation of the electrode compartments in this way may lead to significant iR drop. There are ways in which iR drop can be avoided, such as changing experimental parameters: reducing electrode area, lowering scan-rate, minimising analyte concentration. Alternatively, cell construction can be improved, for example using a ‘Luggin’ capillary to connect the reference and working electrode compartments in place of a glass frit.

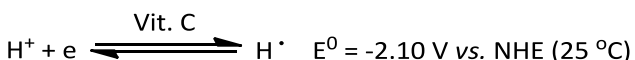
However, for controlled potential electrolysis it is imperative that the cell used consists of three chambers separated by glass frits. One chamber has the working electrode. This chamber should be stirred to provide maximum mass transport to the electrode during electrolysis. The reference electrode is usually housed in a separated second compartment and the third chamber houses the secondary electrode. Both the working and secondary electrodes should have a large surface area, so are typically platinum meshes, large pieces of vitreous carbon or mercury electrodes. Changes in the applied potential during electrolysis are a major problem since different chemical reactions can be accessed at different potentials. A bare silver wire is rarely used as a reference electrode during a controlled potential electrolysis since its potential depends on the composition of the solution with which it is in contact. The point of a controlled potential electrolysis is to change the solution composition, so a shifting reference potential will result in drift in the applied potential. Therefore, either a fixed potential reference electrode such as Ag/AgCl or SCE is used or the compartment containing a *pseudo* reference electrode must only be exposed to solution whose composition does not change.

2.1.7 Electrodes

2.1.7.1 Working Electrodes

Working electrodes are extremely diverse as the design is completely dependent on the type of experiment studied. In experiments for examining mechanisms and kinetics, the working electrode is a small sphere or disc, or a short wire, with the area normally no more than 0.25 cm^2 as this reduces resistivity. Other larger types of electrodes that can be incorporated are metal foils, semiconductors, evaporated thin films or powders pressed into pellets. The most essential feature of a working electrode however, is chemical resistance to the solvent, electrolyte and any other components that it could come into contact with. In addition to this, it is preferable for the electrode surface to be smooth so the geometry and mass transport are then better defined. The working electrodes employed here are vitreous carbon, platinum, gold, mercury pool and semiconductor electrodes.

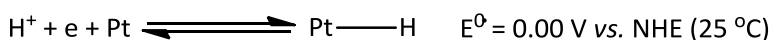
Vitreous carbon (or glassy carbon) electrodes are nearly ubiquitous in the laboratory today because of their availability in various shapes and forms, and usefulness over a wide potential range. It is made by pyrolyzing a carbon polymer to a temperature of around 2000 °C. The resulting material retains high conductivity, hardness and inertness. The exact structure of glassy carbon has long been a subject of debate and there are currently two hypotheses. The two suggested structures are an intertwining ribbon-like structure¹⁹ and a fullerene type structure.²⁰ The inert behaviour of vitreous carbon to nearly all substrates leads to the versatility. This is particularly useful when looking into hydrogen evolution catalysis.



(Equation 2.37)

The very negative reduction potential for the homogeneous activation of protons means that catalytic behaviour of hydrogen evolution can confidently be attributed to the catalyst under investigation at a vitreous carbon electrode over a wide potential range.

Platinum electrodes are implemented as working electrodes mainly for the purpose of giving a reference potential for proton reduction from different acid sources as a means to compare hydrogen evolution catalysts to.



(Equation 2.38)

Platinum is currently still the most efficient catalyst for hydrogen evolution owing to the high intrinsic exchange current density for proton reduction. This is attributed to the properties of platinum which stabilizes a covalent Pt-H bond.²¹

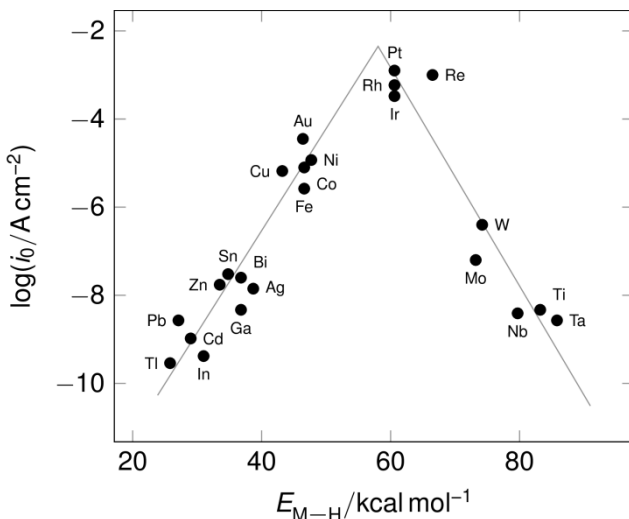


Figure 10 Volcano plot of $\log i_0$ values for the HER as a function of M-H bond energy.²²

This special property of platinum is displayed conveniently in the volcano plot of exchange current density for the hydrogen evolution reaction against metal-hydrogen bond energy shown in Figure 10. Platinum sits at the very top of the volcano owing to the fact that the metal hydrogen bonds that platinum makes are ‘just right’. The bonds are not so weak that they are broken before dihydrogen can be formed and not too strong as to form metal hydride bonds; rendering dihydrogen formation unfavourable.

Mercury pool electrodes are very practical for controlled potential electrolysis experiments. As they are liquid electrodes, the surface can be easily refreshed by agitating the surface using a stirrer. This results in very efficient electrolysis experiments. Mercury also has a large overpotential for hydrogen evolution so also allows a considerable working range at negative potentials. Mercury oxidises at a very modest potential so is not suitable for oxidative studies.

Semiconductor electrodes implemented here are p-type silicon. These are used for reductive electrochemistry with a photocurrent achieved when the electrode is illuminated using a fibre-optic white light source.

2.1.7.2 Secondary electrodes

The purpose of the secondary electrode is to supply the current required by the working electrode without in any way limiting the measured response of the cell, so should therefore have a larger area than the working electrode. Numerous

reactions can take place at the secondary electrode, including breakdown of solvents. These can affect the response at the working electrode, so it is wise to segregate the working and secondary electrode compartments with a glass frit. Platinum is usually employed as the secondary electrode due to the excellent electrochemical properties.

2.1.7.3 Reference electrodes

The role of the reference electrode is to provide a fixed potential that is invariable during the experiment. This can then be related to the agreed standard in the electrochemistry field, the normal hydrogen electrode (NHE). As the reference electrode holds a fixed potential, any change applied to the cell by the potentiostat is transferred directly across the working electrode/solution interface. The reference electrodes implemented are saturated calomel electrode (SCE), silver/silver chloride (Ag/AgCl) and silver wire.

The saturated calomel electrode is reversible to chloride ion and is made up in saturated aqueous potassium chloride and can be widely used in many solvents.

Silver/silver chloride electrode is a non-aqueous electrode containing a mixed solution of 0.45 M $[\text{Bu}_4\text{N}][\text{BF}_4]$ and 0.05 M $[\text{Bu}_4\text{N}][\text{Cl}]$ so can be used in halide solutions. It is also useful if the experiment is water sensitive.

The availability of various reference electrodes is because the ions used in the solutions of the electrodes can have adverse effects on the electrochemical response of the compound under analysis. If none are suitable, the best external reference to use is a silver wire. This is because, although the reference potential output is changeable, the electrochemistry is not compromised. The reference potential can be calibrated afterwards, by using an internal reference such as ferrocene (Fc^+/Fc couple).

2.2 Digital simulation

Digital simulation is a very useful technique which ‘fits’ digitally simulated electrochemical data to experimentally achieved data by use of the mathematical

equations relating to electrode kinetics and thermodynamics outlined earlier. Although the technique is now commonly known as ‘digital simulation’, the actual numerical techniques employed are much older than the digital computer. The technique dates back to at least as early as use by Richardson in 1911.²³ In these early times electrochemical engineers would ‘simulate’ their expected results by hand. It was during these early years that most of the theoretical groundwork and refinements were done, leading to the two theories of electrochemical kinetics used today. The Butler-Volmer method was developed by John Alfred Valentine Butler and Max Volmer, and is currently the most widely used theory for electrochemical simulation. It describes how the electrical current on an electrode depends on the electrode potential, considering that both a cathodic and an anodic reaction occur on the same electrode. To include mass transfer effects, the general form of the Butler-Volmer equation is taken as shown in Equation 2.39.

$$I = A \cdot i_0 \cdot \left\{ \frac{C_O(0,t)}{C_O^*} \exp \left[\frac{\alpha_a nF}{RT} (E - E_{eq}) \right] - \frac{C_R(0,t)}{C_R^*} \exp \left[\frac{\alpha_c nF}{RT} (E - E_{eq}) \right] \right\}$$

(Equation 2.39)

The competitor to this theory is the Marcus theory which was developed by Rudolph A. Marcus, starting in 1956, to explain the rates of electron transfer reactions, that is the rate at which an electron can move from the electron donor to the electron acceptor. This is a more indirect method of calculating the electrode kinetics as it determines the Gibbs free energy of activation of the electron transfer, and thus the reaction rate. It is calculated from the reorganisation energies of solvent molecules as a result of the rearrangement of charges associated with the electron transfer. There are many equations connected with this theory and it is still in development, with the Compton group leading research in this area.^{24, 25}

The digital simulation software used in this work is *DigiElch*, engineered by Rudolph in 2004. It is a variation of *DigiSim*, which was in part also produced by Rudolph along with Feldberg in 1994. *DigiElch* simulates user defined mechanisms consisting of a number of charge transfer steps and first or second order chemical reactions. All simulations can account for effects such as *iR* drop and/or double layer charging and kinetics of the system can obey either Butler-Volmer or Marcus equations. To run a

simulation of experimental data, the electrochemical system is outlined by the charge transfer reactions, the coupled chemical reactions, and the initial concentrations and diffusion coefficients of the species in solution. There are then two methods by which the simulated data can be fitted to the experimental data. These are the user trial and error method, where the simulation parameters are altered until the simulated data closely resembles the experimental data. Alternatively, multiple voltammograms employing different parameters such as scan rate or concentration can be imported and fit to the same model by computer iteration by an isotherm to get reliable kinetic and thermodynamic properties.

2.3 Spectroelectrochemistry

Electrochemistry can elucidate formal reaction mechanisms via kinetic analysis. However, this technique alone is often not immediately suitable for identification of unknown species formed as intermediates or products in a redox reaction. This is because little to no structural information is provided about the analyte. Conversely, isolated spectroscopic techniques can only provide structural information about species that are stable on a relatively long timescale. Therefore, combination of reaction-oriented electrochemistry with species-focussed spectroscopy in spectroelectrochemistry (SEC) can solve this problem, allowing a more complete analysis of electron transfer processes and complex redox reactions. As the combined techniques are performed *in situ* over a much shorter timescale, short lived intermediates or unstable products may be characterised. There are many different examples where electrochemistry is coupled with spectroscopic techniques.²⁶ These include electronic absorption, vibrational modes, light emission, magnetic resonance and circular dichroism. SEC systems have been constructed to be applied to small molecule systems, but struggle to reach sub-second timescale and as a result many transient species are missed.

Infrared spectroelectrochemistry (IR-SEC) provides insight into redox reaction mechanisms that cannot be obtained using either technique individually. This is achieved by time-resolved monitoring of strongly IR absorbant systems, such as complexes containing IR active ligands like CO, CN or N₂. The power of the

measurement is in the complementary nature of the spectroscopic and electrochemical information available when obtained simultaneously. The combination of measurements, however, requires compromise between the IR spectroscopy and electrochemistry because of their different sampling requirements.

No commercially available SEC cell was suitable for research undertaken within the Energy Materials Laboratory due to the second timescale of detection. This is attributed both to the intrinsic SEC cell design and the method of detection. Therefore a SEC cell was designed in house to achieve fast timescale detection.

Spectroelectrochemistry Partners SP-02 cell was designed in such a way that it could be mounted directly upon an ATR plate, Figure 11.



Figure 11 Picture of ATR-SEC setup.

The ATR used is a Pike MIRacle ATR fitted with single-bounce silicon crystal and a Northumbria Optical Coatings filter (pass band 4.76 μm to 5.60 μm), which is connected to a fast response Bruker Vertex 80 spectrometer equipped with a mercury cadmium telluride (MCT) detector giving a detection time limit as low as 80 ms.

Even with this fast response IR detection, the SEC cell has to be designed so that electrochemical conversion of the species under analysis at least matches the speed of the IR detection. For this to be possible a thin layer of the analyte solution is required, so the cell was designed as follows.

SEC cell SP-02 employs the usual electrochemical setup of three electrodes as shown in Figure 12.

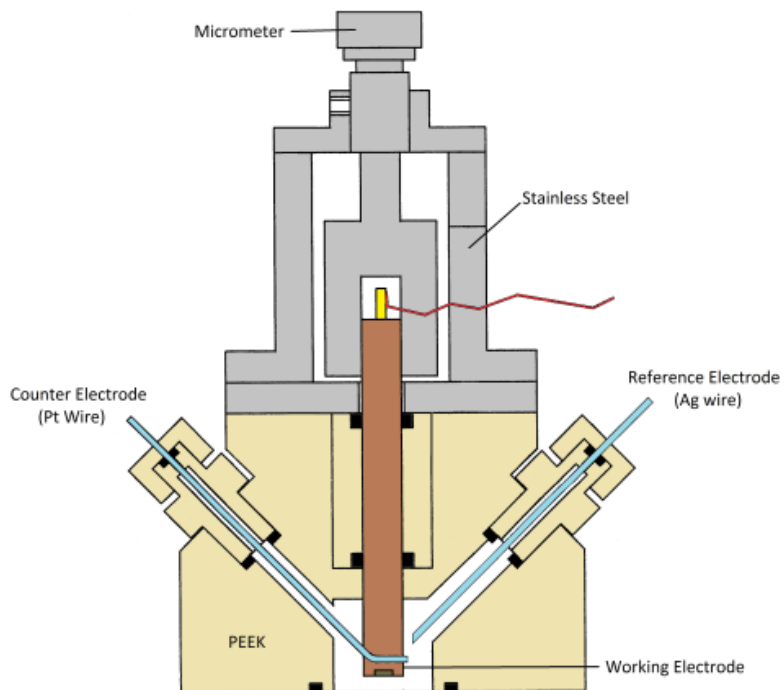


Figure 12 Diagram of overall cell design.

The silver wire *pseudo* reference electrode is positioned in the bulk solution and is therefore less susceptible to potential shifts as concentration fluctuations in the bulk solution are negligible. To minimise iR drop, the platinum counter electrode is positioned as close as possible to the vitreous carbon working electrode (area = 0.071 cm²), which itself is attached to a micrometer. The micrometer allows the depth of the working electrode to be adjusted relative to the ATR plate. A thin analyte solution layer of typically 10 µm can be achieved between the electrode surface and the ATR silicon crystal by use of the micrometer. The thin layer of analyte is rapidly electrolysed at a rate comparable to IR sampling.

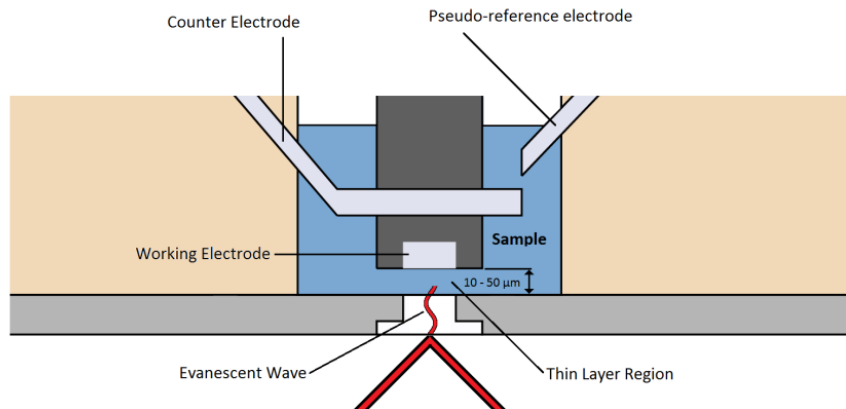


Figure 13 Close up diagram of thin layer region between working electrode and IR source.

The thin layer also limits mass transport to and from the diffusion layer by the electrode surface, trapping electrochemically produced species in close proximity to the detector, thus improving the chance of detecting short-lived intermediates.

A typical spectroelectrochemical experiment involves initially performing a cyclic voltammetric analysis with the working electrode raised to several hundred micrometers so that the process is not diffusion limited. CV data can then be collected with the minimum amount of iR drop. As the cyclic voltammetry is recorded against a *pseudo* reference electrode, it can be compared to a cyclic voltammetric experiment performed independently using a definitive reference electrode such as Ag/AgCl. The cyclic voltammetry identifies the potential at which to perform bulk electrolysis of the thin layer during spectroelectrochemical analysis. Results from SEC of the thin layer are recorded as time-resolved difference spectra where an IR spectra of the starting material is subtracted from subsequent spectra recorded for the duration of the experiment, Figure 14.

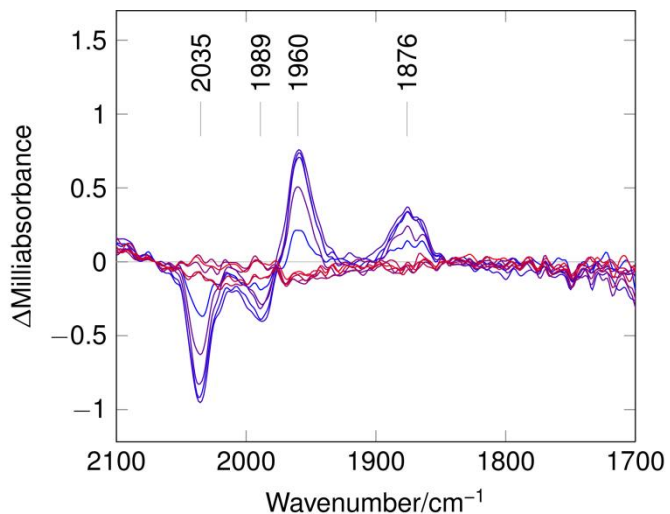


Figure 14 Example of time-resolved IR spectroelectrochemical difference spectra.

Difference spectra consist of a series of spectra recorded over time (blue to red) containing IR absorbance peaks of both negative and positive intensities. Negative peaks signify a loss in the species, so typically corresponds to the consumption of the starting material. Positive peaks correspond to an increase in the species and therefore are attributed to the formation of a product.

2.4 References

1. J. W. Turner, F. A. Schultz, *Coord. Chem. Rev.* **2001**, *81*, 219
2. R. S. Nicholson, *Anal. Chem.* **1965**, *37*, 1351
3. M. L. Helm, M. P. Stewart, R. M. Bullock, M. R. DuBois, D. L. DuBois, *Science*, **2011**, *333*, 863
4. R. G. Compton, C. E. Banks, *Understanding Voltammetry 2nd Ed.* Imperial College Press, **2010**
5. L. Nadjo, J. M. Saveant, *J. Electroanal. Chem.* **1971**, *30*, 41
6. C. Costentin, S. Drouet, M. Robert, J. M. Saveant, *J. Am. Chem. Soc.* **2012**, *134*, 11235
7. A. Fujishima, K. Honda, *Nature*, **1972**, *238*, 37
8. M. S. Wrighton, *Pure & Appl. Chem.* **1985**, *57*, 57
9. A. B. Bocarsly, D. C. Bookbinder, R. N. Dominey, N. S. Lewis, M. S. Wrighton, *J. Am. Chem. Soc.* **1980**, *102*, 3683
10. F. Williams, A. J. Nozik, *Nature*, **1978**, *271*, 137
11. A. J. Nozik, D. S. Boudreaux, R. R. Chance, F. Williams, *Am. Chem. Soc. Adv. Chem. Ser.* **1980**, *184*, 155
12. D. S. Boudreaux, F. Williams, A. J. Nozik, *J. Appl. Phys.* **1980**, *51*, 2158
13. J. A. Turner, J. Manassen, A. J. Nozik, *Appl. Phys. Lett.* **1980**, *37*, 488
14. B. Oregan, M. Gratzel, *Nature*, **1992**, *353*, 737
15. C. A. Koval, J. N. Howard, *Chem. Rev.* **1992**, *92*, 411
16. L. M. Peter, *Chem. Rev.* **1990**, *90*, 753
17. N. S. Lewis, *Acc. Chem. Res.* **1990**, *23*, 176
18. Adapted from <http://pveducation.org/pvcdrom/solar-cell-operation/fill-factor>
19. G. M. Jenkins, K. Kawamura, *Nature*, **1971**, *231*, 175
20. P. J. F. Harris, *Phys. Mag.* **2004**, *84*, 3159
21. D. T. Sawyer, A. Sobkowiak, J. L. Roberts, *Electrochemistry for Chemists 2nd ed.* New York: John Wiley & Sons. **1995**
22. M. M. Jaksic et al. *J. New Mat. Electrochem. Systems*, **2000**, *3*, 167
23. L. F. Richardson, *Phil. Trans.* **1911**, *A210*, 307
24. E. Laborda, M. C. Henstridge, R. G. Compton, *J. Electroanal. Chem.* **2012**, *667*, 48
25. D. Suwatchara, C. M. Henstridge, N. V. Rees, E. Laborda, R. G. Compton, *J. Electroanal. Chem.* **2012**, *667*, 120
26. S. P. Best, *Coord. Chem. Rev.* **2005**, *249*, 1536

Chapter 3

Photoelectrocatalysis of hydrogen production at p-type silicon by molybdenum hydride systems

3.1 Introduction

3.1.1 Overview

The cationic molybdenum^{IV} hydride complex, $[\text{MoH}_2(\eta^2\text{-O}_2\text{CCH}_3)(\text{dppe})_2]^+$ represented by Figure 1 has been shown to electrocatalyse hydrogen evolution in non-aqueous solution.¹

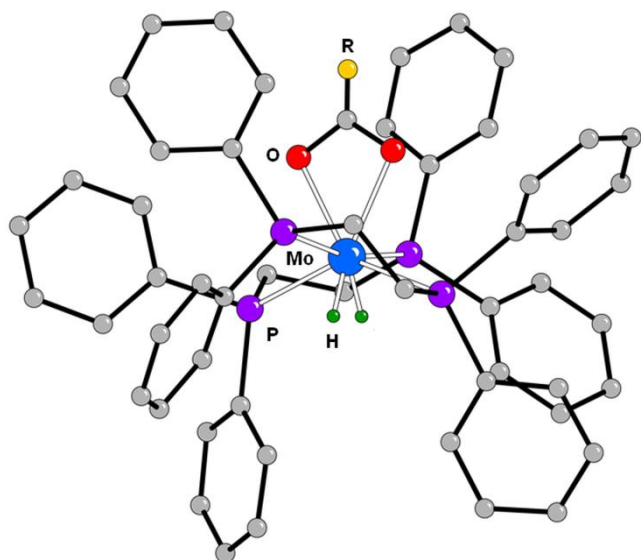


Figure 1 Pictorial representation of $[\text{MoH}_2(\eta^2\text{-O}_2\text{CR})(\text{dppe})_2]^+$.

Although the electrocatalysis is neither fast nor occurs at a low overpotential, the system is robust and can serve as a model system for probing photoelectrocatalysis at semiconductor electrodes. This chapter describes in detail the electrochemistry of such molybdenum and tungsten hydride complexes at inert electrodes, their behaviour as electrocatalysts for hydrogen evolution and how this compares with their electrochemistry at p-type silicon photocathodes.

3.1.2 The hydride complexes: synthesis and background chemistry

Cationic hydrido-, carboxylato- complexes of molybdenum^{IV} were first synthesised and characterised by Ito,² who reported well-defined mononuclear carboxylato- complexes of molybdenum containing tertiary phosphines. The synthesis was achieved by treating $[\text{MoH}_4(\text{dppe})_2]$ (dppe = 1,2-bis(diphenylphosphino)ethane) with $[\text{RCO}_2\text{H}]$ ($\text{R} = \text{CH}_3, \text{CF}_3$ or H) followed by anion exchange with $[\text{NaBPh}_4]$. The mechanism was uncovered by reaction with the corresponding deuterated carboxylic acid, $[\text{RCO}_2\text{D}]$. This showed that the first step in the reaction was protonation of $[\text{MoH}_4(\text{dppe})_2]$ which gave an intermediate pentahydrido- cation, followed by selective evolution of H_2 accompanied by binding of the acetate group. Various simple reactions were undertaken including air and temperature sensitivity. The complexes were found to be moderately stable to air in the solid state and in solution when kept in the dark. The complex, $[\text{MoH}_2(\eta^2-\text{O}_2\text{CCH}_3)(\text{dppe})_2]^+$ was reported to be stable *in vacuo* up to 150 °C, making it very thermally stable. Upon irradiation with a high pressure mercury lamp for 5 hours, the neutral monohydride complex was formed, $[\text{MoH}(\eta^2-\text{O}_2\text{CCH}_3)(\text{dppe})_2]$, revealing that light can greatly affect the stability of these complexes.

3.1.3 Early studies of the electrochemistry of cationic hydrido-carboxylato- complexes of molybdenum and tungsten

3.1.3.1 Basic electron-transfer chemistry: primary and secondary reduction steps

The M^{IV} complexes $[MH_2(\eta^2-O_2CR)(dppe)_2]^+$ ($M = Mo$ or W , $R = CH_3$ or CF_3) undergo a quasi-reversible single electron transfer at a vitreous carbon electrode.¹ The reduction potentials for these first electron transfer steps varied according to the electrochemical properties of the metal and the electron withdrawing capabilities of the R group, which affects the electron density at the metal centre. If the R group is altered to contain highly electronegative atoms, such as fluorine when $R = CF_3$, a powerful electron withdrawing group is created, moving the reduction potential more positive. Replacing tungsten by molybdenum also results in a more positive potential for reduction as the M-O bonds are weaker for molybdenum than for tungsten.³ Quantifiable electrochemical variables of these quasi-reversible steps have been measured for the complexes. For $M = Mo$ and $R = CH_3$, the standard heterogeneous rate constant, $k_s = 1.7 \times 10^{-3} \text{ cm s}^{-1}$ at 301 K in the electrolyte solution 0.2 M $[Bu_4N][PF_6]$ -dimethylformamide (DMF), the electron transfer coefficient, $\alpha = 0.65$ and the activation energy, $E_{A,\text{het}} = 30 \text{ kJ mol}^{-1}$, were estimated by numerical simulation of current-potential data. The $E_{A,\text{het}}$ was suggestive of an inner sphere structural rearrangement associated with the slow electron transfer and this was consistent with the cleavage of a metal-oxygen bond whereby the 18 electron, η^2 -carboxylate parent Mo^{IV} cation is reduced to the 17-electron η^1 -carboxylate Mo^{III} . The corresponding tungsten complex $[WH_2(\eta^2-O_2CCH_3)(dppe)_2]^+$ behaved in an analogous way apart from that the electron transfer kinetics were slower with k_s approaching $10^{-4} \text{ cm s}^{-1}$ at 300 K. The slower electron transfer kinetics can be explained by a stronger W-O bond. Reducing the strength of the tungsten-oxygen bond by introducing an electron-withdrawing group as in $[WH_2(\eta^2-O_2CCF_3)(dppe)_2]^+$, increases the electron transfer rate constant, k_s by about an order of magnitude.

The 17-electron primary product, $[MH_2(\eta^1-O_2CR)(dppe)_2]$, undergoes a single electron transfer giving the 18-electron anion. The process was fast and reversible at reduced

temperatures ($0\text{ }^{\circ}\text{C}$ for $\text{M} = \text{W}$, $\text{R} = \text{CH}_3$; $-20\text{ }^{\circ}\text{C}$ for $\text{M} = \text{Mo}$, $\text{R} = \text{CH}_3$). The unstable anions could not be electrosynthesised in bulk, however $[\text{WH}_2(\eta^1\text{-O}_2\text{CCH}_3)(\text{dppe})_2]^-$ was trapped by protonation. Thus controlled potential electrolysis of $[\text{WH}_2(\eta^2\text{-O}_2\text{CCH}_3)(\text{dppe})_2]^+$ in the presence of one equivalent of $\text{CH}_3\text{CO}_2\text{H}$ gave the stable trihydride $[\text{WH}_3(\eta^1\text{-O}_2\text{CCH}_3)(\text{dppe})_2]$, Figure 2, essentially quantitatively.⁴

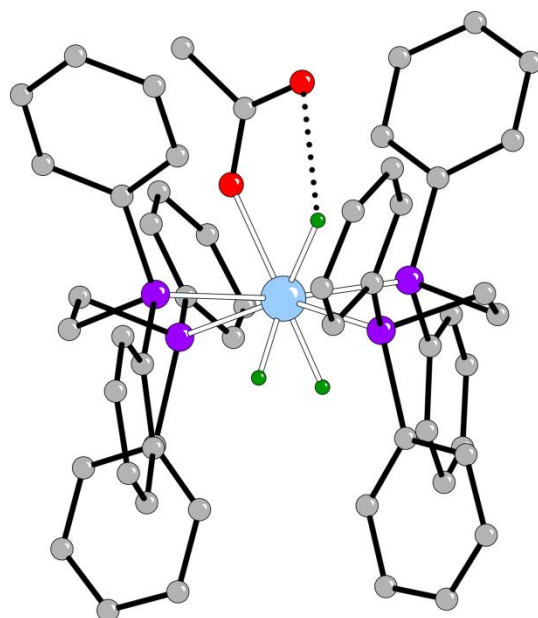


Figure 2 Crystal structure of $[\text{WH}_3(\eta^1\text{-O}_2\text{CCH}_3)(\text{dppe})_2]$ as determined by single crystal X-ray analysis.

The carboxylate possessing the η^1 -coordination mode was fully consistent with the $\eta^2 \rightarrow \eta^1$ conversion associated with the primary electronation step. Correspondingly, $[\text{MoH}_3(\eta^1\text{-O}_2\text{CCH}_3)(\text{dppe})_2]$ (peak Y in Figure 3) was detected in the cyclic voltammetry of $[\text{MoH}_2(\eta^2\text{-O}_2\text{CCH}_3)(\text{dppe})_2]^+$ upon reduction in the presence of a proton source. However, $[\text{MoH}_3(\eta^1\text{-O}_2\text{CCH}_3)(\text{dppe})_2]$ was thermally unstable and lost dihydrogen to form the monohydride complex $[\text{MoH}(\eta^2\text{-O}_2\text{CCH}_3)(\text{dppe})_2]$ (peak X in Figure 3). The two species can be seen on the cyclic voltammetric timescale in the CV of $[\text{MoH}_2(\eta^2\text{-O}_2\text{CCH}_3)(\text{dppe})_2]^+$ in the absence of acid, Figure 3.

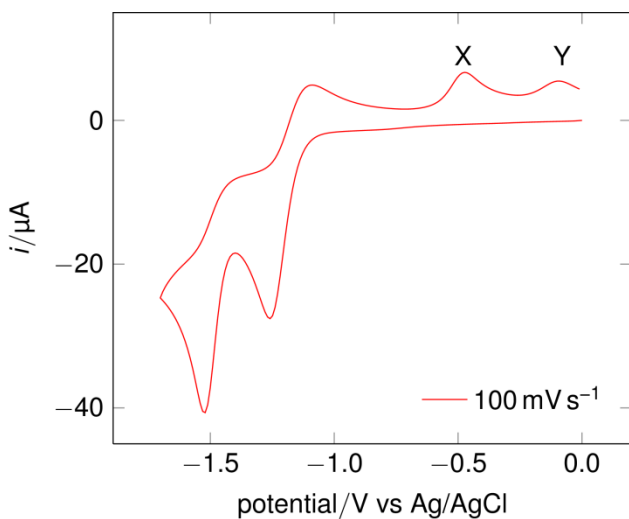


Figure 3 Cyclic voltammetry of 1.47 mM $[\text{MoH}_2(\eta^2\text{-O}_2\text{CCH}_3)(\text{dppe})_2]\text{[BPh}_4]$ complex in 0.1 M $[\text{NBu}_4]\text{[BF}_4]$ -MeCN at a vitreous carbon electrode at 100 mV s^{-1} .

In the presence of an excess of acid, electroreduction of $[\text{MH}_2(\eta^2\text{-O}_2\text{CCH}_3)(\text{dppe})_2]^+$ sustained a dihydrogen evolution cycle. For the tungsten system, the mechanism was postulated to proceed *via* protic attack on the trihydride to generate the parent cation and dihydrogen, as solutions of $[\text{WH}_3(\eta^1\text{-O}_2\text{CCH}_3)(\text{dppe})_2]$ reacted with protic acids which quantitatively gave $[\text{WH}_2(\eta^2\text{-O}_2\text{CCH}_3)(\text{dppe})_2]^+$ and H_2 . For the Mo compound, protonation was described to take place on one of two pathways, either protonation of the trihydride gave the parent molecule and dihydrogen or following thermal H_2 loss from $[\text{MoH}_3(\eta^1\text{-O}_2\text{CCH}_3)(\text{dppe})_2]$, protonation of the monohydride gave $[\text{MoH}_2(\eta^2\text{-O}_2\text{CCH}_3)(\text{dppe})_2]^+$.

The mechanism is supported by stopped flow UV-Vis studies on the selective release of dihydrogen upon deuteration of $[\text{WH}_3(\eta^1\text{-O}_2\text{CCH}_3)(\text{dppe})_2]$ with DCl or DBr .⁵

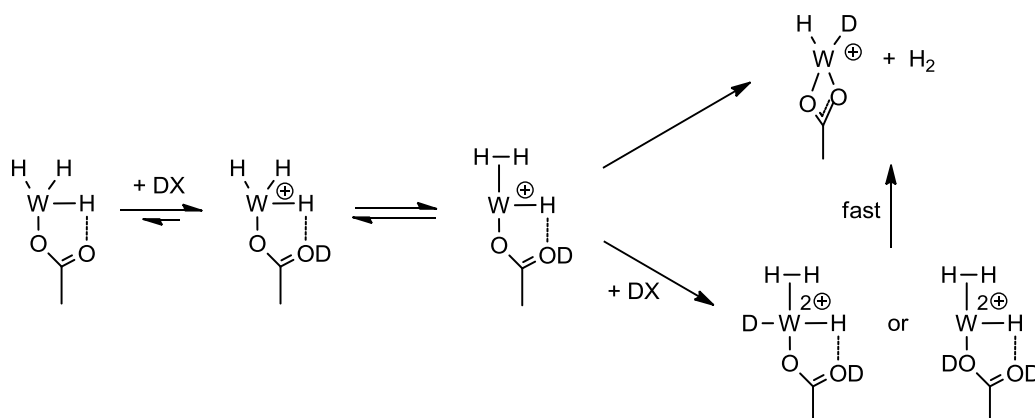


Figure 4 Mechanism for the selective elimination of dihydrogen from the reaction between $[\text{WH}_3(\eta^1\text{-O}_2\text{CCH}_3)(\text{dppe})_2]$ and DX ($\text{X} = \text{Cl}$ or Br) (dppe ligands omitted for clarity).

The spectrophotometric study conducted showed that one equivalent of acid was consumed in the formation of the first detectable intermediate, and that was most likely the deuteration of the pendant acetate group which formed $[WH_3(\eta^1\text{-OCCH}_3\text{OD})(dppe)_2]^+$. The kinetics of the formation of $[WHD(\eta^2\text{-O}_2\text{CCH}_3)(dppe)_2]^+$ from $[WH_3(\eta^1\text{-OCCH}_3\text{OD})(dppe)_2]^+$ exhibited first order dependence on the concentration of the complex, but a complicated dependence on the concentration of acid, which led to the conclusion that multiple pathways may operate as shown in Figure 4. The reason for the selective production of H_2 was found in the original crystal structure of $[WH_3(\eta^1\text{-O}_2\text{CCH}_3)(dppe)_2]$. The hydride nearest the oxygen of the acetate group was distinguishable from the other two as it was within close enough proximity to participate in hydrogen bonding. Proton NMR also reflected this distinction (δ 2.92, 1H; δ -2.78, 2H) and consequently the complex was considered a two site molecule. The pendant acetate was regarded as the deuteration site and the metal the H_2 evolving site.

3.1.3.2 Binding of substrates at Mo^{II} and W^{II} centres

Two-electron reduction labilises the carboxylate ligand in complexes $[MH_2(\eta^2\text{-O}_2\text{CR})(dppe)_2]^+$. Thus in the absence of acid, the carboxylate was completely cleaved from the metal after the two successive electronations, as opposed to being trapped when a proton was present. The expulsion of carboxylate exposed a site at which various small molecules bound. Thus cyclic voltammetry of $[MoH_2(\eta^2\text{-O}_2\text{CCH}_3)(dppe)_2]^+$ under dihydrogen revealed the formation of $[MoH_4(dppe)_2]$, whilst $[MoH_2(N_2)(dppe)_2]$ was formed under one atmosphere of dinitrogen. Under an atmosphere of carbon monoxide, both the carboxylate along with the two hydrides were lost and *trans*- $[Mo(CO)_2(dppe)_2]$ was formed.¹

3.1.3.3 Bioinorganic context: carboxylate as a leaving group at the active site of the MoFe-protein of nitrogenase

Complexes of the type $[MH_2(\eta^2\text{-O}_2\text{CCH}_3)(dppe)_2]^+$ hold structural relevance to the molybdenum atom within the active site of the [MoFe]-nitrogenase, whereby the

carboxylate of homocitrate is mimicked by the carboxylate of the analogue complexes in the neutral η^1 state. These complexes were therefore used for mechanistic studies of dinitrogen binding and reduction in relation to the enzyme.¹ This work may no longer be of interest to nitrogenase functionality research, as the latest studies suggest that it is two iron atoms that are the site of dinitrogen binding and reduction.⁶⁻⁹

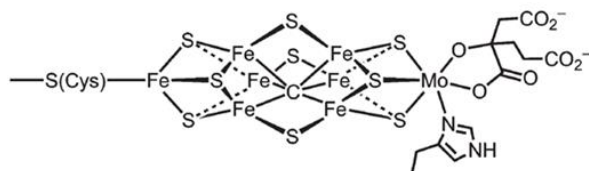


Figure 5 Structure of the MoFe nitrogenase.

The η^1 -carboxylate coordinated to Mo in the molybdenum nitrogenase might have similarly acted as the leaving group as illustrated by the Mo and W hydrido-carboxylato- complexes with the ligated *gem*-alkoxy group of homocitrate serving to tether the released carboxylate in the vicinity of the metal so it was available for reattachment in the latter stages of an enzymic cycle.¹⁰ In the model systems, when the η^1 -carboxylate became dissociated, the vacant site could be taken up by dinitrogen when exposed to one atmosphere of dinitrogen gas to form $[\text{MoH}_2(\text{N}_2)(\text{dppe})_2]$. This dihydride was unstable and slowly lost dihydrogen to produce *trans*- $[\text{Mo}(\text{N}_2)_2(\text{dppe})_2]$, detected by cyclic voltammetry. Stoichiometric dihydrogen loss from a Mo centre often occurred after dinitrogen binding, which suggested that obligatory hydrogen evolution in the enzymic reaction was produced as a by-product, rather than used as a mechanism for site generation before the substrate bound. Major elements of the Lowe and Thorneley biochemical model for nitrogenase function¹⁰ were adopted by this chemical model, whereby suppressible hydrogen evolution, substrate binding and stoichiometric release of dihydrogen involved the *gem*-alkoxy secured carboxylate to function as a leaving group at molybdenum.

3.1.4 Early studies of the photoelectrocatalytic systems at p-type silicon

3.1.4.1 Photoelectrocatalysis of proton and CO₂ reduction on p-type Si

Visible light driven photoelectrochemical conversion of protons to dihydrogen is a half-cell reaction of relevance to the generation of H₂ as a clean energy vector; a solar fuel. A similar cell can be produced for the reduction of carbon dioxide.¹¹ By far the most advanced technology for converting light to electrical energy is based on semiconducting silicon. These readily available and well-characterised photovoltaic materials can also provide a means of directly converting solar energy to stored chemical energy in a photoelectrochemical device. Such conversions at semiconductor electrodes were delineated over thirty years ago by Wrighton, Bard and their co-workers who showed that illuminated doped silicon could be used to drive solution oxidation (n-type Si) or reduction reactions (p-type Si) at bias potentials some 500 mV 'uphill' of their reversible thermodynamic potentials.¹²⁻¹⁴ Bradley gave an early example of the electrocatalytic capabilities of p-type silicon by performing photocatalytic reduction of carbon dioxide at a p-type Si photocathode with a tetra-azamacrocyclic nickel complex as the electron mediator.¹⁵ Conversion of carbon dioxide to carbon monoxide and hydrogen in a 2:1 molar ratio was achieved with current efficiencies around 95 %. Kubiak and co-workers have very recently shown that similar photovoltages on p-type Si can offset the potential necessary for the electrocatalytic reduction of carbon dioxide to carbon monoxide by Re pyridine species¹⁶ and generation of hydrogen by a [FeFe]-hydrogenase active site mimic.¹⁷ Controlled potential electrolysis of the illuminated photocathode gave selective photoreduction of CO₂ to CO in the presence of Re(bipy-Bu^t)(CO)₃Cl { (bipy-Bu^t) = 4,4'-di-t-butyl-2,2'-bipyridine} with a Faradaic efficiency of ca 95 %. A short-circuit quantum efficiency of 61 % for light-to-chemical energy conversion was observed for the photoelectrochemical production of CO. Photoreduction of [Fe₂(bdt)(CO)₆] (bdt = benzene dithiolate) at an illuminated p-type Si electrode achieved a homogeneous photocatalytic reduction of protons to hydrogen with 100 % Faradaic efficiency and monochromatic light to chemical energy conversion of 8 %.

This has stimulated further work on p-type Si systems. For example, early work on direct photoreduction of protons on illuminated p-type Si was shown to be sluggish unless platinum was incorporated in a surface layer;¹⁸ Chorkendorff and co-workers have now shown silicon surface modification is possible with a more earth abundant metal based catalyst.¹⁹ Surface bound Mo₃S₄ centres can catalyse the evolution of hydrogen, at rates comparable to that of platinum,¹⁸ when coupled to a p-type Si semiconductor that harvests red light. The current density of the system implies a solar-to-hydrogen efficiency in excess of 10 %.

3.1.4.2 Photoelectrocatalysis at other semiconducting materials

Many other semiconducting materials have been designed in a hope to improve the essential properties for light to energy conversion. The quantum efficiency of the material needs to improve as much as possible so that the light absorbed is converted to usable electrons and not simply lost through recombination with holes. Also, the band gap is required to be large enough that as much of the visible spectrum can be absorbed as possible for efficient use of sunlight. This separation between the valence band and the conduction band signifies the amount of energy that is required to excite an electron across this gap and therefore has a dramatic effect on the magnitude of the potential shift observed when the cyclic voltammetry of a system at the illuminated material is measured. The trend is generally the bigger the band gap, the greater the potential shift, although there other factors that alter this bias potential, such as the ‘dark’ (non-shifted) redox potential and illumination intensity.

Material	Formula	Band Gap / eV
Tin dioxide	SnO ₂	3.7
Gallium nitride	GaN	3.44
Zinc oxide	ZnO	3.37
Titanium dioxide anatase/rutile	TiO ₂	3.2/3.02
Cadmium sulfide	CdS	2.42
Gallium phosphide	GaP	2.26
Tin sulfide	SnS ₂	2.2
Gallium selenide	GaSe	2.1
Cadmium selenide	CdSe	1.74
Indium phosphide	InP	1.35
Copper sulfide	Cu ₂ S	1.2
Silicon	Si	1.11
Tin sulfide	SnS	1.0
Iron disulfide	FeS ₂	0.95
Indium nitride	InN	0.7
Germanium	Ge	0.67

Table 1 Various semiconductor materials and their band gap.^{20,21}

Photoelectrocatalysis has been investigated with some of these materials including an early study by Wrighton *et al.*²² In water, the photoelectrochemical reduction to H₂ was effected by illumination of p-type WS₂ surface modified with Pd⁰ or Pt⁰ in a photoefficiency for H₂ evolution of 6-7 %.

Another study applying a less common semiconductor involved the study of imidazole and pyridine catalysed reduction of carbon dioxide at illuminated iron pyrite electrodes.²³ The illuminated iron pyrite electrode resulted in a shift of 77 mV in the potential of the reduction of the amine electrocatalysed CO₂ reduction. This small shift was attributable to the high density of defect states in the natural pyrite samples used, in combination with the small band gap of iron pyrite.

An artificial photocatalytic H₂ evolution system assembled using semiconducting cadmium sulfide (CdS), cobaloximes, and triethanolamine (TEOA) as a sacrificial electron donor showed high hydrogen evolution activity.²⁴ Under visible light irradiation, turnover numbers of up to 171 were achieved based on the cobaloxime

catalyst and a calculated overall quantum efficiency of 9.1 %. CdS only has excited state lifetime of the nanosecond timescale,²⁵ so the only way the promoted electron can be used by the electrocatalyst is by the quenching of holes (h^+) by the sacrificial electron donor. Long-lived electrons (microsecond to second) can be produced by semiconductor when it is exposed to a sacrificial electron donor:^{26, 27} this is why sacrificial electron donors are widely used in semiconductor-electrocatalyst photoelectrocatalysis reactions.²⁸⁻³¹

Organic photovoltaic (OPV) cells have rarely been used in conjunction with hydrogen evolution, however a photocathode for the formation of hydrogen has recently been constructed using poly-3-hexylthiophene (P3HT): phenyl-C₆₁-butyric acid (PCBM) as the heterojunction directly coupled to molybdenum sulphide nanoparticles.³² MoS₃ nanoparticles were either spin- or spray-coated onto the surface of the organic light-harvesting system which in turn was supported on indium-tin oxide coated glass. The completed photocathode gave the most efficient current responses for MoS₃ film thicknesses in the range of 40-90 nm when subjected to a very strong aqueous acid source, 0.5 M H₂SO₄. Gas chromatography confirmed light induced hydrogen evolution. The efficiency was improved when TiO₂ was incorporated into the catalytic layer to aid electron transfer.

3.1.5 Scope of the Chapter

The work of this chapter was to extend the understanding of the electrochemistry of [MH₂(η²-O₂CR)(dppe)₂]⁺ systems, how they function as electrocatalysts for hydrogen evolution at inert electrodes, and how they support electrocatalysis at a light harvesting p-type Si photocathode. The following aspects are covered:

- (i) Digital simulation of the cyclic voltammetry of the complexes was used to relate structure to heterogeneous electron transfer rate constants. DFT calculations were used to provide information on structural changes following the primary electron transfer.
- (ii) Electron paramagnetic resonance (EPR) studies were used to gain information on the spin-states of the system following single electron transfer.

- (iii) Kinetic and mechanistic aspects of hydrogen evolution are discussed and a model for the electrocatalysis is presented, supported by digital simulation of experimental data.
- (iv) The photoelectrochemical and photoelectrocatalytic behaviour of the complexes at p-type silicon is described.

3.2 Results and Discussion

3.2.1 Basic electrochemistry of $[\text{MH}_2(\eta^2\text{-O}_2\text{CR})(\text{dppe})_2]^+$ systems

3.2.1.1 The primary electron-transfer step

In earlier work measurements were made for the Mo acetato- complex, $[\text{MoH}_2(\eta^2\text{-O}_2\text{CCH}_3)(\text{dppe})_2]^+$, in 0.1 M $[\text{Bu}_4\text{N}][\text{BF}_4]$ -MeCN electrolyte. It was found that this polar solvent leads to decomposition of the trifluoroacetate derivatives and therefore an alternative electrolyte system was sought in which to compare all the complexes. DCM (dichloromethane) has a limited potential window in the cathodic regime, THF (tetrahydofuran) is suitable but *iR* drop (potential drop) tends to be problematic and the lone pairs of electrons on the oxygen atom could potentially lead to coordination to the complexes. The 1:3 molar ratio $[\text{Bu}_4\text{N}][\text{BF}_4]$ -toluene solution forms an inert electrolyte with good conductivity at above 301 K.³³ This solvent was therefore chosen to examine the behaviour of the complexes. Comparative data for Mo acetate complex in the two solvents is provided.

Figure 6 shows the cyclic voltammogram for $[\text{MoH}_2(\eta^2\text{-O}_2\text{CCH}_3)(\text{dppe})_2][\text{BPh}_4]$ recorded in 1:3 molar ratio $[\text{Bu}_4\text{N}][\text{BF}_4]$ -toluene electrolyte at a vitreous carbon electrode.

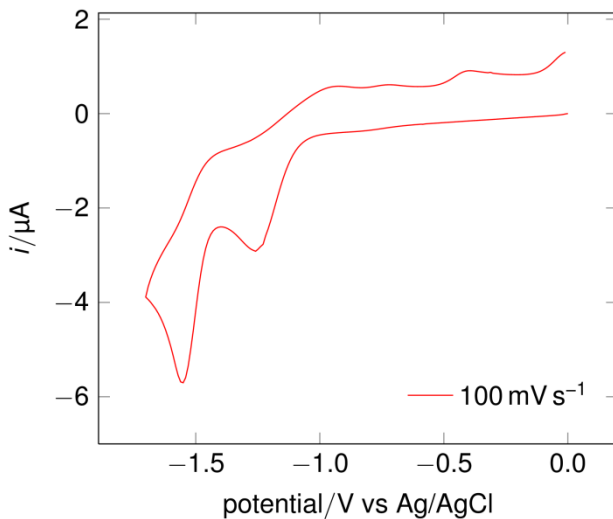


Figure 6 Cyclic voltammetry of 1.12 mM $[\text{MoH}_2(\eta^2\text{-O}_2\text{CCH}_3)(\text{dppe})_2]\text{[BPh}_4]$ complex in 1:3 molar ratio $[\text{NBu}_4]\text{[BF}_4]$ -toluene at a vitreous carbon electrode at 303 K at a scan rate of 100 mV s^{-1} .

There are two successive one-electron reduction steps. The primary process is quasi-reversible, the secondary process is partially reversible and gives rise to the product oxidation peaks shown in the voltammogram and labelled peaks X and Y in Figure 3. The following chemistry has been discussed in earlier work and will not be addressed here.¹ The quasi-reversible nature of the primary process is evident from the scan rate dependence of the voltammograms. At slow scans the separation of the peak potentials is substantially less than the peak separation at a faster scan, as is illustrated by Figure 7.

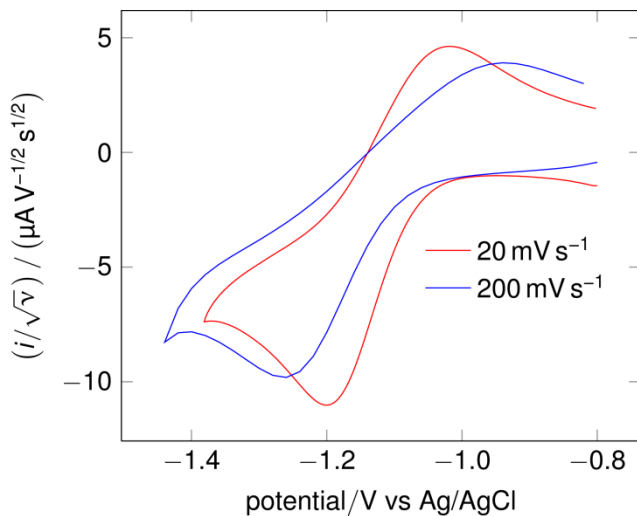
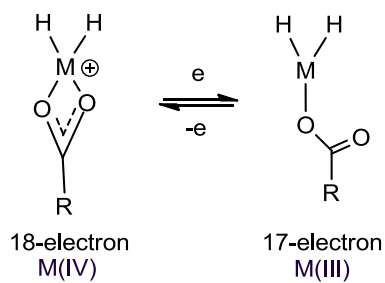


Figure 7 Scan rate normalised cyclic voltammetry of 1.12 mM $[\text{MoH}_2(\eta^2\text{-O}_2\text{CCH}_3)(\text{dppe})_2]\text{[BPh}_4]$ complex in 1:3 molar ratio $[\text{NBu}_4]\text{[BF}_4]$ -toluene at a vitreous carbon electrode at various scan rates at 303 K.

The slow electron transfer associated with a quasi-reversible system cannot support a Nernstian equilibrium at the faster scan rates. Slow electron transfer at an electrode can be associated with structural change concerted with electron transfer events or a spin state change. The earlier work on this system establishing the trapping of a monodentate carboxylato- species provided strong evidence that an η^2 to η^1 structural rearrangement is concerted with the primary electron transfer, Scheme 1.



Scheme 1 Chemical structural change associated with slow electron transfer (dppe ligands omitted for clarity).

3.2.1.2 EPR detection of the primary Mo^{III} reduction product

The formation of a Mo^{III} species by one-electron reduction of the (low spin) Mo^{IV} parent should lead to the generation of a EPR (electron paramagnetic resonance) active species; either a 19-electron η^2 -acetate or a 17-electron η^1 -acetate complex. The reduction of $[\text{MoH}_2(\eta^2\text{-O}_2\text{CCH}_3)(\text{dppe})_2]^+$ at controlled potential was carried out in a 0.2 M $[\text{NBu}_4][\text{BF}_4]$ -THF electrolyte in the cavity of an EPR cell at room temperature (X-band, 9.5 GHz), sweeping the magnetic field from 3200 to 3600 G. THF was used as the solvent in these EPR experiments due to the fact that it has a low dielectric constant when compared to acetonitrile. Toluene also has a low dielectric constant but it was not feasible to maintain the warm temperature required for the toluene electrolyte system within the cavity of the EPR setup. It was important that the solvent had a low dielectric constant so that the polarisation was kept to a minimum when the magnetic field was applied, thus maximising the signal to noise ratio for the response from the complex. Figure 8 shows the spectrum obtained after 200 scans with the potential held at the onset of primary reduction. There is one major signal centred at 3383 G with a minor signal at 3491 G.

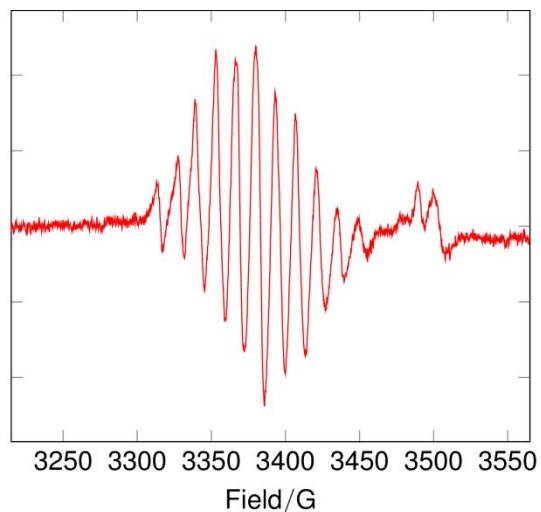


Figure 8 EPR spectrum of the reduced complex $[\text{MoH}_2(\eta^1\text{-O}_2\text{CR})(\text{dppe})_2]$ (Power = 2.012 mW, Modulation amplitude = 1.0 G).

The major component has $g_{\text{av}} = 2.006$ which is slightly higher than the free electron value of 2.002 and consistent with coupling to other spin $\frac{1}{2}$ nuclei. This eleven line spectrum must arise from hydride and phosphorus hyperfine coupling. Four equivalent phosphorus atoms would be expected to give a five line spectra. The two equivalent hydrides, with a smaller hyperfine coupling than phosphorus, split this further to give eleven lines. The fact that the four phosphorus atoms must be equivalent for the above spectrum to be observed means that they must all lay in the same plane. For this to occur, the four atoms must rotate from their out of plane arrangement observed in the starting material confirmed by the X-ray structure in Figure 1,¹ and two signals in the P^{31} NMR¹ which signifying that there are two pairs of equivalent P atoms. Planar arrangement of the phosphorus atoms can then only be reached by relieving steric hinderance about the metal and thus breaking of one of the metal-oxygen bonds: η^2 to η^1 structural conversion. This structural conversion is illustrated in the DFT calculations in Section 3.1.2.3.

The deuterated species was also prepared, $[\text{MoD}_2(\text{O}_2\text{CCH}_3)(\text{dppe})_2]^+$, and the *in situ* generation of the paramagnetic species repeated, Figure 9.

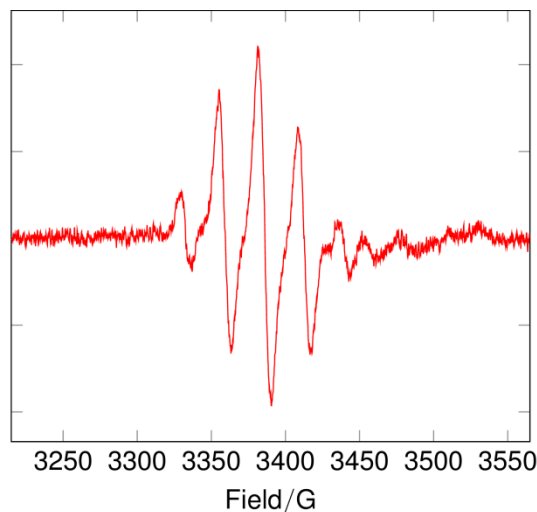


Figure 9 EPR spectrum of the reduced complex $[\text{MoD}_2(\eta^1\text{-O}_2\text{CR})(\text{dppe})_2]$ (Power = 2.012 mW, Modulation amplitude = 1.0 G).

The clear loss of proton hyperfine is evident. Deuterium hyperfine coupling is six times smaller, so is poorly resolved and therefore the resulting spectrum is dominated by the five lines expected for four equivalent phosphorus atoms. Thus, the results are consistent with the retention of the hydrides, with the phosphorus ligands in a planar arrangement, and therefore the formation of a Mo^{III}, 17-electron, η^1 -acetate complex.

3.2.1.3 DFT calculations on the parent and one electron reduced species

In order to gain further insight into the primary one electron transfer step of the η^2 -carboxylate, DFT calculations were undertaken. Attempts to simulate the 1,2-bis(diphenylphosphino)ethane system proved difficult because of the large number of atoms involved: optimisation did not converge after several weeks of calculations. A simplified model of the complex was therefore chosen, the dmpe [1,2-bis(dimethylphosphino)ethane] complex. Calculations for $[\text{MoH}_2(\eta^2\text{-O}_2\text{CCH}_3)(\text{dmpe})_2]^+$ and related systems were carried out at the B3LYP hybrid GGA functional level of theory. Molybdenum atoms were described using the SDD basis set, all other atoms used the 6-31++(d,p) basis set (full details can be found in the experimental section). The structure of the parent, η^2 species is shown in Figure 10.

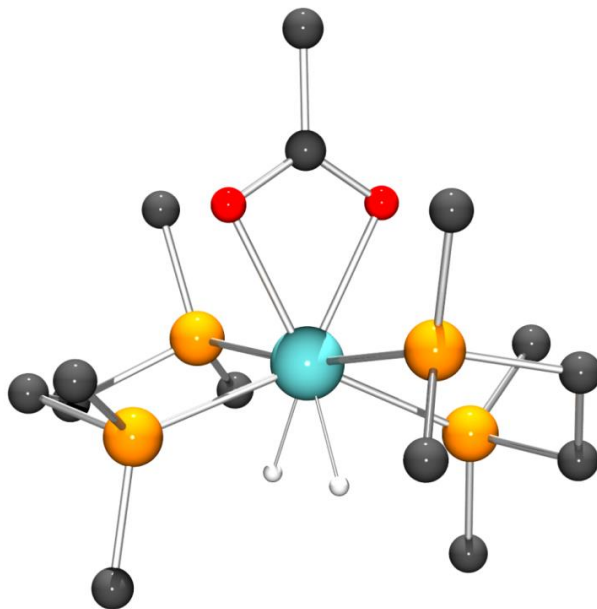


Figure 10 Pictorial representation of $[\text{MoH}_2(\eta^2\text{-O}_2\text{CCH}_3)(\text{dmpe})_2]^+$ as calculated by DFT.

As expected the acetate ligand adopts the η^2 -configuration with the hydride and phosphine ligands deployed in a similar fashion as to that found in X-ray crystal structure of the complex $[\text{MoH}_2(\eta^2\text{-O}_2\text{CCH}_3)(\text{dppe})_2]^+$, Figure 1. Calculations were repeated for the one-electron reduced system which showed a geometry with the acetato- ligand now in the η^1 open form, as shown by Figure 11.

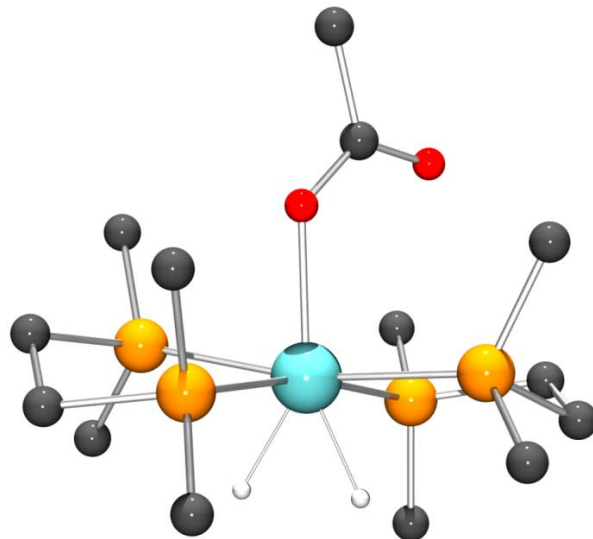


Figure 11 Pictorial representation of $[\text{MoH}_2(\eta^1\text{-O}_2\text{CCH}_3)(\text{dmpe})_2]$ as calculated by DFT.

The addition of a second electron gives a structure similar to that of the one electron reduced species consistent with the fast partially reversible electron transfer observed for the secondary process, Figure 12.

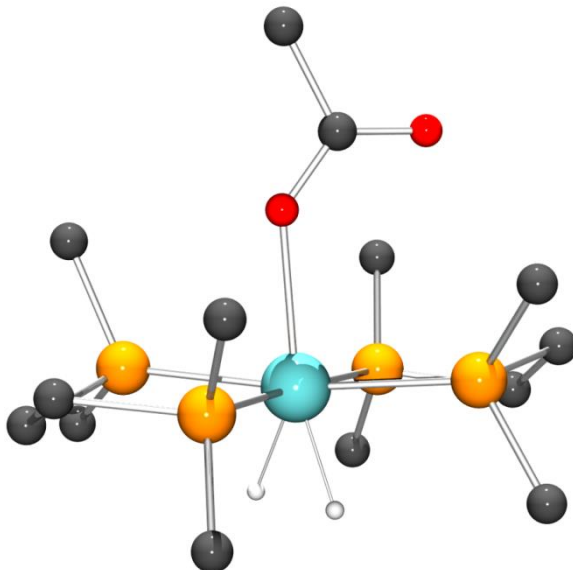


Figure 12 Pictorial representation of $[\text{MoH}_2(\eta^1\text{-O}_2\text{CCH}_3)(\text{dmpe})_2]$ as calculated by DFT.

However, the Mo-O bond length is lengthened by about 0.14 Å. This weakening of the Mo-O bond is consistent with the lability of the acetate group at this redox level and replacement by ligands such as N₂, CO or H₂.

From the calculated structures of the Mo acetate complex in the Mo^{IV, III, II} redox states, it was possible to calculate theoretical infra-red features in the gas phase. Figure 13 shows the calculated spectra in the range 1300-2100 cm⁻¹, which encompasses vibrations associated Mo-H and C=O.

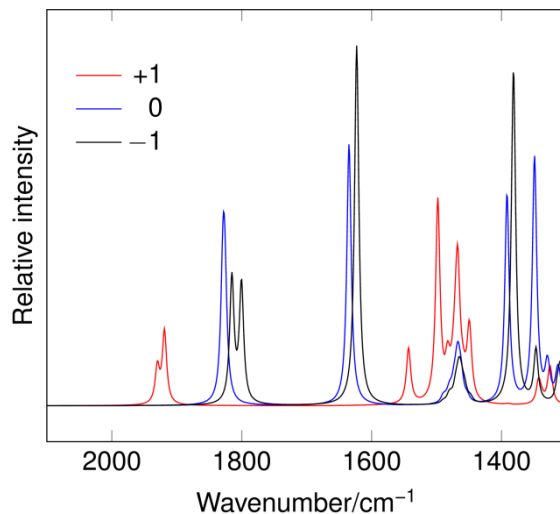


Figure 13 Simulated infrared stretching frequencies of $[\text{MoH}_2(\eta^2\text{-O}_2\text{CCH}_3)(\text{dmpe})_2]^+$ (+1), $[\text{MoH}_2(\eta^1\text{-O}_2\text{CCH}_3)(\text{dmpe})_2]$ (0) and $[\text{MoH}_2(\eta^1\text{-O}_2\text{CCH}_3)(\text{dmpe})_2]^-$ (-1) in the gas phase as calculated by DFT.

The calculated bands for $[\text{MoH}_2(\eta^2\text{-O}_2\text{CCH}_3)(\text{dmpe})_2]^+$ and the experimental bands of $[\text{MoH}_2(\eta^2\text{-O}_2\text{CCH}_3)(\text{dppe})_2]^+$ are in very good agreement when considering the fact that the phenyl groups on the phosphine ligands are replaced by methyl groups in the modelled complex. This increases the electron donating capabilities of the phosphine ligands, as the electron withdrawing phenyl substituent has been removed, and therefore shifts the IR stretching frequencies to a higher wavenumber.

IR Stretch	a) Experimental IR for $[\text{MoH}_2(\eta^2\text{-O}_2\text{CCH}_3)(\text{dppe})_2]^+ / \text{cm}^{-1}$	b) Calculated IR for $[\text{MoH}_2(\eta^2\text{-O}_2\text{CCH}_3)(\text{dmpe})_2]^+ / \text{cm}^{-1}$
$\nu(\text{Mo-H})$	1880	1915 (sym), 1900 (asym)
$\nu(\text{OCO})_{\text{asym}}$	1470	1561
$\nu(\text{OCO})_{\text{sym}}$	1410	1510

Table 2 Experimental and calculated IR stretching frequencies for the complexes $[\text{MoH}_2(\eta^2\text{-O}_2\text{CCH}_3)(\text{dppe})_2]^+$ and $[\text{MoH}_2(\eta^2\text{-O}_2\text{CCH}_3)(\text{dppe})_2]^+$ respectively. (a measured as KBr disc, b simulated in the gas phase).

From comparison of the IR data for the experimental and simulated complex for the analogous stretches, it is clear that the calculated data is positively shifted in accordance with the increased electron donating capability of the methyl substituent on the phosphine ligand compared to phenyl in the experimental case. However, when the two sets of values are plotted against each other they fall onto a straight line, Figure A3.1. This shows that there is good agreement between the experimental and simulated complexes with respect to the structure.

On the conversion of the η^2 acetato- ligand to the η^1 form following the single electron reduction, the CO bands at 1561 and 1510 cm^{-1} disappear and a new band for C=O is calculated to occur at *ca* 1630 cm^{-1} . There is also a substantial shift in the Mo-H stretch to a lower frequency, from 1915 and 1900 cm^{-1} to one band 1820 cm^{-1} . On addition of the second electron, the calculated shifts of CO and Mo-H frequencies to lower wavenumber are relatively small.

In summary, the DFT calculations support the conclusion from the experimental data that the single electron transfer leads to an opening of η^2 -carboxlato- ligand to the η^1 ligated form and a further electron transfer weakens the Mo-O bond, consistent with lability of the acetate group at the Mo^{II}.

Confirming these theoretical results experimentally to prove the validity of the DFT calculations would be beneficial. In principle, this should be possible by thin layer spectroelectrochemical studies of the Mo^{III} system. However hydride bands are weak and signal to noise ratio in preliminary SEC studies prevented detection of these bands. The CO stretches have a stronger IR absorbance than the hydride bands, so would potentially have a response above the noise level, but only if a filter transmitting in the correct range, 1300-1700 cm⁻¹, is used to cut down the amount of data to process. Unfortunately, this was not available at the time of undertaking the work, so no experimental time-resolved IR data could be recorded.

3.2.1.4 Influence of the metal and the carboxylate ligand on the primary electron transfer

Figure 14 shows the cyclic voltammogram of $[\text{MoH}_2(\eta^2\text{-O}_2\text{CCH}_3)(\text{dppe})_2]\text{[BPh}_4]$ and of its tungsten analogue.

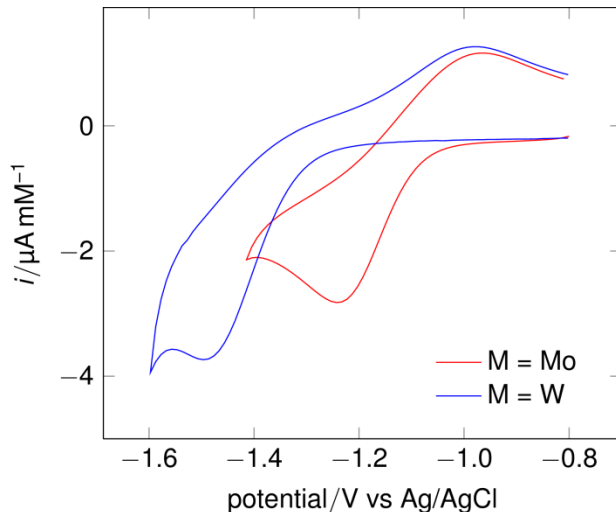


Figure 14 Concentration-normalised cyclic voltammetry of $[\text{MH}_2(\eta^2\text{-O}_2\text{CCH}_3)(\text{dppe})_2]\text{[BPh}_4]$ complex in 1:3 molar ratio $[\text{NBu}_4]\text{[BF}_4]$ -toluene at a vitreous carbon electrode at 303 K at a scan rate of 100 mVs⁻¹.

It is evident that under the same experimental conditions the electron transfer rate for the tungsten complex is slower than that for the molybdenum complex. As is also generally the case, the tungsten complex is harder to reduce than its molybdenum analogue.³ Figure 15 shows the behaviour of the three structurally related tungsten complexes with formate, acetate and trifluoroacetate ligands.

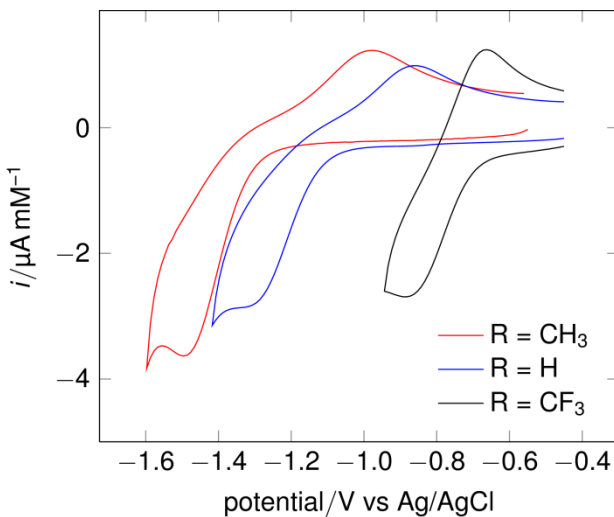


Figure 15 Concentration normalised cyclic voltammetry of $[\text{WH}_2(\eta^2\text{-O}_2\text{CR})(\text{dppe})_2][\text{BPh}_4]$ complex in 1:3 molar ratio $[\text{NBu}_4][\text{BF}_4]$ -toluene at a vitreous carbon electrode at 303 K at a scan rate of 100 mVs^{-1} .

As would be expected, the trifluoroactate complex that possesses the electron withdrawing CF_3 group is substantially easier to reduce than the formate complex, which is in turn more easily reduced than the acetate. What is also clear from this diagram is that the more electron withdrawing the group, the faster the heterogeneous electron transfer. This can be explained by electron withdrawing groups weakening the W-O bonds and lowering the activation energy for η^2 to η^1 structural rearrangement accompanied with electron transfer.

3.2.1.5 Determination of heterogenous rate constants for the primary electron transfer step

The experimental data for variation in the shape of the voltammogram with scan rate can be digitally simulated and from this the value of the heterogenous rate constant estimated. A set of data showing the primary reduction of $[\text{MoH}_2(\eta^2\text{-O}_2\text{CCH}_3)(\text{dppe})_2]^+$ in 0.1 M $[\text{NBu}_4][\text{BF}_4]$ -MeCN at 303 K for a range of scan rates is shown by Figure 16. From this data k_s (MeCN) was estimated to be $6.35 \times 10^{-4} \text{ cm s}^{-1}$ at 303 K.

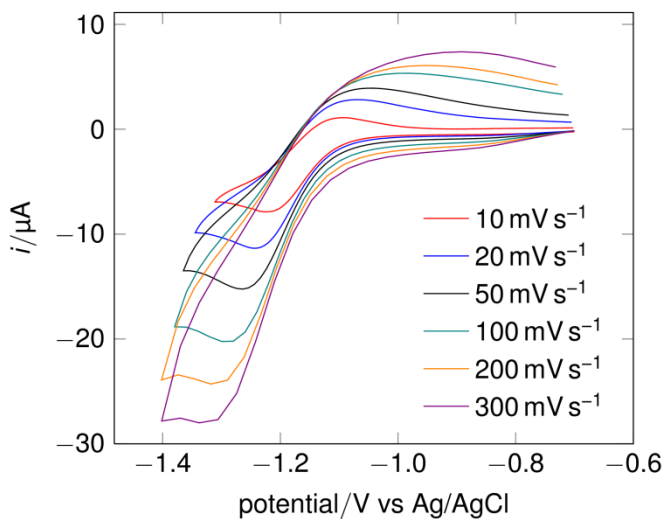


Figure 16 Cyclic voltammetry of 0.98 mM $[\text{MoH}_2(\eta^2\text{-O}_2\text{CCH}_3)(\text{dppe})_2]\text{[BPh}_4]$ complex in 0.1 M $[\text{NBu}_4]\text{[BF}_4]$ -MeCN at 303 K at a vitreous carbon electrode at various scan rates.

In the toluene electrolyte the corresponding set of voltammograms is shown by Figure 17, from which a heterogeneous rate constant of k_s (toluene) = $1.09 \times 10^{-4} \text{ cm s}^{-1}$ was estimated for the primary electron transfer step, also at 303 K.

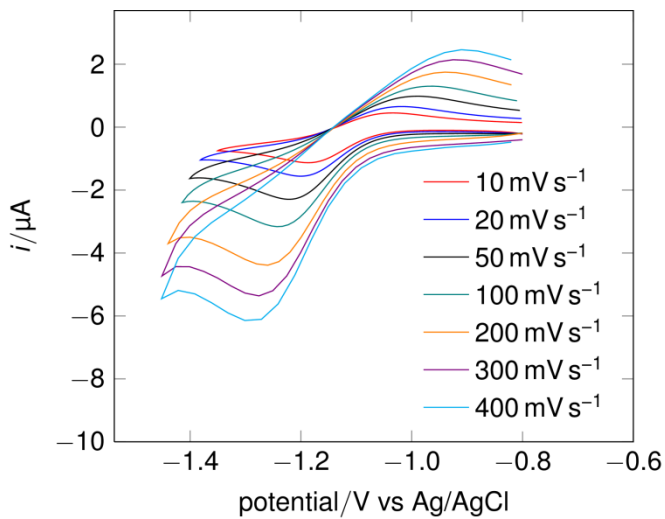


Figure 17 Cyclic voltammetry of 0.98 mM $[\text{MoH}_2(\eta^2\text{-O}_2\text{CCH}_3)(\text{dppe})_2]\text{[BPh}_4]$ complex 1:3 molar ratio $[\text{NBu}_4]\text{[BF}_4]$ -toluene at 303 K at a vitreous carbon electrode at various scan rates.

Clearly the solvent-electrolyte system has an effect upon the heterogeneous rate constant with that measured in MeCN being about six-fold greater, Table 3. This is possibly associated with the $\eta^2 \rightarrow \eta^1$ conversion where solvation by the more polar solvent of the carbonyl group stabilises the transition state, leading to faster electron-transfer kinetics.

Table 3 shows the parameters obtained by digital simulation of the experimental cyclic voltammetric data for the cyclic voltammetry of the set of Mo and W complexes studied in the toluene electrolyte, Figures A3.2-A3.11.

M	R	$E^{\circ'}$ / V	α / eV	$k_s / 10^{-4} \text{ cm s}^{-1}$	D / $10^{-7} \text{ cm}^2 \text{ s}$	C / mM
Mo	H	-0.94	0.50	2	3	1.11
W	H	-1.09	0.55	0.2	3	1.13
Mo	CH ₃	-1.10	0.50	1	3	1.12
W	CH ₃	-1.27	0.62	0.2	3	1.10
W	CF ₃	-0.76	0.50	2	3	0.60
Mo ^a	CH ₃	-1.15	0.50	6	10	1.11

Table 3 Digital simulation of electrochemical values for complexes $[\text{MH}_2(\eta^2\text{-O}_2\text{CR})(\text{dppe})_2]^+$ in 1:3 molar ratio [NBu₄][BF₄]-Toluene electrolyte (a = in 0.1 M [Bu₄N][BF₄]-MeCN electrolyte) at 303 K at a vitreous carbon electrode ($A = 0.071 \text{ cm}^2$) ($E^{\circ'}$ = potential, α = electron transfer coefficient, k_s = electron transfer rate constant, D = diffusion coefficient, C = concentration).

For the analogous complexes, the electron transfer rate constant is about an order of magnitude greater for Mo than it is for W. Metal-ligand bond strengths are generally greater for W than for Mo and since cleavage of an M-O bond accompanies electron transfer the slower rate and more negative $E^{\circ'}$ potentials for the tungsten systems are consistent with this, Table 3. The nature of the carboxylate group ($\eta^2\text{-O}_2\text{CR}$, where R = CH₃, H or CF₃) on the magnitude of k_s is shown in Table 3 for the W complexes. The rate increases in the order CH₃ < H < CF₃, which parallels the expected order of the electron-withdrawing effect of these groups. An order of magnitude change in the rate constants is usually necessary for the values to be declared as significantly different to be in line with the accuracy of these types of simulations, therefore these results alone should not be used to explain the effect of changing the R group on the rate constant k_s . However, the trend in the values of k_s is reinforced by the reduction potential trend: the values of $E^{\circ'}$ decrease in the same order as k_s , CH₃ < H < CF₃ as the effective electron withdrawing capabilities of R decreases. The influence of the strongly electron withdrawing CF₃ group on the quasi-reversibility of the primary reduction is the most dramatic, as can be seen from Figure 15.

3.2.1.6 Effect of electrode material on electron transfer kinetics

The effect of the electrode material on the heterogeneous electron transfer rate constant was investigated. Table 4 lists k_s data measured in an MeCN-electrolyte for the primary reduction step for the η^2 -acetate complex, $[\text{MoH}_2(\eta^2\text{-O}_2\text{CCH}_3)(\text{dppe})_2]^+$.

Electrode material	$E^{0'}$ / V	α / eV	$k_s / 10^{-3} \text{ cm s}^{-1}$	Work function of metal / eV ^{34, 35}
Au(Hg)	-1.16	0.71	5	4.48
C	-1.16	0.71	0.6	ca 5
Si	-0.54	0.50	0.6	4.15
Au	-1.16	0.61	0.3	5.10 – 5.47
Pt	-1.23	0.68	0.2	5.12 – 5.93

Table 4 Digital simulation of electrochemical values for the complex $[\text{MoH}_2(\eta^2\text{-O}_2\text{CCH}_3)(\text{dppe})_2]^+$ in 0.1 M $[\text{Bu}_4\text{N}][\text{BF}_4]$ -MeCN electrolyte at various electrode materials, Au(Hg) electrode is a mercury coated gold electrode, k_s for Si estimated from peak separation, ΔE_p ($E^{0'}$ = potential; α = electron transfer coefficient; k_s = electron transfer rate constant; A = electrode area; temperature, T = 298 K; diffusion coefficient; D = $6 \times 10^{-6} \text{ cm}^2 \text{ s}$; concentration; C = $9.8 \times 10^{-4} \text{ mol L}^{-1}$).

It is quite remarkable that the electron transfer rate for this system is very sensitive to the nature of the electrode material with k_s varying by around one order of magnitude. It is evident that this system may provide a sensitive probe of interfacial electron transfer dynamics in the inner reaction layer adjacent to the electrode surface. The heterogeneous rate constant increases for the different electrode materials in the order of Pt ≈ Ag < C ≈ Si < Hg. If the premise is correct that the $\eta^2 \rightarrow \eta^1$ interconversion of the carboxylate is concerted with the electron transfer, then how the structure of the electrode-solution interface facilitates or inhibits this process may explain the variation in k_s . It has been shown that the nature of the solvent can influence the heterogeneous rate constant. Dipolar and ionic interactions at the inner reaction layer (inner Helmholtz plane) are likely to perturb the energetics of the rearrangement. It is not known why these effects vary from material to material, but perhaps there is an effect on the composition of the electrical double layer as a consequence of the different surface groups of the electrode materials. There is some correlation between the workfunction of the materials^{34, 35} and the observed heterogeneous rate constant, in that the materials with a lower workfunction gave a faster rate.

In summary, the effects of the four variable discussed above on the electrochemistry of the systems $[\text{MH}_2(\eta^2\text{-O}_2\text{R})(\text{dppe})_2]^+$ are shown in Table 5.

Variable	Influences
Electrode material	k_{het}
Solvent	k_{het}
R group	$k_{\text{het}}, E^{0'}$
Metal	$k_{\text{het}}, E^{0'}$

Table 5 Summary of factors affecting the electrochemistry of $[\text{MH}_2(\eta^2\text{-O}_2\text{R})(\text{dppe})_2]^+$

3.2.2 Electrocatalysis of Hydrogen Evolution

3.2.2.1 Effect of addition of acid on the cyclic voltammetry of $[\text{MoH}_2(\eta^2\text{-O}_2\text{CCH}_3)(\text{dppe})_2]^+$

The effect of acid on the cyclic voltammetry of $[\text{MoH}_2(\eta^2\text{-O}_2\text{CCH}_3)(\text{dppe})_2]^+$ was examined in 0.1 M $[\text{NBu}_4][\text{BF}_4]$ -MeCN at a vitreous carbon electrode. The acid CH_3COOH ($\text{pK}_a = 22.30$ in MeCN)³⁶ was employed because it is not directly reducible at the vitreous carbon electrode in the regime where the complex is electroactive and because complications where ligand exchange might take place between bound acetate and conjugate bases or counter ions needed to be avoided. Figures 18 and 19 show the effect of the addition of increasing amounts of $\text{CH}_3\text{CO}_2\text{H}$ on the cyclic voltammetry of a 0.8 mM solution of the complex.

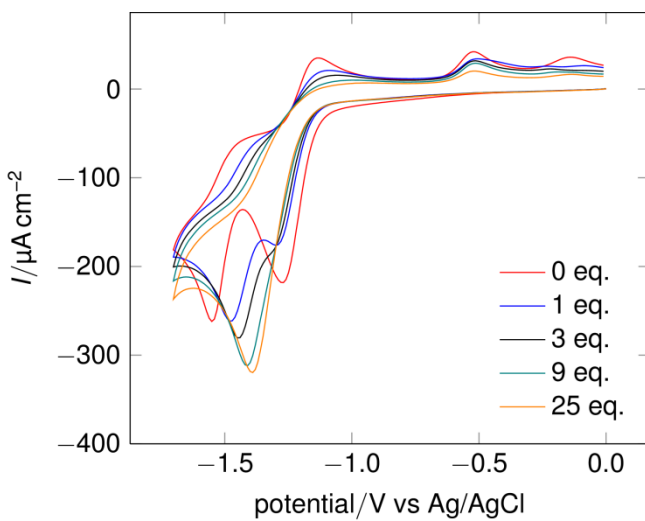


Figure 18 Cyclic voltammetry of 0.8 mM $[\text{MoH}_2(\eta^2\text{-O}_2\text{CCH}_3)(\text{dppe})_2]\text{[BPh}_4]$ complex in 0.1 M $[\text{NBu}_4]\text{[BF}_4]$ -MeCN at a vitreous carbon electrode with increasing number of equivalents of acetic acid at a scan rate of 100 mV s^{-1} .

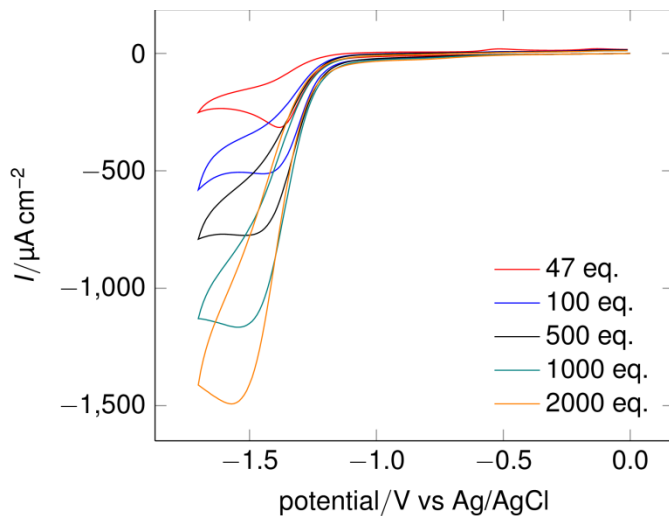


Figure 19 Cyclic voltammetry of 0.8 mM $[\text{MoH}_2(\eta^2\text{-O}_2\text{CCH}_3)(\text{dppe})_2]\text{[BPh}_4]$ complex in 0.1 M $[\text{NBu}_4]\text{[BF}_4]$ -MeCN at a vitreous carbon electrode with increasing number of equivalents of acetic acid at a scan rate of 100 mV s^{-1} .

In the range of acid 1-2000 eq. (0.8-20.0 mM of $\text{CH}_3\text{CO}_2\text{H}$), it can be seen that the primary and secondary processes merge as the concentration of acid is increased, giving a single irreversible process at 20.0 mM acid which occurs at a potential close to that of the primary step. As the concentration of the acid is further increased, the reduction peak increases in magnitude until at *ca* 1.6 M acid the current reaches a plateau, Figure 19. The cyclic voltammetric results are consistent with electrocatalytic

reduction of proton to dihydrogen. The formation of this product was unequivocally demonstrated by bulk electrolyses which gave dihydrogen in high current efficiency as described in detail below.

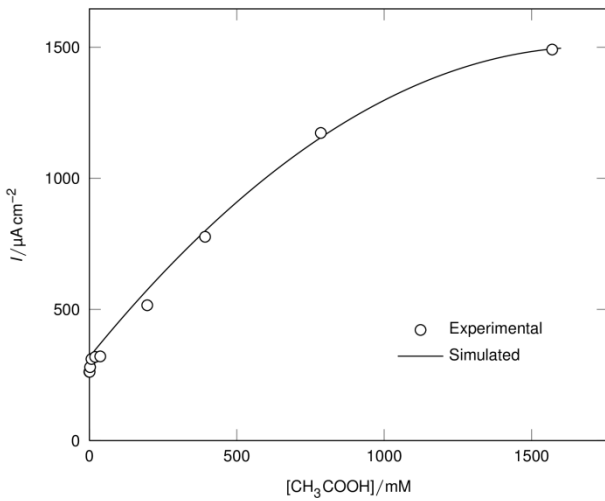


Figure 20 Catalytic current density *versus* concentration of $\text{CH}_3\text{CO}_2\text{H}$ at vitreous carbon electrode. The solid line is the digitally simulated response for the system.

It is evident that the current approaches a plateau at high acid concentrations. Using Equation 3.1,

$$k_{obs} = \nu \cdot \left(\frac{i_{cat}/i_p}{0.72} \right)^2 \quad (\text{Equation 3.1})$$

the value of k_{obs} for the process was calculated, which is related to the second order rate constant, k_{cat} , by the relationship in Equation 3.2.

$$k_{cat} = \frac{k_{obs}}{[H^+]} \quad (\text{Equation 3.2})$$

This gave the value $k_{cat} = 5.13 \pm 0.26 \text{ M}^{-1} \text{ s}^{-1}$ at 1000 equivalents of acid. To gain further insight into the electrocatalysis the experimental data across a range of acid concentrations has been fitted to a theoretical model. This model involves the generation of a trihydride intermediate by protonation of the two electron reduced parent cation. As discussed in Section 3.1.3, evidence for a trihydride intermediate is

based upon the isolation of a stable tungsten analogue which has been crystallographically characterised, Figure 2, and the correspondence between the electrochemistry of the intermediate detected in the Mo system and that of the W trihydride.¹ At low acid concentration the rate-determining step is protonation to give a ‘ MoH_4 ’ intermediate which loses H_2 to regenerate the parent cationic catalyst. This is modelled with a second order rate constant, $k_2 = 20 \pm 1 \text{ M}^{-1} \text{ s}^{-1}$. At higher acid concentration, this step is fast compared with H_2 loss. Therefore, the loss of H_2 from the tetrahydride becomes the acid-independent rate-determining step which is fitted with a rate constant, $k_{\text{H}} = 40 \pm 2 \text{ s}^{-1}$, Scheme 4. This mechanism accords with that for hydrogen evolution from $[\text{WH}_3(\eta^2\text{-O}_2\text{CCH}_3)(\text{dppe})_2]$ upon attack by HCl .³⁷

3.2.2.2 Bulk electrolysis and detection of dihydrogen

Controlled potential electrolysis was carried out in a closed cell at low and high acid concentrations and dihydrogen was measured by gas chromatography as described in the experimental section. Figure 21 shows the current vs charge passed plot for an electrolysis at a vitreous carbon cathode in 0.1 M $[\text{NBu}_4][\text{BF}_4]$ -MeCN electrolyte in the presence of 13.4 mM acetic acid (9 equivalents) and 1.49 mM of the catalyst, $[\text{MoH}_2(\eta^2\text{-O}_2\text{CCH}_3)(\text{dppe})_2][\text{BPh}_4]$.

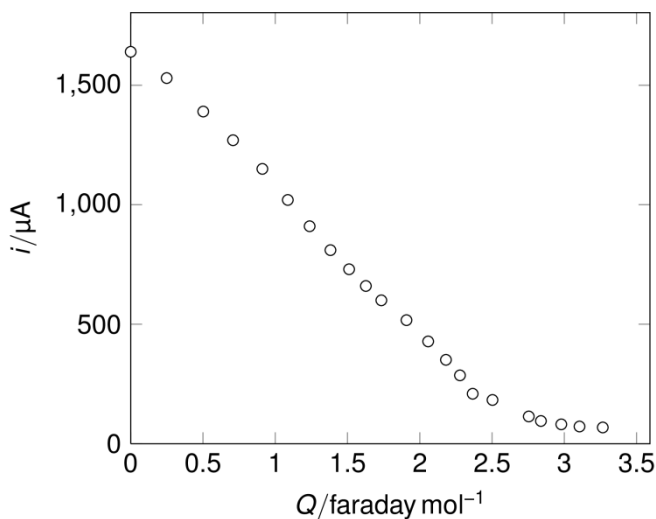


Figure 21 Coulometry for the reduction of 1.49 mM $[\text{MoH}_2(\eta^2\text{-O}_2\text{CCH}_3)(\text{dppe})_2]^+$ in presence of 9 eq. of protons at a vitreous carbon electrode in 0.1 M $[\text{Bu}_4\text{N}][\text{BF}_4]$ -MeCN electrolyte.

The current decays steadily to a low value over a period of *ca* 3 h during which time the colour of the catholyte changes from magenta to orange-yellow. After the passage of 3.26 electrons per mole of complex the electrolysis was terminated and analysed for dihydrogen. The electrolysis produced 8.28 µmols of dihydrogen corresponding to its formation with a current efficiency of 84 % based upon the *total* charge passed, Table A3.1. At termination of the electrolysis 28 % of the total proton available had been converted to dihydrogen. Data for electrolyses at 6, 9 and 15 equivalents of acid summarised in Table A3.1, show similar high current efficiencies (yields) of 80-90 %.

Figure 22 shows the current *vs* charge passed plot for an electrolysis under similar conditions to that described above but using 100 equivalents of acid (137 mM).

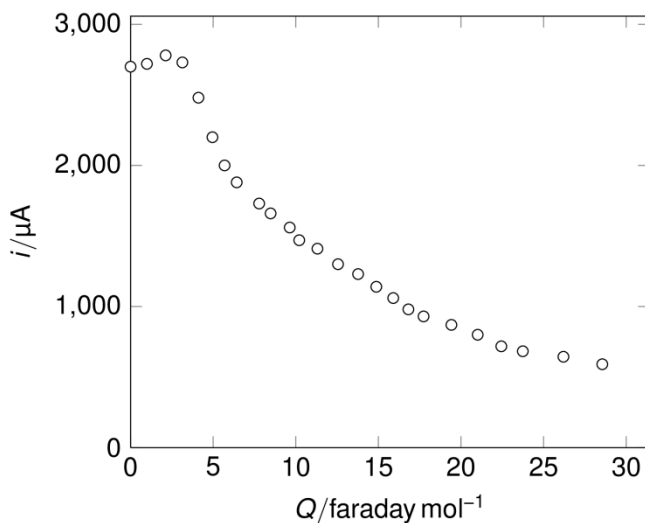


Figure 22 Coulometry for the reduction of 1.37 mM $[\text{MoH}_2(\eta^2\text{-O}_2\text{CCH}_3)(\text{dppe})_2]^+$ in presence of 100 eq. of protons at a vitreous carbon electrode in 0.1 M $[\text{Bu}_4\text{N}][\text{BF}_4]$ -MeCN electrolyte.

The current efficiency for dihydrogen formation was 88 % and at the termination of the electrolysis 17 % of the total available acid was consumed. However, it can be seen from the plot that a very substantial cell current is observed before the cell is switched out. This is about 20 % of the initial current and clearly further turnover of proton reduction is taking place. Notably, the catholyte remained pale magenta indicative of the presence of the parent catalyst.

The high current efficiency but low acid consumption suggests the catalyst is not turning over. An analysis of the catholyte was undertaken to try to understand this problem.

3.2.2.3 Cyclic voltammetry of the catholyte at the termination of electrolysis: detection of a molybdenum product

After the electrolysis in the presence of nine equivalents of acid was stopped, the catholyte was examined by cyclic voltammetry at a vitreous carbon electrode. Figure 23 shows the response.

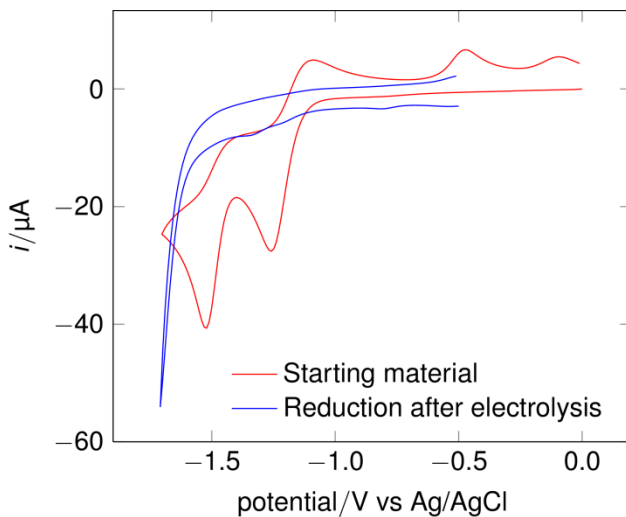


Figure 23 Cyclic voltammetry of 1.49 mM $[\text{MoH}_2(\eta^2\text{-O}_2\text{CCH}_3)(\text{dppe})_2][\text{BPh}_4]$ complex in 0.1 M $[\text{NBu}_4]\text{[BF}_4]$ -MeCN before electrolysis with no acid present and after electrolysis in the presence of 9 eq. $\text{CH}_3\text{CO}_2\text{H}$ at a vitreous carbon electrode at a scan rate of 100 mV s^{-1} .

On scanning between -0.5 and -1.7 V vs Ag/AgCl the cyclic voltammetric response shows that most of the parent complex has been consumed as there is little electroactive species detected near -1.4 V vs Ag/AgCl. On scanning between -0.5 and 0.3 V vs Ag/AgCl, a well-defined wave near -0.15 V vs Ag/AgCl is detected, corresponding to the oxidation of a stable reduction product formed during catalysis. This species, which will be referred to as **A**, is a major product of the electrolysis because the peak current for its oxidation is *ca* 60 % of that of the parent complex, Figure 24.

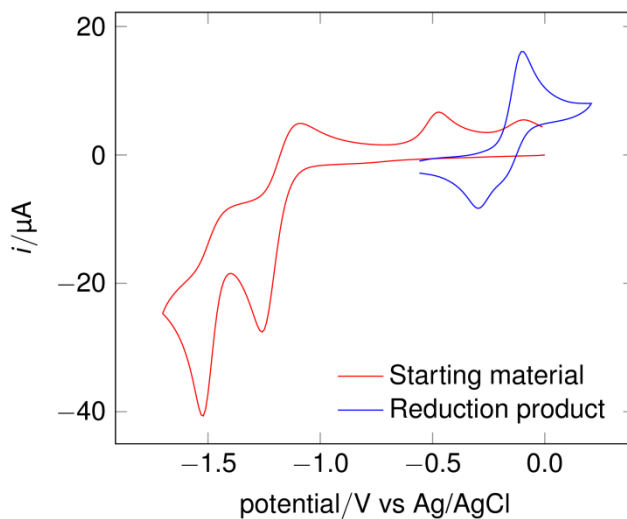


Figure 24 Cyclic voltammetry of 1.49 mM $[\text{MoH}_2(\eta^2\text{-O}_2\text{CCH}_3)(\text{dppe})_2]\text{[BPh}_4]$ complex in 0.1 M $[\text{NBu}_4]\text{[BF}_4]$ -MeCN after electrolysis in the presence of 9 eq. $\text{CH}_3\text{CO}_2\text{H}$ at a vitreous carbon electrode and at a scan rate of 100 mV s^{-1} .

At low temperature, **A** displays a reversible single electron oxidation in its cyclic voltammetric response, Figure 25.

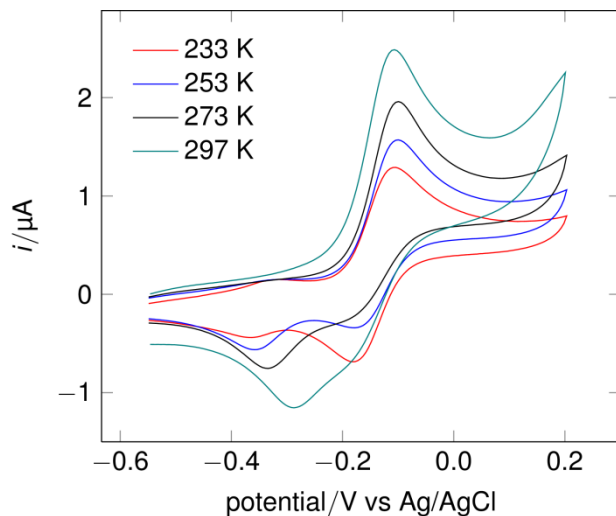
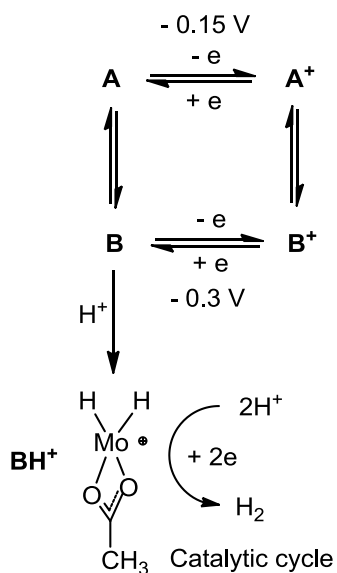


Figure 25 Cyclic voltammetry of 1.49 mM $[\text{MoH}_2(\eta^2\text{-O}_2\text{CCH}_3)(\text{dppe})_2]\text{[BPh}_4]$ complex in 0.1 M $[\text{NBu}_4]\text{[BF}_4]$ -MeCN after electrolysis in the presence of 9 eq. $\text{CH}_3\text{CO}_2\text{H}$ at a vitreous carbon electrode and at a scan rate of 100 mV s^{-1} at various temperatures.

At room temperature, this oxidation becomes irreversible and a new reduction peak is observed in the voltammetry. This arises from conversion of **A**⁺ to an electroactive form **B**⁺ which reduces irreversibly near -0.3 V vs Ag/AgCl, to give initially **B**, Scheme 2.



Scheme 2 Mechanistic pathway for deactivation of catalyst (diphosphine ligands omitted for clarity).

The scan rate dependence of the oxidation process at room temperature is shown in Figure 26.

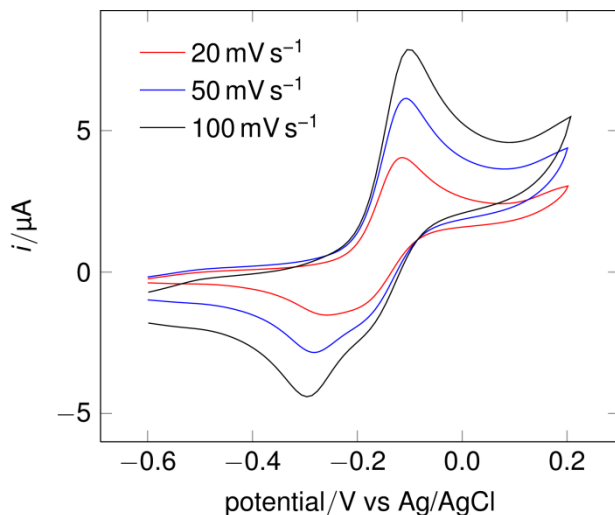


Figure 26 Cyclic voltammetry of 1.49 mM $[\text{MoH}_2(\eta^2\text{-O}_2\text{CCH}_3)(\text{dppe})_2][\text{BPh}_4]$ complex in 0.1 M $[\text{NBu}_4][\text{BF}_4]$ -MeCN after electrolysis in the presence of 9 eq. $\text{CH}_3\text{CO}_2\text{H}$ at a vitreous carbon electrode at various scan rates.

It can be seen that at slower scan rates the process approaches reversibility as the reduction component is shifted to more positive potentials. This behaviour is consistent with a redox mechanism involving the redox interconversion ‘square’ shown in Scheme 2. Using this model, the voltammograms can be simulated, as shown in Figure 27, using the thermodynamic and kinetic parameters given in Scheme 4.

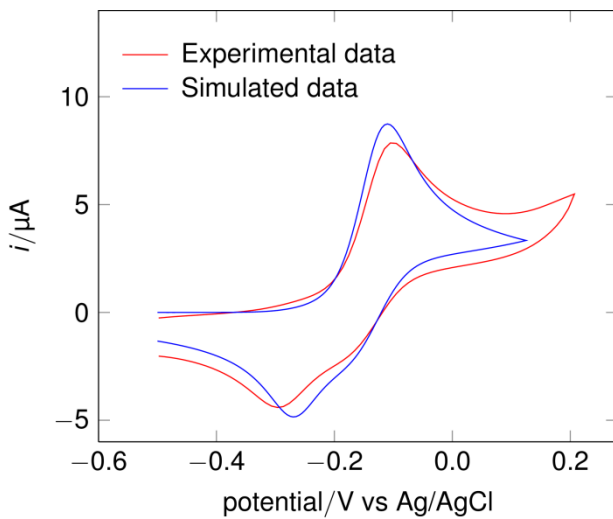


Figure 27 Comparison of simulated and experimental cyclic voltammetry of the oxidation of the deactivated catalyst, 1.49 mM $[\text{MoH}_2(\eta^2\text{-O}_2\text{CCH}_3)(\text{dppe})_2]\text{[BPh}_4]$ complex in 0.1 M $[\text{NBu}_4]\text{[BF}_4]$ -MeCN after electrolysis in the presence of 9 eq. $\text{CH}_3\text{CO}_2\text{H}$ at a vitreous carbon electrode and at a scan rate of 100 mV s^{-1} ($A = 0.071 \text{ cm}^2$, $\alpha = 0.5$, $k = 1 \times 10^4$).

Extending the reverse scan range to -1.7 V vs Ag/AgCl after oxidation of product **A** to form **B** reveals two additional peaks at -1.25 and -1.35 V vs Ag/AgCl, Figure 28.

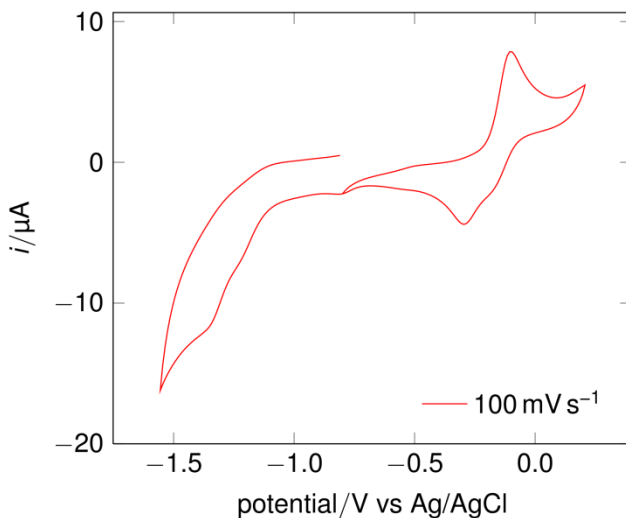


Figure 28 Cyclic voltammetry of 1.49 mM $[\text{MoH}_2(\eta^2\text{-O}_2\text{CCH}_3)(\text{dppe})_2]\text{[BPh}_4]$ complex in 0.1 M $[\text{NBu}_4]\text{[BF}_4]$ -MeCN after electrolysis in the presence of 9 eq. $\text{CH}_3\text{CO}_2\text{H}$ at a vitreous carbon electrode and at a scan rate of 100 mV s^{-1} .

The peaks must arise from chemistry following the generation of **B**. Their magnitude increases with scan rate as would be expected because, at the shorter time intervals of the faster scans, there is less time for the product derived from **B** to diffuse away from the electrode.

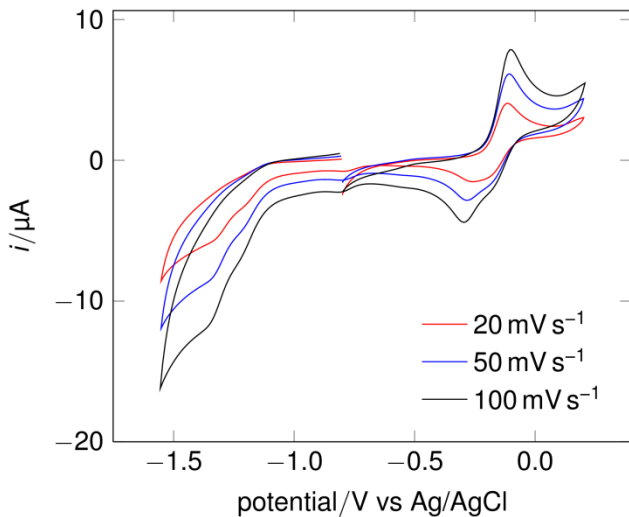
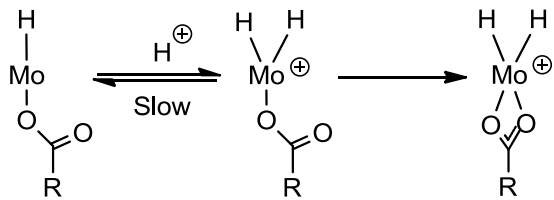


Figure 29 Cyclic voltammetry of 1.49 mM $[\text{MoH}_2(\eta^2\text{-O}_2\text{CCH}_3)(\text{dppe})_2]\text{[BPh}_4]$ complex in 0.1 M $[\text{NBu}_4]\text{[BF}_4]$ -MeCN after electrolysis in the presence of 9 eq. $\text{CH}_3\text{CO}_2\text{H}$ at a vitreous carbon electrode at various scan rates.

Additionally, if following reduction of the oxidation product there is a slow rearrangement to the parent product, BH^+ , as suggested by the reversibility at slow scans, this would also contribute to the enhanced currents observed at the faster scans where the ‘slow’ rearrangement is beaten. The peak potentials associated with reduction near -1.4 V vs Ag/AgCl correspond to the small peaks observed after termination of the electrolysis, but are of course much enhanced. Their potential is consistent with regeneration of $[\text{MoH}_2(\eta^2\text{-O}_2\text{CCH}_3)(\text{dppe})_2]^+$ which can engage in catalysis of proton reduction in the presence of the excess acid. Therefore, there must be a pathway which allows conversion of **A** to the Mo^{IV} cation, BH^+ as shown in Scheme 2.

There is a noticeable loss in current for the oxidation of **A** at corresponding scan rates in the order of i_p^{ox} : Figure 24 > Figures 26, 28, 29 > Figure 25. This was the order in which the scans were performed, so the loss in current could be associated with slow chemical conversion of **A** over time to **B** by protonation from the excess acid in solution followed by closure of the η^1 -acetate, Scheme 3.



Scheme 3 Slow protonation step of $[\text{MoH}(\eta^1\text{-O}_2\text{CCH}_3)(\text{dppe})_2]$ to chemically regenerate the catalyst (diphosphine ligands omitted for clarity).

Slow catalytic turnover could be sustained during the electrolysis experiment with reprotonation of the open monohydride, **A** being the rate-limiting step. This would account for the significant steady current observed at the end of the electrolysis in the presence of 100 eq. of acid, Figure 22, and the colour remaining a pale magenta.

3.2.2.4 The nature of the electrolysis product **A** and relationship to \mathbf{A}^+ , \mathbf{B}^+ and **B**

The redox potential of the product falls in a region where Mo^0 or Mo^{II} species are observed to undergo reversible oxidation. An explanation for these observations is that at the lower acid concentrations, electrocatalysis takes place but the rate of proton attack on the Mo trihydride intermediate is sufficiently slow for this species to decay by a competing pathway. A plausible competing pathway is thermal loss of dihydrogen to give a monohydride species with a closed η^2 -acetato-ligand. It would be reasonable that this species could reprotonate with acetic acid to regenerate the catalyst, Scheme 4. However, this species could plausibly rearrange *via* a competitive pathway by opening up of the bidentate acetato-ligand to give a high spin η^1 species. This would be analogous to known high spin Mo^{II} dihalide systems such as $[\text{MoCl}_2(\text{dppe})_2]$.³⁸ The η^2 to η^1 conversion would leave less electron density on the metal and a system less likely to protonate to give a hydride. This would provide a pathway for catalyst deactivation consistent with the fall off of catalytic current during electrolysis to a low steady state level. Thus it is proposed that species **A** is $[\text{MoH}(\eta^1\text{-O}_2\text{CCH}_3)(\text{dppe})_2]^+$. This assignment now provides a self-consistent explanation of the electrochemistry of **A** described above. Thus one electron oxidation of 16-electron $[\text{MoH}(\eta^1\text{-O}_2\text{CCH}_3)(\text{dppe})_2]^+$, (**A** to \mathbf{A}^+) is reversible at low temperature, as is observed for $[\text{MoCl}_2(\text{dppe})_2]$. At room temperature the positive charge on Mo in \mathbf{A}^+ favours ring

closure to give the 17-electron $[\text{MoH}(\eta^2\text{-O}_2\text{CCH}_3)(\text{dppe})_2]^+$ system which is assigned to **B**⁺, Scheme 4. $[\text{MoH}(\eta^2\text{-O}_2\text{CCH}_3)(\text{dppe})_2]^+$, **B**⁺ is electroactive and reduces to **B** which rapidly protonates to give **BH**⁺, which is the parent electrocatalyst $[\text{MoH}_2(\eta^2\text{-O}_2\text{CCH}_3)(\text{dppe})_2]^+$. Ito has reported the ³¹P NMR of the monohydride **B** in benzene,³⁹ a solvent which might be expected to favour the closed configuration. The spectrum shows two triplets at δ 75.4 and 101.0 ppm referenced to PPh₃. ³¹P{¹H} NMR of the catholyte containing **A** shows a singlet at δ 42.8 ppm (δ 48.4 ppm when referenced to PPh₃) which is consistent with a square planar arrangement of four equivalent phosphorus atoms as would be expected for **A**.

Strong support that interconversion of **A** and **B** is a plausible mechanism is provided by DFT calculations on the model monohydride structures. The calculated structures for the closed system and the open triplet, **A** and the closed system, **B** are shown by Figures 30 and 31.

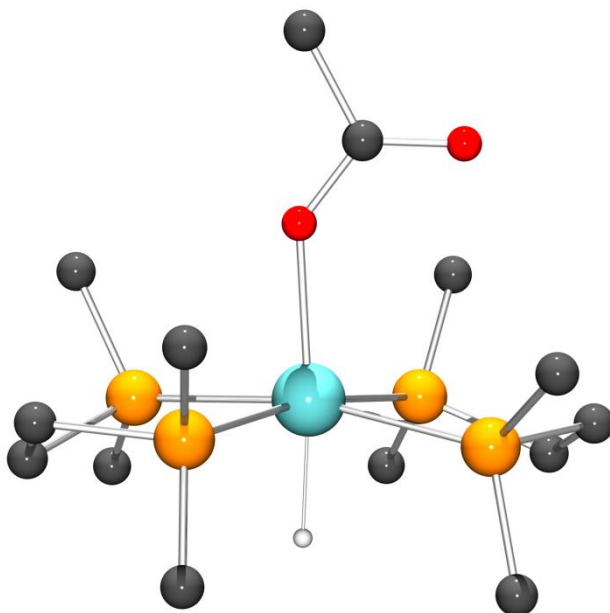


Figure 30 Pictorial representation of the open triplet **A**, $[\text{MoH}(\eta^1\text{-O}_2\text{CCH}_3)(\text{dmpe})_2]$ as calculated by DFT.

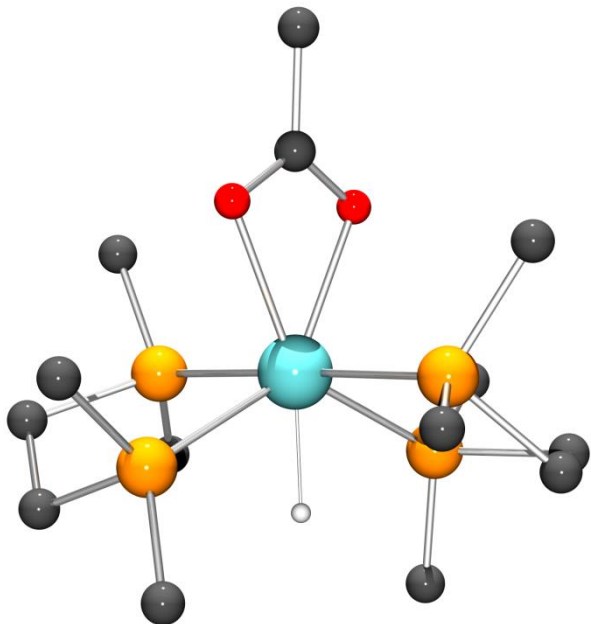
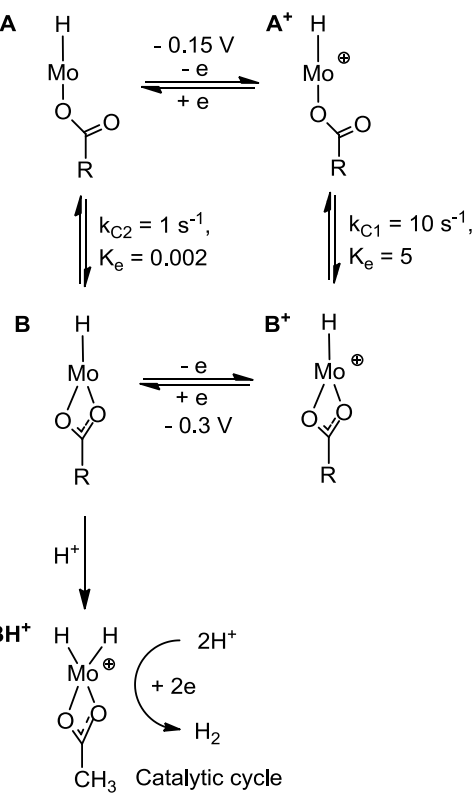


Figure 31 Pictorial representation of the closed system **B**, $[\text{MoH}(\eta^2\text{-O}_2\text{CCH}_3)(\text{dmpe})_2]$ as calculated by DFT.

Importantly, the calculated energy difference between these structures in an MeCN media is less than 6 kJ mol^{-1} . In such DFT calculations, a difference greater than about 8 kJ mol^{-1} (*ca* 2 kcal mol^{-1}) can be considered significant. That **A** has a high spin triplet configuration rather than a singlet arrangement is consistent with the latter structure being 22 kJ mol^{-1} higher in energy. To fully support the mechanism, it would be expected that the one electron oxidised structure **A**⁺ is less stable than the rearranged form **B**⁺, DFT calculations show that this is indeed the case. **B**⁺ in an MeCN solvent is 36 kJ mol^{-1} more stable than **A**⁺.

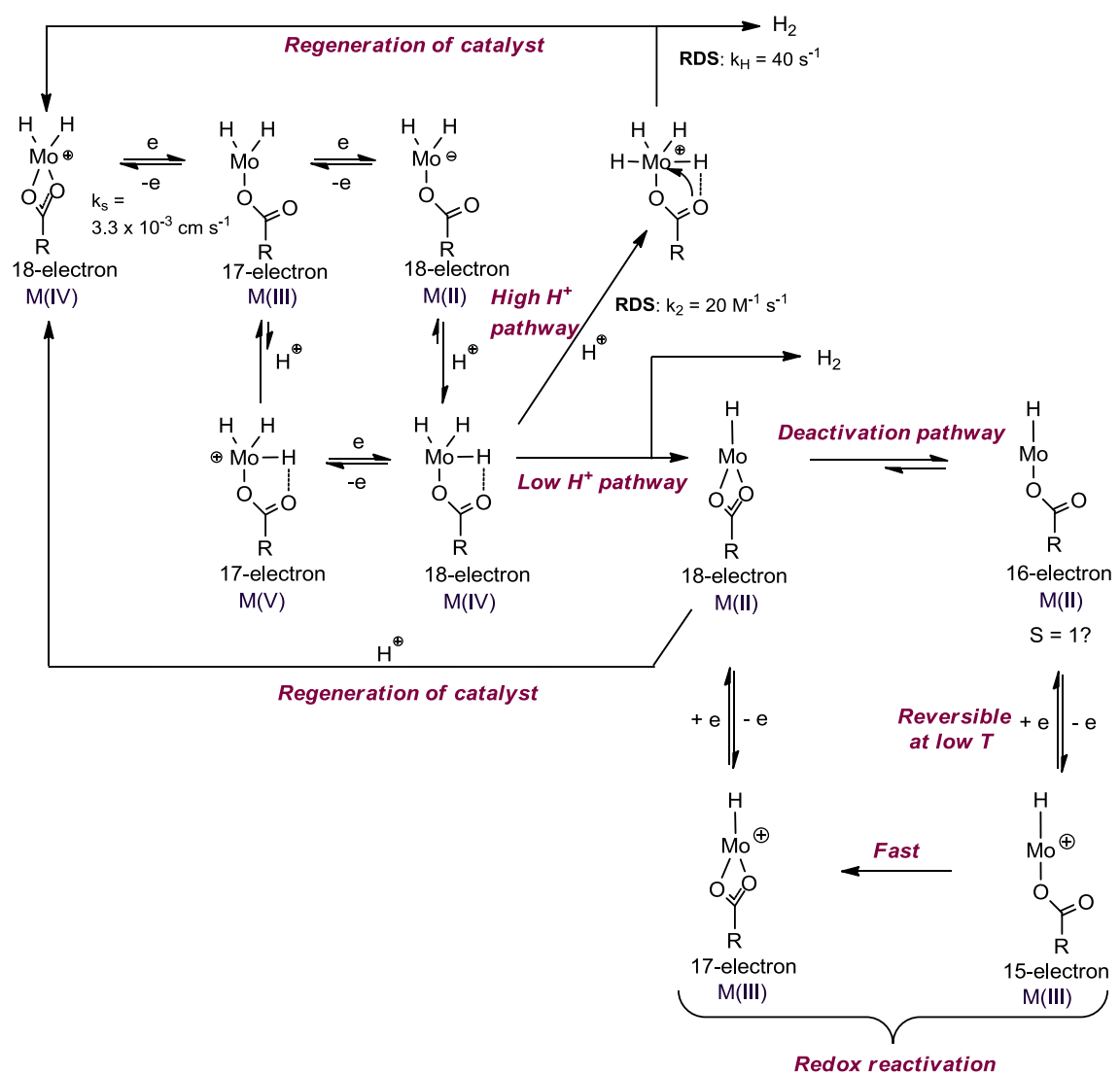
Finally, structures assigned to **A**, **A**⁺, **B**, **B**⁺, **BH**⁺ and their interrelationship, are shown in Scheme 4.



Scheme 4 Pathway for reactivation of deactivated catalyst (diphosphine ligands are omitted for clarity), rate constants from simulation where $a = 0.5 \text{ eV}$, $k_e = 1 \times 10^5 \text{ cm s}^{-1}$, $A = 0.071 \text{ cm}^2$, $T = 298 \text{ K}$, $D = 6 \times 10^{-6} \text{ cm}^2 \text{ s}^{-1}$.

3.2.3 Global scheme for electrocatalysis of hydrogen evolution

Scheme 5 provides an overview of electrocatalysis of proton reduction by $[\text{MoH}_2(\eta^2-\text{O}_2\text{CCH}_3)(\text{dppe})_2]^+$ showing the primary electron transfer steps, the involvement of a trihydride species and the deactivation pathways where $[\text{MoH}_3(\eta^1-\text{O}_2\text{CCH}_3)(\text{dppe})_2]$ is converted to the η^1 -monohydride.



Scheme 5 Proposed pathways for hydrogen evolution electrocatalysed by Mo hydride species
(diphosphine ligands are omitted for clarity).

Here it can be seen that fast protonation of $[\text{MoH}_3(\eta^1\text{-O}_2\text{CCH}_3)(\text{dppe})_2]$ or fast protonation of $[\text{MoH}(\eta^2\text{-O}_2\text{CCH}_3)(\text{dppe})_2]$ are important in sustaining a fast catalytic cycle. The Mo trifluoroacetato- complex in the presence of the stronger acid $\text{CF}_3\text{CO}_2\text{H}$ ($\text{pK}_a = 12.65$ in MeCN)⁴⁰ can sustain electrocatalysis in 0.2 M $[\text{Bu}_4\text{N}] [\text{BF}_4] \text{-DCM}$ electrolyte whereby a plateau current is observed and the chemical yield of dihydrogen based upon available proton is *ca* 90 %.⁴¹ This $[\text{MoH}_2(\eta^2\text{-O}_2\text{CCF}_3)(\text{dppe})_2]^+$ electrocatalysis system cannot be directly compared with the acetate system because in MeCN the parent trifluoroacetato- complex is unstable, whilst in DCM the acetato-complex reduces at a potential close to that of discharge of the solvent. Although not a very convenient solvent for preparative bulk electrolyses, the toluene-electrolyte

might prove useful for directly comparing electrocatalysis by these systems in the same solvent.

3.2.4 Photoelectrochemistry of $[\text{MoH}_2(\eta^2\text{-O}_2\text{CCH}_3)(\text{dppe})_2]^+$ at p-type silicon

3.2.4.1 Light and dark cyclic voltammetric studies

Figure 32 below shows the cyclic voltammetric response of $[\text{MoH}_2(\eta^2\text{-O}_2\text{CCH}_3)(\text{dppe})_2]^+$ at a p-type Si electrode (1–10 Ω cm resistivity, Si–H terminated surface)⁴² in the dark and when illuminated with a halogen fibre optic lamp (Krüss, $\lambda_{\text{max}} = 650$ nm; output at λ_{max} 90 mW cm^{-2}).

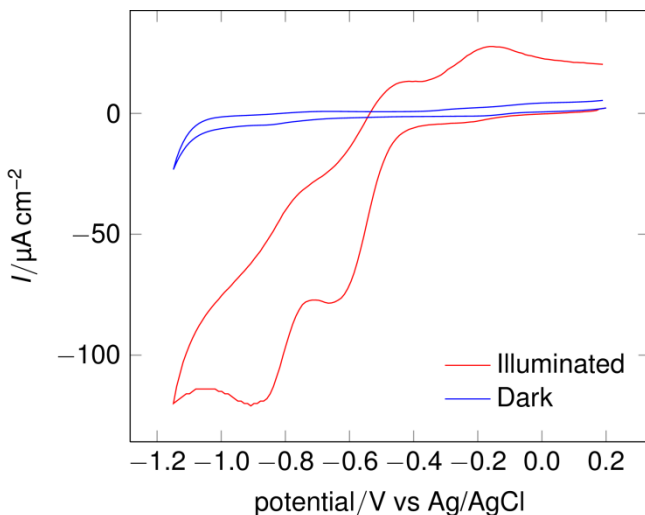


Figure 32 Cyclic voltammetry of 0.5 mM $[\text{MoH}_2(\eta^2\text{-O}_2\text{CCH}_3)(\text{dppe})_2]^+$ in 0.1 M $[\text{NBu}_4]\text{[BF}_4]$ -MeCN at a dark and an illuminated 1–10 Ω cm p-type Si electrode at a scan rate of 100 mV s^{-1} .

In the dark, as expected, the complex is electrochemically inactive in the range 0.2 V to –1.1 V vs Ag/AgCl but upon illumination a well-defined response for the two successive one-electron reduction processes of the Mo-species is observed.

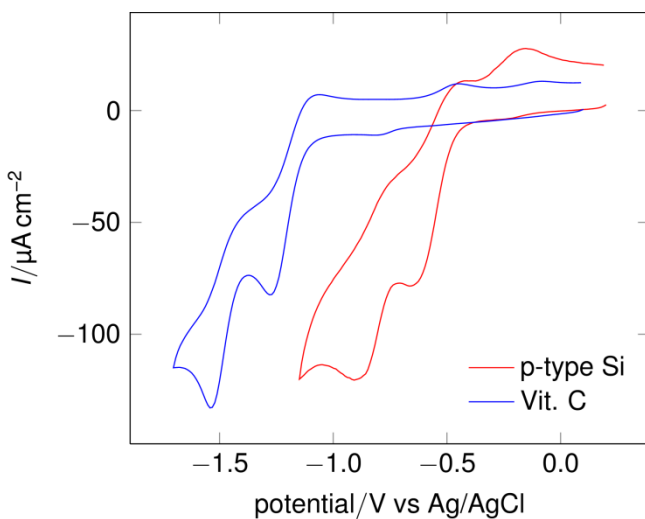


Figure 33 Cyclic voltammetry of 0.5 mM $[\text{MoH}_2(\eta^2\text{-O}_2\text{CCH}_3)(\text{dppe})]^{+}$ complex in 0.1 M $[\text{NBu}_4]\text{[BF}_4]$ -MeCN at a vitreous carbon electrode and an illuminated 1–10 $\Omega \text{ cm}$ p-type Si electrode at a scan rate of 100 mV s^{-1} .

Comparison of the cyclic voltammetric response for the complex at the photoinert vitreous carbon electrode and at the illuminated p-type silicon is shown by Figure 33. There is a dramatic shift in the faradaic response of the complex at the p-type Si electrode, with the overall voltammogram translocated by some 500–600 mV *positive* of that observed on carbon. The magnitude of the photovoltage is comparable to those reported earlier on this type of material.^{12,13,16} It is evident here that at vitreous carbon and at the p-type Si photocathode the diffusional peak current densities for the primary process are very similar and this is indicative of the electrochemically active areas of the photoilluminated Si-H terminated semiconductor being close to that of the polished vitreous carbon electrode.

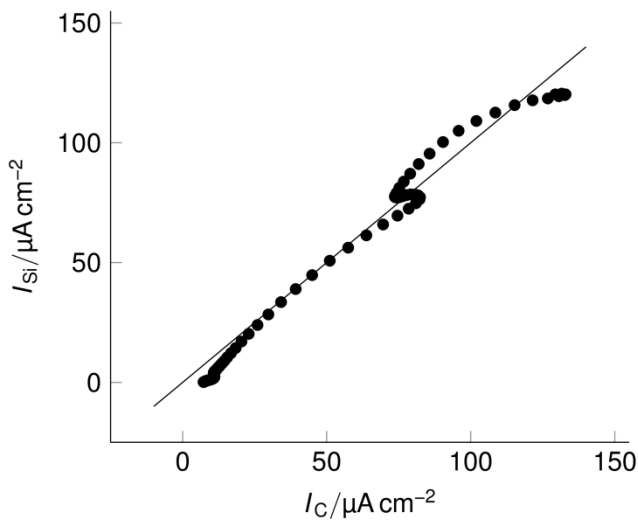


Figure 34 Comparison of current density at vitreous carbon with that at illuminate p-type silicon : $E_{\text{photo}} = 640 \text{ mV}$.

The plot shown in Figure 34 shows the values of the current density at vitreous carbon ($I_{p,\text{carbon}}$) measured at E_{applied} *versus* the corresponding values of the photocurrent density ($I_{p,\text{light}}$) recorded at the illuminated p-type Si at $E_{\text{applied}} - E_{\text{photo}}$, where E_{photo} is the photovoltage. The value of E_{photo} is estimated from $E_{p/2, \text{illuminated Si}} - E_{p/2, \text{carbon}}$, *i.e.* the difference in half-peak potentials for the primary step at the illuminated Si and for the vitreous carbon electrode, respectively, and has value $E_{\text{photo}} = 640 \text{ mV}$. The plot further emphasises that active electrochemical area of these two distinct materials, are close and within a $ca \pm 5\%$ range.

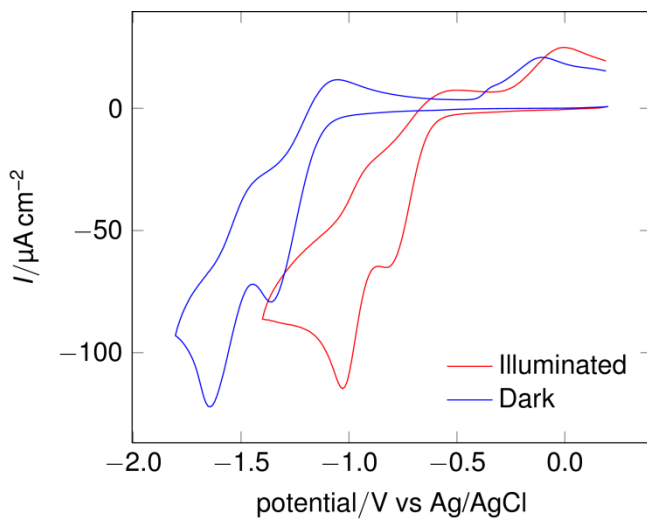


Figure 35 Cyclic voltammetry of 0.5 mM $[\text{MoH}_2(\eta^2-\text{O}_2\text{CCH}_3)(\text{dppe})_2]^+$ complex in 0.1 M $[\text{NBu}_4][\text{BF}_4]$ -MeCN at the same dark and illuminated 1-10 Ω cm p-type Si electrode at a scan rate of 100 mV s^{-1} .

The scan-range on p-type Si *in the dark* was extended to potentials which encompass the conventional electroactive behaviour of the complex at 'metal-like' electrodes. In the dark, the silicon behaves as an ohmic (metal-like) conductor: a well-defined redox response for the system is observed which is quite similar to that measured on vitreous carbon under the same experimental conditions, Figure 33. This observation is surprising as it has been reported that H-terminated p-type Si *does not* conduct in the dark.¹² There is only one other example of dark and light 'shifted' voltammetry recorded at the *same* electrode on this type of material.¹³ This behaviour is consistent with the mechanism of electron transfer from semiconductor to electrolyte described in Chapter 2, whereby the high concentration of majority carriers compared to minority carriers dominate the current, concluding that electron transfer occurs from the valence band.⁴³

In a separate experiment, the potential of the p-type silicon photocathode was held at -0.9 V vs Ag/AgCl and the incident light chopped at 1 Hz, Figure 36.

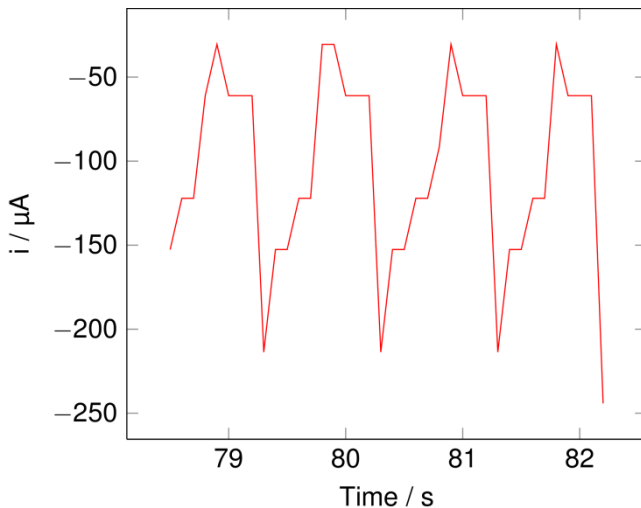


Figure 36 Chopping incident light at 1 Hz during electrolysis 0.5 mM $[\text{MoH}_2(\eta^2\text{-O}_2\text{CCH}_3)(\text{dppe})_2]^+$ complex in 0.1 M $[\text{NBu}_4][\text{BF}_4]$ -MeCN at the an illuminated 1-10 $\Omega \text{ cm}$ p-type Si electrode.

This clearly showed the light dependent photoreduction current and, *in the dark segments, an oxidation current*. This can be understood as follows. At the photopotential at which the primary product, $[\text{MoH}_2(\eta^1\text{-O}_2\text{CCH}_3)(\text{dppe})_2]$ is generated, in the dark it will be reoxidised at the p-type silicon, giving another example of this material functioning as a metallic conductor.

3.2.4.2 Photoelectrocatalysis of hydrogen evolution

The cyclic voltammetric response of $[\text{MoH}_2(\eta^2\text{-O}_2\text{CCH}_3)(\text{dppe})_2]^+$ at a p-type silicon electrode in the presence of increasing concentrations of acid is shown by Figures 37 and 38.

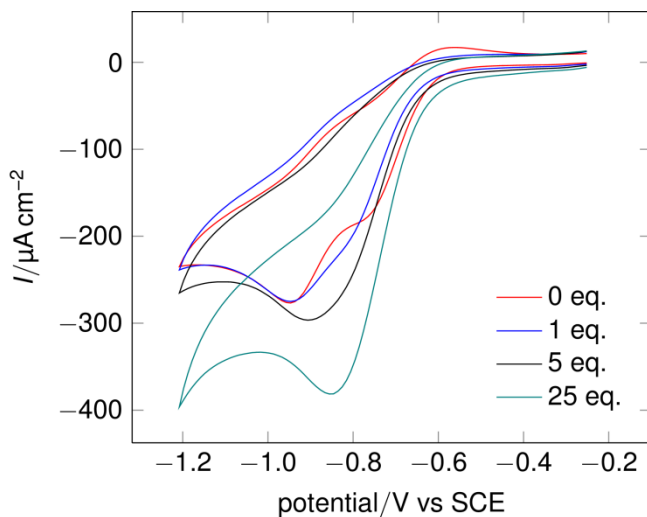


Figure 37 Cyclic voltammetry of 0.5 mM $[\text{MoH}_2(\eta^2\text{-O}_2\text{CCH}_3)(\text{dppe})_2]^+$ in 0.1 M $[\text{NBu}_4]\text{[BF}_4]$ -MeCN at an illuminated 1-10 Ω cm p-type Si electrode with increasing number of equivalents of acetic acid at a scan rate of 100 mV s^{-1} .

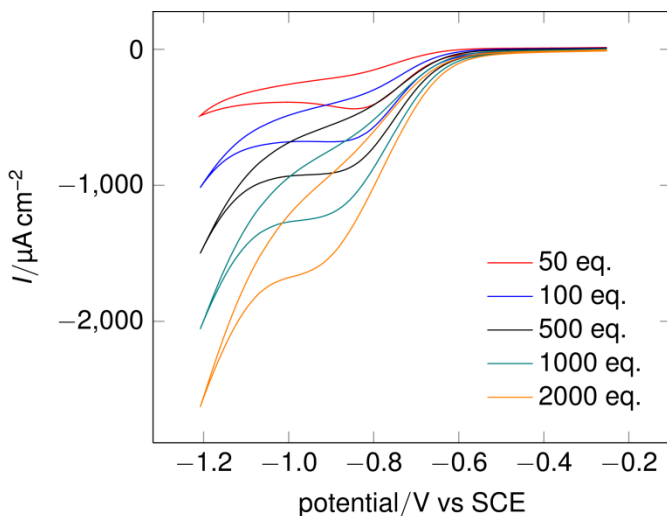


Figure 38 Cyclic voltammetry of 0.5 mM $[\text{MoH}_2(\eta^2\text{-O}_2\text{CCH}_3)(\text{dppe})_2]^+$ in 0.1 M $[\text{NBu}_4]\text{[BF}_4]$ -MeCN at an illuminated 1-10 Ω cm p-type Si electrode with increasing number of equivalents of acetic acid at a scan rate of 100 mV s^{-1} .

The peak catalytic current as a function of acid concentration at the illuminated electrode is plotted in Figure 39 which, for comparison, also includes the corresponding data obtained at vitreous carbon.

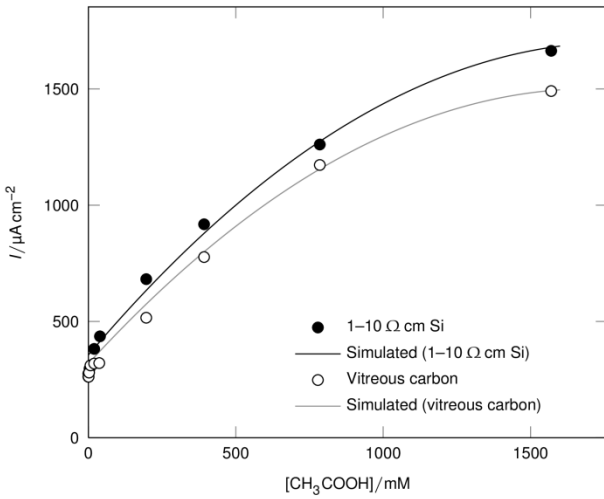


Figure 39 Catalytic current density *versus* concentration of $\text{CH}_3\text{CO}_2\text{H}$ at vitreous carbon and at illuminated p-type Si electrodes. The solid line is the digitally simulated response for the system.

There is a close correspondence of the two peak current density data sets, mirroring the behaviour in the absence of acid. The theoretical curve for the response at vitreous carbon as discussed in Section 3.2.2.1 above is also shown. The similar current densities and the same acid concentration for the catalytic plateau indicates that the photocatalysis is not limited by the photon flux.

It is unlikely that polyhydride intermediates are photolabile under the experimental conditions as this would modify kinetics and/or mechanism at the illuminated electrode. At an illuminated vitreous carbon electrode the cyclic voltammetric response is unperturbed from that in the dark.

The stability of the system under illumination also extends to preparative scale electrocatalysis at p-type silicon as shown below.

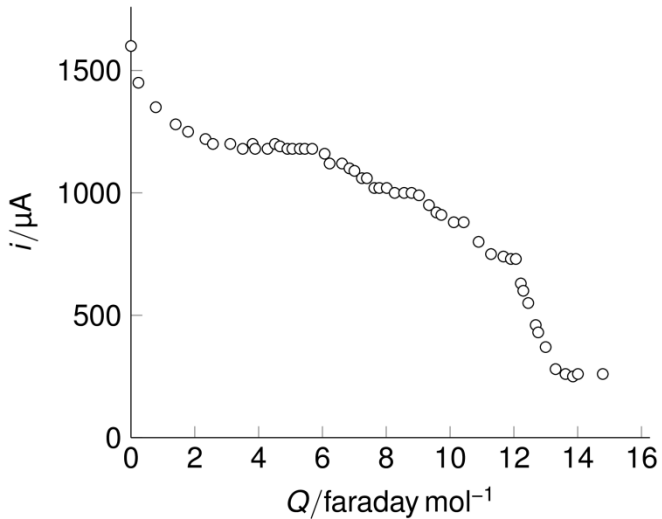


Figure 40 Coulometry for the reduction of $[\text{MoH}_2(\eta^2\text{-O}_2\text{CCH}_3)(\text{dppe})_2]^+$ in presence of 6 eq. of acetic acid at an illuminated p-type Si photocathode held at -1 V vs Ag/AgCl in 0.1 M $[\text{Bu}_4\text{N}][\text{BF}_4]$ -MeCN electrolyte.

The current density *versus* charge passed response for bulk electrolysis at an illuminated p-type Si electrode is shown by Figure 40. The current yield of dihydrogen was determined as $91 \pm 5\%$ by GC after the passage of 11 faradays per mole of catalyst (electrons per mole catalyst) with an overall chemical yield of 98 %. The rapid fall off in current between 12 and 13 faradays per mole of catalyst corresponds to the exhaustion of the proton source, and the formation of the stable, yellow monohydride complex.

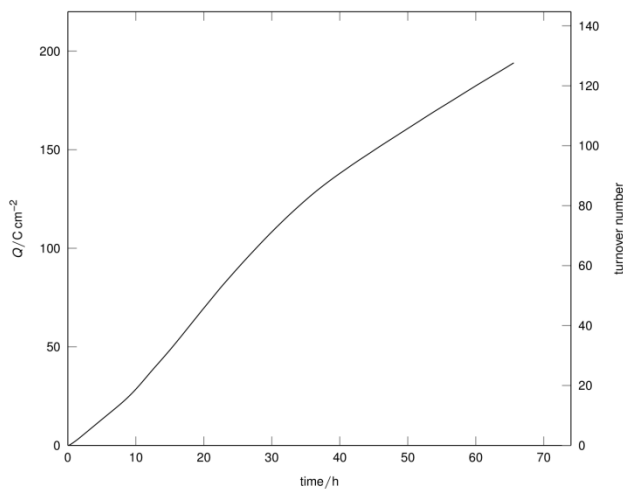


Figure 41 Coulometry of 2 mM $[\text{MoH}_2(\eta^2\text{-O}_2\text{CCH}_3)(\text{dppe})_2]^+$ in the presence of 2 M acetic acid in 0.1 M $[\text{NBu}_4][\text{BF}_4]$ -MeCN at an illuminated $1\text{-}10 \Omega \text{cm}$ p-type Si electrode held at -1.2 V vs Ag/AgCl: catalytic current of between $\text{ca } 600\text{--}1200 \mu\text{A cm}^{-2}$ is sustained over 65 hours, the right hand axis is the corresponding turnover number (TON) for this photoelectrochemical system.

Bulk electrolyses have been performed for extended periods of time in the presence of a large excess of acid. Figure 41 shows the coulometry and the turnover number against time for the illuminated system under constant stirred conditions. The photoelectrocatalytic current was maintained at 40–60 mA cm⁻² over a 65 hour period and the charge-passed, Q , steadily increased without decay. A turnover number (TON) of 125 was reached when the electrolysis was terminated.

3.2.4.3 Comparison between bulk electrolysis on illuminated p-type silicon and on vitreous carbon electrodes

On the cyclic voltammetric timescale, the electrocatalysis on vitreous carbon and on the illuminated p-type silicon have remarkably similar kinetics and acid dependency. However, the illuminated silicon electrode supports a higher steady state catalytic current and the conversion of available protons to hydrogen occurs with a greater chemical yield. The electrolyses on vitreous carbon have been performed under illumination but this does not give a higher steady state turnover current. A photoeffect can therefore be ruled out involving, for example, conversion of the high spin inactive form of the catalyst, **A**, to the active form **B**. One explanation is that the silicon surface catalyses the interconversion of **A** and **B** which would otherwise be a slow process. This catalysis might involve transfer of an electron from **A** to h⁺ states in the Si, formation of **B**⁺ and its re-reduction and protonation to give the catalyst **BH**⁺. This would involve no net current flow associated with the catalysis. The **A/A**⁺ couple lies at -0.15 V vs Ag/AgCl, therefore if this mechanism were operative then h⁺ surface states near this potential would need to be available. Band bending might provide access for hole quenching by **A** at such potentials. An alternative explanation might be that energetic electrons available at the photocathode at potentials greater than that demanded for the electrocatalysis allow reduction of **A** to a protonatable state which re-enters the catalytic cycle. Both mechanisms are illustrated in Figure 42.

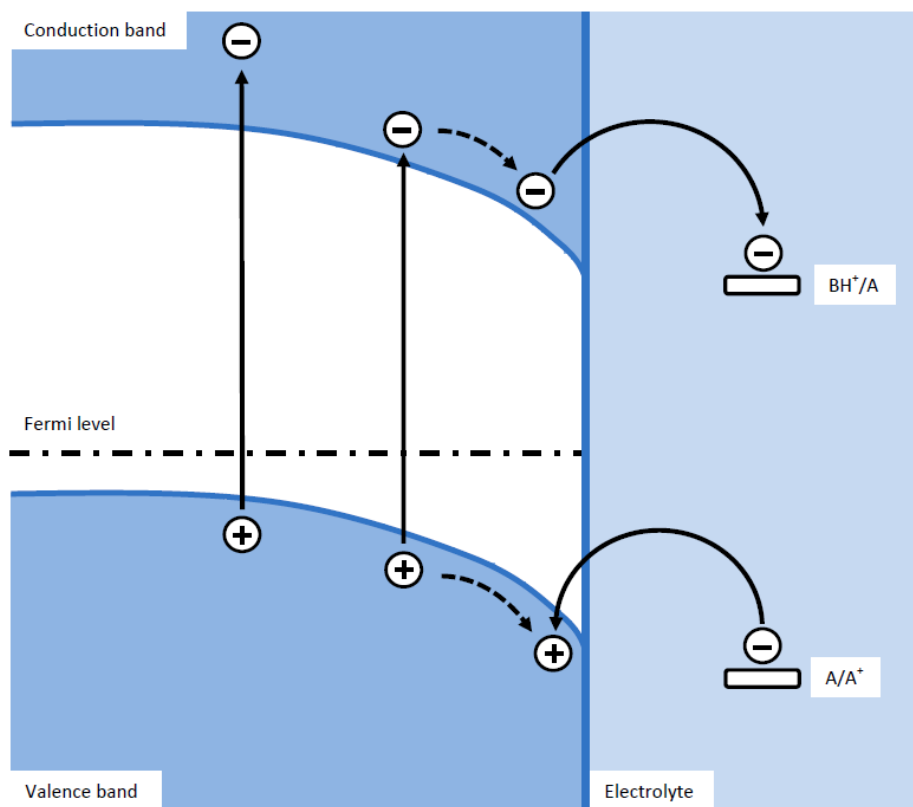


Figure 42 Energy level diagram explaining possible pathways for preventing deactivation of catalyst at the semiconductor.

3.2.4.4 Photoelectrochemical efficiency

Some indication of the efficiency of conversion of light to photoelectrochemical energy is provided. The Krüss lamp output was filtered to restrict the incident radiation to the range of 600-700 nm, providing a measured output of 37 mW cm^{-2} . The peak current density for the system at $1.6 \text{ M CH}_3\text{CO}_2\text{H}$ with a scan-rate of 100 mV s^{-1} is 1.6 mA . At a photovoltage of 0.6 V , this corresponds to a photoelectrochemical output of 0.96 mW and an energy conversion of *ca* 2.6% under the 600-700 nm red light conditions employed. Correcting for a fill factor of 66% gives an overall photoelectrochemical efficiency of 1.7% .

3.3 Conclusions

A combination of electrochemical, spectroscopic and theoretical approaches has provided a more detailed understanding of the basic electron transfer chemistry of the Mo and W η^2 -dihydride systems. This includes determining heterogeneous rate constants for the primary one electron reduction, the detection of the paramagnetic intermediate associated with this step by EPR spectroscopy and DFT calculations which firmly support the $\eta^2 \rightarrow \eta^1$ transformation accompanying the reduction. Cyclic voltammetric studies, in combination with digital simulations, have provided a mechanistic understanding of the rate-limiting processes in electrocatalytic hydrogen production by this type of system. Bulk electrolysis studies have shown that with a trifluoroacetato- complex, $[\text{MoH}_2(\eta^2\text{-O}_2\text{CCF}_3)(\text{dppe})_2]^+$, an electrocatalytic current is sustained at low acid concentration until the acid is exhausted. In contrast, the acetato- system, $[\text{MoH}_2(\eta^2\text{-O}_2\text{CCH}_3)(\text{dppe})_2]^+$, supports essentially quantitative consumption of electrons to give dihydrogen but, at low acid concentration, the catalytic current is not sustained. This has been explained by a pathway in which a monohydride η^2 intermediate, $[\text{MoH}_2(\eta^2\text{-O}_2\text{CCH}_3)(\text{dppe})_2]^+$, is removed from the catalytic cycle by conversion to a high spin η^1 species, $[\text{MoH}(\eta^1\text{-O}_2\text{CCH}_3)(\text{dppe})_2]$, effectively deactivating the catalyst. This species has been detected during electrolyses by cyclic voltammetry. Evidence is presented that oxidation of this species and subsequent reduction provides a pathway for reactivating the catalyst. At high acid concentration the acetato- system can sustain a catalytic current.

On a p-type silicon electrode, it has been shown that the complex $[\text{MoH}_2(\eta^2\text{-O}_2\text{CCH}_3)(\text{dppe})_2]^+$ supports photoelectrocatalytic reduction of protons to dihydrogen with high current efficiency and chemical yield. Cyclic voltammetry at the semiconductor shows that the electrocatalysis, on the seconds timescale, is very similar to that observed on vitreous carbon. Current densities are slightly higher than on the inert electrode. Bulk photoelectrolysis at illuminated p-type silicon differs from that at vitreous carbon; a higher steady state current is sustained over the course of the electrolysis at low acid concentrations. An explanation of why the two electrode materials differ has been proposed. At p-type silicon, it is suggested that the deactivation pathway is inhibited by a redox cycle involving hole (h^+) oxidation of the

deactivated catalytic intermediate, $[\text{MoH}(\eta^1\text{-O}_2\text{CCH}_3)(\text{dppe})_2]$, although other explanations are possible.

The photoefficiency of hydrogen production has been estimated to be *ca* 1.7 % based on the photon flux provided at 600-700 nm and a fill factor of 66 %. This is somewhat lower than that reported by Kubiak and co-workers who have described a CO₂ reducing system on p-type silicon which has a photoelectrochemical energy conversion of 9 %, excluding the fill factor.¹⁶ In the case of the work presented in this chapter, no optimisation for the cell configuration to minimise reflectance or light dispersion was undertaken. In terms of generating a ‘solar fuel’ the efficiency calculations are rather limited since only a part of the solar spectrum is utilised. Efficiency is defined as the ratio of chemical energy output from the solar cell to input energy from the sun. In addition to reflecting the performance of the solar cell itself, the efficiency depends on the spectrum and intensity of the incident sunlight, and also the temperature of the solar cell. Therefore, conditions under which light to chemical efficiency is measured must be moderated in order to compare the performance of one device to another. A recent paper has been published along these lines, calling for guidelines to be followed so a reasonable comparison can be made among all photoelectrochemical conversion materials.⁴⁴ It is emphasised here that solar to chemical efficiency is the only figure of merit suitable for wide-scale benchmarking.

3.4 Future avenues of research

The structure of these electrocatalysts offer considerable scope for modification and changes to the structure of the catalyst can lead to improved catalytic activity. For example, changing the ligating carboxylate ligand to $\eta^2\text{-CF}_3\text{COO}^-$ lowers the reduction potential by *ca* 300 mV, increases the catalytic current and sustains steady state catalysis without catalyst deactivation.⁴¹ However, the trifluoroacetate analogue is only stable in dichloromethane electrolyte.

Thus, the design of a new photoelectrochemical cell that would relieve the solvent electrolyte constraints from solely 0.1 M [Bu₄N][BF₄]-MeCN would be extremely beneficial. The process of doing this has been initiated with the design and

manufacture of a three compartment, glass cell with a peek attachment where a silicon electrode can be inserted as to form part of the wall of the cell, Figure 43.



Figure 43 Picture of photoelectrochemical cell prototype.

With the electrode introduced in this way, there is no requirement for the back of the electrode to be insulated as it is exterior to the cell. However, preliminary photoelectrochemical studies using this cell gave poor CV responses, seemingly due to extensive iR drop, so this needs to be addressed.

Although progress has been made in defining the chemical and physical understanding of the processes that occur at a semiconductor/electrolyte interface, this is mainly a theoretical understanding based upon a Schottky barrier (metal/semiconductor interface). Semiconductor/electrolyte interfacial behaviour seems to be sufficiently different that more work should be performed to fully understand the electron transfer capabilities of semiconductor materials. A thorough comprehension of semiconductor/electrolyte interfaces should imply that improvements in the desirable properties for solar fuel cells, such as quantum efficiency, could be achieved more easily. The light/dark and light chopping electrochemical experiments have some weight in showing the metallic nature of semiconductor electron transfer in the dark. This has only been performed at a p-type silicon electrode, so should be extended to other semiconducting materials.

The rate of catalysis can be greatly improved by securing the catalyst onto the electrode surface. With the catalyst suspended, mass transport is confined solely to

the substrate which is generally much smaller than the catalyst and in high concentration, and thus diffuses much faster. Direct attachment to electrode surfaces is difficult as it commonly requires modification of the catalyst to include a functional group for tethering. To remove this constraint, catalysts can be incorporated into polymer films that are electropolymerised directly onto the electrode surface^{45, 46} and this would be a good approach to take in this case at both vitreous carbon and p-type silicon electrodes.

3.5 References

1. D. L. Hughes, S. K. Ibrahim, G. Querne, A. Laouenan, J. Talarmin, A. Queiros, A. Fonseca, C. J. Pickett, *Polyhedron*, **1994**, *13*, 3341
2. T. Ito, A. Takahashi, S. Tamura, *Bull. Chem. Soc. Jpn.* **1986**, *59*, 2489–2494
3. G. C. Tucci, J. P. Donahue, R. H. Holm, *Inorg. Chem.* **1998**, *37*, 1602
4. S. A. Fairhurst, R. A. Henderson, D. L. Hughes, S. K. Ibrahim, C. J. Pickett, *J. Chem. Soc. Chem. Commun.* **1995**, 1569
5. R. A. Henderson, S. K. Ibrahim, K. E. Oglieve, C. J. Pickett, *J. Chem. Soc. Chem. Commun.* **1995**, 1571
6. P. C. Dos Santos, R. Y. Igarashi, H. I. Lee, B. M. Hoffman, L. C. Seefeldt, D. R. Dean, *Acc. Chem. Res.* **2005**, *38*, 208
7. B. M. Barney, R. Y. Igarashi, P. C. Dos Santos, D. R. Dean, L. C. Seefeldt, *J. Biol. Chem.*, **2004**, *279*, 53621
8. L.C. Seefeldt, I. G. Dance, D. R. Dean, *Biochemistry*, **2004**, *43*, 1401
9. P. C. C. Benton, M. Laryukhin, S. M. Mayer, B. M. Hoffman, D. R. Dean, L. C. Seefeldt, *Biochemistry*, **2003**, *42*, 9102
10. R. N. F. Thorneley, D. J. Lowe, *Metal Ions in Biology Series, Vol. 7: Molybdenum Enzymes*, p 117, Wiley-Interscience, New York, **1985**
11. S. Sato, T. Arai, T. Morikawa, K. Uemura, T. M. Suzuki, H. Tanaka, T. Kajino, *J. Am. Chem. Soc.* **2011**, *133*, 15240
12. A. B. Bocarsly, R. N. Dominey, D. C. Bookbinder, N. S. Lewis, M. S. Wrighton, *J. Am. Chem. Soc.* **1980**, *102*, 3683
13. D. Laser, A. J. Bard, *J. Phys. Chem.* **1976**, *80*, 459
14. D. C. Bookbinder, N. S. Lewis, M. G. Bradley, A. B. Bocarsly, M. S. Wrighton, *J. Am. Chem. Soc.* **1979**, 7721
15. M. G. Bradley, T. Tsyak, D. J. Graves, N. A. Vlachopoulos, *J. Chem. Soc. Chem. Commun.* **1983**, 349
16. B. Kumar, J. M. Smieja, C. P. Kubiak, *J. Phys. Chem. C*, **2010**, *114*, 14220
17. B. Kumar, M. Beyler, C. P. Kubiak, S. Ott, *Chem. Eur. J.* **2012**, *18*, 1295
18. R. N. Dominey, N. S. Lewis, J. A. Bruce, D. C. Bookbinder, M. S. Wrighton, *J. Am. Chem. Soc.* **1982**, *104*, 467
19. Y. D. Hou, B. L. Abrams, P. C. K. Vesborg, M. E. Bjorketun, K. Herbst, L. Bech, A. M. Setti, C. D. Damsgaard, T. Pedersen, O. Hansen, J. Rossmeisl, S. Dahl, J. K. Norskov, I. Chorkendorff, *Nat. Mater.* **2011**, *10*, 434.
20. <http://www.ioffe.ru/SVA/NSM/Semicond/>
21. S. O. Kasap, P. Capper, *Springer handbook of electronic and photonic materials*. Springer, **2006**, p 54, 327.
22. J. A. Baglio, G. S. Calabrese, D. J. Harrison, E. Kamieniecki, A. J. Ricco, M. S. Wrighton, G. D. Zoski, *J. Am. Chem. Soc.* **1983**, *105*, 2246
23. A. B. Bocarsly, Q. D. Gibson, A. J. Morris, R. P. L'Esperance, Z. M. Detweiler, P.S. Lakkaraju, E. L. Zeitler, T. W. Shaw, *ACS Catal.* **2012**, *2*, 1684

24. F. Wen, J. Yang, B. Ma, D. Wang, C. Li, *J. Catal.* **2011**, *281*, 318
25. C. H. Henry, K. Nassau, *Phys. Rev. B*, **1970**, *1*, 1628
26. T. Chen, Z. H. Feng, G. P. Wu, J. Y. Shi, G. J. Ma, P. L. Ying, C. Li, *J. Phys. Chem. C*, **2007**, *111*, 8005
27. A. Yamakata, T. Ishibashi, H. Onishi, *J. Phys. Chem. B*, **2002**, *106*, 9122; A. Yamakata, T.A. Ishibashi, J. Onishi, *J. Phys. Chem. B*, **2003**, *107*, 9820
28. P. W. Du, K. Knowles, R. Eisenberg, *J. Am. Chem. Soc.* **2008**, *130*, 12576
29. B. Probst, C. Kolano, P. Hamm, R. Alberto, *Inorg. Chem.* **2009**, *48*, 1836
30. P. W. Du, J. Schneider, G. G. Luo, W. W. Brennessel, R. Eisenberg, *Inorg. Chem.* **2009**, *48*, 4952
31. T. Lazarides, T. McCormick, P. W. Du, G. G. Luo, B. Lindley, R. Eisenberg, *J. Am. Chem. Soc.* **2009**, *131*, 9192
32. T. Bourgetteau, D. Tondelier, B. Geoffroy, R. Brisse, C. Laberty-Robert, S. Campidelli, R. de Bettignies, V. Artero, S. Palacin, B. Jousselme, *Energy Environ. Sci.* **2013**, *6*, 2706
33. C. J. Pickett, *J. Chem. Soc. Chem. Commun.* **1985**, 323
34. CRC Handbook of Chemistry and Physics, **2008**, p 12-114
35. <http://www.el-cat.com/silicon-properties.html>
36. I. M. Kolthoff, M. K. Chantooni, S. Bhowmik, *J. Am. Chem. Soc.* **1968**, *90*, 23
37. R. A. Henderson, K. E. Ogilive, S. K. Ibrahim, C. J. Pickett, *J. Chem. Soc., Chem. Commun.* **1995**, 1571
38. T. A. Salih, M. T. Duarte, J. J. R. Frausto da Silva, A. M. Galvão, M. F. C. Guedes da Silva, P. B. Hitchcock, D. L. Hughes, C. J. Pickett, A. J. L. Pombeiro, R. L. Richards, *J. Chem. Soc. Chem. Commun.* **1993**, 3015
39. T. Ito, T. Matsubara, K. Hamamoto, Y. Yamashita, S. Kurishima, *Polyhedron*, **1989**, *8*, 1751
40. T. Jasinski, A. A. El-Harakany, F. G. Halaka, H. Sadek, *Croat. Chem. Acta*, **1978**, *51*, 1
41. A. Amghamdi, S. K. Ibrahim, *Unpublished data*, **2010**
42. S. Wanatabe, N. Nakayama, T. Ito, *Appl. Phys. Lett.* **1991**, *59*, 1458
43. C. A. Koval, J. N. Howard, *Chem. Rev.* **1992**, *92*, 411
44. Z. Chen, T. F. Jaramillo, T. G. Deutsch, *J. Mater. Res.* **2010**, *25*, 3
45. J. Moutet, C. J. Pickett, *J. Chem. Soc. Chem. Commun.* **1989**, 188
46. S. Cosnier, A. Deronzier, J. C. Moutet, J. F. Roland, *J. Electroanal. Chem.* **1989**, *271*, 69

Chapter 4

Electrochemistry of molybdenum and tungsten dithiolenes

4.1 Introduction

4.1.1 Overview and biological significance

Metal complexes with dithiolene ligands were first investigated during the 1960s.¹ They remain a focus of study 50 years later because of their many unusual properties. Metal dithiolenes also have significant roles in biological catalysis^{2,3} and in materials research,^{4,5} particularly electronics and sensor applications.^{6,7}

Recent research by the Sawers group has shown formate dehydrogenase enzymes Fdh-N (induced in the presence of nitrate) and Fdh-O (detected during aerobic growth) of *Escherichia coli* have hydrogen oxidising activity, therefore identifying a potential new class of hydrogenase enzyme.⁸ The work involved anaerobically growing genetically modified bacteria which prevented the expression of conventional [NiFe]-hydrogenases and showing that the bacteria remained capable of oxidising molecular hydrogen and transferring the electrons to benzyl viologen or phenazine methosulfate/nitroblue tetrazolium. When the genes for Fdh-N and Fdh-O were knocked out, *the bacteria were unable to grow on dihydrogen*.

The idea that simple molybdenum- or tungsten- bis(dithiolene) systems related to the active site of such formate dehydrogenase enzymes might function as hydrogen evolution or uptake electrocatalysts is very interesting. In this initial study, Mo and W dithiolene complexes which possess CO co-ligands were chosen to be investigated. All hydrogenases so far characterised possess CO ligands at their active site. Additionally, the complexes chosen do not possess Mo=O or W=O functionality. Such species would be likely to require the reductive removal of the oxide as water in order to generate a reactive catalyst.⁹

4.1.2 Established hydrogenases

There are currently three recognised hydrogenase enzymes, the mono-iron, the di-iron and the nickel-iron hydrogenases; the structures of the active sites of the enzymes are shown in Figure 1.¹⁰

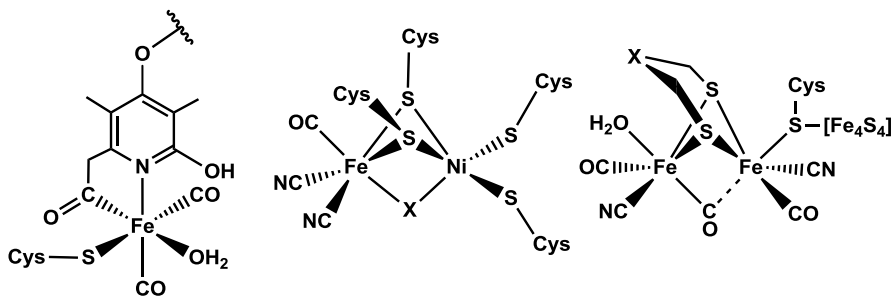


Figure 1 Structures of the active sites of the three hydrogenases.

The first pictured hydrogenase is the mono-iron hydrogenase ($[\text{Fe}]$ -hydrogenase), named as only one iron is involved in the structure of the active site. This enzyme is less widely researched than the bimetallic enzymes, as it is solely concerned with the reversible heterolytic transformation of hydrogen into H^+ and H^- , with H^- transferred to a specific substrate. Therefore, it is less related to hydrogen production, but more relevant to hydride generation as a method of hydrogen storage. The reversible homolytic conversion of hydrogen into protons and electron is carried out by the nickel-iron and the di-iron hydrogenases, with the di-iron being the faster of the two enzymes, thus the most widely studied.

Given that all the aforesaid hydrogenases use iron at the active site, a molybdenum or tungsten pterin type complex acting as a hydrogenase must involve a completely new type of biochemistry.

4.1.3 Molybdenum and tungsten enzymes containing pyranopterin

The pyranopterin dithiolene ligand is present in all molybdenum and tungsten containing enzymes with the exception of nitrogenases.¹¹ These enzymes, known as mononuclear Mo/W enzymes, play pivotal roles in metabolism, global geochemical cycles, and microbial metabolic diversity.¹²⁻¹⁴

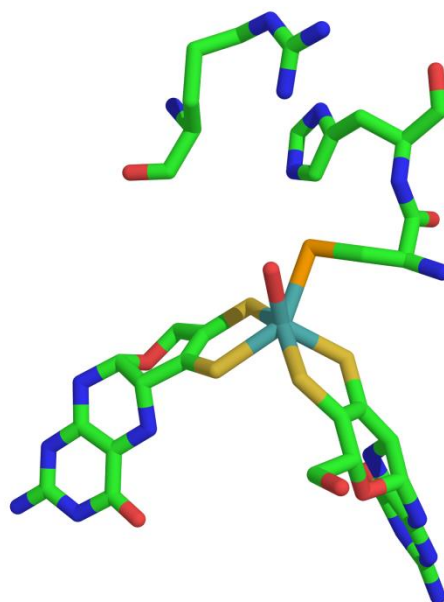


Figure 2 Structure of an bis(pyranopterin) enzyme Fdh-H (Atoms are defined as green = carbon, blue = nitrogen, red = oxygen, yellow = sulfur, orange = selenium, teal = molybdenum; PYMOL, PDB code 1FDO).¹⁵

Their active sites, comprising a Mo or W metal centre and one or two pyranopterins, catalyse a diverse range of redox reactions in carbon, sulfur and nitrogen chemistry, spanning a reduction potential range of approximately one volt.¹⁶

The majority catalyse the oxidative oxygen atom transfer from water and/or its backward reaction as indicated in Equation 4.1, where X denotes a substrate.



(Equation 4.1)

This is achieved by utilising a Fe–S cluster, haem or flavin as the physiological electron acceptor of the proton coupled electron transfer (PCET) mechanism.^{17, 18}

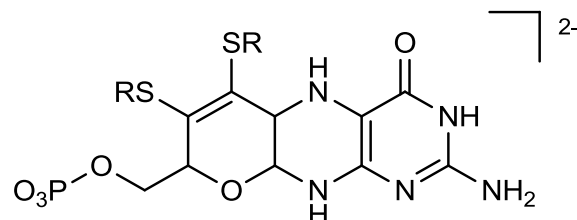


Figure 3 Basic structure of pyranopterin ligand.

The structure of the pyranopterin ligand as shown in Figure 3 was derived from crystallographic data of two enzymes, an aldehyde oxido-reductase¹⁹ and a DMSO reductase.²⁰ The role of the pterin cofactor in the reaction mechanisms of mononuclear Mo/W enzymes has been the subject of considerable speculation.^{21, 22} Two specific roles for the cofactor have been inferred: mediation of electron transfer to other redox active centres with a change in oxidation state of the pterin and modulation of the metal reduction potential.¹⁷

The numerous mononuclear Mo/W enzymes are classified based on their ligation environment.¹⁷ Mono-pyranopterin coordinated metals fall into one of either the xanthine oxidase or sulfite oxidase family. Di-pyranopterin coordinated metals are organised into the DMSO reductase family, which is then subdivided into additional groups. Structures akin to those used in this study with bis(dithiolene) coordination and two additional ligands, which are normally a doubly bound oxygen, sulfur or possibly selenium, and an –OR group which generally binds another protein residue, are most closely related to the subgroup of formate dehydrogenase (FDH) enzymes.

The recent solving of an X-ray structure of one example of a tungsten formate dehydrogenase²³ confirmed the prediction of Hille¹⁷ that tungsten derivatives do have a close structural relationship to more common molybdenum formate dehydrogenases, despite there being only minimal protein sequence homology.²⁴⁻²⁷

Despite the great similarities in the properties of the two metals, replacing Mo for W in many studies had debilitating effects. Various organisms, such as plants and rats that were grown on or subjected to tungsten produced either inactive metal free molybdoenzymes or W substituted enzymes with little or no activity.²⁸⁻³⁰ So, clearly the chemical properties of Mo and W are sufficiently different that biology selects one or other of these metals specifically.

4.1.3.1 Formate dehydrogenase enzymes

Formate dehydrogenase enzymes are responsible for the reversible interconversion of carbon dioxide and formate, however not by the conventional mononuclear Mo/W enzyme method of oxygen atom transfer. Catalysis of the oxidation of formate is achieved by direct transfer of a hydride from formate to NAD(P)⁺, but the most common classes of FDH have difficulty to drive the reverse reaction because the reduction potential of NAD(P)⁺ is more positive than that of CO₂.³¹ Some FDH active sites form one part of more complex enzymes that contain Mo or W cofactors to transfer the electrons obtained from formate oxidation to another active site where a reductive reaction is carried out.^{15, 32, 33}

A recent study by Hirst showed reversible interconversion of carbon dioxide and formate by an electroactive FDH enzyme.³⁴ FDH1, a tungsten containing formate dehydrogenase from anaerobic bacterium *S. fumaroxidans*, was shown to be able to electrocatalytically effect the reversible conversion of CO₂ to HCO₂H, both as a homogeneous catalyst and when absorbed onto the surface of an electrode. Cyclic voltammetric analysis showed that both CO₂ reduction and formate oxidation are initiated at approximately -0.4 V vs SHE and their rates increased sharply with increasing overpotential. The rate of formate oxidation was greatest at pH 8.4, and CO₂ reduction at pH 5.5. However, the catalytic current of the electrode absorbed species reached only 10-20 % of the value expected values estimated from the solution assays and the density of a monolayer of the enzyme on the electrode. Thus, the number of molecules of enzyme on the electrode surface that are electrocatalytically active was much lower than that required to constitute a monolayer, illustrating the difficulty of

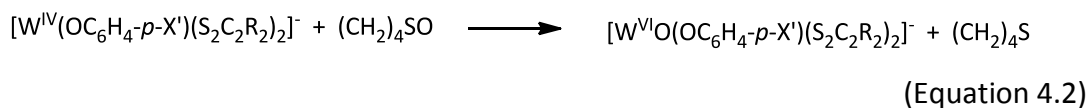
creating a catalytic system for renewable fuels based upon enzymes. Nonetheless, the enzyme reached a turnover number of 112 s^{-1} for CO_2 reduction, at pH 5.9 and -0.8 V vs SHE, with formate the exclusive product.

4.1.4 Current studies of Mo/W bis(dithiolene) active site analogues

A number of simple bis(dithiolene)tungsten^{IV,VI} thiolate and selenolate compounds have been synthesised to mimic the active sites of formate dehydrogenases, but exhibit no catalytic activity with respect to CO_2 .³⁵ They have been subsequently more useful for modelling oxygen atom transfer reactions of mononuclear Mo/W enzymes within the DMSO reductase family.³⁶

Early work in this area involved proving that bis(dithiolene) complexes with a Mo=Q group (Q = O, S, Se) may be readily synthesised,³⁷ which accords with research of Hille who noticed the possible occurrence of the Mo=Q group within enzymes.¹⁷

Later, a detailed kinetic evaluation of the oxo transfer reaction between desoxo W^{IV} complexes with the substrate $(\text{CH}_2)_4\text{SO}$ was undertaken.³⁸



Kinetic UV-visible studies suggested that the first transition state in the mechanism involved W^{IV}-OS bond making, followed by a second transition state where the O-S bond is largely weakened and the doubly bond W=O interaction develops. The reaction is completed by separation of the reduced substrate, S, from the complex and the primary W-O bond formation is determined to be the rate-limiting step.

The existence of molybdenum and tungsten isoenzymes, originally detected in the formate dehydrogenase family led the Holm group to develop the chemistry of molybdenum and tungsten bis(dithiolene) complexes in parallel. This has provided a

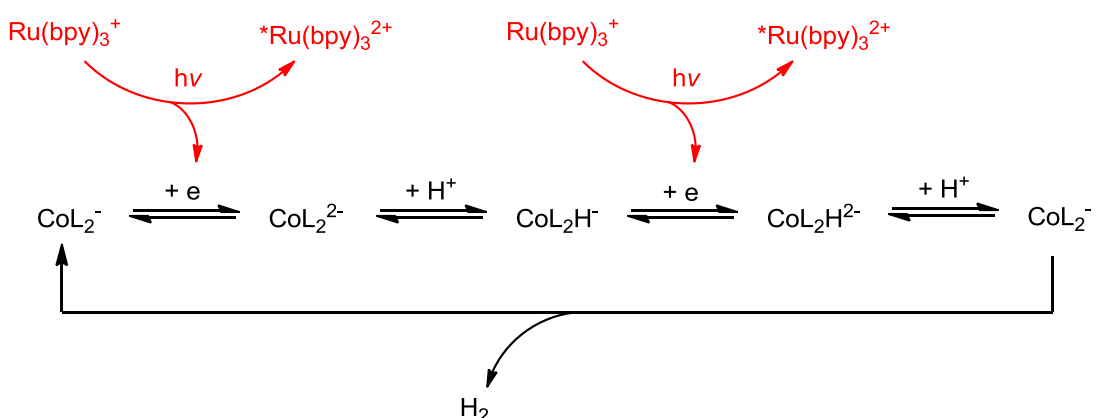
comparison of catalytic rates of the isostructural active site analogues.³⁹ It was discovered that oxo transfer to the metal is faster with tungsten and oxo transfer from the metal to the substrate is faster with molybdenum. This is likely to be because W-O bond formation is more favourable than that for Mo-O, therefore forming the W-O bond for oxo transfer to the metal is more straightforward than for molybdenum. However, the oxo group at a tungsten metal centre is then harder to remove to be transferred to the substrate, making this step slower than for Mo, because of the greater affinity of tungsten for oxygen. The results demonstrated that there is a kinetic metal effect in direct oxo transfer for isostructural active site analogues and this may be applicable to the enzymes.

The latest result in this area involved DFT calculations of barrier heights for oxo transfer reactions to Mo and W bis(dithiolene) sites.³⁶ Reaction coordinates were calculated for oxo transfer from substrates (X) with varying X-O bond strength (Me_3NO , Me_2SO , Me_3PO) to the dithiolene complex $[\text{Mo}(\text{OMe})(\text{S}_2\text{C}_2\text{Me}_2)_2]^-$ and oxo transfer from Me_2SO to the analogous W^{IV} complex. Results showed that two successive transition states are involved in oxygen atom transfer; the first was simply the binding of the substrate. The second transition state was where oxo transfer takes place and therefore requires the most energy. Replacing Mo for W lowered the energy requirements of the second transition state and this was rationalised in terms of relativistic effects destabilising the redox active molecular orbital.⁴⁰ Changing the X-O bond strength of the substrate, as might be expected, also had an effect on the energy of the second transition state, so this rate-limiting step was both substrate and metal dependant.

4.1.5 Catalysis involving metal dithiolene systems

The majority of studies of dithiolene complexes are concerned with modelling the stoichiometric reactions of the active sites of various enzymes to which they are structurally closely related.⁹ Thus there are very few examples of catalysis of hydrogen evolution by metal dithiolene complexes, as this is not currently related to the biological activity of any enzymes containing dithiolenes.

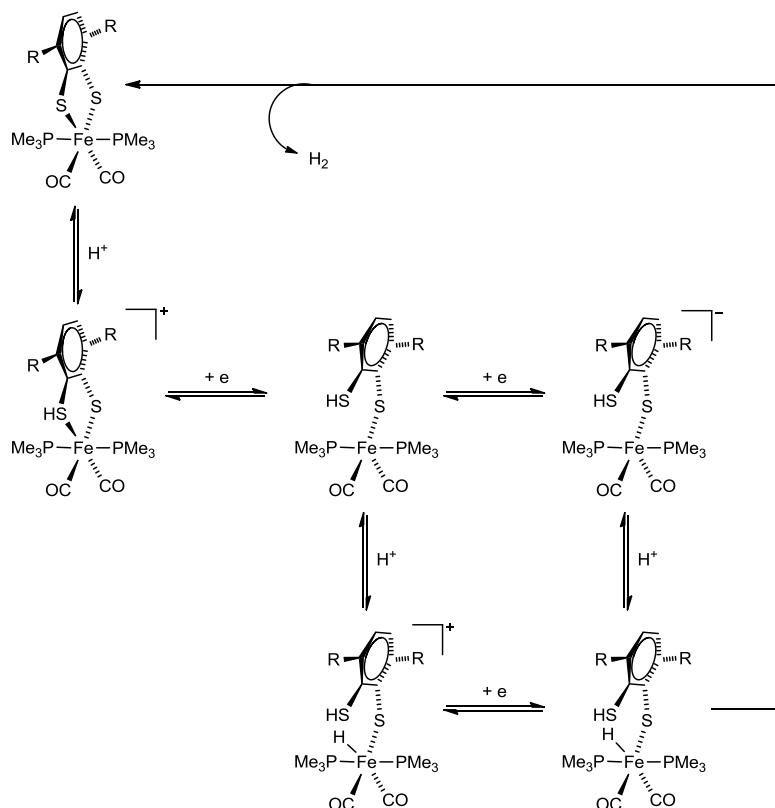
Four cobalt dithiolene complexes were examined by Holland and co-workers, both photochemically and photoelectrochemically, in both organic and aqueous solutions to probe proton reduction and hydrogen turnover ability.⁴¹ It was found that the group of complexes gave the most impressive turnover numbers (TONs) and turnover frequencies (TOFs) in an aqueous/organic media blend of acetonitrile and water. The trend in the hydrogen production activity illustrated that the cobalt dithiolene complexes with the most electron withdrawing groups, and therefore the least negative reduction potentials, had the highest turnover rates. An electrocatalytic mechanism was also proposed from cyclic voltammetric data to be an ECEC mechanism. This was rationalised by the Co dithiolene undergoing rapid protonation on the first reduction to the two minus species, followed by subsequent reduction and reaction with H⁺ to form H₂. The photoelectrocatalysis performed here linked the Co dithiolenes with [Ru(bipy)₃]²⁺ used as the photosensitiser, which was eventually destroyed as a result of the catalysis. Ruthenium falls in the category of precious metals and is arguably unsustainable for practical photoelectrocatalysis.



Scheme 1 Proposed mechanism for H₂ generation from cobalt dithiolene complexes (L = benzene dithiolate).

Another example of catalysis by a metal complex containing a dithiolene ligand is hydrogen evolution from a mononuclear iron^{II} carbonyl complex that is a mimic for the distal iron atom, with respect to the [4Fe4S] cluster, in the [FeFe]-hydrogenase.⁴² Reversible protonation of the two synthesised complexes, as monitored by IR spectroscopy, showed a small positive shift in the CO stretching frequencies, consistent with reduced M-CO backbonding by the reduction in electron density at the metal. Addition of pyridine deprotonated the complexes fully reversibly when up to

three molar equivalents of HClO_4 were added, any more and the Fe complexes were irreversibly decomposed. ^1H and ^{31}P NMR data suggested the protonation takes place at the sulfur of the dithiolene ligand. Cyclic voltammetry of the complexes under acidic conditions (trifluoroacetic acid) formed two new cathodic peaks at more positive potentials than that observed for the complexes under acid-free conditions. Controlled potential electrolysis experiments showed that hydrogen evolution could be sustained at both reduction potentials as measured by gas chromatography, with a maximum turnover of 15 at the more negative reduction potential (-1.7 vs Fc^+/Fc). The observations of two catalytic peaks led to the conclusion that hydrogen evolution can occur by one of two possible pathways, Scheme 2.



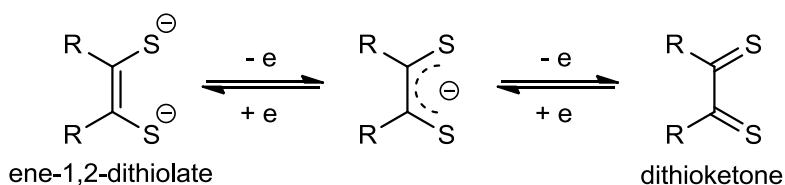
Scheme 2 Proposed catalytic cycle of mononuclear iron^{II} carbonyl complex.⁴²

The first catalytic wave was rationalised by CECEC mechanism in which protonation of the monoprotonated and monoreduced species allowed further reduction at a similar potential, then H_2 was released, possibly by a proton-hydride reaction if the second protonation occurred at the metal. The larger catalytic wave at the more negative potential is instead attributed to a CEECC mechanism that involved the formation of a doubly reduced, monoprotonated intermediate, followed by release of H_2 upon

further protic attack. The rate-limiting step was determined to be the bimolecular formation of hydrogen; therefore catalytic turnover was not limited by the reactivity of hydrides.

4.1.6 The ‘non-innocent’ dithiolene ligand

A ligand is to be regarded as ‘innocent’ if it allows the oxidation state of a metal in a complex to be defined. Dithiolenes have been regarded as ‘non-innocent’ ligands since it is possible to consider a ligand of this type to be present in a complex as either an ene-1,2-dithiolate dianion, a neutral dithioketone or as a delocalised radical monoanion, Scheme 3. On this basis, the electronic structure of a dithiolene complex can be described by a set of resonance structures, each of which involves the dithiolene in one of the forms with the oxidation state of the metal centre being adjusted accordingly.



Scheme 3 Redox related forms of a dithiolene ligand.

The oxidation state of the metal cannot be easily defined due to the uncertainty in the oxidation state of the ligand(s), leading to the use of ‘dithiolene’ as an equivocal description that does not imply that such ligands are present in a particular state.^{43, 44} The relative importance of these structures is expected to be reflected in the corresponding molecular structure and spectroscopic properties.

Extensive structural and spectroscopic investigations of dithiolene complexes have been reported,⁴⁵ often with the aim to determine the oxidation state of the metal and the ligand(s).⁴⁶ One means of assessing the nature of the dithiolene ligand(s) in a complex is to compare the length of the dithiolene C-C and C-S bonds with standard single and double bond distances.⁴⁷ However, the vast majority of structurally characterised dithiolene complexes involve C-C and C-S bond lengths that are

intermediate between the two extreme forms of the ligand. The ^1H NMR chemical shift has proved a useful probe of the nature of dithiolene groups in diamagnetic complexes. For complexes that, on the basis of other evidence, appear to involve the dithiolene(s) present as an ene-1,2-dithiolate, the ^1H resonance is in the region of the NMR spectrum typical of olefinic protons (6-7 ppm). Other dithiolene complexes manifest ^1H chemical shifts of 9-10 ppm, shifts that are typical of an aromatic proton; such values have been rationalised on the basis of an induced diamagnetic ring current in the metalldithiolene ring.⁴⁸

4.2 Scope of the chapter

Molybdenum and tungsten bis(dithiolene) complexes of the type $[\text{M}(\text{CO})_2(\text{S}_2\text{C}_2\text{Ph}_2)_2]$ ($\text{M} = \text{Mo}, \text{W}$) have been synthesised to investigate the possibility of catalysis of hydrogen evolution from this type of system. This is of relevance to the potential activity of FDH type enzymes behaving as hydrogenases, as suggested by the work of Sawer and co-workers.⁸ The following aspects are covered in this chapter:

- (i) The basic electrochemistry of the synthetic dithiolene models in predominantly the reductive regime is first described. Used in conjunction with infrared spectroelectrochemical studies in the $\nu(\text{CO})$ region, an understanding of the behaviour of the ‘non-innocent’ dithiolene ligands could be achieved. Conclusions from the experimental studies were reinforced by computational studies calculated using DFT methods, where infrared data and structural models of the complexes were isolated.
- (ii) (Spectro)electrochemistry of the complexes in the presence of a proton source / hydrogen were implemented to determine if hydrogenase type catalysis was evident by these types of metal bis(dithiolene) structures.

4.3 Results and discussion

4.3.1 Basic redox properties of $[\text{M}(\text{CO})_2(\text{S}_2\text{C}_2\text{Ph}_2)_2]$

4.3.1.1 Reductive cyclic voltammetry

Cyclic voltammetry of the basic redox chemistry of the Mo and W dithiolene complexes show two successive single electron reductions; $\text{M}^{\text{IV}/\text{III}}$ and $\text{M}^{\text{III}/\text{II}}$ as previously described by the Holm group.^{38, 49}

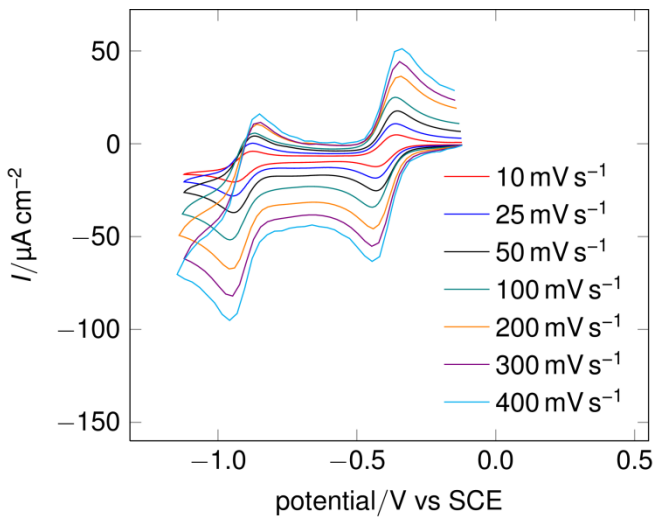


Figure 4 Cyclic voltammetry of 0.24 mM $[\text{Mo}(\text{CO})_2(\text{S}_2\text{C}_2\text{Ph}_2)_2]$ complex in 0.2M $[\text{NBu}_4][\text{BF}_4]\text{-CH}_2\text{Cl}_2$ at a vitreous carbon electrode at various scan rates.

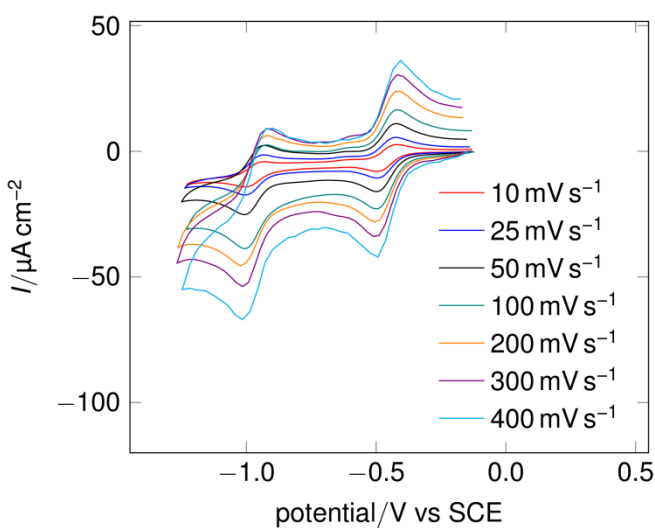


Figure 5 Cyclic voltammetry of 0.18 mM $[\text{W}(\text{CO})_2(\text{S}_2\text{C}_2\text{Ph}_2)_2]$ complex in 0.2M $[\text{NBu}_4][\text{BF}_4]\text{-CH}_2\text{Cl}_2$ at a vitreous carbon electrode at various scan rates.

Figures 4 and 5 show the cyclic voltammetric responses for $[\text{Mo}(\text{CO})_2(\text{S}_2\text{C}_2\text{Ph}_2)_2]$ and $[\text{W}(\text{CO})_2(\text{S}_2\text{C}_2\text{Ph}_2)_2]$ respectively in a 0.2 M $[\text{NBu}_4][\text{BF}_4]$ -dichloromethane electrolyte. The voltammograms for both the Mo and W complexes show two successive redox steps. The ratio of the peak current for the back scan, i_p^{back} , to that of the forward scan, i_p^{forward} , is close to one for both the first and second reduction steps, even at the slowest scan rates: this is consistent with reversible electrochemistry. The peak separations for both Mo and W complexes, at a scan rate of 100 mV s^{-1} , are *ca* 60 mV as would be expected for one electron steps. Figure 6 and Figures A4.1-4.4 show the linear response of the peak currents for both the primary and secondary reductions of the Mo and W complexes as a function of the square-root of the scan rate: this establishes the diffusion controlled nature of the electrochemistry.⁵⁰

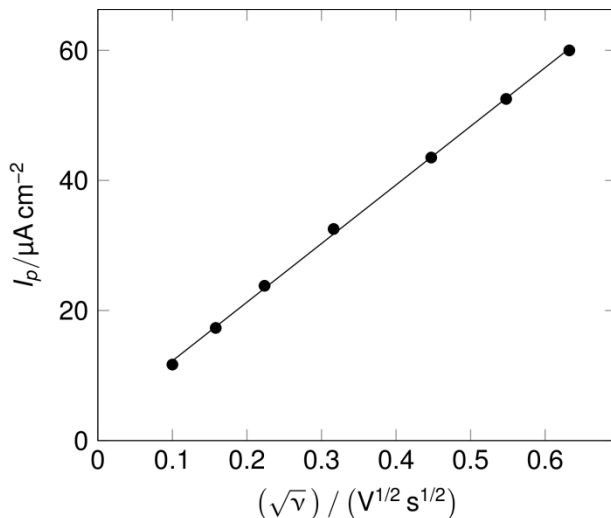


Figure 6 Plot of cathodic peak current vs square root of scan rate for the first reduction of $[\text{Mo}(\text{CO})_2(\text{S}_2\text{C}_2\text{Ph}_2)_2]$. (Plots for the other redox waves can be seen in the appendix, Figures A4.1-A4.4).

In summary, these results establish that the Mo and W complexes undergo two successive, diffusion controlled, one electron reduction steps which are fully reversible on the cyclic voltammetric timescale of seconds and in accord with that reported earlier by Holm and co-workers.^{37, 49}

The redox couples for the tungsten analogue take place *ca* 50-70 mV more negative than the molybdenum species, Figure 7.

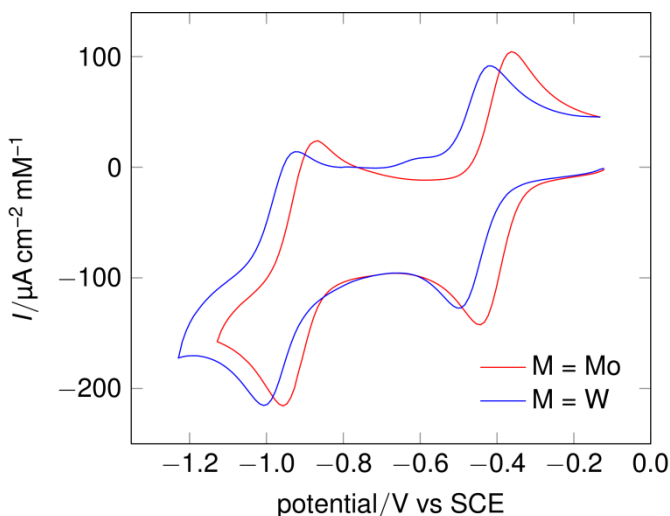
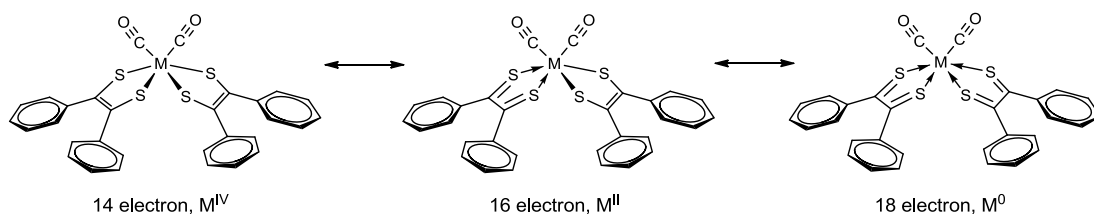


Figure 7 Concentration normalised cyclic voltammetry of $[\text{M}(\text{CO})_2(\text{S}_2\text{C}_2\text{Ph}_2)_2]$ complexes in 0.2M $[\text{NBu}_4][\text{BF}_4]$ - CH_2Cl_2 at a vitreous carbon electrode at 100 mV s^{-1} .

This is a general observation for Mo vs W, for example *trans*- $[\text{MoOCl}(\text{dppe})_2]^+$ is easier to reduce than its tungsten analogue.⁵¹ Many more comparative examples can be found in the literature and have been tabulated elsewhere.⁵² The explanation for this probably lies with tungsten forming stronger metal-ligand bonds, *i.e.* possessing lower energy molecular orbitals than molybdenum, with correspondingly higher energy anti-bonding orbitals including the LUMO. The relativistic effect is greater for the tungsten 5d orbital than for the molybdenum 4d orbital and it is therefore easier for the former to lose electrons to form bonds with ionic character. The small shift in reduction potential associated with interchanging the metal centre is consistent with the ‘non-innocent’ nature of dithiolene ligands.

It is somewhat ambiguous to assign the redox waves to $\text{M}^{\text{IV}/\text{III}}$ and $\text{M}^{\text{III}/\text{II}}$ oxidation state changes without further analysis of the data as a result of the ‘non-innocent’ nature of the dithiolene ligands. The electronic arrangement of the dithiolene ligands can be represented by three limiting canonical structures, Scheme 4.



Scheme 4 Possible resonance structures of $[\text{M}(\text{CO})_2(\text{S}_2\text{C}_2\text{Ph}_2)_2]$.

The low reduction potentials and the ability to add two electrons reversibly suggest the parent complexes are electron-deficient, which implies that the 14 electron, M^{IV} configuration or the 16 electron M^{II} structures are dominant.

As suggested by Allen⁴⁷, possibly the most informative method for characterising the electronic configuration of a dithiolene complex is to analyse the C-C and C-S bond lengths in the dithiolene backbone to rationalise whether they conform with single or double bond lengths.

The Holm group have isolated the three redox species for the series $[\text{Mo}(\text{CO})_2(\text{S}_2\text{C}_2\text{Me}_2)_2]^{2-,1-,0}$ and $[\text{W}(\text{CO})_2(\text{S}_2\text{C}_2\text{Me}_2)_2]^{2-,1-,0}$ and obtained X-ray crystallography characterisation, enabling a bond length analysis.⁴⁵ It was confirmed that the C-C and C-S bonds matched expected values for respective double and single bonds, verifying that the ligands structurally behaved as classical ene-1,2-dithiolate dianions. This is consistent with the parent complexes with which this chapter is concerned, $[\text{M}(\text{CO})_2(\text{S}_2\text{C}_2\text{Ph}_2)_2]$ ($\text{M} = \text{Mo, W}$), also possessing a 14 electron, $\text{M}(\text{IV})$ configuration and successively reducing to 15-electron $\text{M}(\text{III})$ and 16-electron $\text{M}(\text{II})$ species. This cannot therefore be dithiolene/dithiolate ligand based redox chemistry, the LUMO is more associated with metal and CO orbital character as is discussed below.

4.3.1.2 Spectroelectrochemistry

The presence of multiple carbonyl ligands allows infrared spectroelectrochemical measurements in the range $1700\text{-}2100\text{ cm}^{-1}$ to be obtained across all three redox states of the Mo and W complexes.

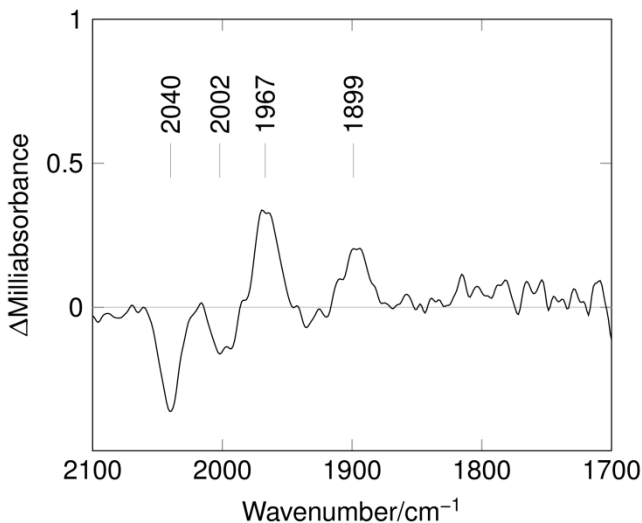


Figure 8 Difference spectrum for the first reduction ($M^{IV/III}$) of 9 mM $[Mo(CO)_2(S_2C_2Ph_2)_2]$ in 0.2 M $[Bu_4N]BF_4$ - CH_2Cl_2 for a scan at 0.88 s relative to a scan at 0.08 s.

The spectroelectrochemical data that is shown in Figures 8 & 9 is for $M = Mo$ (full sets of data for both the molybdenum and tungsten complexes is available in appendix, Figures A5.5-16). The difference spectral data in Figure 8 is for the $[Mo(CO)_2(S_2C_2Ph_2)_2]^{IV/III}$ redox couple with the two negative peaks corresponding to the disappearance of the Mo^{IV} species (starting material) and the positive peaks corresponding to the growth of the Mo^{III} species (product). The two IR peaks correspond to the symmetric and asymmetric stretching modes of the two CO ligands, with the symmetric stretch observed at the higher wavenumber.⁵³ The shift upon reduction to lower wavenumbers is indicative of adding electron density to a metal centre, as this increases π backbonding to π^* antibonding orbitals in multiply bonded ligands such as CO, weakening the $C\equiv O$ triple bond and reducing the vibrational energy. The same pattern is seen for the $[W(CO)_2(S_2C_2Ph_2)_2]$ redox couples as displayed in the appendix (Figures A5.11-.16). A typical response when the potential is reversed and the complex is re-oxidised back to the starting material is shown in Figure 9.

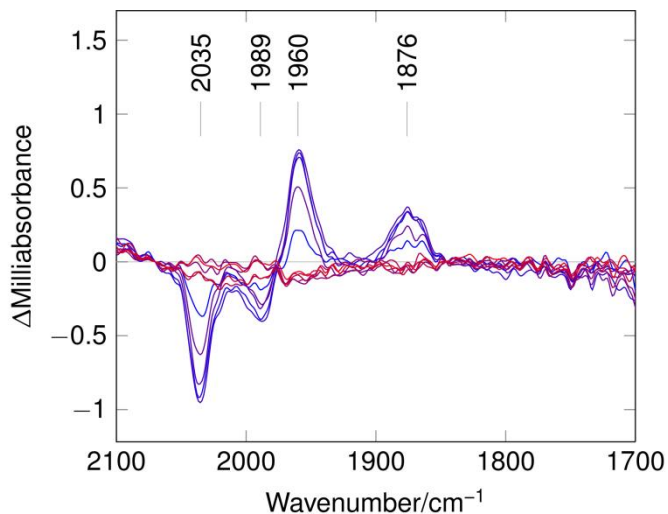


Figure 9 Difference spectrum for the first reduction ($M^{IV/III}$) of 9 mM $[W(CO)_2(S_2C_2Ph_2)_2]$ in 0.2 M $[Bu_4N]BF_4$]- CH_2Cl_2 in the time range 0.34 s (blue) to 14.00 s (red) relative to a scan at 0.08 s.

In this figure the red trace shows a flat line, indicating that the complex has been fully oxidised back to the starting material, thus the depletion bands of the starting material and the growth bands for the product are eliminated. Similar potential ‘reversal’ spectra for other reduction couples are given in the appendix, Figures A4.6-A4.16 (even numbered only).

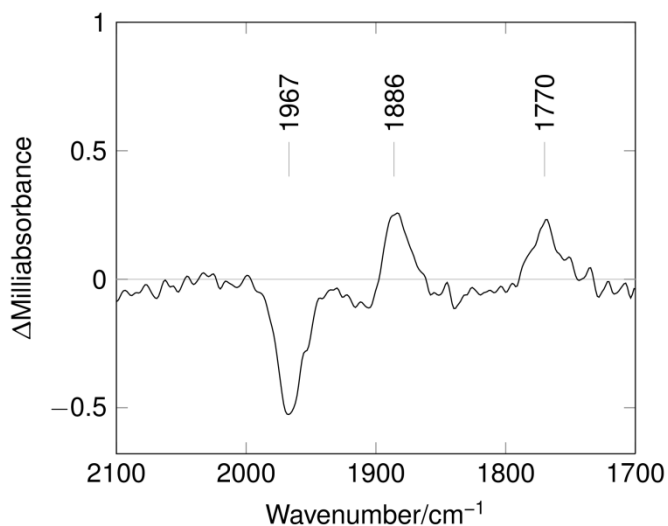


Figure 10 Difference spectrum for the second reduction ($M^{III/II}$) of 9 mM $[Mo(CO)_2(S_2C_2Ph_2)_2]$ in 0.2 M $[Bu_4N]BF_4$]- CH_2Cl_2 for a scan at 0.88 s relative to a scan at 0.08 s.

For the reduction of $Mo^{III/II}$, only one negative loss peak was seen and the stretch seen at 1886 cm^{-1} is of low intensity, Figure 10. This is due to an overlap between the two absorptions and the overall sum of the two peaks at similar wavenumbers is a small

gain at 1886 cm^{-1} , corresponding to one of the peaks associated with the appearance of the M^{II} species.

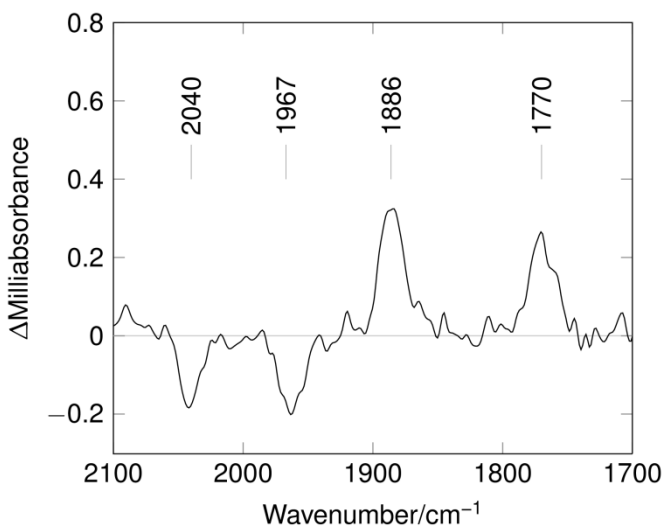


Figure 11 Difference spectrum for the direct second reduction ($\text{M}^{\text{IV}/\text{II}}$) of 9 mM $[\text{Mo}(\text{CO})_2(\text{S}_2\text{C}_2\text{Ph}_2)_2]$ in 0.2 M $[\text{Bu}_4\text{N}] \text{BF}_4^-$ -DCM for a scan at 0.88 s relative to a scan at 0.08 s.

Stepping directly from M^{IV} to M^{II} revealed all three sets of peaks as illustrated by Figure 11, therefore including the M^{III} CO peaks. Why this is the case can be explained by the configuration of the spectroelectrochemical cell, Figure 12.

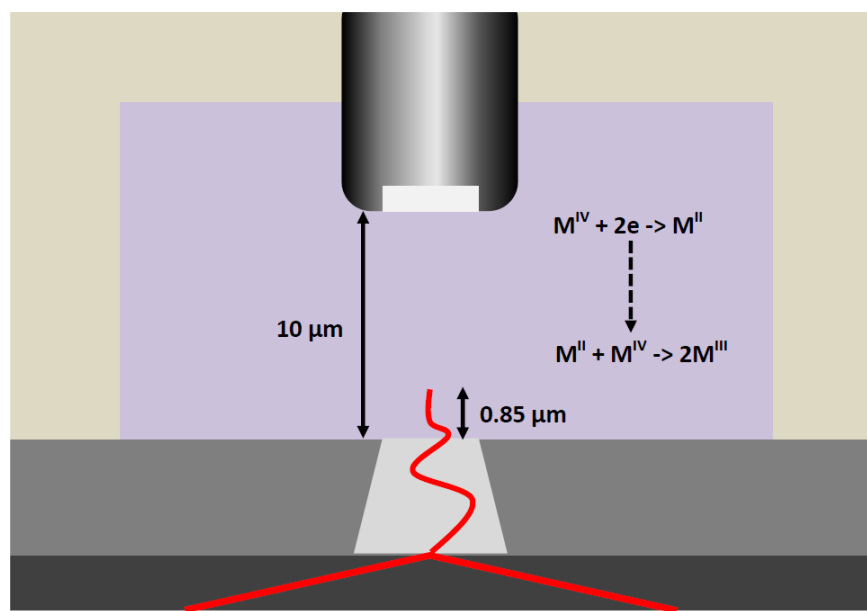


Figure 12 Schematic diagram of electrolyte compartment of spectroelectrochemical cell.

After the M^{IV} starting material is doubly reduced at the surface of the electrode to the M^{II} species, it must diffuse out towards the evanescent infrared wave of the ATR to be

detected. In this region, the reduced M^{II} material may encounter a molecule of the M^{IV} starting material, Figure 12. Electron transfer can occur between the two species, creating two molecules of the M^{III} species, which is why this intermediate species is detected by IR even though it is not directly electrosynthesised in the experiment.

Complex	M ^{IV} IR values / cm ⁻¹	M ^{III} IR values / cm ⁻¹	M ^{II} IR values / cm ⁻¹
[Mo(CO) ₂ (S ₂ C ₂ Ph ₂) ₂]	2040, 2002	1967, 1899	1886, 1770
ⁿ [Mo(CO) ₂ (S ₂ C ₂ Me ₂) ₂]	2026, 1962	1952, 1885	1875, 1757
[W(CO) ₂ (S ₂ C ₂ Ph ₂) ₂]	2035, 1989	1960, 1876	1870, 1752
ⁿ [W(CO) ₂ (S ₂ C ₂ Me ₂) ₂]	2023, 1951	1942, 1865	1864, 1742

Table 1 Stretching frequencies of the CO ligands shifted by reduction of [M(CO)₂(S₂C₂Ph₂)₂] determined by spectroelectrochemistry in comparison with nujol mulls of ⁿ[M(CO)₂(S₂C₂Me₂)₂] isolated by Holm.⁵²

The complete set of CO stretching frequencies for all the oxidation states of both the molybdenum and tungsten analogue complexes are shown in Table 1. The spectroelectrochemical data shows that the corresponding tungsten peaks are between 5 and 14 cm⁻¹ lower in energy than are their molybdenum counterparts, the difference increasing as the oxidation state is lowered. Evidently tungsten is modestly better at back-donation into CO π^* orbitals as the electron complement is increased because the donor/acceptor synergy is more effective.⁵³

Holm and co-workers have reported infrared data for the three redox levels of the [Mo(CO)₂(S₂C₂Me₂)₂] and [W(CO)₂(S₂C₂Me₂)₂] in nujol mulls and these are also given for comparison in Table 1.⁵² The plot of v(CO) data for the [S₂C₂Ph₂] series of complexes *versus* those for the [S₂C₂Me₂] series reported by Holm is shown in Figures 13 and 14.

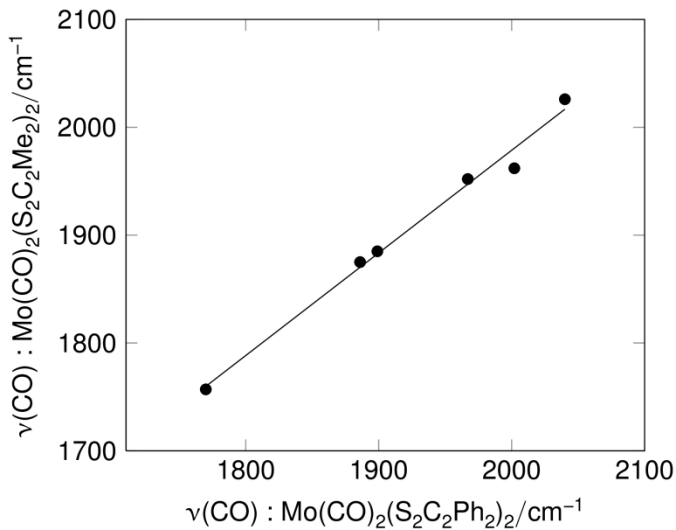


Figure 13 $\nu(\text{CO})$ data for $M = \text{Mo}$, for $[\text{S}_2\text{C}_2\text{Ph}_2]$ series versus the $[\text{S}_2\text{C}_2\text{Me}_2]$.

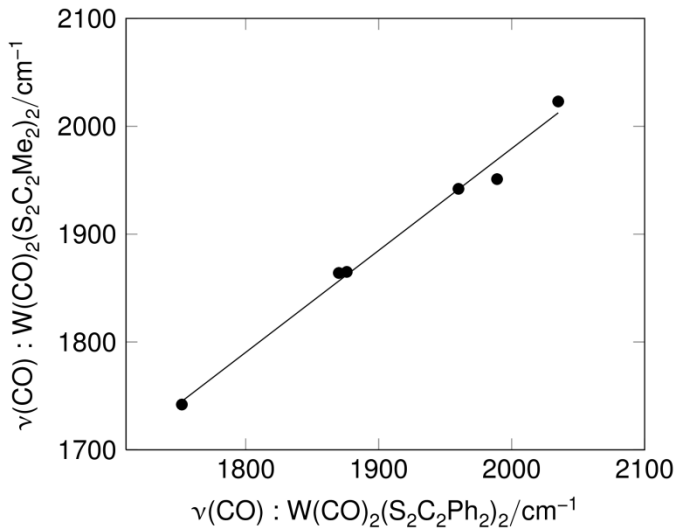


Figure 14 $\nu(\text{CO})$ data for $M = \text{Mo}$, for $[\text{S}_2\text{C}_2\text{Ph}_2]$ series versus the $[\text{S}_2\text{C}_2\text{Me}_2]$.

The linearity of the plots and the slope close to unity confirm that the electronic influence of these two types of dithiolene ligands are very similar.

For all of the complexes, the *separation* between the peaks varies with change in oxidation state, increasing with lowering of oxidation state. This is shown in Figures 15 and 16. This type of effect has been attributed to an increase in stretch-stretch interaction constants of a pair of cis-carbonyls as π -backbonding increases.^{53, 54}

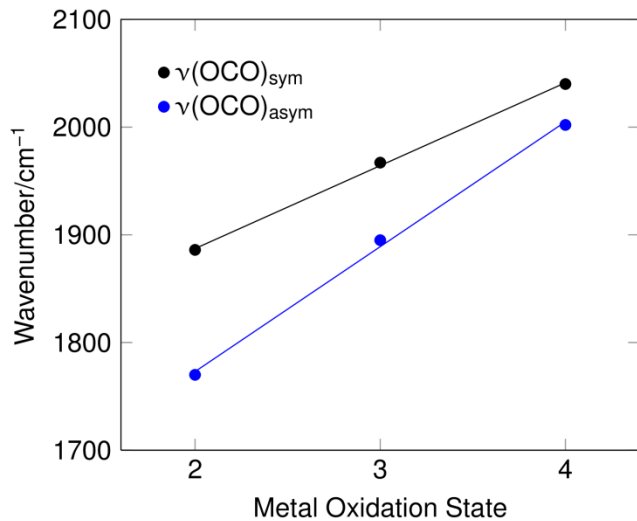


Figure 15 Plot of molybdenum oxidation state against wavenumber of the corresponding CO IR peaks.

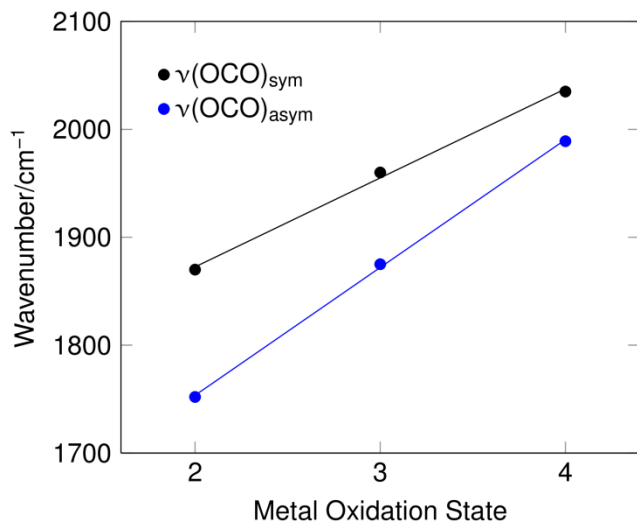


Figure 16 Plot of tungsten oxidation state against wavenumber of the corresponding CO IR peaks.

4.3.1.3 DFT calculations

DFT calculations were undertaken, by Dr. Joseph Wright and Ms. Aušra Jablonskytė, to obtain further insight into how the structural, electronic and spectroscopic properties of the complexes change with oxidation state.

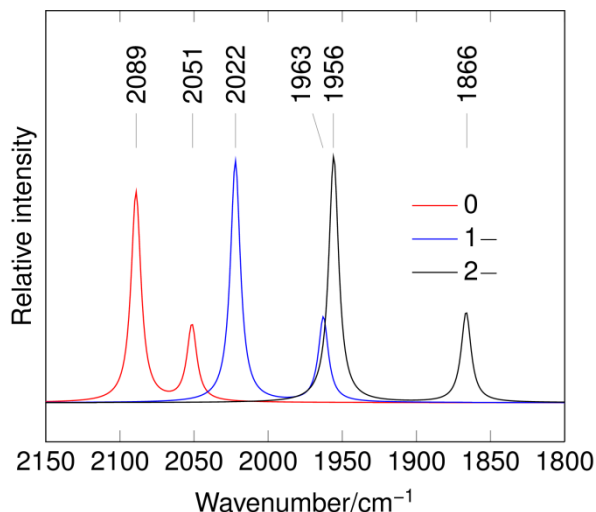


Figure 17 Simulated infrared stretching frequencies of $[\text{Mo}(\text{CO})_2(\text{S}_2\text{C}_2\text{Ph}_2)_2]^{0,1,2^-}$.

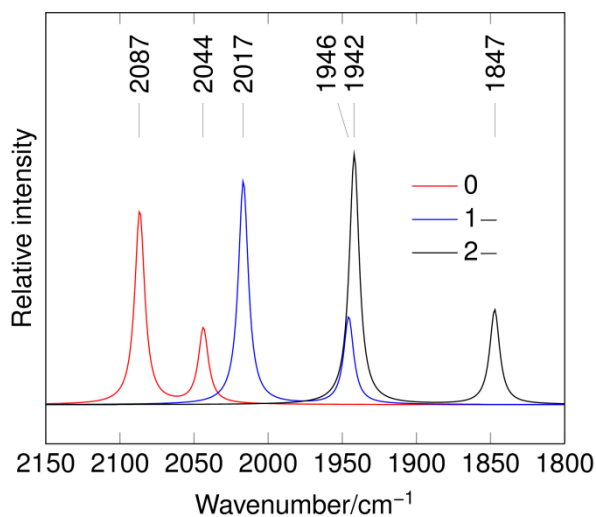


Figure 18 Simulated infrared stretching frequencies of $[\text{W}(\text{CO})_2(\text{S}_2\text{C}_2\text{Ph}_2)_2]^{0,1,2^-}$.

Figures 17 and 18 above show the relative positions of the carbonyls stretching frequencies for all three oxidation states of the molybdenum and tungsten dithiolene complexes as generated by DFT. When compared to the experimental spectroelectrochemical data, the simulated IR data showed the same trends. There are two peaks seen for each oxidation state with the separation between the peaks increasing upon reduction. Also, similar shifts in wavenumber are observed for both experimental and *in silico* results upon change in metal oxidation state. Thus, there is an excellent linear correlation between the experimental and calculated CO stretching frequencies for the Mo and W redox series, Figures 19 and 20.

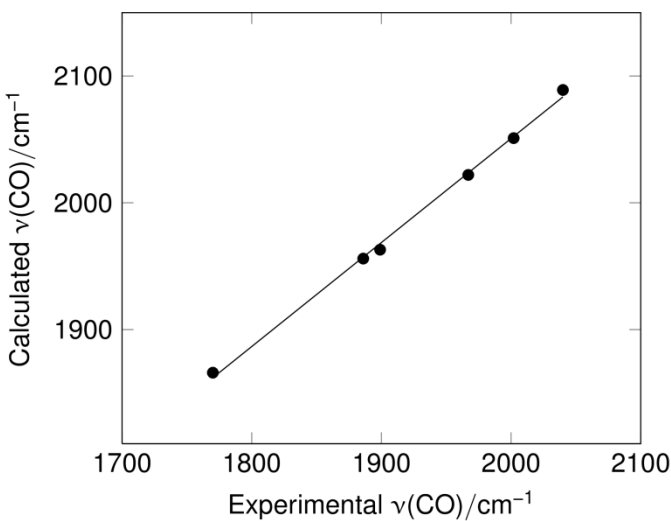


Figure 19 Plot of experiment versus calculated CO stretching frequencies for $[\text{Mo}(\text{CO})_2(\text{S}_2\text{C}_2\text{Ph}_2)_2]^{0,1-,2-}$.

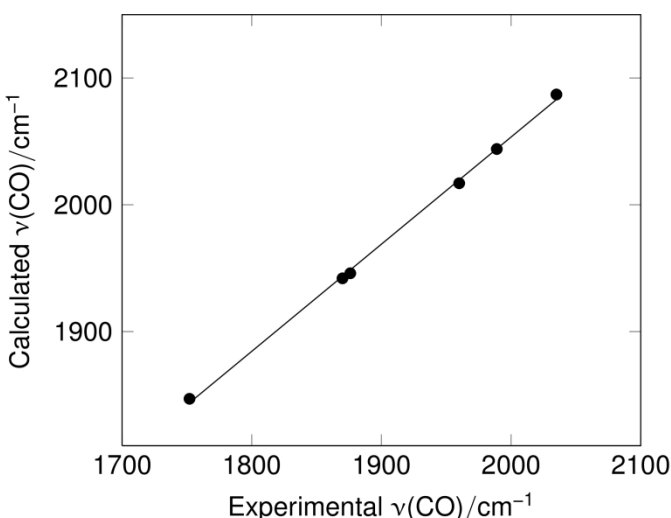


Figure 20 Plot of experiment versus calculated CO stretching frequencies for $[\text{W}(\text{CO})_2(\text{S}_2\text{C}_2\text{Ph}_2)_2]^{0,1-,2-}$.

The DFT data also contains information about the structures of all the species which enables analysis of changes in geometry with the redox state. Table 2 shows how the *cis*-OC-M-CO bond angle changes with the formal redox state.

Complex	$\text{M}^{\text{IV}} \text{C}-\text{M}-\text{C}$ angle / °	$\text{M}^{\text{III}} \text{C}-\text{M}-\text{C}$ angle / °	$\text{M}^{\text{II}} \text{C}-\text{M}-\text{C}$ angle / °
$[\text{Mo}(\text{CO})_2(\text{S}_2\text{C}_2\text{Ph}_2)_2]$	82.7	78.7	74.3
$[\text{W}(\text{CO})_2(\text{S}_2\text{C}_2\text{Ph}_2)_2]$	83.5	78.7	74.2

Table 2 Angle between the two carbonyl ligands altered by reduction of the complex determined by

DFT.

As electrons are added to the system, the bond angle decreases by about 9° in total for both the Mo and W series. The origin of this decrease may involve an increase in O-C \cdots C-O bonding interactions^{53, 54} as discussed in more detail below.

Support for this comes from an examination of the evolution of the HOMO and SOMO/LUMO of $[\text{Mo}(\text{CO})_2(\text{S}_2\text{C}_2\text{Ph}_2)_2]$. Figures 21, 22 and 23 show the orbital distribution pattern for the three redox states of only the Mo series, as both series show the same trend. Tungsten data can be found in the appendix, Figures A4.17-A4.19.

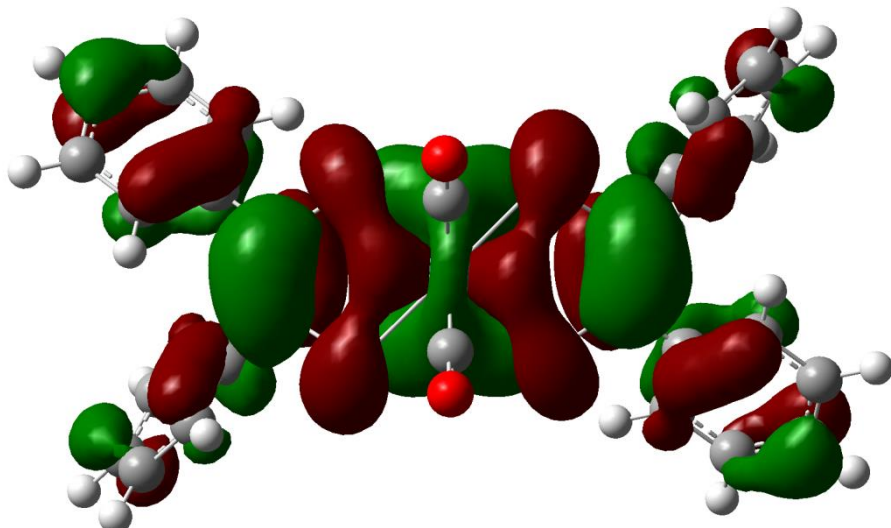


Figure 21 Electron distribution in the HOMO of $[\text{Mo}(\text{CO})_2(\text{S}_2\text{C}_2\text{Ph}_2)_2]$.

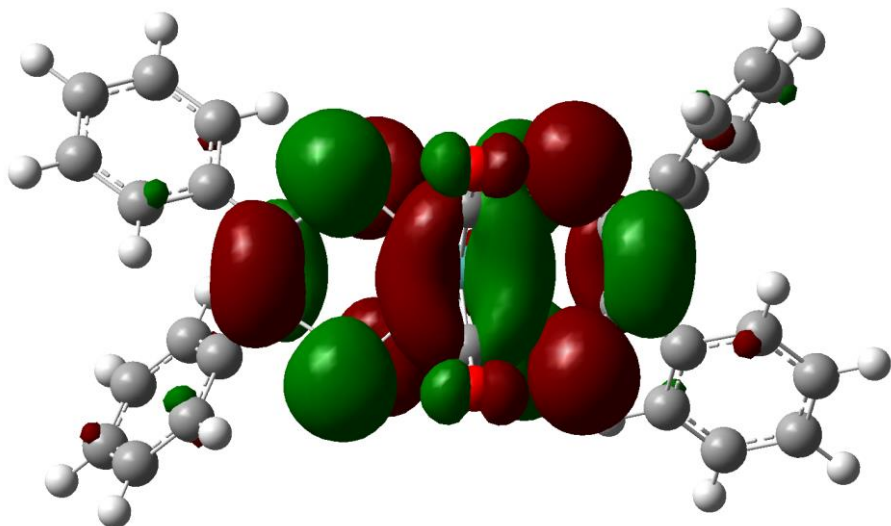


Figure 22 Electron distribution in the SOMO of $[\text{Mo}(\text{CO})_2(\text{S}_2\text{C}_2\text{Ph}_2)_2]^{1-}$.

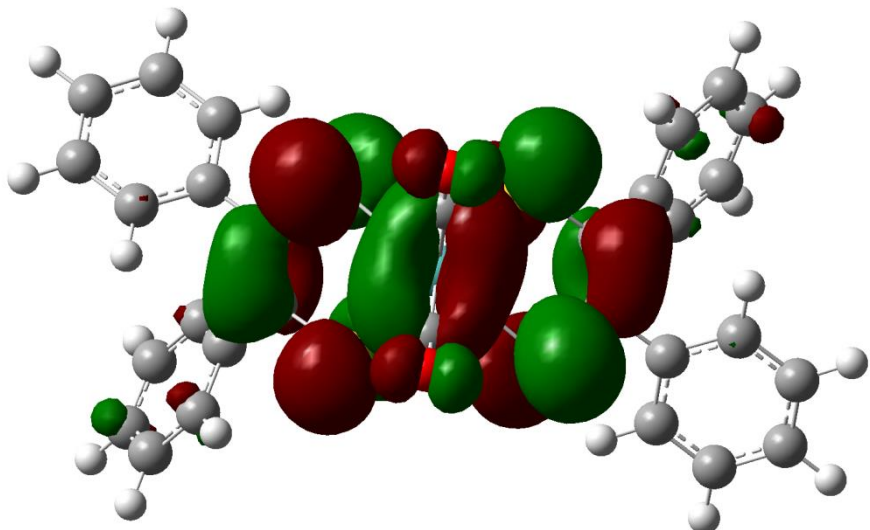


Figure 23 Electron distribution in the LUMO of $[\text{Mo}(\text{CO})_2(\text{S}_2\text{C}_2\text{Ph}_2)_2]^{2-}$.

At the M^{IV} level the HOMO is predominantly metal and dithiolene in character, Figure 21, whereas upon successive one and two electron reduction there is electron density distributed in the SOMO/LUMO, Figures 22 and 23, which indicates shared $\text{OC}\cdots\text{CO}$ bonding character.

Structural changes associated with the addition of electrons within the complexes are clearly seen in the ‘ball and stick’ representations drawn from the DFT calculations, Figures 24, 25 and 26. These again are only shown for molybdenum because the same trends for the isostructural complexes of tungsten are observed; the tungsten data can be found in the appendix, Figures A4.20-A4.22.

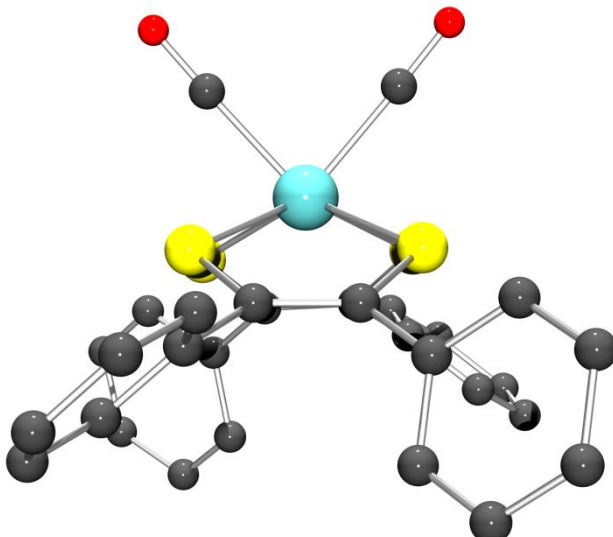


Figure 24 Structural representation of $[\text{Mo}(\text{CO})_2(\text{S}_2\text{C}_2\text{Ph}_2)_2]$ using geometries from DFT simulation.

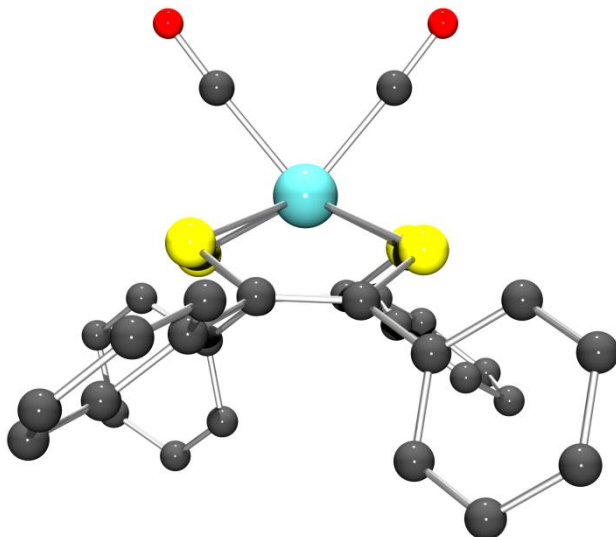


Figure 25 Structural representation of the one electron reduced, $[\text{Mo}(\text{CO})_2(\text{S}_2\text{C}_2\text{Ph}_2)_2]^{1-}$ using geometries from DFT simulation.

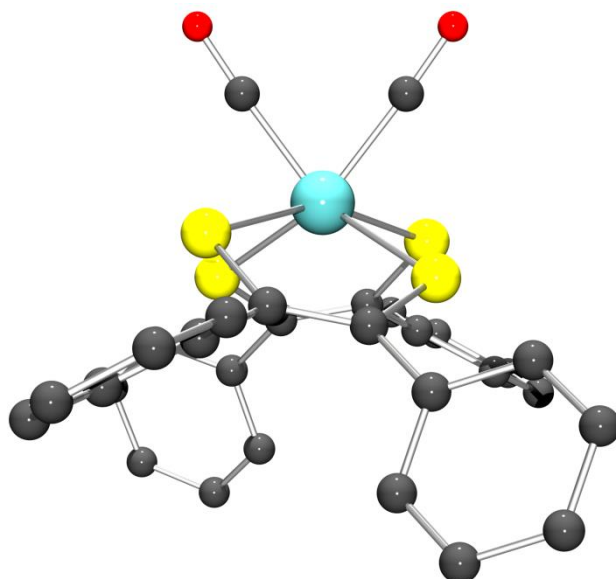


Figure 26 Structural representation of the two electron reduced, $[\text{Mo}(\text{CO})_2(\text{S}_2\text{C}_2\text{Ph}_2)_2]^{2-}$ using geometries from DFT simulation.

From this ‘side-on’ view of the complexes, the decline in the magnitude of the OC-M-CO angle as the complex is reduced can evidently be seen. What is also notable is that the sulfur atoms of the dithiolene ligands, which remain in a plane for the neutral and 1- species, are distorted upon the second reduction. It is possible that the increase in electron density within the OC···CO unit upon reduction repels the pπ-electron density on the alkene component of the dithiolene and this distorts the MoS₄ framework. Increased antibonding electron density on the CO ligands back-donated by the metal

as the complex is reduced repelling the lone pairs of electrons on the sulfur atoms of the dithiolene would also lead to this distorted geometry of the MoS_4 framework.

4.3.2 Hydrogen evolution

4.3.2.1 Cyclic voltammetry

Dihydrogen production by the complexes $[\text{M}(\text{CO})_2(\text{S}_2\text{C}_2\text{Ph}_2)_2]$ was first examined by cyclic voltammetry in 0.2 M $[\text{Bu}_4\text{N}][\text{BF}_4]\text{-CH}_2\text{Cl}_2$ in the presence of a proton source, trifluoroacetic acid ($\text{CF}_3\text{CO}_2\text{H}$), Figures 27 and 28.

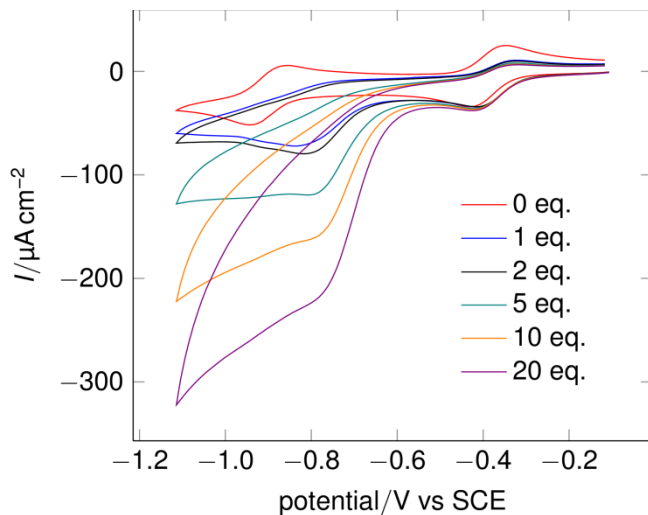


Figure 27 Cyclic voltammetry of 0.24 mM $[\text{Mo}(\text{CO})_2(\text{S}_2\text{C}_2\text{Ph}_2)_2]$ complex in 0.2 M $[\text{NBu}_4][\text{BF}_4]\text{-CH}_2\text{Cl}_2$ at a vitreous carbon electrode with increasing equivalents of trifluoroacetic acid at a scan rate of 100 mVs^{-1} .

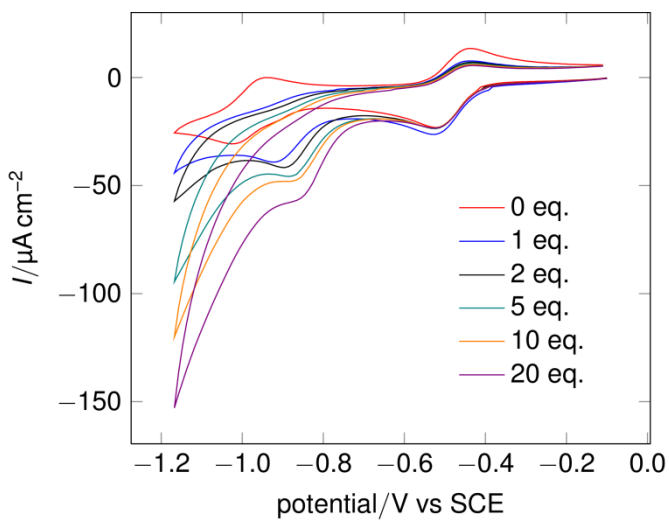


Figure 28 Cyclic voltammetry of 0.18 mM $[\text{W}(\text{CO})_2(\text{S}_2\text{C}_2\text{Ph}_2)_2]$ complex in 0.2 M $[\text{NBu}_4][\text{BF}_4]\text{-CH}_2\text{Cl}_2$ at a vitreous carbon electrode in the presence of equivalents of trifluoroacetic acid at a scan rate of 100 mVs^{-1} .

The first reduction of both the molybdenum and tungsten complexes remains unperturbed by the presence of low concentrations of trifluoroacetic acid, 0 to 20 equivalents, as shown by Figures 27 and 28 respectively. This indicates that the complexes are stable under the acidic conditions of the experiment. The faradaic response of both the molybdenum and tungsten analogues increases at the $[\text{M}(\text{CO})_2(\text{S}_2\text{C}_2\text{Ph}_2)_2]^{1/2^-}$ level as increasing amounts of the acid source are added and the peak progressively shifts for both complexes to more positive values. This behaviour is indicative of an electrocatalytic response. Figures 29 and 30 show the corresponding response at higher acid concentrations. Up to about 640 equivalents of acid, the electrocatalytic behaviour is well-defined for both complexes at the $[\text{M}(\text{CO})_2(\text{S}_2\text{C}_2\text{Ph}_2)_2]^{1/2^-}$ level.

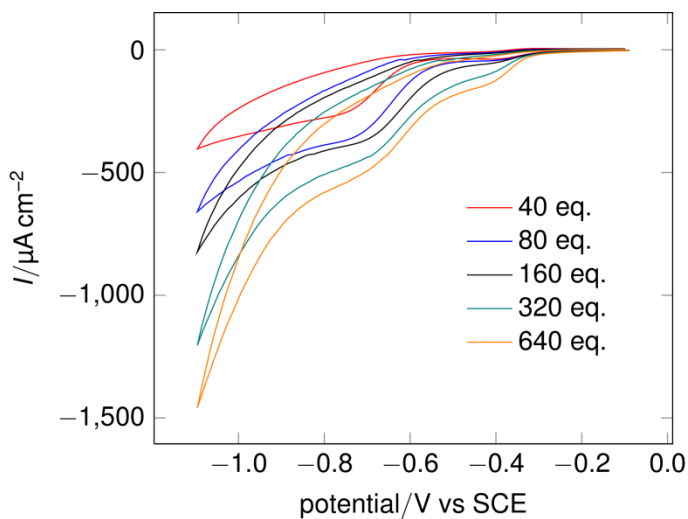


Figure 29 Cyclic voltammetry of 0.24 mM $[\text{Mo}(\text{CO})_2(\text{S}_2\text{C}_2\text{Ph}_2)_2]$ complex in 0.2 M $[\text{NBu}_4]\text{[BF}_4]$ - CH_2Cl_2 at a vitreous carbon electrode with increasing equivalents of trifluoroacetic acid at a scan rate of 100 mVs^{-1} .

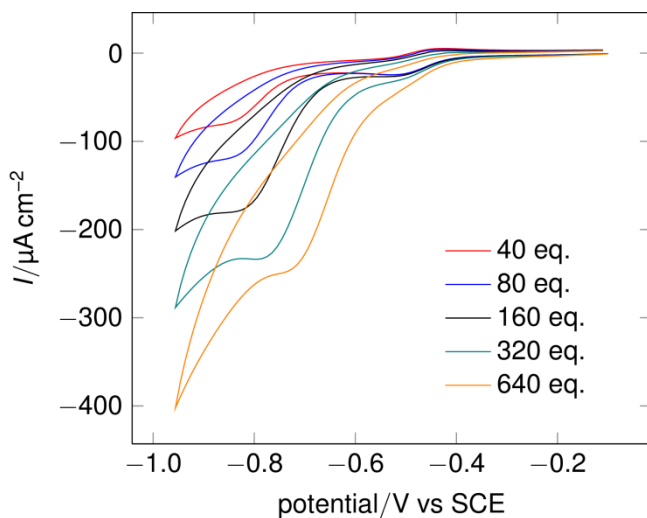


Figure 30 Cyclic voltammetry of 0.18 mM $[\text{W}(\text{CO})_2(\text{S}_2\text{C}_2\text{Ph}_2)_2]$ complex in 0.2 M $[\text{NBu}_4]\text{[BF}_4]$ - CH_2Cl_2 at a vitreous carbon electrode in the presence of equivalents of trifluoroacetic acid at a scan rate of 100 mVs^{-1} .

Normalised for the concentration of the parent complex, the plateau current at 640 equivalents is about twice that for Mo as for the W complex suggesting the former is the faster electrocatalyst, Figure 31.

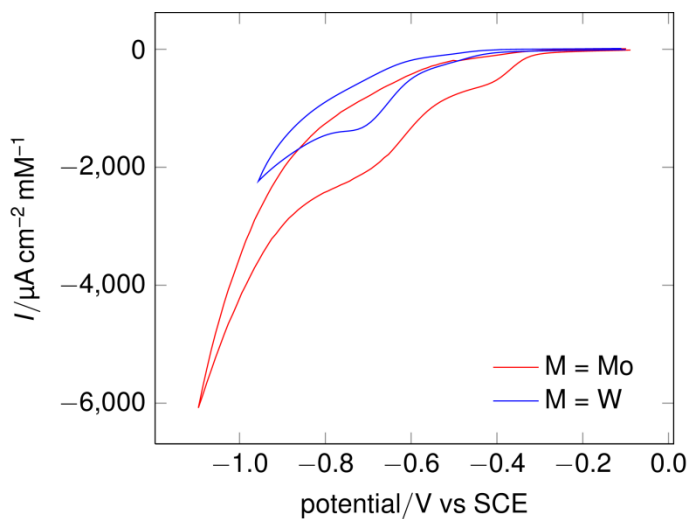


Figure 31 Concentration normalised cyclic voltammetry of $[\text{M}(\text{CO})_2(\text{S}_2\text{C}_2\text{Ph}_2)_2]$ complex in 0.2 M $[\text{NBu}_4]\text{[BF}_4]$ - CH_2Cl_2 at a vitreous carbon electrode in the presence of 640 equivalents of trifluoroacetic acid and at a scan rate of 100 mVs^{-1} .

At the highest acid concentration, 640 equivalents, the first reduction wave increased substantially in magnitude indicative of a slower electrocatalysis involving the $[\text{M}(\text{CO})_2(\text{S}_2\text{C}_2\text{Ph}_2)_2]^{0/-1}$ couple, this was accompanied by the emergence of another reduction process.

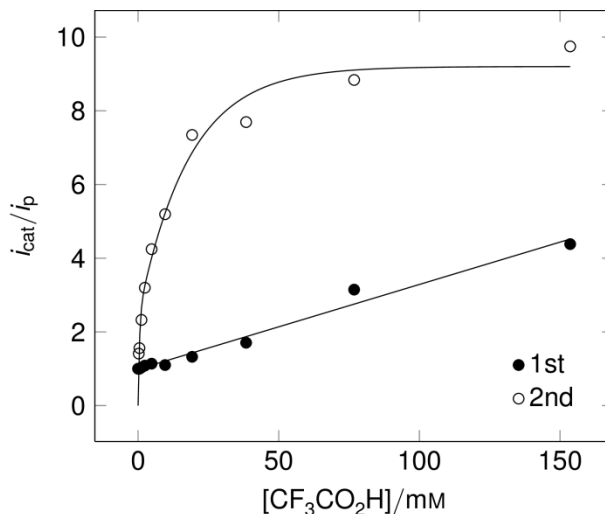


Figure 32 Peak current versus acid concentration at the 1st and 2nd reductions of 0.24 mM $[\text{Mo}(\text{CO})_2(\text{S}_2\text{C}_2\text{Ph}_2)_2]$ complex in 0.2 M $[\text{NBu}_4]\text{[BF}_4]$ - CH_2Cl_2 at a vitreous carbon electrode at a scan rate of 100 mVs^{-1} .

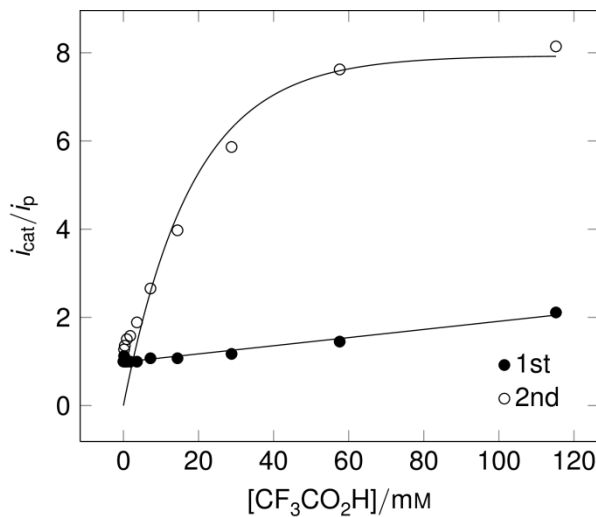


Figure 33 Peak current *versus* acid concentration at the 1st and 2nd reductions of 0.18 mM [W(CO)₂(S₂C₂Ph₂)₂] complex in 0.2 M [NBu₄][BF₄]-CH₂Cl₂ at a vitreous carbon electrode at a scan rate of 100 mV s⁻¹.

Figures 32 and 33 show the plots for the ratio ¹i_{cat} / i_p and ²i_{cat} / i_p *versus* acid concentration, for the Mo and W complexes respectively, in the acid regime where the response is uncomplicated by an additional redox process. The value of i_p is that for the primary process in the absence of acid at 100 mV s⁻¹; ¹i_{cat} and ²i_{cat} are the apparent electrocatalytic currents associated with the [M(CO)₂(S₂C₂Ph₂)₂]^{0/1-} and [M(CO)₂(S₂C₂Ph₂)₂]^{1/2-} couples respectively. As can be seen from both of these plots, the low potential electrocatalysis reaches a plateau level at high acid concentrations, *ca* 40 mM. In this acid independent regime, the catalytic rate constants, ^{2Mo}k_{obs} = 18.3 ± 0.92 s⁻¹ and ^{2W}k_{obs} = 12.8 ± 0.64 s⁻¹, for the Mo and W complexes respectively, as estimated using the relationship shown in Equation 4.1 and 4.2 and discussed in Chapter 2, where x is the reaction order with respect to proton concentration.

$$\frac{i_{cat}}{i_p} = \frac{n}{0.4463} \sqrt{\frac{RT(k[H^+]^x)}{F\nu}}$$

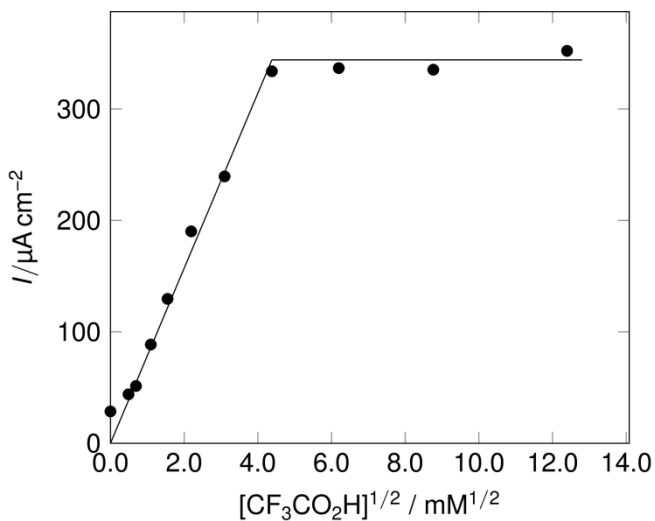
(Equation 4.1)

$$k_{obs} = \nu \left(\frac{i_{cat}/i_p}{0.72} \right)^2$$

(Equation 4.2)

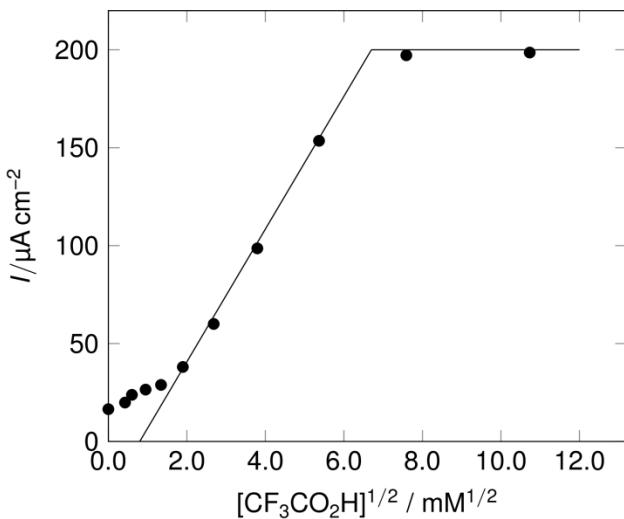
Given that k_{obs} is independent of the acid concentration, it can be equated directly with k_{cat} . Since it is not associated with an acid dependent step, it may be associated with the rate-limiting step involving loss of dihydrogen.

In the acid dependent regime, i_{cat}/i_p for the Mo complex does not show the expected linear correlation with the acid concentration which would correspond to second order in $[\text{H}^+]$ dependence. The correlation shows excellent linearity with $[\text{H}^{+}]^{\frac{1}{2}}$ as shown by Figure 34 indicative of a rate-limiting first-order protonation step.



Figures 34 Peak current vs square root of acid concentration for 0.24 mM $[\text{Mo}(\text{CO})_2(\text{S}_2\text{C}_2\text{Ph}_2)_2]$ complex in 0.2 M $[\text{NBu}_4][\text{BF}_4]\text{-CH}_2\text{Cl}_2$ at a vitreous carbon electrode at a scan rate of 100 mVs⁻¹.

The W complex also shows a linear correlation with $[\text{H}^{+}]^{\frac{1}{2}}$ in the acid dependent regime, Figure 35.



Figures 35 Peak current *versus* square root of acid concentration for 0.18 mM $[\text{W}(\text{CO})_2(\text{S}_2\text{C}_2\text{Ph}_2)_2]$ complex in 0.2 M $[\text{NBu}_4][\text{BF}_4]\text{-CH}_2\text{Cl}_2$ at a vitreous carbon electrode at a scan rate of 100 mVs⁻¹.

Notably, zero, first order and second order dependence of proton concentration has been reported by Dubois and co-workers for closely related Ni complexes which catalyse hydrogen evolution.⁵⁵

Estimates of the *pseudo* first order rate constant, k_{obs} , obtained from the acid dependent portion of the curve provide values of ^{Mo} $k_{\text{cat}} = 232 \pm 12 \text{ M}^{-1} \text{ s}^{-1}$ and ^W $k_{\text{cat}} = 26 \pm 1.3 \text{ M}^{-1} \text{ s}^{-1}$ for the second order rate constants, when divided by the acid concentration.

It appears that there is a slow catalysis associated with the primary process at very high acid concentrations (high potential); i_{cat} for the Mo complex at 2000 equivalents is *ca* four times that in the absence of acid, i_p . For both the Mo and W complexes, there is a linear dependence of i_{cat}/i_p on $[\text{H}^+]$ consistent with a second order dependence. The rate constants estimated under the acid dependent and independent regimes for the low potential and high potential catalytic cycles of the Mo and W complexes are summarised in Table 3.

Complex	High potential, 1k	Low potential, 2k	
	Acid dependent / $M^{-2} s^{-1}$	Acid dependent / $M^{-1} s^{-1}$	Acid independent / s^{-1}
Mo	18.7 ± 0.94	232 ± 12	18.3 ± 0.92
W	9.29 ± 0.46	216 ± 11	12.8 ± 0.64

Table 3 Rate constants of hydrogen evolution in the acid dependent and independent regimes for the high and low potential cycles for both $[Mo(CO)_2(S_2C_2Ph_2)_2]$ and $[W(CO)_2(S_2C_2Ph_2)_2]$.

4.3.2.2 Controlled potential electrolysis

[Mo(CO)₂(S₂C₂Ph₂)₂] as the electrocatalyst

Controlled potential electrolysis experiments provided confirmation of dihydrogen formation which was detected in the gas phase by gas chromatography (GC). Figure 36 shows the current *versus* charge-passed plot for the reduction of the Mo complex in the presence of five equivalents of trifluoroacetic acid. The current decays towards 6-7 moles of electrons per mole catalyst, reasonably consistent with the consumption of proton and reduction of the parent complex. At the end of this electrolysis, the chemical yield of dihydrogen was 69 % (GC) and the current efficiency for its formation was close to 68 % based on an overall theoretical consumption of five electrons for the proton source and two electrons for the complex. At the end of electrolysis the solution had changed from purple to pale yellow. Cyclic voltammetry showed the absence of electroactive species in the range 0 to -1.2 V *versus* SCE, thus the catalyst was lost during the course of electrolysis. Theoretically, a turnover number of 2.5 was expected; experimentally this was 1.7 consistent with the loss of catalyst during turnover.

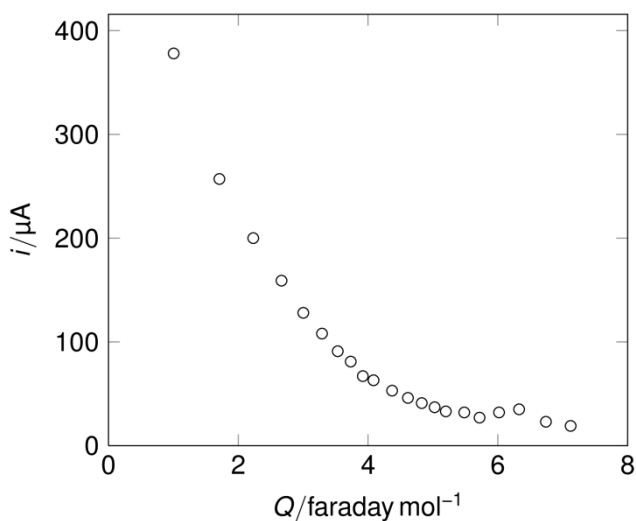


Figure 36 Controlled potential electrolysis of 0.30 mM $[\text{Mo}(\text{CO})_2(\text{S}_2\text{C}_2\text{Ph}_2)_2]$ complex in 0.2M $[\text{NBu}_4][\text{BF}_4]$ - CH_2Cl_2 at a vitreous carbon electrode in the presence of 5 equivalents of trifluoroacetic acid (Exp. No. 8 in Table A4.1).

Controlled potential electrolysis experiments were also performed at -0.5 V *versus* SCE in the presence of a high concentration of acid where catalysis occurs at the high potential associated with the $[\text{Mo}(\text{CO})_2(\text{S}_2\text{C}_2\text{Ph}_2)_2]^{0/1^-}$ couple. Figure 37 shows the current charge passed plot in the presence of 2000 equivalents of trifluoroacetic acid. A substantial current remained after the passage of 14 F mol^{-1} catalyst with dihydrogen formed with a current efficiency of 23 %, Table A4.2. In a similar experiment, where the electrolysis was terminated after the passage of 9 F mol^{-1} catalyst the current efficiency was close to 31%.

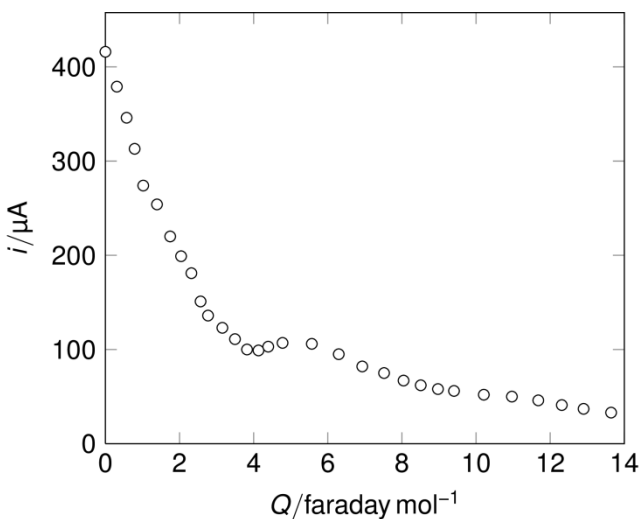


Figure 37 Controlled potential electrolysis of 0.59 mM $[\text{Mo}(\text{CO})_2(\text{S}_2\text{C}_2\text{Ph}_2)_2]$ complex in 0.2M $[\text{NBu}_4][\text{BF}_4]$ - CH_2Cl_2 at a vitreous carbon electrode in the presence of 2000 equivalents of trifluoracetic acid (Exp. No. 1 in Table A4.2).

Other electrolysis conditions were explored. Figure 38 shows the current *versus* charge passed plot for an electrolysis carried out using $[\text{Mo}(\text{CO})_2(\text{S}_2\text{C}_2\text{Ph}_2)_2]$ as the electrocatalyst with seven equivalents of a pyridinium tetrafluoroborate salt as the acid source in MeCN. A modestly high current yield of 76 % was obtained with a corresponding chemical yield of 75 % with a turnover number TON of 2.64. These conditions gave chemical and current yields quite similar to the experiment described above using trifluoroacetic acid in DCM, but the turnover number was somewhat higher.

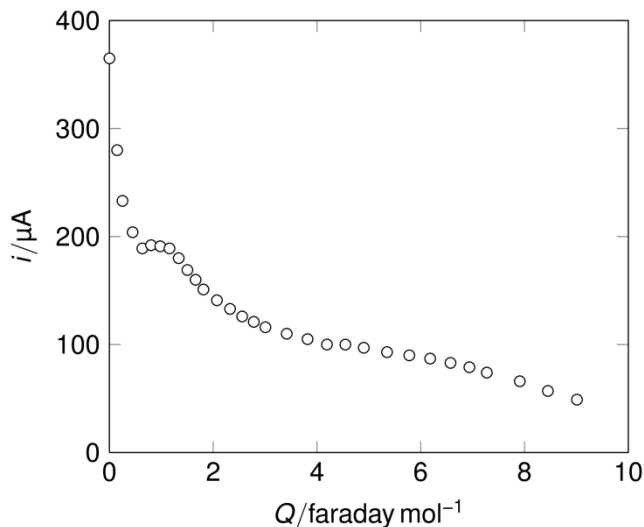


Figure 38 Controlled potential electrolysis of 0.58 mM $[\text{Mo}(\text{CO})_2(\text{S}_2\text{C}_2\text{Ph}_2)_2]$ complex in 0.2M $[\text{NBu}_4][\text{BF}_4]$ - CH_2Cl_2 at a vitreous carbon electrode in the presence of 7 equivalents of pyridinium (Exp. No. 4 in Table A4.1).

Table A4.1 summarises the data collected for a range of electrolyses performed on the molybdenum complex under various conditions. The yields measured for hydrogen formation are variable with the chemical yield ranging from 11 to 75 % (with an average value of 41 %). The current efficiency ranged from 24 to 76 % (with an average efficiency of 46 %). The best current efficiencies of 52-76 % were generally associated with the lower catalyst concentrations below 1 mM. It is possible that the variability in the experimental yields is dependent on the rate of catalyst deactivation.

***W(CO)₂(S₂C₂Ph₂)₂* as the electrocatalyst**

Controlled potential electrolysis of the tungsten analogue in DCM in the presence of trifluoroacetic acid was undertaken. Figure 39 shows a current *versus* charge passed

plot in the presence of 5 equivalents of the acid. Dihydrogen was produced in 71 % chemical yield with a TON of 3.2. The current efficiency, 41 %, was low with an overall consumption of over 17 F mole^{-1} catalyst.

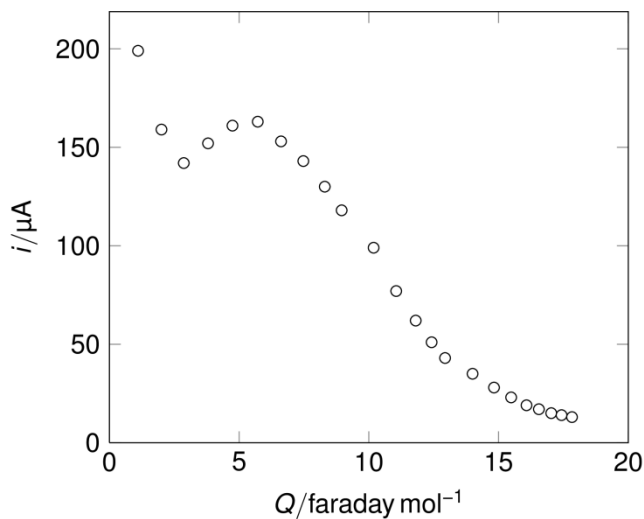


Figure 39 Controlled potential electrolysis of 0.09 mM $[\text{W}(\text{CO})_2(\text{S}_2\text{C}_2\text{Ph}_2)_2]$ complex in 0.2M $[\text{NBu}_4][\text{BF}_4]$ - CH_2Cl_2 at a vitreous carbon electrode in the presence of 5 equivalents of trifluoroacetic acid (Exp. No. 6 in Table A4.3).

As for the Mo complex, controlled potential electrolysis experiments were performed at -0.6 V *versus* SCE catalysis in the presence of a high concentration of acid where catalysis occurs at the high potential associated with the $[\text{W}(\text{CO})_2(\text{S}_2\text{C}_2\text{Ph}_2)_2]^{0/1^-}$ couple. Figure 40 shows the current charge passed plot in the presence of 4000 equivalents of trifluoroacetic acid. The current decays smoothly approaching a plateau of *ca* 180 μA after the passage of 30 F mol^{-1} catalyst. Table A4.4 summarises data for two experiments which show dihydrogen was produced with current efficiencies (uncorrected for the two electrons required to reach the catalytic species) of *ca* 20-25 %.

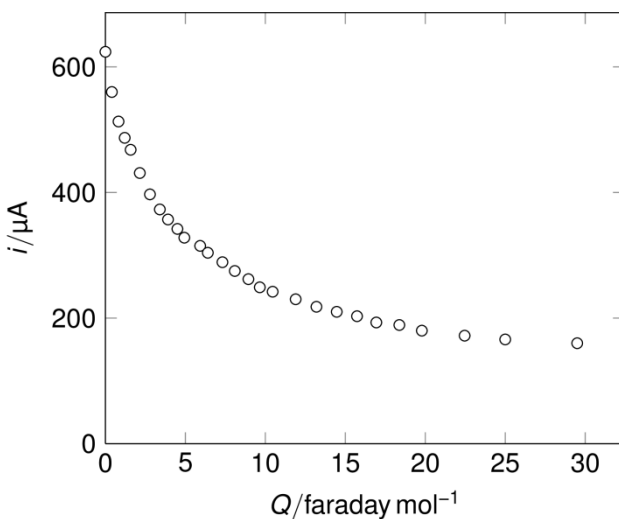


Figure 40 Controlled potential electrolysis of 0.67 mM $[\text{W}(\text{CO})_2(\text{S}_2\text{C}_2\text{Ph}_2)_2]$ complex in 0.2M $[\text{NBu}_4]\text{[BF}_4]$ - CH_2Cl_2 at a vitreous carbon electrode in the presence of 4000 equivalents of trifluoracetic acid (Exp. No. 1 in Table A4.4).

The low potential electrocatalysis experiments exhibited very low chemical yields, as expected for the high excess of acid, but relatively good current efficiency and turnover numbers. The tungsten complex exhibited a higher turnover than the molybdenum counterpart in similar timescale experiments, again indicating that it is a faster catalyst at high acid concentrations.

4.3.2.3 Spectroelectrochemistry

Spectroelectrochemical studies were undertaken to further probe the electrocatalytic process. The timescale for the experiments were *ca* 0.1 to 60 s, which is closer to the time frame of the cyclic voltammetry rather than to that of the bulk electrolysis experiments which took *ca* 3 h.

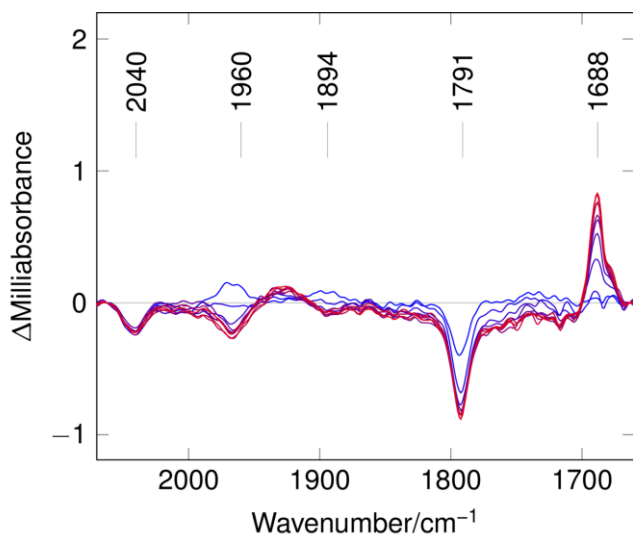


Figure 41 Difference spectrum for the direct second reduction of 9 mM $[\text{Mo}(\text{CO})_2(\text{S}_2\text{C}_2\text{Ph}_2)_2]$ in the presence of 5 eq. TFA, in 0.2 M $[\text{Bu}_4\text{N}] \text{BF}_4$ - CH_2Cl_2 in the time range 1.36 s (blue) to 56.00 s (red) relative to a scan at 0.08 s.

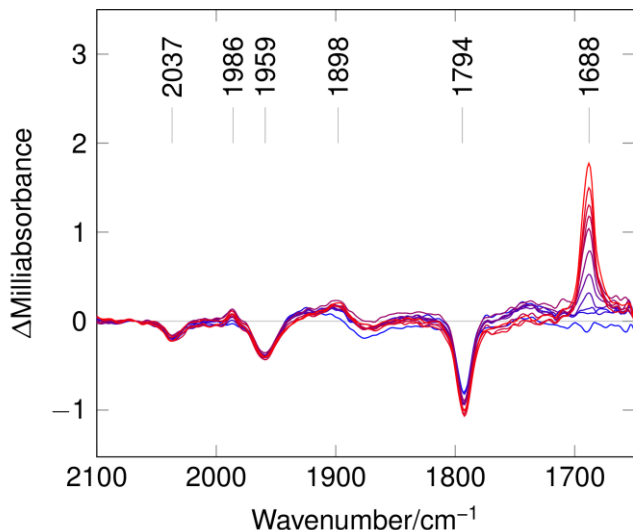


Figure 42 Difference spectrum for the direct second reduction of 9 mM $[\text{W}(\text{CO})_2(\text{S}_2\text{C}_2\text{Ph}_2)_2]$ in the presence of 5 eq. TFA, in 0.2 M $[\text{Bu}_4\text{N}] \text{BF}_4$ - CH_2Cl_2 in the time range 1.36 s (blue) to 56.00 s (red) relative to a scan at 0.08 s.

Figures 41 and 42 show difference spectra of the Mo and W systems respectively, in the presence of 5 equivalents of trifluoroacetic acid. The results for both systems are qualitatively similar. Those for the Mo complex are better resolved and discussion is focussed on these.

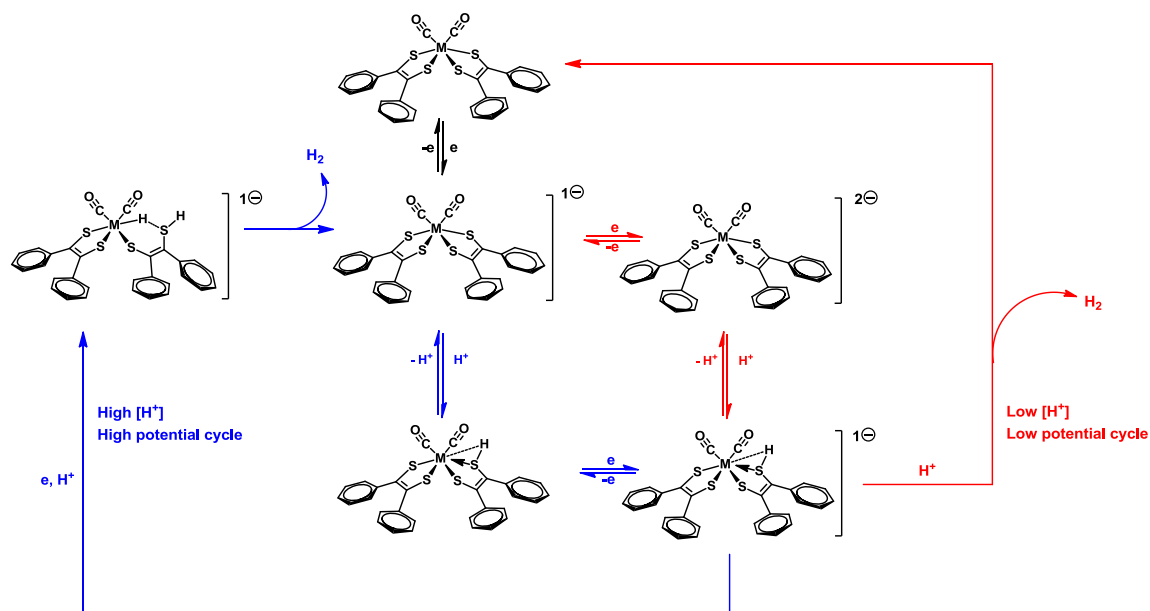
In the CO region, the depletion of the carboxylic acid (CF_3COOH) band at $\text{ca } 1790 \text{ cm}^{-1}$ is observed together with the growth of the band for the conjugate base, the

carboxylate (CF_3COO^-) at ca 1690 cm^{-1} . This is fully consistent with the consumption of protons in the thin-layer cell as a consequence of the electrocatalysis.

At short times, a depletion band of the parent complex is observed at 2040 cm^{-1} together with those for the growth, and subsequent decay, of the monoanionic species $[\text{Mo}(\text{CO})_2(\text{S}_2\text{C}_2\text{Ph}_2)_2]^{1-}$ at 1960 and 1894 cm^{-1} , Figure 41. The formation of the dianion is not observed which suggests this species is consumed and regenerated during turnover. No other metal carbonyl peaks build up to a detectable level during the thin layer electrolysis.

4.3.2.4 Possible mechanism of electrocatalysis

Evaluation of all the available electrochemical and spectroelectrochemical data has allowed a mechanism for hydrogen evolution by molybdenum and tungsten dithiolene complexes to be suggested.



Scheme 5 Proposed catalytic cycle for hydrogen evolution by $[\text{M}(\text{CO})_2(\text{S}_2\text{C}_2\text{Ph}_2)_2]$ ($\text{M} = \text{Mo}, \text{W}$) showing both the high and low potential cycles.

Throughout the postulated mechanism, all the ligands remain coordinated or partially coordinated to the metal centre. In practice the electrocatalytic species is probably destroyed by side reactions which may involve CO loss, de-coordination of dithiolene ligands, and/or attack by residual water to give $\text{M}=\text{O}$ species.

Two possible hydrogen evolution pathways are incorporated into the mechanism, the high and low potential cycles. The pathway taken is dependent upon acid concentration and whether M = Mo or W, with the high potential cycle being established at $[\text{Mo}(\text{CO})_2(\text{S}_2\text{C}_2\text{Ph}_2)_2]$ at lower acid concentration than that for the tungsten analogue.

In Scheme 5, protonation is suggested to take place at one of the sulfur atoms ligating the dithiolene to the metal. Although there is no spectroscopic evidence to support this, the ligand sulfur atom lone pairs are likely to be basic, and therefore should have a high affinity for protons. Thiols have been implicated as intermediates for the hydrogen evolution from an iron monodithiolene complex by Ott,⁴¹ however in this instance, computational studies show that the metal-sulfur bond in question is broken. DFT studies of the Mo and W complexes studied here show that in the reduced states the sulfur atoms of the dithiolene ligands contribute substantially to the HOMO and thus present electron-rich sites for protonation.

4.3.3 Oxidative Electrochemistry

The oxidative electrochemistry of the complexes $[\text{M}(\text{CO})_2(\text{S}_2\text{C}_2\text{Ph}_2)_2]$ showed two redox steps, Figures 43 and 44. The peak current for the primary oxidation of the Mo-species, i_p^{ox} , is linearly related to the square root of the scan rate establishing that it is a diffusion controlled process. The primary oxidation is essentially irreversible at all scan rates up to 400 mVs^{-1} in the 0.5 to 0.9 V range. The ratio $i_p^{\text{ox}} / i_p^{\text{red}}$, where i_p^{red} is the peak current for the primary reduction of the $\text{Mo}^{\text{IV}/\text{III}}$ couple is 8.4 at 100 mVs^{-1} which is indicative of a multi-electron oxidation and must involve ligand oxidation. The behaviour of the tungsten complex is less defined. Inspection of the electrode upon excursion into the oxidation regime shows film formation. Plots of anodic peak current versus square root of scan rate confirmed that this is probably the case as the correlation is lower for $[\text{W}(\text{CO})_2(\text{S}_2\text{C}_2\text{Ph}_2)_2]$ than for $[\text{Mo}(\text{CO})_2(\text{S}_2\text{C}_2\text{Ph}_2)_2]$, Figures A4.23-A4.26.

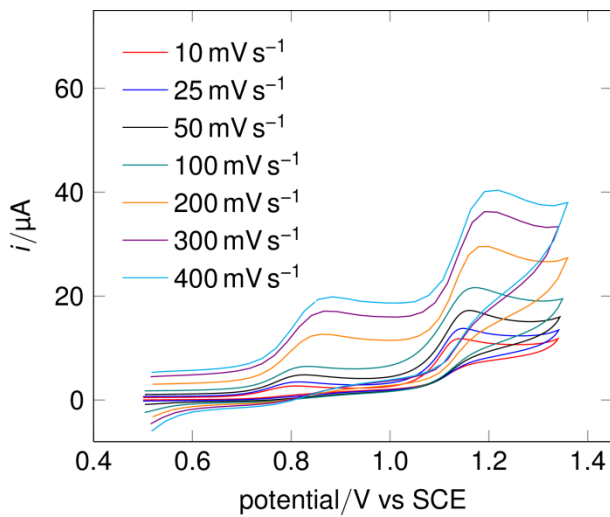


Figure 43 Cyclic voltammetry of 1.20 mM $\text{Mo}(\text{CO})_2(\text{S}_2\text{C}_2\text{Ph}_2)_2$ in 0.1 M $[\text{Bu}_4\text{N}][\text{BF}_4]$ -MeCN at various scan rates.

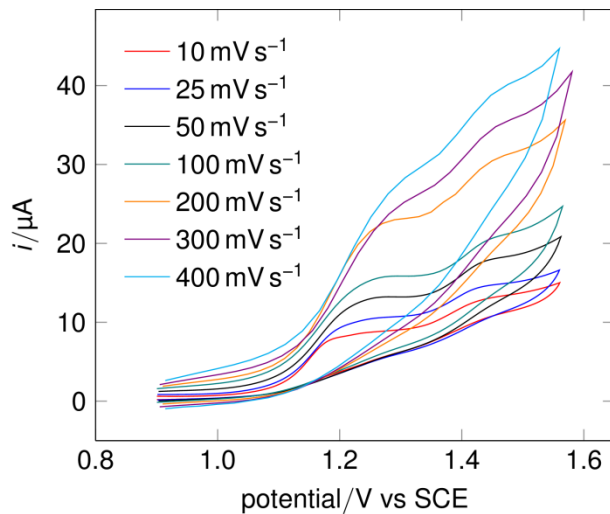


Figure 44 Cyclic voltammetry of 0.80 mM $\text{W}(\text{CO})_2(\text{S}_2\text{C}_2\text{Ph}_2)_2$ in 0.1 M $[\text{Bu}_4\text{N}][\text{BF}_4]$ -MeCN at various scan rates.

4.3.3.1 Hydrogen oxidation

Although the oxidation process of the Mo and W species are multi-electron, the behaviour of the complexes under an atmosphere of dihydrogen was examined. When dihydrogen gas was introduced to the Mo system by purging the cell, there was a small increase in the anodic peak current at the second oxidation. This increase in current suggested there was *possible* catalysis of hydrogen oxidation to protons, Figure 45 and 46.

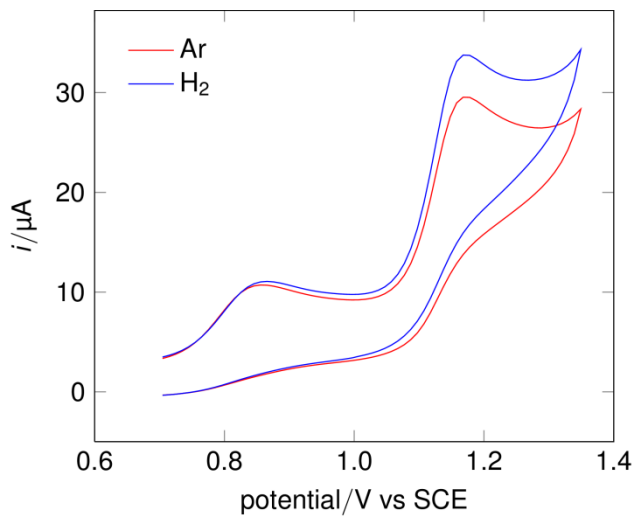


Figure 45 Cyclic voltammetry of 1.20 mM $\text{Mo}(\text{CO})_2(\text{S}_2\text{C}_2\text{Ph}_2)_2$ in 0.1 M $[\text{Bu}_4\text{N}][\text{BF}_4]$ -MeCN in the presence of argon and hydrogen gas at a scan rate of 100 mV s^{-1} .

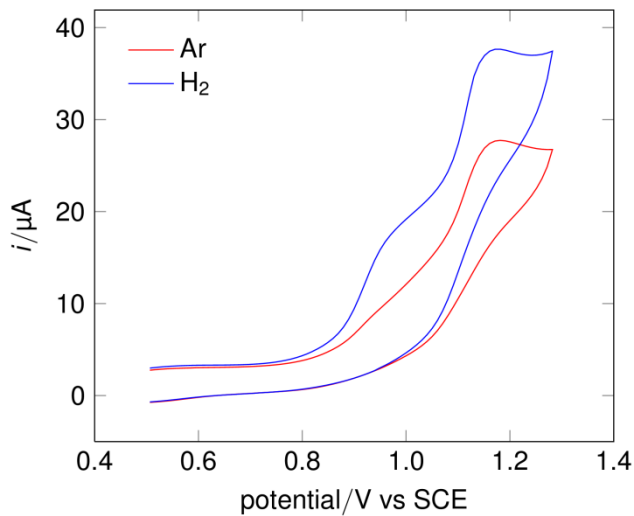


Figure 46 Cyclic voltammetry of 0.80 mM $\text{W}(\text{CO})_2(\text{S}_2\text{C}_2\text{Ph}_2)_2$ in 0.1 M $[\text{Bu}_4\text{N}][\text{BF}_4]$ -MeCN in the presence of argon and hydrogen gas at a scan rate of 100 mV s^{-1} .

However, when the cell was re-purged with argon the peak current for the oxidative processes was not returned to its original state. Having removed all of the hydrogen with purging, no catalytic current should be observed. The tungsten system also apparently showed an effect of dihydrogen on the cyclic voltammetry, but again the original response was not restored on purging with argon. The increase in current seen in the voltammetry is therefore possibly due to an electrode adsorption process. Preliminary CPE experiments of the complexes in the presence of hydrogen also gave little to no evidence for the oxidation of hydrogen.

4.4 Conclusions

The work described in this chapter set out to explore the possibility that Mo and W dithiolene assemblies might electrocatalyse hydrogen evolution or uptake and that this could provide chemical precedence for a recently recognised hydrogen metabolism involving molybdo-pterin enzymes related to formate dehydrogenases.

In a spectroelectrochemical and DFT study, the basic electron transfer chemistry of the $[M(CO)_2(S_2C_2Ph_2)_2]^{0/1/-2}$ redox series was established. This reinforced the observations of Holm on related species that the dithiolene ligand retains dithiolate character and substantially contributes to the frontier orbitals of the redox series.

It has been shown that the oxidation of the complexes is an irreversible multi-electron process on the cyclic voltammetric timescale and that dihydrogen oxidation is not electrocatalysed. In contrast, evidence is presented which shows that the $[Mo(CO)_2(S_2C_2Ph_2)_2]$ and $[W(CO)_2(S_2C_2Ph_2)_2]$ species are capable of electrocatalysing hydrogen evolution. This is suggested to involve a fast, low potential cycle at low acid concentrations and a slower, high potential cycle at high acid concentrations for both the Mo and W complexes. The low potential process occurs at a potential of *ca* -0.8 V *versus* SCE for the Mo complex corresponding to an approximate overpotential of 320 mV for reduction of trifluoroacetic acid.⁵⁶ The plateau current for the low potential process, i_{cat} , clearly shows a linear dependence on $[H^+]^\frac{1}{2}$ below 1280 equivalents from which an overall second order rate constant of $232 \pm 12 \text{ M}^{-1} \text{ s}^{-1}$ was estimated (first order in $[H^+]$). The corresponding plot for the W complex gave a similar value, $216 \pm 11 \text{ M}^{-1} \text{ s}^{-1}$. The high potential processes for both the Mo and W species showed a second order dependence on $[H^+]$ with rate constants of 18.7 and $9.29 \text{ M}^{-2} \text{ s}^{-1}$, respectively. At high acid concentrations, the low potential process becomes independent of $[H^+]$, indicative of a rate-determining step which is zero order in $[H^+]$. First order rate constants for the Mo and W species in this regime were estimated to be 18.3 and 12.8 s^{-1} , respectively.

Controlled potential electrolysis unequivocally confirmed that dihydrogen was produced during bulk electrolyses in both the low and high potential catalytic regimes and for both the Mo and W complexes. Current efficiencies were maximally *ca* 75 %

with turnover numbers of up to 3 ($M = Mo$). The systems are not stable, as at high acid concentrations low turnover numbers were observed.

The results obtained provide chemical precedence for catalysis of dihydrogen formation by Mo and W dithiolenes and this may be of possible relevance to the hydrogen metabolism reported by Sawers *et al.* involving Mo pterins.⁸ Dihydrogen oxidation was not observed. Notably the complexes used in this study have CO ligands, a common feature in all the known hydrogenases. There are examples of dithiolene complexes of other metals which electrocatalyse hydrogen evolution and which do not possess CO ligands. For example, Holland and co-workers have reported fast hydrogen evolution catalysis by certain cobalt dithiolene complexes in an aqueous/organic electrolyte mixtures.⁴⁰

4.5 Future avenues of research

As the catalysis of hydrogen evolution by the systems described in this chapter is not especially fast or of high turnover, steps should be taken to improve this as much as possible. It has been shown that the catalyst decomposes after *ca* 3 turnovers and that this is most likely to be caused by the instability of the doubly reduced catalytic species. Toluene electrolyte that was used for the cationic hydrido- complex in Chapter 3 may provide the correct environment to do this. Another possibility is to use an aqueous/organic (water/acetonitrile) electrolyte mixture as used by Holland and co-workers to increase the rate of catalysis of dithiolene complexes. However, phenyl substituents situated on the dithiolene ligands will make solubility an issue and the presence of water could extenuate catalyst deactivation by formation of oxo species.

4.6 References

1. E. I. Stiefel, R. Eisenberg, R. C. Rosenberg, H. B. Gray, *J. Am. Chem. Soc.* **1966**, *88*, 2956
2. S. J. N. Burgmayer, *Prog. Inorg. Chem.* **2004**, *52*, 491
3. P. Basu, S. J. N. Burgmayer, *Coord. Chem. Rev.* **2011**, *255*, 1016
4. M. L. Kirk, M. E. Helton, R. L. McNaughton, *Prog. Inorg. Chem.* **2004**, *52*, 111
5. R. Kato, Y. L. Liu, S. Aonuma, H. Sawa, *Synth. Met.* **1997**, *86*, 2087
6. R. S. Pilato, K. A. Van Houten, *Prog. Inorg. Chem.* **2004**, *52*, 369
7. L. Marbella, B. Serli-Mitasev, P. Basu, *Angew. Chem. Int. Ed.* **2009**, *48*, 3996
8. B. Soboh , C. Pinske, M. Kuhns, M. Waclawek, C. Ihling, K. Trchounian, A. Trchounian, A. Sinz, G. Sawers, *BMC Microbiology*, **2011**, *11*, 173
9. J. H. Enemark, J. J. A. Cooney, J. J. Wang, R. H. Holm, *Chem. Rev.* **2004**, *104*, 1175
10. C. Tard, C. J. Pickett, *Chem. Rev.* **2009**, *109*, 2245
11. A. Magalon, J. G. Fedor, A. Walburger, J. H. Weiner, *Coord. Chem. Rev.* **2011**, *255*, 1159
12. M. J. Romao, *J. Chem. Soc. Dalton Trans.* **2011**, 4053
13. R. Hille, *Met. Ions Biol. Syst.* **2002**, *39*, 187
14. G. Schwarz, R. R. Mendel, M. W. Ribbe, *Nature*, **2009**, *460*, 839
15. J. C. Boyington, V. N. Gladyshev, S. V. Khangulov, T. C. Stadtman, P. D. Sun, *Science*, **1997**, *275*, 1305
16. R. A. Rothery, B. Stein, M. Solomonson, M. L. Kirk, J. H. Weiner, *Proc. Natl. Acad. Sci.* **2012**, *109*, 14773
17. R. Hille, *Chem. Rev.* **1996**, *96*, 2757
18. S. J. N. Burgmayer, *Prog. Inorg. Chem.* **2004**, *52*, 491
19. M. J. Romao, M. Archer, I. Moura, J. J. G. Moura, J. LeGall, R. Engh, M. Schneider, P. Hof, R. Huber, *Science*, **1995**, *270*, 1170
20. H. Schindelin, C. Kisker, J. Hilton, K. V. Rajagopalan, D. C. Rees, *Science*, **1996**, *272*, 1615
21. K. V. Rajagopalan, *Adv. Enzymol.* **1991**, *64*, 215
22. K. V. Rajagopalan, J. L. Johnson, *J. Biol. Chem.* **1992**, *267*, 10199
23. G. N. George, C. M. Colangelo, J. Dong, R. A. Scott, S. V. Khangulov, V. N. Gladyshev, T. C. Stadtman, *J. Am. Chem. Soc.* **1998**, *120*, 1267
24. A. Kletzin, S. Mukund, T. L. Kelley-Crouse, M. K. Chan, D. C. Rees, M. W. W. Adams, *J. Bacteriol.* **1995**, *177*, 4817
25. I. Yamamoto, M. Wada, T. Ujiye, M. Tachibana, M. Matsuzaki, S yamazaki, *Biosci. Biotechnol. Biochem.* **1995**, *59*, 1850
26. M. J. Barber, H. van Valkenburgh, A. Trimboli, V. V. Pollock, P. J. Neame, N. R. Bastian, *Arch. Biochem. Biophys.* **1995**, *320*, 266
27. J. C. Hilton, K. V. Rajagopalan, *Biochim. Biophys. Acta*, **1996**, *1294*, 111
28. R. H. Scott, G. T. Sperl, J. A. DeMoss, *J. Bacteriol.* **1979**, *137*, 719
29. Y. M. Heimer, J. L. Wray, P. Filner, *Plant Physiol.* **1969**, *44*, 1197
30. C. Chauret, R. Knowles, *Can. J. Microbiol.* **1991**, *37*, 744

31. R. K. Thauer, *FEBS Lett.* **1972**, *27*, 111
32. M. Jormakka, S. Tornroth, B. Byrne, S. Iwata, *Science*, **2002**, *295*, 1863
33. A. Vorholt, R. K. Thauer, *Met. Ions in Biol.* **2002**, *39*, 571
34. T. Reda, C. M. Plugge, N. J. Abram, J. Hirst, *Proc. Natl. Acad. Sci.* **2008**, *105*, 10654
35. S. Groysman, R. H. Holm, *Inorg. Chem.* **2007**, *46*, 4090
36. A. L. Tenderholt, K. O. Hodgson, B. Hedman, R. H. Holm, E. I. Solomon, *Inorg. Chem.* **2012**, *51*, 3436
37. B. S. Lim, J. P. Donahue, R. H. Holm, *Inorg. Chem.* **2000**, *39*, 263
38. K. M. Sung, R. H. Holm, *J. Am. Chem. Soc.* **2002**, *124*, 4312
39. K. M. Sung, R. H. Holm, *J. Am. Chem. Soc.* **2001**, *123*, 1931
40. A. L. Tenderholt, R. K. Szilagyi, R. H. Holm, K. O. Hodgson, B. Hedman, E. I. Solomon, *J. Inorg. Biochem.* **2007**, *101*, 1594
41. W. R. McNamara, Z. Han, C. J. Yin, W. W. Brennessel, P. L. Holland, R. Eisenberg, *Proc. Natl. Acad. Sci.* **2012**, *109*, 15594
42. S. Kaur-Ghumaan, L. Schwartz, R. Lomoth, M. Stein, S. Ott, *Angew. Chem. Int. Ed.* **2010**, *49*, 8033
43. J. A. McCleverty, *Prog. Inorg. Chem.* **1968**, *10*, 49
44. R. H. Holm, M. J. O'Connor, *Prog. Inorg. Chem.* **1971**, *14*, 241
45. E. I. Stiefel, *Prog. Inorg. Chem.* **2004**, 52
46. D. V. Fomitchev, B. S. Lim, R. H. Holm, *Inorg. Chem.* **2001**, *40*, 645
47. F. H. Allen, *Acta Crystallogr. B*, **2002**, *58*, 380
48. S. Boyde, C. D. Garner, J. A. Joule, D. J. Rowe, *J. Chem. Soc. Chem. Commun.* **1987**, 800
49. C. A. Goddard, R. H. Holm, *Inorg. Chem.* **1999**, *38*, 5389
50. E. R. Brown, R. F. Large, *In Physical Methods of Chemistry Vol. 1*, Wiley Interscience, New York, **1971**
51. D. L. Hughes, M. Y. Mohammed, C. J. Pickett, *J. Chem. Soc. Chem. Commun.* **1988**, 1481
52. G. C. Tucci, J. P. Donahue, R. H. Holm, *Inorg. Chem.* **1998**, *37*, 1602
53. F. A. Cotton, C. S. Kraihanzel, *J. Am. Chem. Soc.*, **1962**, *84*, 4432
54. *Advanced Inorganic Chemistry 5th Ed.*, F. A. Cotton, G. Wilkinson, Wiley, **1988**, p 1036
55. M. L. Helm, M. P. Stewart, R. M. Bullock, M. R. DuBois, D. L. DuBois, *Science*, **2011**, *333*, 863
56. G. A. N. Felton, R. S. Glass, D. L. Lichtenberger, D. H. Evans, *Inorg. Chem.* **2006**, *45*, 9181

Chapter 5

(Photo)electrosynthesis of ammonia

5.1 Introduction

5.1.1 Biological nitrogen fixation

Nature uses nitrogenases to convert atmospheric nitrogen to ammonia.¹ These enzymes are responsible for all biologically fixed nitrogen.² The discovery that natural systems have the capability to biologically fix nitrogen was initiated by German scientist Hermann Hellriegel, in collaboration with Hermann Wilfarth, who together recognised that the legume root nodules were responsible for the conversion of atmospheric nitrogen to ammonia.³ The organisms inside the nodule were thought by some to be vibrio-like or bacteria-like organisms, but others were of the opinion that they were fungi. The microorganisms were first isolated and cultured from nodules of a number of different legume species by Martinus Beijerinck, the Dutch microbiologist.^{4, 5}

There are now three known types of nitrogenases, which are distinguished by the metal composition of their active site metalloclusters and therefore known as the [MoFe]-, [VFe]- and the [Fe only]-nitrogenase.⁶ The most widely researched is the molybdenum dependent enzyme, the [FeMo]-nitrogenase.⁷ Although all three types have similar activity, the Mo based nitrogenase is the most common, with the other two enzymes only produced under molybdenum deficient conditions.⁸ The structure of

the [FeMo]-nitrogenase enzyme consists of two separate protein clusters, denoted the MoFe and Fe proteins. The Fe protein is comprised of a [4Fe-4S] cluster which supplies electrons one at a time to the MoFe protein. The MoFe protein contains the active site: the multimetallic FeMo-cofactor which consists of seven iron atoms and one molybdenum atom bridged by nine sulfur atoms, and an auxiliary ‘P’ cluster which most probably mediates electron transfer from the Fe protein to FeMo-co.⁹ Refined crystal data of FeMo-co revealed the existence of a central atom within the iron sulfur cluster¹⁰ and latest data indicates this is a carbon atom, Figure 1.^{11,12}

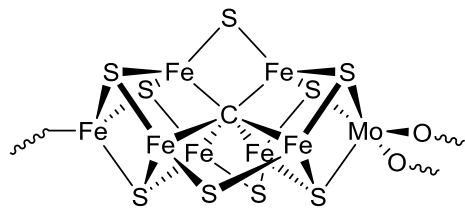


Figure 1 Structure of FeMo cofactor in nitrogenase.^{11,12}

The importance of the presence of this carbon atom on the catalysis of dinitrogen reduction has been investigated by Peters and co-workers using an iron complex containing a tris(phosphino)alkyl ligand which features an iron-carbon interaction, Figure 2.¹³

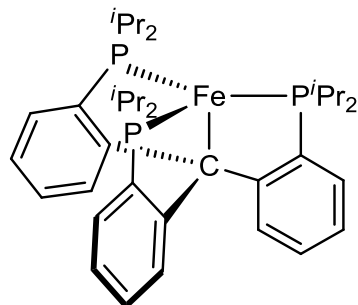


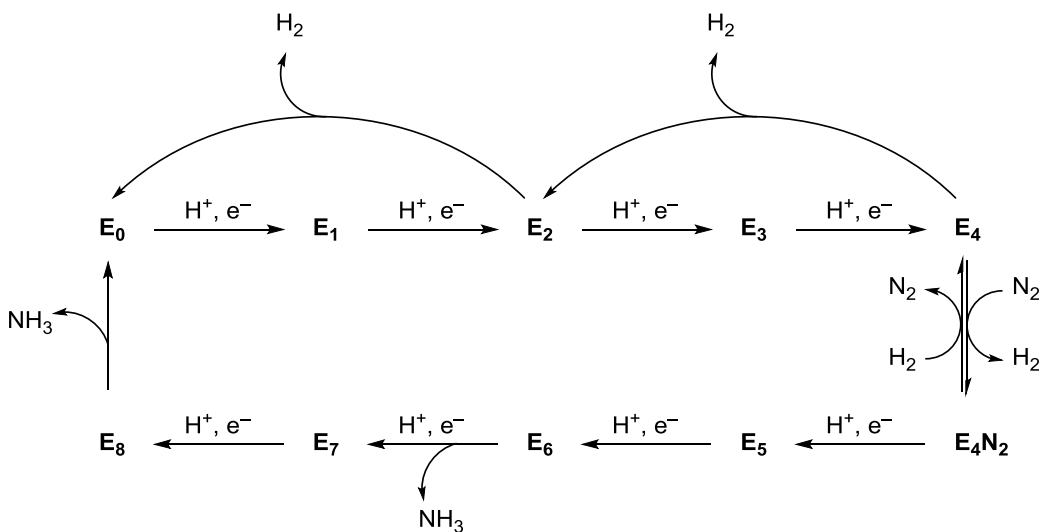
Figure 2 Structure of iron tris(phosphino)alkyl complex.¹³

It is established that the iron center in this arrangement binds dinitrogen trans to the alkyl carbon anchor in three oxidation states. Fe-C bond lengthening is observed upon reduction, reflective of significant ionic character in the Fe-C interaction. This decrease in the covalency of the Fe-C interaction is confirmed by spectroscopic and computational studies and is suggested to support a hypothesis wherein modulation of a belt Fe-C interaction in FeMo-co facilitates substrate binding and reduction.¹⁴

5.1.2 Lowe-Thorneley (LT) model

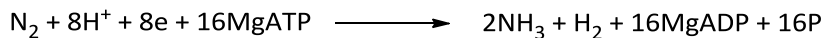
The Lowe and Thorneley kinetic model for nitrogenase catalysis was developed in the early to mid 1980s, and describes kinetics related to the cyclic turnover of molecular nitrogen (dinitrogen) to ammonia. It has been of great value in accounting for many aspects of nitrogenase catalysis and provides a model for predicting new catalytic behaviour. Since the original publication, new results have been successfully incorporated into the model.

The model was originally based on pre-steady state kinetics of the *Klebsiella pneumonia* enzyme using stopped-flow spectrophotometry and rapid-quench EPR spectroscopy,¹⁵ but has evolved over years of study, Scheme 1.¹⁶



Scheme 1 Simplified Lowe-Thorneley mechanism (E_n = state, no. of protons and electrons).¹⁶

The mechanism illustrates that multiple rounds of electron transfer and protonation are necessary for the reduction of dinitrogen to ammonia, with the overall stoichiometry shown by Equation 5.1.



(Equation 5.1)

The enzymatic reaction is therefore expensive, as two MgATP are required to be hydrolysed for each reducing equivalent. Interestingly, the fact that eight electrons are needed to reduce one mole of dinitrogen to two moles of ammonia and not six is

because two electrons are apparently ‘wasted’ through the evolution of one mole of dihydrogen.

The Lowe-Thorneley mechanism is formulated in terms of states, denoted E_n , that are indexed by the number of electrons and protons, n , that have been delivered to the MoFe protein: E_0 (resting state) up to E_8 . Notably, the iron protein delivers one electron at a time to the MoFe protein, as the adjacent [4Fe-4S] cluster cycles between 1+ and 2+ oxidation states, driven by the binding and hydrolysis of two molecules of MgATP within the iron protein.⁹ The release of MgADP from the iron protein, after delivery of the electron, is the rate-limiting step of catalysis.¹⁷

Two avenues of research have arisen from these early studies: analysis of structurally related transition metal analogues delineated by Chatt and Schrock, and enzyme studies undertaken by Hoffman and Seefeldt.

5.1.3 Studies of the site of dinitrogen binding within FeMo-co

The FeMo-cofactor is accepted to be the site of nitrogen binding, but at which metal(s) remained ambiguous throughout many years of research.

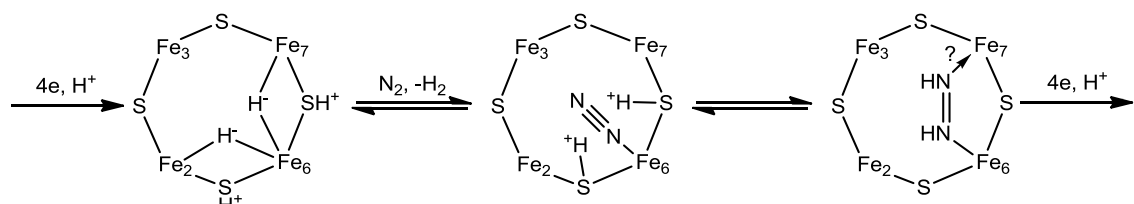
Early work on chemical analysis of structurally related complexes of molybdenum and tungsten detailed by Chatt¹⁸ and Schrock¹⁹ was suggestive that the homocitrate group within FeMo-co was the reaction site. Chemical evidence was deemed strong enough that Schrock stated “the conclusion that reduction (of N₂) takes place at a single Mo centre through intermediates of the type originally proposed by Chatt and his group²⁰ seems inescapable”.²¹

These chemical studies have been challenged and now overtaken by studies of the enzyme itself. The consensus is that iron atoms are the primary site of dinitrogen binding and fixation, and molybdenum plays an electronic or structural role in this multi-electron, multi-proton process.²²

5.1.4 Obligatory dihydrogen evolution and suggested mechanism

Equation 5.1 shows that, during a single catalytic cycle of the nitrogenase, one mole of molecular hydrogen (dihydrogen) is evolved as a by-product to the production of two moles of ammonia from one mole of dinitrogen. This obligatory dihydrogen evolution is now deemed crucial to the action of the enzyme and recent studies in this area show that this is related to the formation of metal hydrides.

When evaluated with respect to the Lowe-Thorneley model, Scheme 1, hydrogen is evolved in the absence of dinitrogen at the E_2 level. In the presence of dinitrogen, electrons are directed towards ammonia production upon achieving the E_4 state and dihydrogen is released in parallel with dinitrogen binding. Direct spectroscopic evidence for hydride formation has been provided by detailed EPR and ENDOR (electron nuclear double resonance) studies. A mechanism has been proposed whereby reductive elimination of hydrides at adjacent iron atoms leaves a vacant site for N_2 binding. Dinitrogen is hydrogenated in the course of binding to generate a metal-bound diazene intermediate, Scheme 2.²³



Scheme 2 Proposed reductive elimination mechanism for N_2 binding at the E_4 stage of the LT cycle.²³

The mechanism is then suggested to proceed via a hydrazine intermediate on route to formation of ammonia.²⁴

A bimetallic iron complex has been synthesised to structurally resemble a portion (Fe_2 and Fe_6 , or Fe_6 and Fe_7 in Scheme 2) of FeMo-co, Figure 3.²⁵

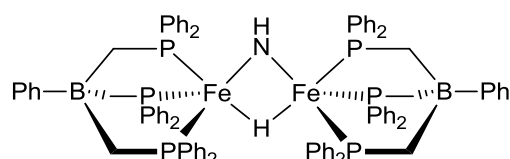


Figure 3 Mixed-valence bridging hydride model for the binding of hydride by FeMo-co.²⁵

It is argued that the structural and electronic properties of this complex support the proposal that FeMo-co contains two [Fe- μ -H-Fe] fragments at the **E₄** stage of the LT model. This further reinforces the need for obligatory hydrogen evolution to enable dinitrogen to bind.

5.1.5 Studies of synthetic systems related to nitrogenase activity

Whether the biological process is iron or molybdenum chemistry, there is still much interest in underpinning the chemistry of dinitrogen bound to one or more transition metals at synthetic sites, such as the work of Schrock along with the Chatt group and successors which is discussed in detail below. This is driven by the need to find alternatives to the high temperature, high pressure Haber process, which also has a considerable CO₂ burden: dihydrogen required in this industrial process is obtained from methane and water; Chapter 1, Scheme 1.

Chatt pioneered research at the Nitrogen fixation Laboratory, University of Sussex, studying binding of dinitrogen to metal bis-diphosphine complexes. Using coordination complexes *cis*-[M(N₂)₂(PMe₂Ph)₄] or *trans*-[M(N₂)₂(PMePh₂)₄] (M = Mo or W), it was his group who first demonstrated the conversion of a dinitrogen ligand into ammonia.²⁶ This work provided some of the first molecular models for nitrogen fixation.²⁷ Over many years of research into the chemistry of molecular nitrogen bound in a linear fashion end on to a transition metal and the study of reactions in compounds of molybdenum or tungsten surrounded by four tertiary phosphine ligands, the Chatt cycle was proposed. Although the cycle is based on nitrogen fixation in a decidedly abiological coordination environment, it provides chemical precedence for reactions that could reasonably take place at Mo (or V or Fe) in a nitrogenase enzyme.

Schrock has been interested in the binding of dinitrogen and partially reduced dinitrogen ligands to one or more transition metal centres since 1980.²⁸ The group focusses on the use of heavier early transition metals, with early studies based upon the synthesis of tantalum imido complexes.²⁹ More recently, molybdenum and tungsten complexes in higher oxidation states have been utilised, particularly half

sandwich compounds featuring a cyclopentadiene ligand. The binding of partially reduced dinitrogen ligands was first examined and hydrazine was reported to bind to the complex $[\text{Cp}^*\text{WMe}_4]^-$.³⁰ The N-N bond was able to be cleaved when one of the methyl ligands was substituted with triflate.^{31, 32} For the past 20 years, the focus of the group switched to the use of molybdenum and tungsten complexes ligated by a new structure, the triamidoamine ligand.³³ Nitrogen fixation catalysts based upon these types of complexes are discussed below.

5.1.6 Background chemistry of Mo and W tertiary phosphine systems

Mo and W tertiary phosphine systems have proved extremely useful in providing mechanistic insights into the possible workings of the nitrogenase. These $[\text{MP}_4]$ systems can adapt to the electronic demands of dinitrogen and support $[\text{N}_x\text{H}_y]$ ($x = 2, y = 1-4; x = 1, y = 0-3$) intermediates on the pathway to ammonia. This remarkable behaviour is attributed to the capability of the ‘soft’ tertiary phosphines in adjusting their relative electron donation properties across Mo or W oxidation states from 0 to +4.

5.1.6.1 Synthesis of dinitrogen complexes

Dinitrogen complexes of the general type *cis*- or *trans*- $[\text{M}(\text{tertiary phosphine})_4(\text{N}_2)_2]$ and *trans*- $[\text{M}(\text{tertiary diphosphine})_2(\text{N}_2)_2]$, where the tertiary phosphines are monodentate or bidentate, have played a key role in research into nitrogen fixation. This is because the molecular nitrogen in these electron rich systems is activated towards protic attack. The mono-tertiary phosphine complexes react with acid to give high yields of ammonia with destruction of the $[\text{MP}_4]$ core, with the six electrons required to give ammonia from one of the dinitrogen ligands coming from the M^0 metal. The bis(ditertiary)phosphine complexes do not give ammonia on protonation, but have provided structural information on partially reduced intermediates.^{18, 34-36} Examples of complexes with monotertiary phosphines are *cis*- $[\text{M}(\text{N}_2)_2(\text{PMe}_3)_4]$ and *cis*- $[\text{M}(\text{N}_2)_2(\text{PMe}_2\text{Ph})_4]$ ($\text{M} = \text{Mo}$ or W),^{37, 38} examples of di-tertiary phosphine dinitrogen

complexes are *trans*-[M(N₂)₂(dmpe)₂] [dmpe = 1,2-bis(dimethylphosphino)ethane; M = Mo³⁹ or Fe⁴⁰

The general route for the synthesis of dinitrogen complexes involves reduction of high-valent $[MoCl_5]$ or $[WCl_6]$ precursors by Mg or Na(Hg) in THF, under an atmosphere of dinitrogen, in the presence of the appropriate mono- or bi-dentate phosphine ligands.^{41, 42}

Electrochemical synthesis from M^{II} or M^{IV} precursors is possible at relatively modest potentials when compared to chemical synthesis, which requires reduction with magnesium (Mg^{2+}/Mg^+ -2.5 V vs Ag/AgCl). For example, reduction of a Mo^{IV} oxo species in protic media affords dinitrogen complexes at *ca* -1.2 V vs Ag/AgCl.⁴³

5.1.6.2 Manner of dinitrogen bonding

The N-N bond length has been used to characterise the extent of activation of coordinated dinitrogen, and thus the manner of the bonding between the metal and the dinitrogen ligand. Therefore, the determination of bond lengths by X-ray crystallography has been of vital importance. As dinitrogen binding is similar to that of CO, the degree of activation of coordinated dinitrogen is, in essence, controlled by the magnitude of back-bonding of electron density into the π^* orbitals of the dinitrogen moiety. This is because an increase in backbonding results in weakening of the N-N bond. Measurement of the bond length will show elongation when compared to free N_2 as a result of the increased antibonding electron density. The bonding can then be described by one of the following bonding modes in Figure 4.⁴⁴



Figure 4 Dinitrogen ligand binding modes.⁴⁴

The majority of dinitrogen compounds contain a dinitrogen moiety that is not significantly elongated from free N₂, and the dinitrogen can be considered only weakly activated. Consequently, the N-N bond length is typically less than 1.12 Å⁴⁴ and therefore the coordinated N₂ is best described as formally neutral. Although little

activation occurs in terms of the formal reduction of N₂, in some cases the dinitrogen will undergo protonation.

5.1.6.3 Protonation of coordinated dinitrogen

The addition of acids to molybdenum and tungsten dinitrogen compounds eventually yielded stable diazenido- and hydrazido- complexes.^{45, 46} Generally, the treatment of mononuclear bis(dinitrogen) complexes with acids resulted in evolution of dinitrogen, often together with dihydrogen. Alternatively, the protonation could lead to the formation of a metal hydride complex without dinitrogen loss. For example, when *trans*-[W(N₂)₂(dppe)₂] [dppe = 1,2-bis(diphenylphosphino)ethane] was treated with 2 molar equivalents of HCl in THF, it underwent protonation at the metal and retained both ligating dinitrogen molecules to form the salt [WH(N₂)₂(dppe)₂]HCl₂, Equation 5.2.⁴⁷



(Equation 5.2)

After the concentration of acid was increased to over five molar equivalents of HCl, one of the dinitrogen ligands was protonated and reduced to give an associated hydrazide, Equation 5.3.



(Equation 5.3)

The corresponding molybdenum bis(dinitrogen) complex performed an analogous reaction with HBr, but not with HCl as this displaced all the dinitrogen from the molybdenum complex.

In all of these reactions, loss of one molecule of dinitrogen as N₂ occurs. However, dinitrogen loss is not a prerequisite for formation of a hydrazido- complex. The complex *trans*-[W(N₂)(MeCN)(dppe)₂] reacts with a sulfuric acid proton source to give *trans*-[W(N₂H₂)(MeCN)(dppe)₂][HSO₄] without ligand loss.⁴⁸

The bonding manner of six-coordinate complexes of the type $[WCl(N_2H_2)(dppe)_2]^+$ have not only been characterised by NMR and IR, but also verified by X-ray crystallography. The structure of *trans*- $[WCl(N_2H_2)(dppe)_2][BPh_4]$ showed that the M-N-N unit is in essence linear, and the N-N bond distance indicated a bond order rather greater than a single bond. The short W-N distance confirmed the expected essentially triple bond character, Figure 5.⁴⁹

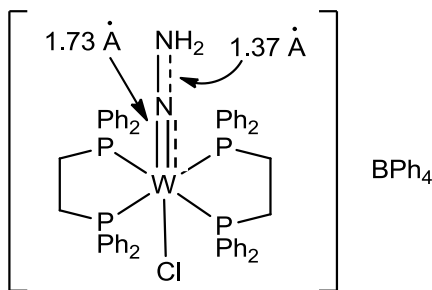


Figure 5 Structure of $[W(NNH_2)Cl(dppe)_2][BPh_4]$.⁴⁹

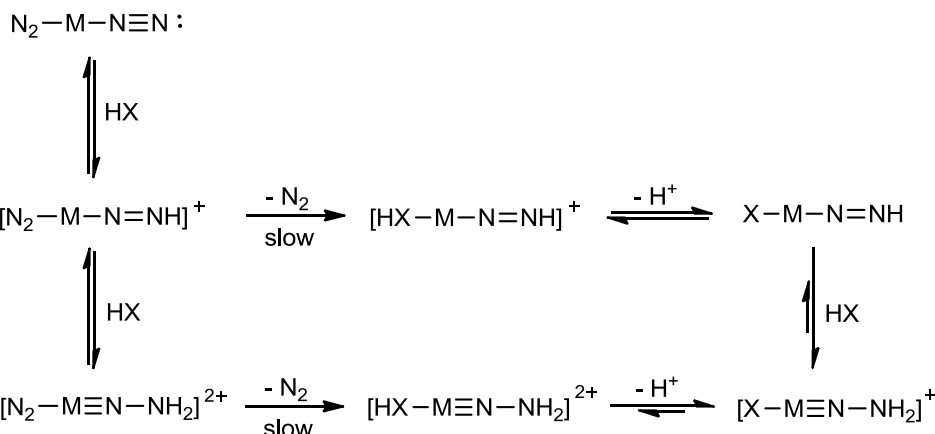
The bonding of metal hydrazido- compounds has been studied by computational methods, with the theoretical results based on 118 X-ray characterised complexes, including those of the type $[MX(N_2H_2)P_4]$ ($M = Mo/W$) used in this Chapter.⁵⁰ Results show that although the hydrazide ligand is generally described as being $[NNH_2]^{2-}$, the oxidation state is often closer to 1- in early transition metal complexes. The occupied hydrazido- π_{NN} orbital, which does not significantly interact with the metal, is largely responsible for the considerable double bond character of the N-N bond. Triple bond character is lost by partial occupation of the π_{NN}^* level. If the assumption is made that the hydrazido- ligand adopts the formal 2- charge, the ligand is a four-electron donor when coordinated linearly, which is the most common arrangement.

5.1.6.4 Kinetics of protonation

Kinetic and mechanistic studies for the majority of these protonations have been undertaken using stopped-flow UV spectrophotometry.^{51, 52}

The proposed mechanism of protonation of coordinated dinitrogen in these types of complexes involves the initial rapid formation of an adduct between the acid source and the ligated dinitrogen substrate. This is followed by protonation of the dinitrogen

by another molecule of acid, prior to the rate-limiting dissociation of the dinitrogen spectator ligand, Scheme 3.⁵¹



Scheme 3 Mechanism of protonation of coordinated dinitrogen.⁵¹

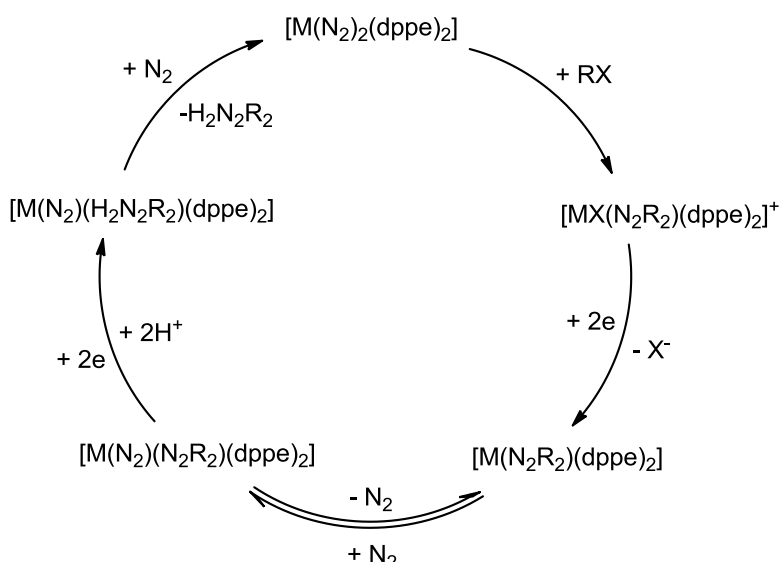
This model is complicated by some reaction conditions, for example, when HCl is used as the acid source, hydrido complexes can be formed. Some molybdenum metal analogues of these types of complexes undergo total loss of dinitrogen ligands to form compounds such as $[\text{MoH}_2\text{Cl}_2(\text{depe})_2]$ [$\text{depe} = 1,2\text{-bis}(\text{diethylphosphino})\text{ethane}$] upon addition of HCl.⁵²

5.1.6.5 Tetrakis monotertiary phosphine dinitrogen complexes: formation of ammonia

The first example of protonation of ligated dinitrogen and reduction to ammonia at a single metal site was described by Chatt and co-workers.^{18, 35} Complexes of the type *cis*- $[\text{M}(\text{N}_2)_2(\text{PR}_3)_4]$ and *trans*- $[\text{M}(\text{N}_2)_2(\text{PR}_3)_4]$ ($\text{M} = \text{Mo}$ or W , $\text{R} = \text{alkyl}$ or aryl) with H_2SO_4 in methanol at 20°C gave ammonia (1.9 NH_3 per W and *ca* 0.7 NH_3 per Mo). It was also found that 1.6 equivalents of ammonia per tungsten atom could be released from *cis*- $[\text{W}(\text{N}_2)_2(\text{PMe}_2\text{Ph})_4]$ when refluxed or irradiated at 20°C in methanol alone. As far as the natural system was concerned, these results showed that molecular nitrogen can be reduced at a single metal centre in a protic medium with negligible evolution of hydrogen or replacement of dinitrogen by hydride ligands. Until this discovery, the most commonly proposed mechanisms of nitrogen fixation involved dimetallic centres.^{53, 54}

5.1.6.6 Bis(ditertiary)phosphine complexes: formation of diazenides and hydrazides and related organohydrazides

The realisation of a catalytic cycle for dinitrogen fixation started to become apparent when electrochemical reduction of dialkylhydrazido-complex, *trans*- $[\text{MoBr}(\text{N}_2\text{R}_2)(\text{dppe})_2]^+$, in the presence of dinitrogen and a proton source gave dialkylhydrazine and the molybdenum dinitrogen complex.⁵⁵ Before this, organo-nitrogen compounds could only be formed with destruction of the metal complex.⁵⁶ From this work, it was concluded that a hydrazido complex could be electrochemically reduced in the presence of dinitrogen and protons to release an organo-nitrogen compound. A metal-dinitrogen complex was also generated, which could be chemically reconverted back to a hydrazido complex, providing a cyclic stepwise pathway, Scheme 4.⁵⁵

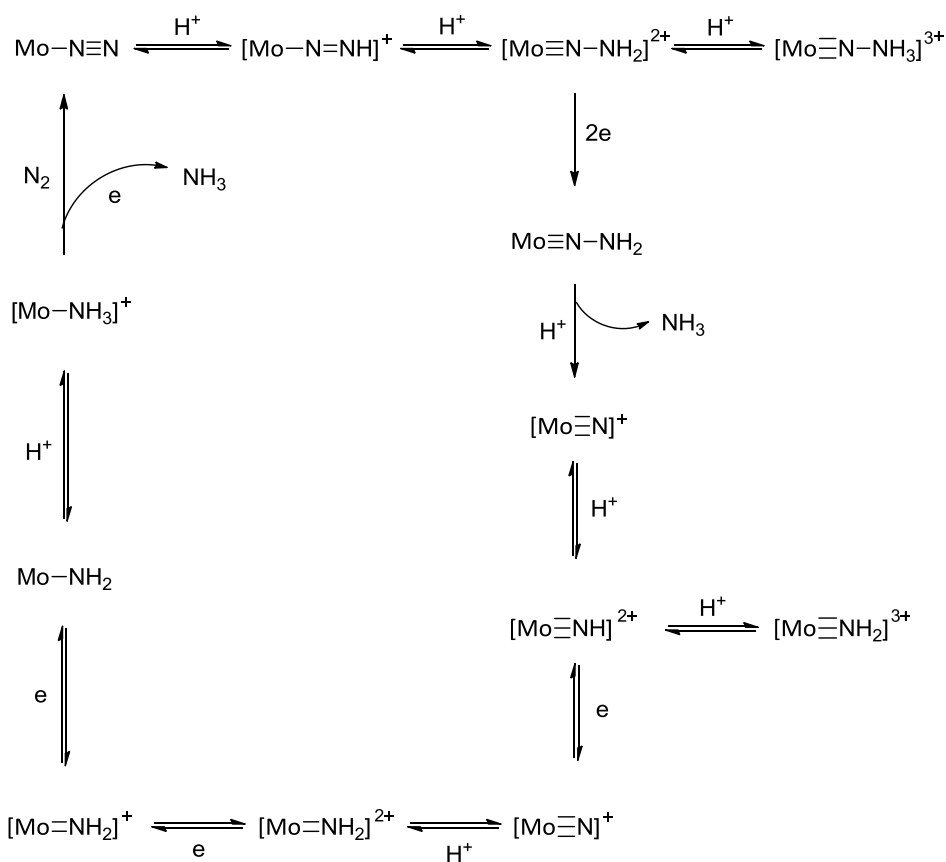


$\text{M} = \text{Mo or W}; \text{dppe} = \text{R}'_2\text{PCH}_2\text{CH}_2\text{PR}'_2; \text{R}' = \text{alkyl or aryl}; \text{R} = \text{alkyl}; \text{X} = \text{Br or I}$

Scheme 4 Cycle for the production of dialkylhydrazide compounds from dinitrogen complexes.⁵⁵

5.1.7 The updated Chatt cycle

The Chatt cycle was updated by Pickett in 1996 to include new information on electron and proton transfer pathways of hydrazides, imides and related organo-N species, Scheme 5.⁵⁷

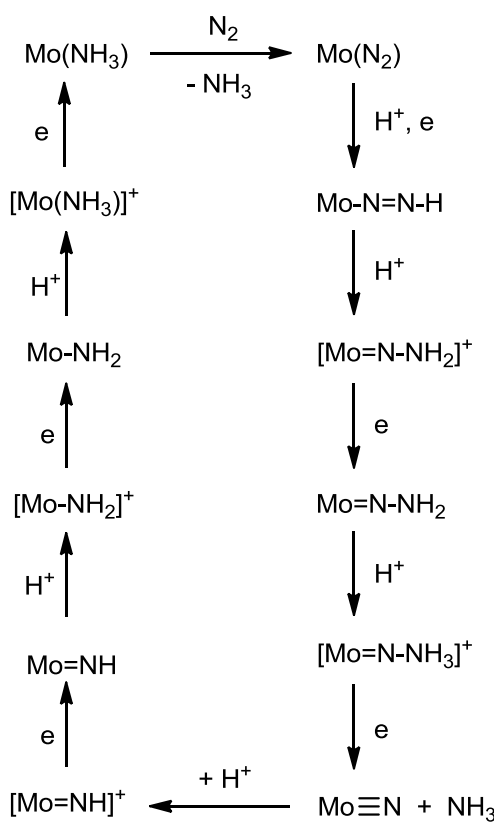


Scheme 5 The modified Chatt cycle.

Throughout the cycle, the molybdenum metal centre retains a closed shell, 18 electron diamagnetic configuration, with the formal oxidation state ranging over four units of charge (Mo^0 to Mo^{IV}).

5.1.8 Related Schrock Chemistry

A catalytic cycle for the protonation and reduction of dinitrogen to ammonia has also been derived by Schrock, which is similar to the Chatt counterpart. The exception is that this cycle operates at different oxidation states, Mo^{II} to Mo^{VI}, Scheme 6.⁵⁸



Scheme 6 Schrock cycle showing proposed intermediates in the reduction of dinitrogen through stepwise additions of protons and electrons.

This was achieved by studying the reactions of a complex comprised of molybdenum coordinated by a triamidoamine ligand, Figure 6.⁵⁹

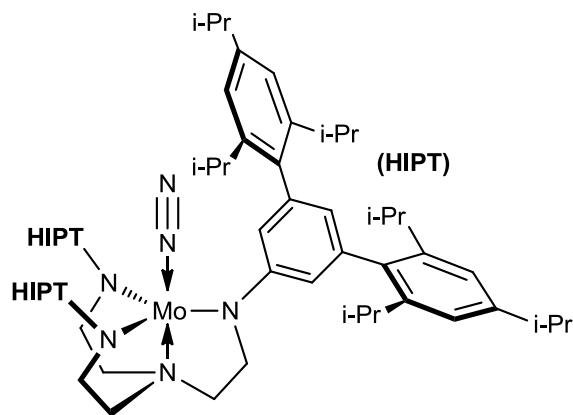


Figure 6 Structure of Schrock catalyst.⁵⁹

While Schrock succeeded in stabilising and structurally characterising several of the presumed intermediates, a precise energetic profile of the reaction was not determined by experimental means. The use of contemporary theoretical methods, in particular those based on density functional theory (DFT), has provided important new

insights. The energy profile of the Schrock cycle derived from DFT calculations pinpoints two stages in the ammonia forming reaction where this negative redox potential is essential: these being the first protonation of coordinated N₂, and the final reduction of the NH₃ complex. According to the theoretical results, the first protonation is the most difficult step of the whole process, so the binding of N₂ to the Mo complex is critical to the conversion taking place.

5.1.9 Cyclic and catalytic systems

5.1.9.1 Schrock chemistry

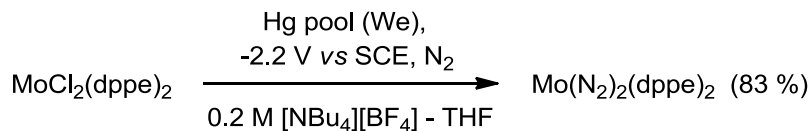
Molybdenum and tungsten complexes containing the triamidoamine ligand, of the type shown in Figure 6, are very sterically hindering, so much so that the metal centre sits in a deep enough cavity that dimerisation of the type [(RN₃N)M-N=N-M(RN₃N)] is no longer possible; preventing this increases the catalytic activity.³³ With the Mo-centred compound, up to 8 equivalents of ammonia are catalytically produced from one equivalent of the Mo compound in the presence of lutidinium as a proton source. This amounts to a yield of *ca* 65 % based on the number of molecules of strong reducing agent, decamethylchromocene ($E_0 = -1.5$ V *versus* the ferrocene/ferrocenium (Fc/Fc⁺) couple), present. More recently with modification of the Schrock chemistry, a system which yielded 23 moles of ammonia per mole of catalyst was achieved; *ca* 12 turnovers based upon dinitrogen, Chapter 1, Section 1.3.3.

In another adaption of the Schrock catalyst, catalytic reduction of dinitrogen to ammonia has been achieved at a similarly well-protected single iron site, [(TPB)Fe(N₂)]⁺ where TPB = tris(isopropylphosphino)borane.⁶⁰ Chemical catalysis of the complex in the presence of dinitrogen, excess [HBAr₄^F·2Et₂O] and strong reductant, [KC₈], at -78 °C gave 7 equivalents of ammonia per iron atom. This is a ten-fold increase in the yield of NH₃ over the analogous complex where the boron atom is replaced by silicon in the phosphine ligand and thus attributed to the increased flexibility of the Fe-B bond.

5.1.9.2 Electrosynthesis of ammonia via tungsten hydrazides

Since Chatt and co-workers reported dinitrogen complexes of the type *cis*-[W(N₂)₂(PR₃)₄] (R = alkyl or aryl) gave ammonia, there had existed a possibility that a cyclic conversion of dinitrogen to ammonia might be achieved at room temperature and pressure *via* mediators possessing an [MP₄] core (M = Mo/W).

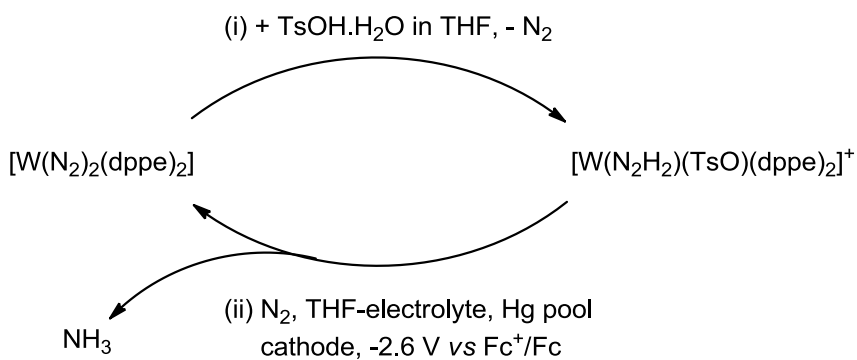
As previous ammonia production attempts by Chatt and co-workers led to degradation of the core by oxidation, coupling the protonation with electronation was hoped to avoid the problem. It was shown in detail that electrosynthesis of complexes such as *trans*-[W(N₂)₂(dppe)₂] from molecular nitrogen and robust precursors was possible in good yields (up to 89 %).⁶¹ For example, the production of *trans*-[W(N₂)₂(dppe)₂] from *trans*-[MoCl₂(dppe)₂] was achieved in a yield of 83 %.



(Equation 5.4)

This suggested that it may be possible to produce *trans*-[M(N₂)₂(dppe)₂] from a M^{IV}, [MX(N₂H₂)] species by reduction to M⁰, following the release of two molecules of NH₃.

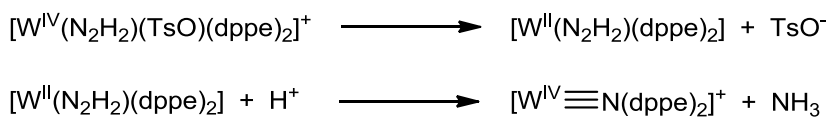
Electrosynthesis of ammonia was then achieved with the complex *trans*-[W(N₂H₂)(TsO)(dppe)₂][TsO·H₂O].⁶² Controlled potential electrolysis of the complex was carried out in a 0.2 M [Bu₄N][BF₄]-THF electrolyte, saturated with dinitrogen, at a mercury pool electrode cathode held at -2.6 V vs Fc⁺/Fc. The complex consumed two moles of electrons, producing 0.22-0.24 moles of ammonia and 0.01-0.02 moles of hydrazine per mole of complex in the process, Scheme 7. In addition, the parent dinitrogen complex, *trans*-[W(N₂)₂(dppe)₂] was generated in a good yield, with 0.85-0.95 molar equivalents produced based on the starting material.



Scheme 7 Basis for ammonia producing cycle.⁶²

Electrolysis on platinum electrodes gave substantially lower yields of the dinitrogen complex (0.6–0.7 molar equivalents compared to starting material).

The basic chemistry that occurs for the production of ammonia is shown below in Scheme 8, with the complex also acting as the proton source for the reaction.



Scheme 8 The reductive steps of ammonia formation involved cleavage of W-OTs bond.⁶²

The global stoichiometry of the reaction is actually much more complicated due to this internal acid supply: the theoretical yield of ammonia is actually 0.286 moles per mole of *trans*-[W(N₂H₂)(TsO)(dppe)₂]⁺. The chemistry leading to this stoichiometry will be discussed in detail later in the Chapter, Section 5.3.1.1.

5.1.10 Photofixation of ammonia

Photoelectrosynthesis of hydrogen and photoelectrochemical reduction of carbon dioxide using molecular or solid-state electrocatalysts have received much recent attention, as discussed in Chapter 3. Photoelectrosynthesis of ammonia has received much less attention and examples are confined to solid-state systems, mainly TiO₂.^{63–66} Irradiated tungsten oxide surfaces have been shown to produce ammonia from nitrogen and water at a rate of 0.2 μg h⁻¹.⁶⁷ Iron-modified titanium oxide surfaces improved photocatalytic activity of nitrogen reduction over unmodified TiO₂.⁶⁸

As far as we are aware, no systems based on molecular catalysts such as those delineated by Schrock or Chatt have been reported as photoelectrocatalysts.

5.2 Scope of this chapter

As discussed above and in Chapter 1, cyclic systems for converting dinitrogen to ammonia are rather limited in scope and are, at best, inefficient in terms of the turnovers that have been achieved. In this chapter, the focus has been on the *trans*- $[W(N_2H_2)(TsO)(dppe)_2]^+$ system. Earlier work showed that ammonia could be produced with regeneration of a dinitrogen complex and subsequent re-protonation allowed repetition of the ammonia producing process. In relation to these studies, this chapter describes:

- (i) Repetition of the original electrosynthesis of ammonia at a Hg electrode experiments to be used as a standard for comparison to the new approaches. Characterisation of the intermediates involved in the electrosynthesis of ammonia at inert electrodes was attempted by use of ^{31}P NMR and infrared spectroelectrochemistry.
- (ii) Approaches to take the system forward to give ammonia in a continuous cycle, rather than in the ‘interrupted’ stepwise fashion using a biphasic electrochemical setup involving an aqueous acid layer and a toluene electrolyte layer containing the complex.
- (iii) Exploring the possibility of driving the process at a lower potential by harvesting light energy at a p-type semiconductor with steps towards photoelectrosynthesis of ammonia explained.

5.3 Results and discussion

5.3.1 Electrosynthesis of ammonia

5.3.1.1 Electrosynthesis of ammonia at a Hg electrode

The study of the electrosynthesis of ammonia from *trans*-[W(N₂H₂)(TsO)(dppe)₂]⁺ (**A**) at a mercury electrode, as previously reported,⁶² was re-examined. This provides both additional information on mechanistic aspects and controls for comparisons with subsequent experiments including the photoelectrosynthesis of ammonia.

Exp No.	A / μmols ([A] / mM)	Moles electrons per mole A / F mol ⁻¹	Mol % NH ₃ per mole A / %	Mol % B per mole A / %
A1	44.85 (4.08)	2.16	22	83
A2	14.59 (1.22)	2.00	30	85

Table 1 Results of bulk electrosynthesis of ammonia from *trans*-[W(NNH₂)(TsO)(dppe)₂]⁺ in 0.2 M [Bu₄N][BF₄]-THF at a Hg pool electrode held at a potential of -1.9 V vs Ag/AgCl.

The bulk electrolysis results for the production of ammonia are shown in Table 1 and are consistent with the previous work. Thus, the overall process consumes *ca* 2 moles of electrons per mole of **A**, yields 22-30 mol % ammonia and gives 83-85 mol % of *trans*-[W(N₂)₂(dppe)₂] (**B**). Figure 7 shows a typical plot of cell current *vs* charge passed during the course of the electrolysis with a non-linear decay approaching 1.8-2 moles electrons per mole of complex.

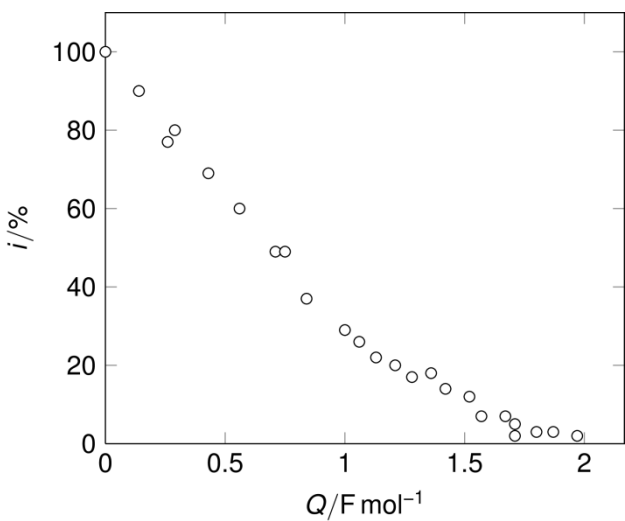
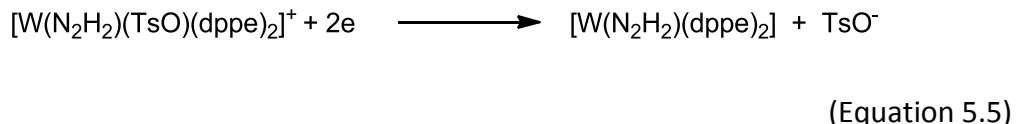


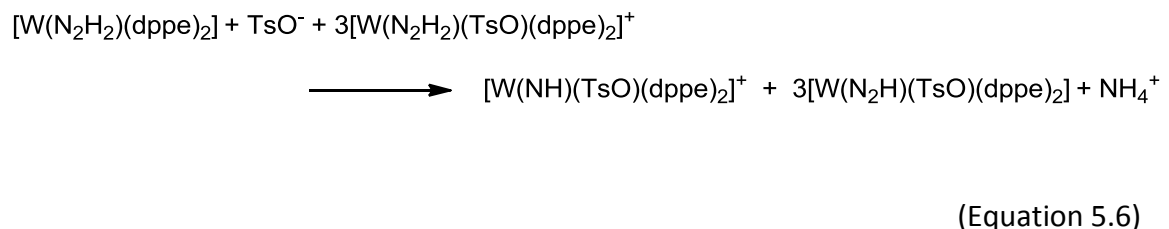
Figure 7 Current vs charge passed plot for the electrolysis of 2 mM *trans*-[W(N₂H₂)(TsO)(dppe)₂]⁺ (**A**) at a Hg electrode held at -2 V vs Ag/AgCl in 0.2 M [Bu₄N][BF₄].

5.3.1.2 Initial stage of electrolysis: ammonia forming phase

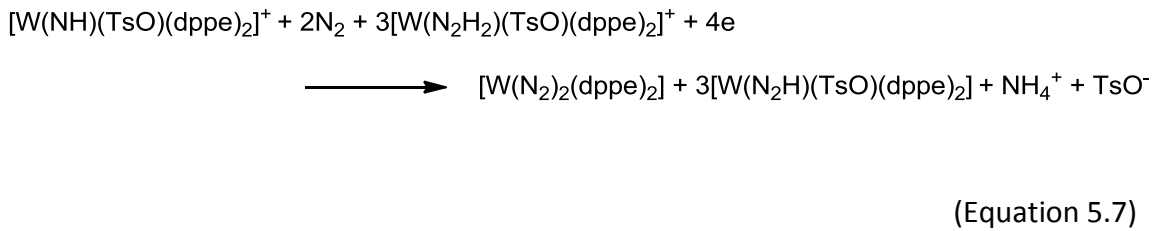
In earlier work, the yield of ammonia was rationalised on the basis of the parent hydrazide behaving as both the reducible species and the source of protons.⁶² The primary reduction of the hydrazide consisted of a two electron process leading to the formation of a reactive intermediate, the W^{II} hydrazide, [W(N₂H₂)(dppe)₂], an analogue of an isolable dialkyl hydrazide, Equation 5.5.⁶⁹



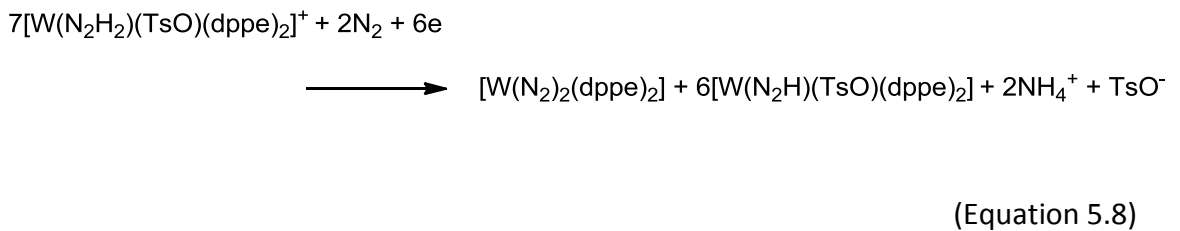
The dialkylhydrazide species, *trans*-[Mo(N₂R₂)(X)(dppe)₂]⁺ (X = Br or I), is known to react with acids with cleavage of the N-N bond to give a M^{IV} imide and an alkylammonium cation.⁶⁹ A similar reaction of the W^{II} hydrazide with the parent W^{IV} species would correspondingly give the ammonium cation and an imide, Equation 5.6.



Electrochemical reduction of a Mo or W imide has been shown to yield ammonia (ammonium) and a dinitrogen complex in the presence of an acid source. A similar fate would yield a second molecule of ammonium, Equation 5.7.



Thus, this overall chemistry can be summarised by the global Equation 5.8.



This can be directly associated with the ‘fast’ first stage of the electrolysis where the current rapidly decays for the following reasons.

Figure 8 shows the rate of consumption of **A** as a function of charge passed, as determined by monitoring the $^{31}\text{P}\{^1\text{H}\}$ NMR peak for this species at 36.5 ppm relative to 85% H_3PO_4 in the electrolyte.

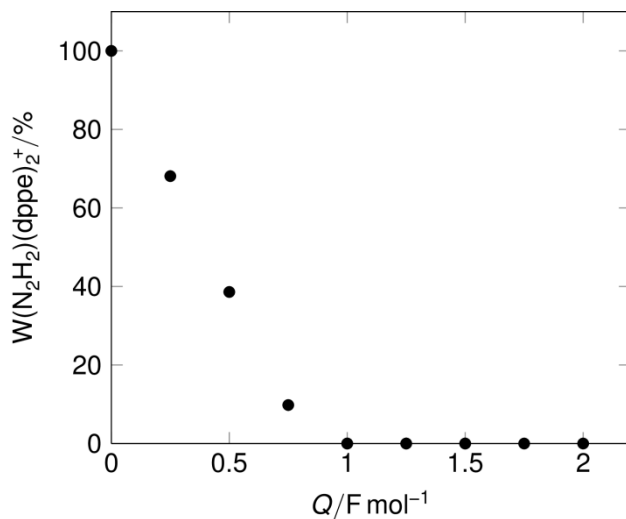


Figure 8 Plot showing the consumption of $[\text{W}(\text{N}_2\text{H}_2)(\text{TsO})(\text{dppe})_2]^+$ during electrolyses at a Hg electrode held at -2 V vs Ag/AgCl in 0.2 M $[\text{Bu}_4\text{N}][\text{BF}_4]$ with respect to the charge passed. The percentage is relative to the $^{31}\text{P}\{^1\text{H}\}$ peak height for the parent complex **A** at zero charged passed.

It is clear that **A** is essentially all consumed after the passage of just under one mole of electrons. This is consistent with the global Equation 5.8 which predicts depletion of the parent complex after the passage of 0.86 mole of electrons.

Figure 9 shows the rate of formation of ammonia, re-drawn from the original data.⁶²

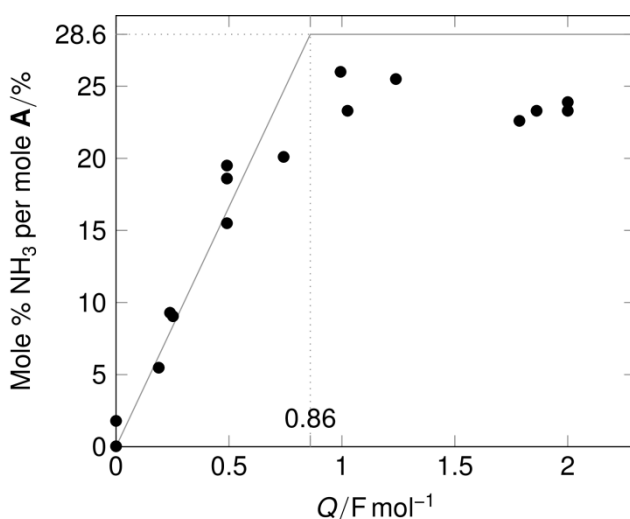


Figure 9 Plot showing the formation of ammonia during electrolyses at a Hg electrode held at -2 V vs Ag/AgCl in 0.2 M [Bu₄N][BF₄] with respect to the charge passed (Grey lines represent theoretical maximum ammonia yield).

Essentially all of the ammonia is released in the first phase of the electrolysis after the passage of *ca* 0.8-1.0 moles of electrons, again consistent with the stoichiometry of Equation 5.8. The predicted yield of ammonia is 28.6 mol % per mole of the parent hydrazide **A**, which is in reasonable agreement with the experimental values, 25 mol % NH₃ per mole **A**.

Finally, the yield of the dinitrogen complex, **B**, has been measured as a function of charge passed by monitoring the growth of the ³¹P{¹H} NMR peak for this species at 43.6 ppm relative to 85% H₃PO₄ in the electrolyte, Figure 10.

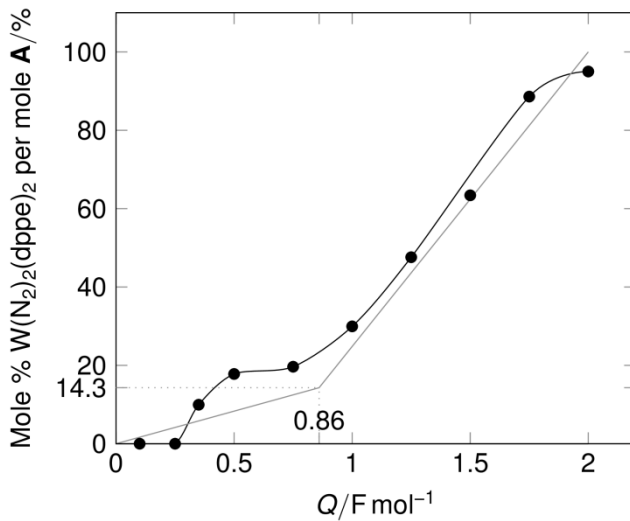
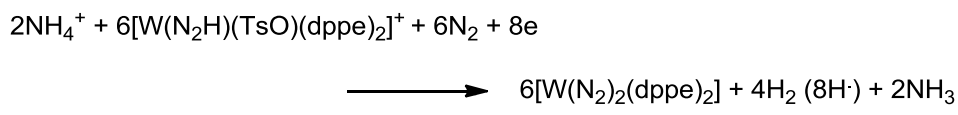


Figure 10 Plot showing the formation of *trans*-[W(N₂)₂(dppe)₂] during electrolyses at a Hg electrode held at -2 V vs Ag/AgCl in 0.2 M [Bu₄N][BF₄] with respect to the charge passed. The percentage is relative to the ³¹P{¹H} peak height for the parent complex **A** at zero charged passed (Grey lines represent theoretical maximum *trans*-[W(N₂)₂(dppe)₂] yield).

The formation of **B** is bi-phasic. In the early stage of electrolysis, up to the passage of *ca* 50 % of the total charge, about 20 mol % of the dinitrogen complex is produced; it is in the second half of the reduction that most of this complex is formed. The global Equation 5.8 predicts a 14.3 mol % yield of the dinitrogen complex after depletion of the parent **A**. The apparent lag in the formation of **B** might reasonably be attributed to the initial formation of an imide intermediate which is then reduced to further ammonia and the dinitrogen complex **B**. Combining Equations 5.6 and 5.7 gives a stoichiometry for imide formation of 0.5 electrons per molecule of the parent hydrazide, which corresponds to the end of the first phase of dinitrogen complex formation.

5.3.1.3 Second phase of electrolysis: detection of intermediates

In the first phase of electrolysis, it is evident that **A** provides protons for the ammonia forming chemistry, whilst the second phase leads to formation of **B** with a stoichiometry corresponding to Equation 5.9.



(Equation 5.9)

That the current decays non-linearly as a function of charge passed implies that one or more electroactive intermediates arising from deprotonation must build-up and decay during the course of electrolysis.

Figure 11 shows (i) the plot of the current *versus* charge passed during the course of electrolysis together with (ii) the predicted current component for **A** based on its concentration as determined by $^{31}\text{P}\{\text{H}\}$ NMR and the stoichiometry of Equation 5.8 and (iii) the net current which is attributable to the electroactive intermediate(s) which builds up and decays during the course of the electrolysis. Part of this current can be attributed to discharge of ammonium which is formed in the catholyte. In support of this, it was found that reduction of $[\text{NH}_4][\text{PF}_6]$ at a Hg electrode at -2.0 V *versus* Ag/AgCl under the same conditions as for the electrolysis of *trans*- $[\text{W}(\text{N}_2\text{H})(\text{TsO})(\text{dppe})_2]^+$ gave H_2 with a current efficiency of 37 %. Low yields of dihydrogen in a non-aqueous solvent is not uncommon at ‘inert’ electrodes where surface catalysis of the coupling of 2H^\cdot cannot take place. Hydrogen radicals formed by discharge of H^+ may attack solvent or the electrolyte rather than couple.

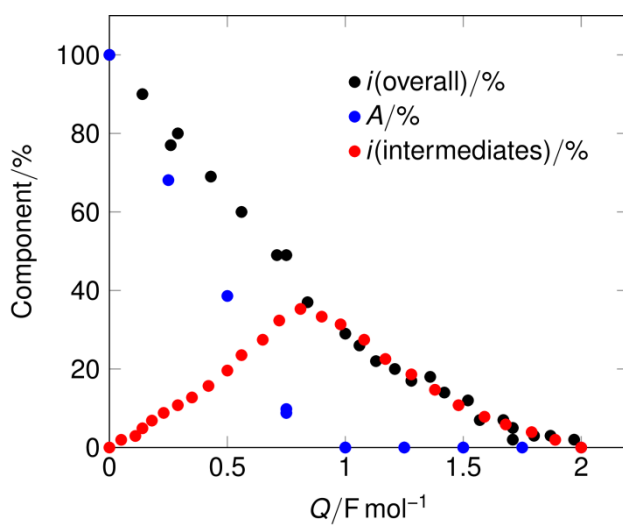
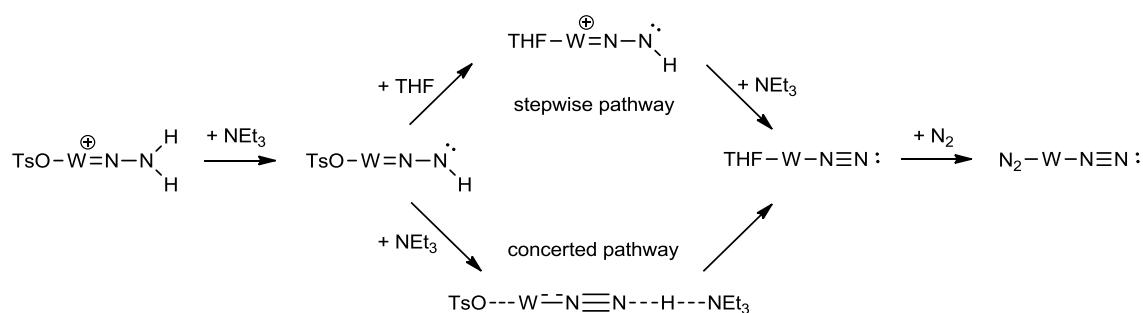


Figure 11 Plot showing the net contribution of the parent and intermediate species to the total current during the course of electrolysis at -2 V *vs* Ag/AgCl in 0.2 M $[\text{Bu}_4\text{N}][\text{BF}_4]$ with respect to the charge passed.

Deprotonation would be expected to afford the diazenide as represented in the global Equation 5.8. This species must be a precursor to **B** formed in the final phase of the electrolysis. Diazenido- complexes are difficult to directly reduce and at the potential of the electrolysis are likely to be electrochemically inactive.⁷⁰ Thus, a pathway to *trans*-[W(N₂)₂(dppe)₂] must involve other chemistry. Earlier kinetic studies have shown that deprotonation of **A** under molecular nitrogen can lead to the formation of **B** when it is treated with a base in THF, and that this proceeds by the mechanism shown in Scheme 9.71



Scheme 9 Mechanism for chemical deprotonation of *trans*-[W(N₂H₂)(TsO)(dppe)₂]⁺ by NEt₃ with proposed intermediates as measured by stopped-flow spectrophotometry (dppe ligands removed for clarity).⁷¹

Thus, loss of tosylate from the diazenide and replacement by THF would produce the intermediate, *trans*-[W(N₂H)(THF)(dppe)₂]⁺. This cationic species will have an acidic proton, which if removed by base or discharged by electrolysis would lead to the generation of the solvato- species *trans*-[W(N₂)(THF)(dppe)₂] and thence *trans*-[W(N₂)₂(dppe)₂]. During the course of electrolysis, ammonium is present in the electrolyte in the early stages but as the acidity of the medium drops, ammonia can be purged from the cell into an acid trap.⁶⁹ Ammonia generated in the cell might provide a pathway for deprotonation of the THF diazenido- intermediate. Such intermediates should be detectable during electrolysis. The catholyte was monitored by ³¹P{¹H} NMR and as noted above, this method was used to show the depletion of **A**. Importantly, at the end of electrolysis, **B** was essentially the exclusive product.⁷¹

Two new ³¹P{¹H} signals grow in and decay during the course of the electrolysis. These are at $\delta = 32$ and 33 ppm relative to 85% H₃PO₄. The relative peak intensities of the two signals are different, thus they must be attributed to two distinct *singlet*

intermediate species, I^1 and I^2 respectively. This is consistent with retention of a *trans* arrangement of the ligating P atoms in each of the intermediates. The charge passed course for their growth and decay is shown by Figures 12 and 13 respectively.

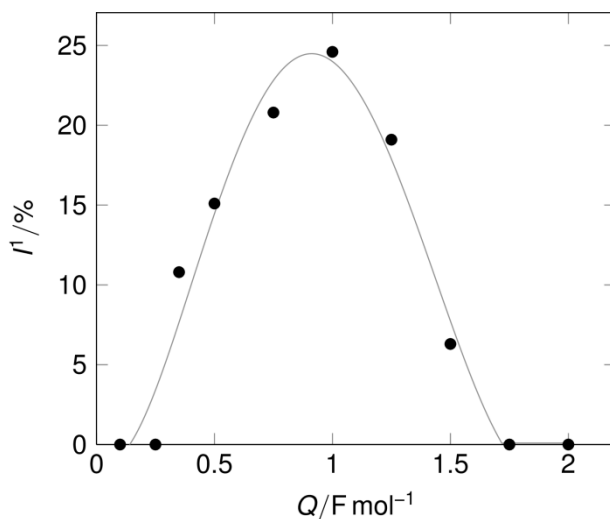


Figure 12 Plot showing the profile of intermediate I^1 during electrolyses at a Hg electrode held at -2 V vs Ag/AgCl in 0.2 M $[Bu_4N][BF_4]$ with respect to the charge passed. The percentage is relative to the $^{31}P\{^1H\}$ peak height for the parent complex **A** at zero charged passed.

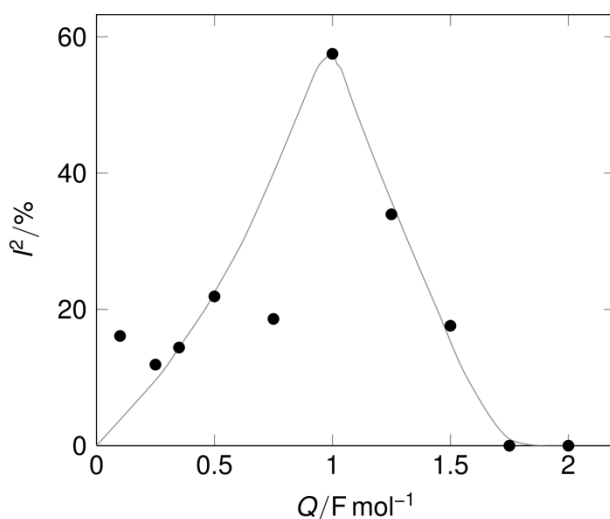


Figure 13 Plot showing the profile of intermediate I^2 during electrolyses at a Hg electrode held at -2 V vs Ag/AgCl in 0.2 M $[Bu_4N][BF_4]$ with respect to the charge passed, the percentage is relative to the $^{31}P\{^1H\}$ peak height for the parent complex **A** at zero charged passed.

The plots represent individual experiments where the electrolysis was stopped and the NMR data recorded rather than by continuous monitoring. This avoids depletion of electrolyte volume in the electrochemical cell. Although the data is somewhat scattered, the trend for both intermediates is clear. The peak intensity for each species

reaches a maximum after the passage of *ca* one electron per molecule of the parent hydrazide. Thus, their generation can be associated with the first stage of the electrolysis, *i.e.* the ammonia forming phase, and the second stage with conversion to **B**.

Whereas $^{31}\text{P}\{^1\text{H}\}$ peak heights measured under the same conditions for a specific species correlate directly with concentration, peak heights for different species in the same sample cannot usually be correlated because of differing relaxation times.⁷² It is found that under the same conditions the singlet peak heights for *trans*- $[\text{W}(\text{N}_2\text{H}_2)(\text{TsO})(\text{dppe})_2]^+$ and *trans*- $[\text{W}(\text{N}_2)_2(\text{dppe})_2]$ at 6 mM are approximately equivalent, that for the hydrazide being 88% of that for **B**. If the approximation is made that *all* the peak heights, including those for **I**¹ and **I**² have similar concentration coefficients then the ‘total’ % complex concentration for **A** + **I**¹ + **I**² + **B** should sum close to 100 % at any time during the course of the electrolysis. Experimentally, after the passage of 0.0 to 2.0 moles electrons per mole of **A** the $^{31}\text{P}\{^1\text{H}\}$ peaks sum to approximately 100 ± 20 % across the course of electrolysis as shown by the plot in Figure 14.

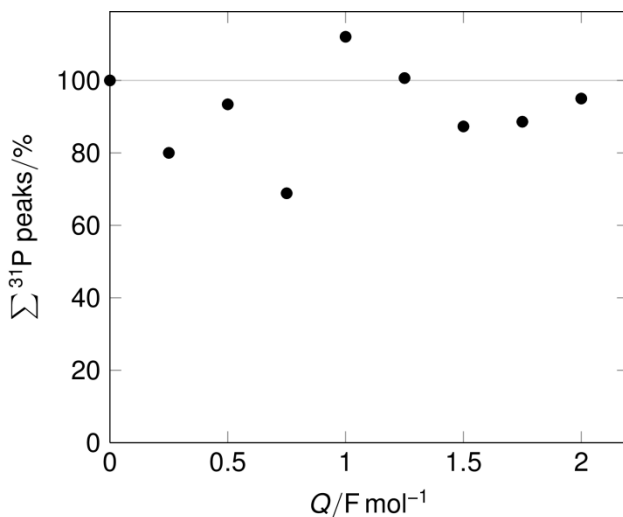


Figure 14 Plot showing the sum of all $^{31}\text{P}\{^1\text{H}\}$ species across the course of the electrolysis at a Hg electrode held at -2 V vs Ag/AgCl in 0.2 M $[\text{Bu}_4\text{N}][\text{BF}_4]$ with respect to the charge passed. The percentage is relative to the $^{31}\text{P}\{^1\text{H}\}$ peak height for the parent complex **A** at zero charged passed.

Figure 15 shows the plot of **I**¹ and **B** *versus* charge passed as estimated from peak intensities. This intermediate tracks the concentration of the dinitrogen complex

remarkably well in the first stage of the reaction, falling off in the latter stage as would be expected.

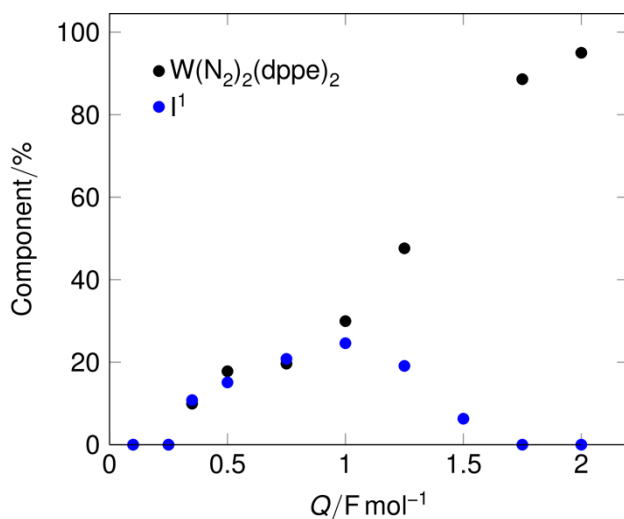


Figure 15 Plot showing the profile of intermediate **I¹** and **B** during electrolyses at a Hg electrode held at -2 V vs Ag/AgCl in 0.2 M [Bu₄N][BF₄] with respect to the charge passed. The percentage is relative to the ³¹P{¹H} peak height for the parent complex **A** at zero charged passed.

Similarly, Figure 16 shows the plot of **I²** and **B** *versus* the charge passed. In this case, the scatter is greater but shows an initial rise phase followed by decay as **B** is produced.

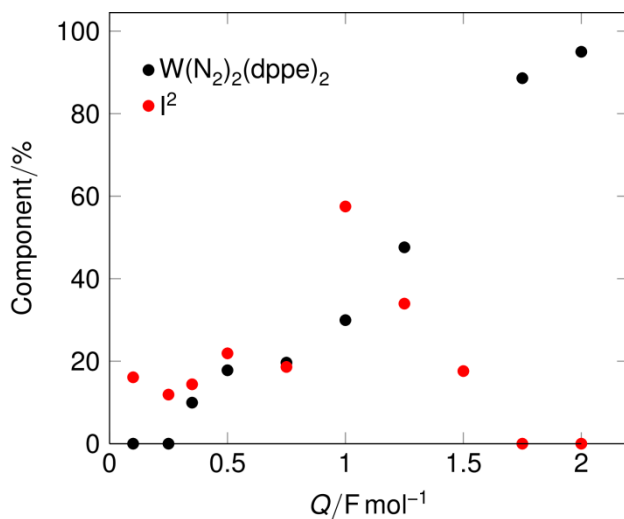


Figure 16 Plot showing the profile of intermediate **I²** and **B** during electrolyses at a Hg electrode held at -2 V vs Ag/AgCl in 0.2 M [Bu₄N][BF₄]-THF with respect to the charge passed. The percentage is relative to the ³¹P{¹H} peak height for the parent complex **A** at zero charged passed.

5.3.1.4 The nature of the intermediates I^1 and I^2

As discussed above, complex **A** supplies protons in the electrolysis and it is likely that I^1 and I^2 are formed by its deprotonation. To test this, complex **A** was reacted with ammonia (0.88 *sg*, aqueous) under dinitrogen in 0.2 M $[Bu_4N][BF_4]$ -THF electrolyte. Two new peaks appeared in the $^{31}P\{^1H\}$ NMR spectra at chemical shifts close to those observed for the intermediates I^1 and I^2 in the electrolysis on Hg at 32.3 and 33.2 ppm, together with an additional peak 31.9 ppm, Figure 17.

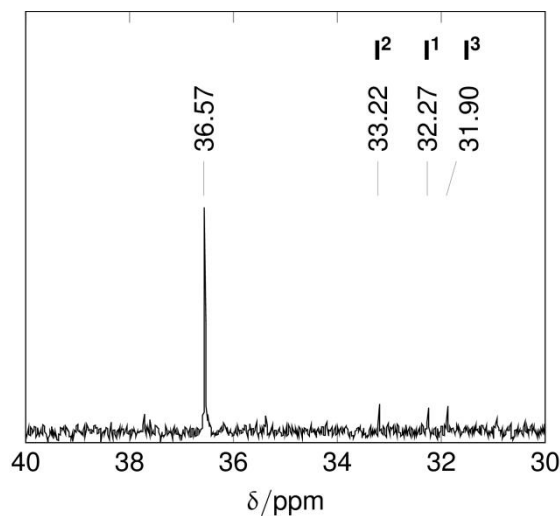
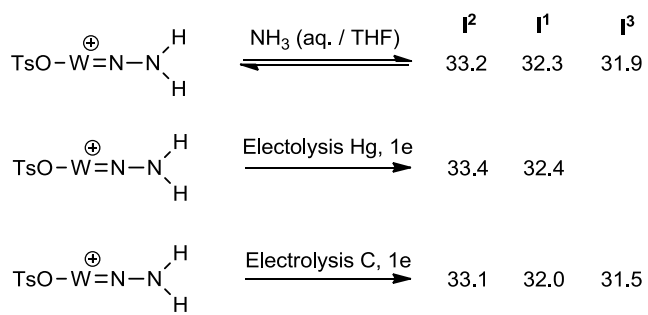


Figure 17 $^{31}P\{^1H\}$ NMR spectra of deprotonation of 1 mM $trans$ - $[W(N_2H_2)(TsO)(dppe)_2]^+$ in the presence of two equivalents of aqueous NH_3 (0.88 *sg*) (Peak at $\delta = 36.57$ ppm represents **A**).

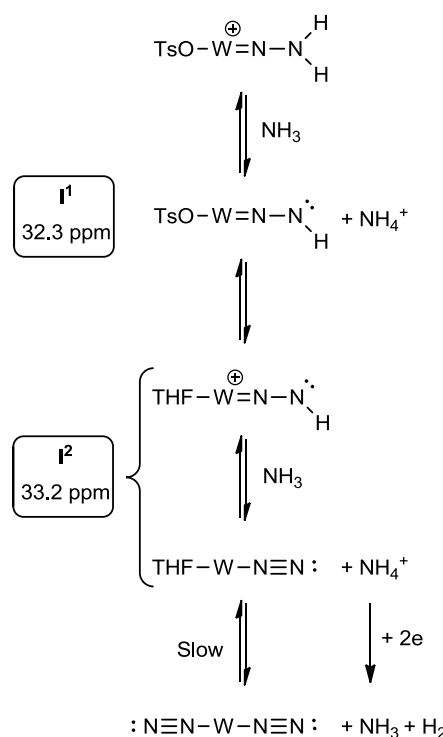
When partial electrolysis is carried out at a vitreous carbon electrode, an additional peak at 31.5 ppm is also observed, Scheme 10.



Scheme 10 Data for observed $^{31}P\{^1H\}$ peaks in ppm under the conditions stated.

Thus, the species observed during electrolyses are likely to arise by deprotonation chemistry. Candidate species for I^1 and I^2 are $trans$ - $[W(N_2H)(TsO)(dppe)_2]$, $trans$ - $[W(N_2H)(THF)(dppe)_2]^+$ and $trans$ - $[W(N_2)(THF)(dppe)_2]$, Scheme 11. All of these could

plausibly arise by deprotonation of the parent complex **A**. Such chemistry is consistent with the earlier studies of the deprotonation of the hydrazide with Et_3N .⁷³



Scheme 11 Intermediates involved in electrolysis of $\text{trans-}[\text{W}(\text{N}_2\text{H}_2)(\text{TsO})(\text{dppe})_2]^+$ together with $^{31}\text{P}\{^1\text{H}\}$ values.

It is therefore suggested that the intermediates detected during electrolysis are *trans*- $[\text{W}(\text{N}_2\text{H})(\text{TsO})(\text{dppe})_2]$, and *trans*- $[\text{W}(\text{N}_2)(\text{THF})(\text{dppe})_2]$ or *trans*- $[\text{W}(\text{N}_2\text{H})(\text{THF})(\text{dppe})_2]^+$. Given *trans*- $[\text{W}(\text{N}_2\text{H})(\text{TsO})(\text{dppe})_2]$ is known to solvate, it is likely that this species is the minor intermediate observed at 32.3 ppm, **I¹**. The signal at 33.2 ppm, **I²**, is therefore attributed to the major electrolysis intermediate, defined as *trans*- $[\text{W}(\text{N}_2\text{H})(\text{THF})(\text{dppe})_2]^+$ formed by solvolysis, although it cannot be excluded from being *trans*- $[\text{W}(\text{N}_2)(\text{THF})(\text{dppe})_2]$. To probe the system further, FTIR spectroelectrochemistry was undertaken.

5.3.1.5 FTIR Spectroelectrochemistry of *trans*- $[\text{W}(\text{N}_2\text{H}_2)(\text{TsO})(\text{dppe})_2]^+$

The cyclic voltammetry of **A** is shown in Figure 18. The irreversible reduction of the complex leads to the detection of two intermediates at a moderately fast scan rate, the reactive W^{II} hydrazide $[\text{W}(\text{N}_2\text{H}_2)(\text{dppe})_2]$,⁶² X, and a species which is reversibly

oxidised, Y. The $E_{\frac{1}{2}}^{\text{ox}} = -0.75$ V vs Ag/AgCl of the latter is consistent with the formation of *trans*-[W(N₂)(THF)(dppe)₂]⁺, I².⁶⁰

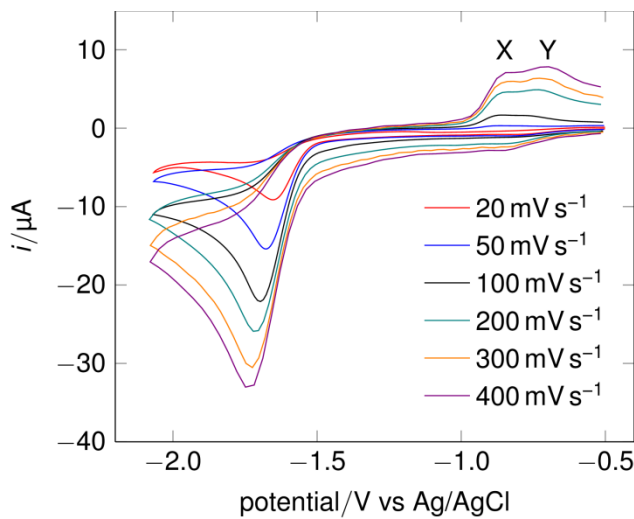


Figure 18 Cyclic voltammetry of 1.20 mM [W(NNH₂)(TsO)(dppe)₂][TsO·H₂O] complex in 0.2M [NBu₄][BF₄]-THF at a vitreous carbon electrode at various scan rates.

FTIR spectroelectrochemistry of *trans*-[W(N₂H₂)(TsO)(dppe)₂]⁺ was undertaken to probe the generation of intermediates in the reaction layer within the confines of a thin-layer electrolysis cell. This differs from bulk electrolysis, because stable intermediates generated are not free to diffuse into the bulk solution and react with, for example, protons from the parent complex.

Figure 19 shows the growth of bands in the 1800-2050 cm⁻¹ region during electrolysis at a vitreous carbon electrode over a period of 110 seconds.

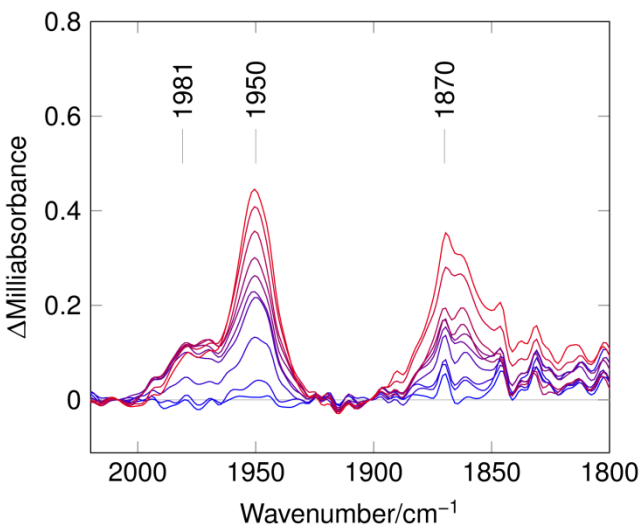


Figure 19 Difference spectrum for the reduction of 12 mM *trans*-[W(N₂H₂)(TsO)(dppe)₂][TsO·H₂O] in 0.2 M [Bu₄N]BF₄]-THF in the time range 8.15 s (blue) to 110 s (red) relative to a scan at 0.08 s.

Three major bands grow in centred at 1981, 1950 and *ca* 1870 cm⁻¹. The band at 1950 cm⁻¹ can be identified with *trans*-[W(N₂)₂(dppe)₂], **B**, the terminal product of bulk electrolysis.⁷⁴ The frequency of the band growing in at 1870 cm⁻¹ is where a moderately electron-rich dinitrogen species would be expected to absorb and this is reasonably attributed to *trans*-[W(N₂)(THF)(dppe)₂], or possibly *trans*-[W(N₂)(NH₃)(dppe)₂].⁴⁸ In the confined thin-layer regime, dinitrogen is likely to be rapidly depleted as it is consumed to form the dinitrogen complex **B**. Thus, not all the solvato-species will be converted to **B**. Notably dinitrogen saturated THF is *ca* 1 mM,⁷⁵ whereas the concentration of **A** employed was 12 mM. In the bulk electrolysis experiments the *trans*-[W(N₂)(THF)(dppe)₂] intermediate is likely to protonate with unreacted **A** to give *trans*-[W(N₂H)(THF)(dppe)₂]⁺, either of which could be **I**². The peak which grows in at 1981 cm⁻¹ is now considered. This is at an N₂ stretching frequency for a complex which is electron-poorer than **B**. It is possible that the band arises from the N≡N stretch of a hydrido- species, possibly [W(N₂)H(THF)(dppe)₂] or [W(N₂)H(TsO)(dppe)₂].

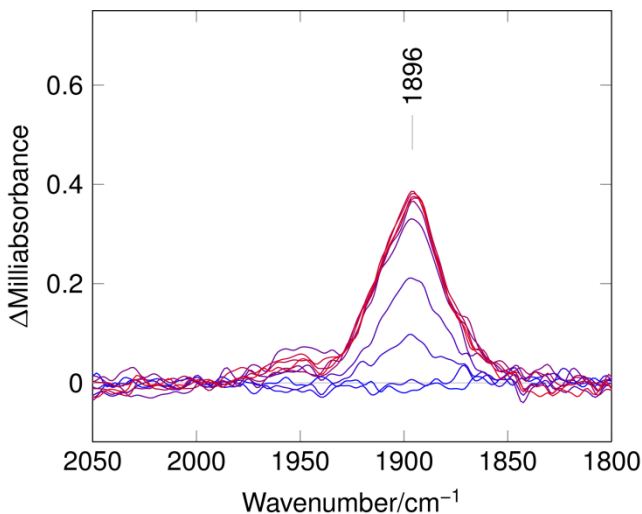


Figure 20 Difference spectrum for the reduction of 12 mM *trans*-[W(N₂H₂)(TsO)(dppe)₂]⁺ in the presence of 24 mM MeCN in 0.2 M [Bu₄N]BF₄]-THF in the time range 1.02 s (blue) to 14.00 s (red) relative to a scan at 0.08 s.

If a more coordinating substrate such as acetonitrile is added to the THF-electrolyte solution of the complex and then it is reduced, the appearance of both the 1950 cm⁻¹ and the 1870 cm⁻¹ peaks are suppressed and in their place a strong absorbance at 1896 cm⁻¹ is observed, Figure 20. This species is identified as *trans*-[W(N₂)(MeCN)(dppe)₂] which has a dinitrogen stretch at this frequency. This is a stable complex with a strongly bound MeCN ligand and most probably arises by displacement of labile THF from *trans*-[W(N₂)(THF)(dppe)₂].⁴⁸

5.3.2 Electrosynthesis of ammonia from a two phase system

In the previous study of the electrosynthesis of ammonia,⁶² three successive electrolysis-protonation cycles were performed on a single catholyte, establishing that cyclic conversion of dinitrogen to ammonia can be achieved. Following the two electron reduction of *trans*-[W(N₂H₂)(TsO)(dppe)₂]⁺, the product *trans*-[W(N₂)₂(dppe)₂] was protonated *in situ* by the addition of two molar equivalents of [TsOH·H₂O] to regenerate the hydrazido- starting material. This was once again electrolysed to reform the dinitrogen complex and ammonia; this reduction-protonation-reduction cycle was repeated a further time. The end result after three cycles and six electrons yielded 73 mol % of NH₃ per mole of *trans*-[W(N₂H₂)(TsO)(dppe)₂]⁺. So in theory, stoichiometric additions can be repeated indefinitely until all the complex is

decomposed, as the yield of the dinitrogen complex from a single cycle is 0.85-0.95 mol % **B** per mole of **A**.

Early attempts to improve the yield further by electrolysis in the presence of excess acid gave a maximum of *ca* 50 mol % NH₃ per mole **A** but the current yield rapidly dropped off as the concentration of free tosylic acid increased and electrons were directed toward proton reduction.

Another approach to ammonia electrosynthesis has been explored in an attempt to make the system continuous rather than step-wise. Cell set-ups involving two immiscible electrolyte phases were constructed. These involved a supernatant 1:3 molar ratio [Bu₄N][BF₄]-toluene electrolyte⁷⁶ phase in which the complex **A** is soluble, and in which the working and reference electrodes are placed, and an aqueous acid phase containing 1 M tosylic acid. The concept was that protons necessary for the reprotonation of **B** formed during electrolysis, or for protonation of intermediates also to regenerate **A**, could occur by transfer across the liquid-liquid interface.

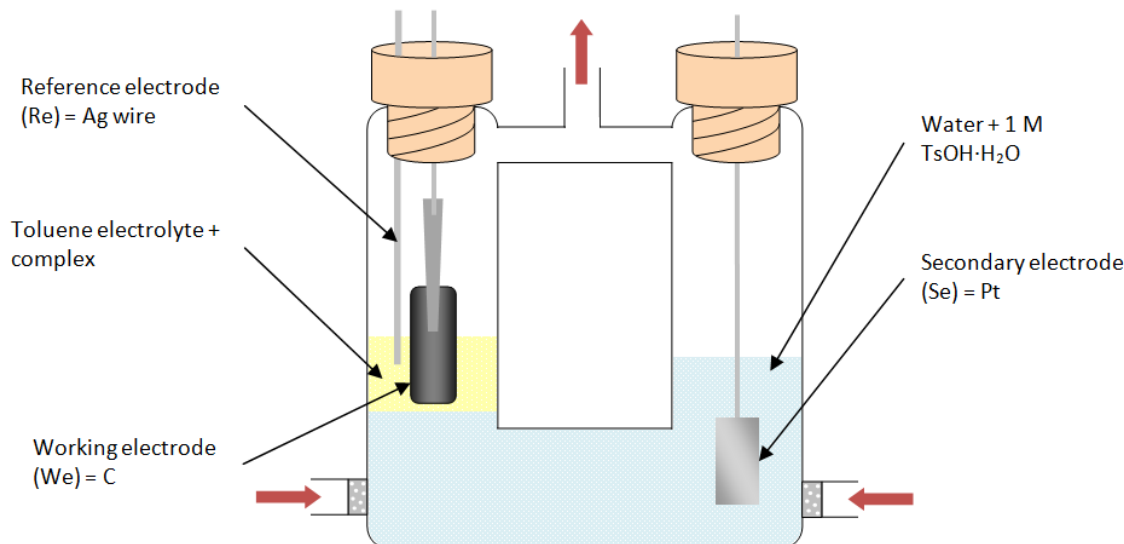


Figure 21 Configuration 1 of two-phase system for electrosynthesis of ammonia (Red arrows show gas inlets/outlets).

Two cell arrangements were employed. Configuration 1 is shown in Figure 21 and is essentially a simple 'U-shaped' cell. The vitreous carbon working electrode and the silver reference electrode are placed in the toluene phase containing **A** and the platinum secondary electrode in the acidic aqueous phase. Each side of the cell was constantly purged to supply the substrate dinitrogen and to minimise damage from

dioxygen generated at the secondary electrode. Equalisation of pressure in the two chambers was difficult and led to variable coverage of the working electrode.

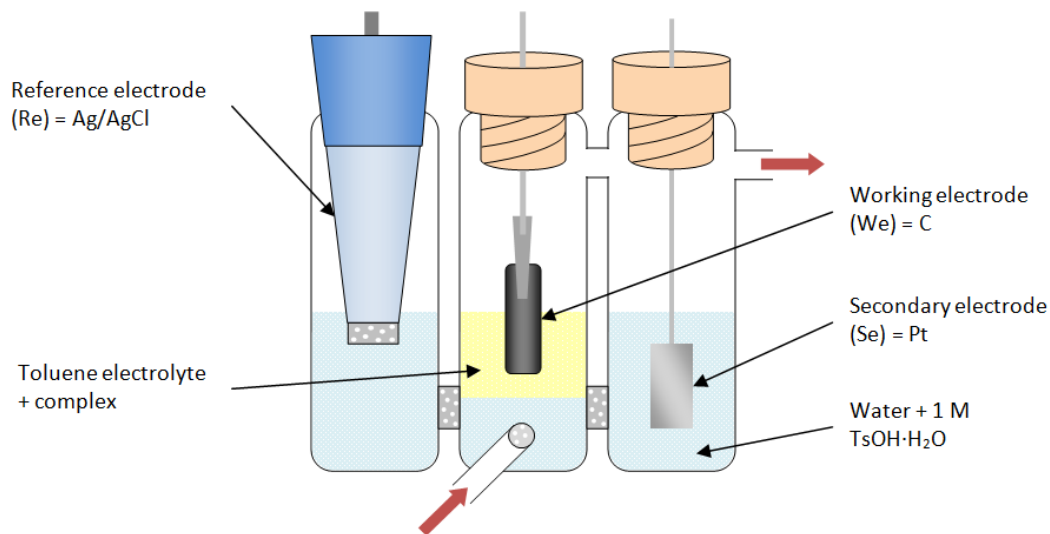


Figure 22 Configuration 2 of two-phase system for electrosynthesis of ammonia(Red arrows show gas inlets/outlets).

The second arrangement consisted of a three electrode, three compartment, H-type cell setup as shown in Configuration 2, Figure 22. This gave fewer problems because the cell pressure was equalised by the connection of the gas chambers. With either configuration, the acidity of the aqueous phase should remain constant as protons consumed on the reduction side should be replaced by water oxidation at the platinum secondary electrode.

Ammonia generated during electrolysis was trapped as ammonium by migration into the aqueous electrolyte phase and from the gas-phase by passage into a 0.1 M aqueous HCl trap.

Exp. No	Cell configuration	A / μmols ([A] / mM)	Moles electrons per mole A / F mol $^{-1}$	Mol % NH ₃ per mole A / %
B1	2	3.06 (0.77)	1271	39
B2	2	3.06 (1.02)	721	105
B3	2	3.50 (0.78)	487	69
B4	1	4.81 (1.20)	438	44
B5	1	3.50 (0.88)	553	62
B6	2	3.79 (0.84)	458	72

Table 2 Results of electrosynthesis of ammonia from two phase system, catholyte was 1:3molar ratio [Bu₄N][BF₄]-toluene electrolyte at a vitreous carbon electrode held at a potential of -1.9 V vs Ag/AgCl. In one experiment, B7, 143 mol % ammonia yield was obtained with a modest current efficiency but this was not reproducible.

The results for the bi-phasic experiments are summarised in Table 2. These are rather variable, averaging 65 ± 20 mol % ammonia per mole of **A**. Overall yields are higher than normal controlled potential electrolysis experiments at a mercury pool electrode where no extra acid source is added (20-30 mol % NH₃ per mole of **A**) but are not significantly better than with excess acid in a THF catholyte. Moreover, the current yields are low.

5.3.3 Photoelectrosynthesis of ammonia

As discussed earlier, no systems based on molecular catalysts such as those delineated by Schrock are known to have been reported as photoelectrocatalysts.

Therefore, the possibility of photo-assisted reduction of *trans*-[W(N₂H₂)(TsO)(dppe)₂]⁺ at a p-type silicon working electrode has been examined, harvesting light energy to be used in electrosynthesis of ammonia from the hydrazide **A**.

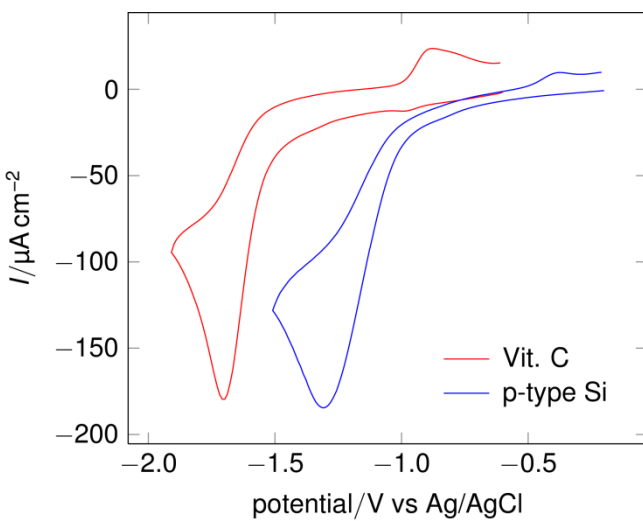


Figure 23 Cyclic voltammetry of 1.00 mM $[W(N_2H_2)(TsO)(dppe)_2]^+$ in 0.2M $[NBu_4][BF_4]$ -THF at a vitreous carbon electrode and at an illuminated 1-10 Ωcm p-type Si electrode at a scan rate of 100 mV s^{-1} .

The cyclic voltammetry of $trans$ - $[W(N_2H_2)(TsO)(dppe)_2]^+$ is shown at both a photoinert vitreous carbon electrode and an illuminated p-type silicon photocathode in Figure 23. The faradaic response of $trans$ - $[W(N_2H_2)(TsO)(dppe)_2]^+$ at the illuminated p-type silicon electrode is located 398 mV more positive than for the same complex at a carbon electrode. This parallels the behaviour of the molybdenum hydride complexes at p-type Si as described in Chapter 3, where electrons are promoted across the silicon band gap to higher energy levels, then transferred over the semiconductor/electrolyte interface to the electrocatalyst present in the solution. The potential shift of *ca* 400 mV is smaller than the *ca* 600 mV shift seen for the molybdenum hydride system. This is probably due to the more negative reduction potential of $trans$ - $[W(N_2H_2)(TsO)(dppe)_2]^+$ ($E_{p/2} = -1.65$ vs. Ag/AgCl) when compared to $[Mo(\eta^2-O_2CCH_3)(dppe)_2]^+$ ($E_{p/2} = -1.50$ vs. Ag/AgCl). The trend of a smaller potential shift associated with a more negative redox potential is supported by the cyclic voltammetry of the first and second reductions of $[CoCp_2][PF_6]$, where the shift in the first reduction is larger than the shift in the second reduction as shown in the appendix (Figures A5.1 & A5.2). The electrochemical responses at both vitreous carbon and p-type silicon are similar in terms of shape and current magnitude, furthering the idea that the electroactive areas of the two types of electrodes are very alike and thus the electrochemical behaviour of both materials is similar.

The light assisted controlled potential electrolysis of *trans*-[W(N₂H₂)(TsO)(dppe)₂]⁺ was examined at a p-type silicon (H-terminated) photocathode and the ammonia yield was measured as described for electrolyses at a mercury pool electrode. Table 3 summarises the results.

Exp. No	A / μmols ([A] / mM)	Moles electrons per mole A / F mol ⁻¹	Mol % NH ₃ per mole A / %
C1	8.39 (1.68)	2.08	67
C2	6.71 (1.34)	2.02	77
C3	6.56 (1.46)	2.21	49
C4	6.78 (1.51)	2.00	38
C5	4.08 (1.02)	0.45	30
C6	3.65 (0.91)	2.41	52
C7	20.1 (5.01)	0.79	19
C8	28.3 (5.66)	1.74	18
C9	23.8 (4.76)	0.87	31
C10	22.6 (4.52)	2.03	25

Table 3 Results of electrosynthesis of ammonia at an illuminated 1-10 Ω cm p-type Si electrode held at a potential of -1.5 V vs Ag/AgCl in 0.2 M [Bu₄N][BF₄]-THF, ³¹P{¹H} NMR and cyclic voltammetry confirmed that only trace amounts of *trans*-[W(N₂)₂(dppe)₂] was formed at the end of electrolyses.

The results of the photoelectrosynthesis of ammonia show that in the concentration range 0.9 to 1.7 mM of **A**, a substantially higher yield of ammonia is obtained than on a conventional mercury electrode; yields range from 30-77 mol % NH₃ per mole of **A**, averaging 52 mol %. At higher concentrations of the parent complex, 4.5-5.7 mM, yields of ammonia are typical of those on mercury, averaging 23 mol % per mole of **A**. In either case, the overall electron consumption is near 2 moles of electrons per mole of **A**. Thus, the higher yield of ammonia may require either diversion of electrons from formation of **B** and/or the parent complex **A** behaving as source of two protons rather than one proton as in the global stoichiometry shown in Equation 5.8.

It is found that on illuminated p-type Si the yield of *trans*-[W(N₂)₂(dppe)₂] is low, when measured by cyclic voltammetry, Figure 24.

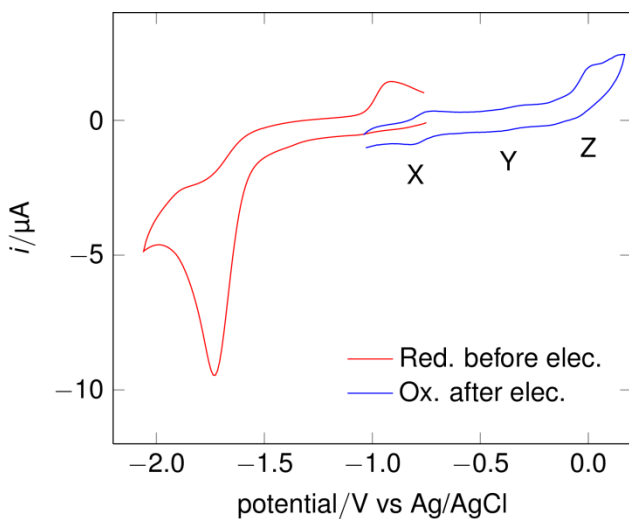


Figure 24 Cyclic voltammetry of 0.91 mM $[\text{W}(\text{N}_2\text{H}_2)(\text{TsO})(\text{dppe})_2][\text{TsO}\cdot\text{H}_2\text{O}]$ complex in 0.2M $[\text{NBu}_4][\text{BF}_4]$ -THF at a vitreous carbon electrode before and after electrolysis at a scan rate of 100 mV s⁻¹.

The cyclic voltammetry at the end of electrolysis shows the presence of low levels of two reversible couples X and Y, Figure 24, corresponding to *ca* 7 and 2 mol % per mole **A** respectively, after electrolysis of the 0.91 mM solution. The potential of the first couple is indicative of an electron-rich species, possibly *trans*- $[\text{W}(\text{N}_2)(\text{THF})(\text{dppe})_2]$. The second couple is probably *trans*- $[\text{W}(\text{N}_2)_2(\text{dppe})_2]$ or $[\text{WH}_4(\text{dppe})_2]$. The irreversible process, Z, is most likely attributed to a secondary oxidation or another product. $^{31}\text{P}\{^1\text{H}\}$ NMR spectroscopy after partial photoelectrolysis of a 1.2 mM of **A** (0.26 moles electrons per mole **A**) showed the starting material, very weak resonances for I¹ and I² and two strong resonances at 26.7 and 24.17 ppm relative to 85% H_3PO_4 which are not observed in deprotonation experiments, Figure A5.3, respectively for electrolyses performed using *ca* 1 mM **A**. In a similar experiment, where an exhaustive electrolysis was performed and the hydrazide complex had been consumed, a major peak at 29.20 ppm is observed together with a resonance at 24.61 ppm, Figure A5.4. The latter probably corresponds to the same species to that which was observed in the partial photoelectrolysis.

These results show that the chemistry on illuminated p-type Si is substantially modified from that occurring on a mercury cathode. A series of experiments were therefore conducted in order to clarify why an improved yield of ammonia was produced without the addition of excess acid and why little *trans*- $[\text{W}(\text{N}_2)_2(\text{dppe})_2]$ was produced at the end of the photoelectrolyses.

Firstly, the standard electrolysis experiments on a mercury pool electrode were repeated but this time under illumination as in the p-type silicon CPE experiments, Table 4.

Exp. No	A / μmols ([A] / mM)	Moles electrons per mole A / F mol $^{-1}$	Mol % NH ₃ per mole A / %	Mol % B per mole A / %
D1	46.0 (3.83)	2.02	25	62
D2	45.8 (3.82)	2.03	35	73
D3	45.2 (3.77)	2.07	23	53

Table 4 Results of electrosynthesis of ammonia at an illuminated Hg pool electrode held at a potential of -1.9 V vs Ag/AgCl in 0.2 M [Bu₄N][BF₄]-THF.

The results for the controlled potential electrolysis of *trans*-[W(N₂H₂)(TsO)(dppe)₂]⁺ at an illuminated mercury pool electrode showed that the amount of ammonia produced was very similar to the original data from CPE at a mercury pool electrode under ambient conditions, with yields in the region of 25 mol % NH₃ per mole of **A**. The yield of *trans*-[W(N₂)₂(dppe)₂] is lower than observed without illumination, averaging 63 mol % **B** per mole of **A**. This suggests that light has some effect on the yield of **B** but cannot account for all of the decrease observed at p-type Si. *Trans*-[W(N₂)₂(dppe)₂] is photolabile under visible light illumination and it is known that mono-dinitrogen intermediates [Mo(N₂)(dppe)₂], besides coordinating a solvent molecule, can also abstract CO from THF under forcing conditions to give carbonyls or hydrides.⁷⁷ It is possible that the lower yields observed on illuminated Hg are because of these types of reactions.

Secondly, controlled potential electrolysis of *trans*-[W(N₂H₂)(TsO)(dppe)₂]⁺ was carried out at a p-type silicon electrode in the dark, Table 5.

Exp. No	A / μmols ([A] / mM)	Moles electrons per mole A / F mol $^{-1}$	Mol % NH ₃ per mole A / %	Mol % B per mole A / %
E1	2.19 (1.09)	2.06	25	34

Table 5 Result of electrosynthesis of ammonia at a 1-10 Ω cm p-type Si electrode held at a potential of -1.9 V vs Ag/AgCl in the dark in 0.2 M [Bu₄N][BF₄]-THF.

Under dark conditions at a p-type silicon electrode, an ammonia yield similar to that on mercury was obtained; 25 mol % per mole of **A**. In the same experiment, the yield of *trans*-[W(N₂)₂(dppe)₂] was 34 mol % per mole of **A**. The low yield of the dinitrogen

complex appears to be related both to the electrode material as well as photochemistry taking place in solution.

To explore the effect of electrode materials, a vitreous carbon electrode was also used as a cathode. Product yields are given in Table 6.

Exp. No	A / μmols ([A] / mM)	Moles electrons per mole A / F mol $^{-1}$	Mol % NH ₃ per mole A / %	Mol % B per mole A / %
F1	5.20 (0.97)	2.25	20	33
F2	6.00 (1.09)	1.82	21	48

Table 6 Results of electrosynthesis of ammonia at a vitreous carbon electrode held at a potential of -1.9

V vs Ag/AgCl in the dark in 0.2 M [Bu₄N][BF₄]-THF.

The results for an electrolysis at a vitreous carbon electrode under ambient conditions gave yields of ammonia within the range found on mercury after the passage of *ca* 2 moles electrons per mole of **A** in the absence of acid, but significantly lower yields of *trans*-[W(N₂)₂(dppe)₂] as found for p-type Si in the dark. This again suggests the nature of the electrode material also has a consequence on the yield of the dinitrogen complex, **B**.

Finally, experiments were performed at an illuminated vitreous carbon electrode to examine the combined effect of light and vitreous carbon, Table 7.

Exp. No	A / μmols ([A] / mM)	Moles electrons per mole A / F mol $^{-1}$	Mol % NH ₃ per mole A / %	Mol % B per mole A / %
G1	23.0 (4.19)	0.91	3.0	2.0
G2	7.50 (1.37)	1.46	17	9.0

Table 7 Results of electrosynthesis of ammonia at an illuminated vitreous carbon electrode held at a

potential of -1.9 V vs Ag/AgCl in 0.2 M [Bu₄N][BF₄]-THF.

The combined effect of both light and the electrode material is dramatic; the yields of ammonia and **B** are both low. It is therefore concluded that together illumination and the type of electrode material; mercury, vitreous carbon or p-type silicon have a pronounced effect on yields. The highest yields of *trans*-[W(N₂)₂(dppe)₂] are observed on mercury whilst the highest yields of ammonia and the lowest yields of **B** are obtained on p-type Si under illumination.

5.3.4 Photoelectrosynthesis of ammonia: a diurnal approach

Given that both light and electrode material affect the yield of **B**, thus breaking the possibility of stepwise regeneration of **A** and thus cyclic production of ammonia, a ‘diurnal’ approach was examined. The concept was that photoelectrosynthetic light assisted generation of ammonia could be performed at p-type Si, and dark generation of **B** undertaken at a mercury pool electrode.

A system was designed with two working electrodes situated in the working electrode compartment, Figure 25.

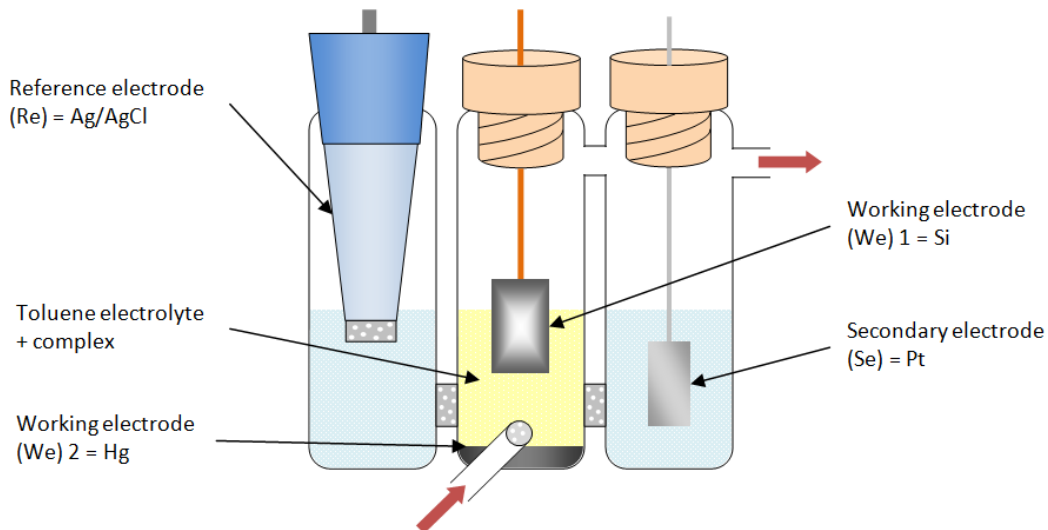


Figure 25 Configuration of cell for photo-assisted electrosynthesis of ammonia (Red arrows show gas inlets/outlets).

The twin working electrode system is designed for each electrode to work in succession, where the primary electroreduction is performed at the illuminated p-type silicon photocathode to produce ammonia. The mercury pool electrode is then connected for reduction of photoelectrochemically derived, ‘{W(dppe)₂}’ products.

Table 8 summarises the results of five experiments in which photo-assisted reduction of **A** at p-type Si was followed by further reduction at a mercury pool cathode under ambient conditions.

Exp. No	A / μmols ([A] / mM)	Total moles electrons per mole A / F mol^{-1}	Total mol % NH ₃ per mole A / %	Total mol % B per mole A / %
H1	5.98 (1.20)	1.27	55	13
H2	6.64 (1.33)	5.15	16	51
H3	6.64 (0.90)	4.04	23	67
H4	4.96 (1.06)	4.49	22	53

Table 8 Results of photo-assisted electrosynthesis of ammonia at an illuminated 1-10 $\Omega \text{ cm}$ p-type Si electrode held at a potential of -1.5 V vs Ag/AgCl and then a dark Hg pool electrode held at a potential of -1.9 V vs Ag/AgCl in 0.2 M [Bu₄N][BF₄]-THF.

Results for the photo-assisted electrosynthesis of ammonia were somewhat variable, ranging from 22 to 55 mol % NH₃ per mole of **A**. The average yield of 25 mol % was in the order of that obtained for reduction of **A** on a mercury pool. The subsequent electrolysis on the mercury pool gave substantially higher yields of the dinitrogen complex, **B**, than observed on p-type Si alone, averaging 41 mol % **B** per mole **A** with a maximum yield of 67 mol % of the dinitrogen complex together with 23 mol % ammonia. An example of recovered *trans*-[W(N₂)₂(dppe)₂] as detected by cyclic voltammetry is shown in Figure A5.5.

5.4 Conclusions

The previous study of the electrosynthesis of ammonia from *trans*-[W(N₂H₂)(TsO)(dppe)₂]⁺ at a mercury pool electrode was repeated to give a standard for comparison of photoelectrosynthetic experiments. The understanding of these experiments was extended by detection and recognition of the intermediates involved in the mechanism of the generation of ammonia and formation of *trans*-[W(N₂)₂(dppe)₂]. Partial electrolysis experiments and separate chemical deprotonation studies identified the same two intermediates. Two ³¹P{¹H} signals grew in and decayed during the course of electrolyses and deprotonation experiments. These were at $\delta = 32$ (**I**¹) and 33 (**I**²) ppm relative to 85% H₃PO₄ and these were assigned as **I**¹ = *trans*-[W(N₂H)(TsO)(dppe)₂], and **I**² = *trans*-[W(N₂)(THF)(dppe)₂] or *trans*-[W(N₂H)(THF)(dppe)₂]⁺. FTIR spectroelectrochemical reduction of *trans*-[W(N₂H₂)(TsO)(dppe)₂]⁺ somewhat clarified this. A strong band for the product *trans*-[W(N₂)₂(dppe)₂], **B**, was detected at 1950 cm^{-1} , together with a band which grew in at

1870 cm^{-1} and which is reasonably attributed to *trans*-[W(N₂)(THF)(dppe)₂]. Although, *trans*-[W(N₂)(NH₃)(dppe)₂] is an alternative possibility. The appearance of hydrido-species was also suggested by the N≡N stretching frequency seen emerging at 1981 cm^{-1} .

Photoelectrosynthesis of ammonia at a p-type silicon photocathode was proven possible and produced greater than expected yields of ammonia. However, the catalytic cycle was broken as the complex *trans*-[W(N₂)₂(dppe)₂] was not produced. This is probably a direct effect of illumination, altering the mechanism from that which takes place in the earlier mercury pool experiments (Sections 5.1.3.2 and 5.1.3.3). This is supported by the fact that different species were observed by ³¹P{¹H} NMR in partial photoelectrolysis experiments as compared to those observed in experiments using a mercury pool working electrode.

The reformation of *trans*-[W(N₂)₂(dppe)₂] was improved by the use of a two working electrode photo-assisted electrochemical setup, where ammonia formation was conducted at an illuminated p-type silicon photocathode and regeneration of **B** was successfully performed at a mercury pool electrode. This gave ammonia yields averaging 25 mol %, and *trans*-[W(N₂)₂(dppe)₂] yields averaging 41 mol %, per mole of **A**.

5.5 Future avenues of research

The challenge with regard to the photoelectrosynthesis of ammonia experiments is to understand the nature of the intermediates produced, and why these can be reduced to *trans*-[W(N₂)₂(dppe)₂] at a mercury cathode if the mechanism differs from that observed in mercury pool experiments, as suggested by preliminary ³¹P{¹H} NMR data. A possible mechanism could involve the light driven generation of coordinatively unsaturated ‘{W(dppe)₂}’ or ‘{W(N₂)(dppe)₂}’ species. These are reactive towards oxygen or carbonyl abstraction from TsO⁻ or THF respectively, or metal hydride formation, or even possibly ortho-metallation involving the phenyl substituents of dppe.⁷⁸ Further NMR studies ought to help prove or disprove these hypotheses.

Cyclic conversion of dinitrogen to ammonia in the two phase system approach needs to be repeated and improved so that more reliable results, with lower deviation, can be obtained to gauge whether this is a viable process for ammonia formation.

5.6 References

1. B. K. Burgess, D. J. Lowe, *Chem. Rev.* **1996**, *96*, 2983
2. J. Postgate, Nitrogen Fixation 3rd Ed. Cambridge University Press, **1998**
3. H. Bothe, F. J. De Bruijn, W. E. Newton, *Nitrogen Fixation: Hundred Years After*, p 3-12, Gustav Fisher, Germany, **1989**
4. M. Beijerinck, *Bot. Ztg.* **1888**, *46*, 725
5. M. Beijerinck, *ZentBl. Bakt. ParasitKde.* **1901**, *7*, 561
6. Y. Zhao, S. M. Bian, H. N. Zhou, J. F. Huang, *J. Integr. Plant Biol.* **2006**, *48*, 745
7. B. K. Burgess, D. L. Lowe, *Chem. Rev.* **1996**, *96*, 2983
8. L. M. Rubio, P. W. Ludden, *J. Bacteriol.* **2005**, *187*, 405
9. B. M. Hoffmann, D. R. Dean, L. C. Seefeldt, *Acc. Chem. Res.* **2008**, *42*, 609
10. O. Einsle, A. Tezcan, S. L. A. Andrade, B. Schmid, M. Yoshida, J. B. Howard, D. C. Rees, *Science*, **2002**, *297*, 1696
11. T. Spatzal, M. Aksoyoglu, L. Zhang, S. L. A. Andrade, E. Schleicher, S. Weber, D. C. Rees, O. Einsle, *Science*, **2011**, *334*, 940
12. K. M. Lancaster, M. Roemelt, P. Ettenhuber, Y. Hu, M. W. Ribbe, F. Neese, U. Bergmann, S. DeBeer, *Science*, **2011**, *334*, 974
13. S. E. Creutz, J. C. Peters, *J. Am. Chem. Soc.* **2014**, *136*, 1105.
14. J. R. Rittle, J. C. Peters, *Proc. Natl. Acad. Sci.* **2013**, *110*, 15898
15. D. J. Lowe, R. N. F. Thorneley, *J. Biochem.* **1984**, *224*, 895
16. L.C. Seefeldt, B. M. Hoffman, D. R. Dean, *Ann. Rev. Biochem.* **2009**, *78*, 701
17. R. N. F. Thorneley, D. J. Lowe, *Molybdenum Enzymes*, Wiley-Interscience: NewYork, **1985**, Vol. 7, p 89
18. J. Chatt, A. J. Pearman, R. L. Richards, *J. Chem. Soc. Dalton Trans.* **1977**, 1852
19. R. R. Schrock, *Angew. Chem.* **2008**, *47*, 5512
20. J. Chatt, G. J. Leigh, *Chem. Soc. Rev.* **1972**, *1*, 12
21. R. R. Schrock, *Proc. Natl. Acad. Sci.* **2006**, *103*, 17087
22. B. M. Hoffman, D. Lukyanov, Z. Y. Yang, D. R. Dean, L. C. Seefeldt, *Chem. Rev.* **2014**, *114*, 4041
23. Z. Y. Yang, N. Khadka, D. Lukyanov, B. M. Hoffman, D. R. Dean, L. C. Seefeldt, *Proc. Natl. Acad. Sci.* **2013**, *110*, 16327
24. (a) B. M. Hoffman, D. R. Dean, L.C. Seefeldt, *Acc. Chem. Res.* **2009**, *42*, 609; (b) B. M. Barney, H. I. Lee, P. C. Dos Santos, B. M. Hoffman, D. R. Dean, L. C. Seefeldt, *J. Chem. Soc. Dalton Trans.* **2006**, 2277; (c) B. M. Barney, D. Lukyanov, T. C. Yang, D. R. Dean, B. M. Hoffman, L. C. Seefeldt, *Proc. Natl. Acad. Sci.* **2006**, *103*, 17113; (d) B. M. Barney, J. McLead, D. Lukyanov, M. Laryukhin, T. C. Yang, D. R. Dean, B. M. Hoffman, L.C. Seefeldt, *Biochemistry*, **2007**, *46*, 6784; (e) B. M. Barney, T. C. Yang, R. Y. Igarashi, P. C. Dos Santos, M. Laryukhin, H. I. Lee, B. M. Hoffman, D. R. Dean, L. C. Seefeldt, *J. Am. Chem. Soc.* **2005**, *127*, 14960; (f) S. Duval, K. Danyal, S. Shaw, A. K. Lytle, D. R. Dean, B. M. Hoffman, E. Antony, L. C. Seefeldt, *Proc. Natl. Acad. Sci.* **2013**, *110*, 16414

25. R. A. Kinney, C. T. Saouma, J. C. Peters, B. M. Hoffman, *J. Am. Chem. Soc.* **2012**, *134*, 12637
26. J. Chatt, A. J. Pearman, R. L. Richards, *Nature*, **1975**, *253*, 2074
27. G. J. Leigh, N. W. Winterton, *Modern Coordination Chemistry: The Legacy of Joseph Chatt*, Springer Verlag, **2002**
28. R. R. Schrock, *J. Chem. Soc. Chem. Commun.* **2003**, 2391
29. S. M. Rocklage, R. R. Schrock, *J. Am. Chem. Soc.* **1980**, *102*, 7808
30. R. C. Murray, R. R. Schrock, *J. Am. Chem. Soc.* **1985**, *107*, 4557
31. R. R. Schrock, T. E. Glassman, M. G. Vale, *J. Am. Chem. Soc.* **1991**, *113*, 725
32. T. E. Glassman, M. G. Vale, R. R. Schrock, *J. Am. Chem. Soc.* **1993**, *115*, 1760
33. R. R. Schrock, *Acc. Chem. Res.* **1997**, *30*, 9
34. J. Chatt, A. A. Diamantis, G. A. Heath, N. E. Hooper, G. J. Leigh, *J. Chem. Soc. Dalton Trans.* **1977**, 688
35. J. Chatt, A. J. Pearman, R. L. Richards, *Nature*, **1975**, *253*, 39
36. G. J. Leigh, R. A. Henderson, C. J. Pickett, *Adv. Inorg. Chem.* **1983**, *27*, 197
37. E. J. Carmona, *Organomet. Chem.* **1988**, *358*, 283 ; T. A. George, C. D. Seibold, *Inorg. Chem.* **1973**, *12*, 2544
38. J. Chatt, G. A. Heath, R. L. Richards, *J. Chem. Soc. Dalton Trans.* **1974**, 2074
39. L. K. Fong, J. R. Fox, B. M. Foxman, N. J. Cooper, *Inorg. Chem.* **1986**, *25*, 1880
40. A. Hills, D. L. Hughes, M. Jimenez-Tenorio, G. J. Leigh, A. T. Rowley, *J. Chem. Soc. Dalton Trans.* **1993**, 3041.
41. T. A. George, R. A. Kovar, *Inorg. Chem.* **1981**, *20*, 287
42. G. J. Leigh, R. A. Henderson, C. J. Pickett, *Adv. Inorg. Chem.* **1983**, *27*, 197
43. M. Y. Mohammed, C. J. Pickett, *J. Chem. Soc. Chem. Commun.* **1988**, 1119
44. M. D. Fryzuk, S. A. Johnson, *Coord. Chem. Rev.* **2000**, *200*, 379
45. J. Chatt, A. J. Pearman, R. L. Richards, *J. Chem. Soc. Dalton Trans.* **1976**, 1520
46. J. Chatt, A. J. Pearman, R. L. Richards, *J. Chem. Soc. Dalton Trans.* **1974**, 2074
47. J. Chatt, R. L. Richards, *Chemistry and Biochemistry of Nitrogen Fixation*, ed. J. R. Postgate, Plenum Press, London, **1971**
48. J. Chatt, G. J. Leigh, H. Neukomm, C. J. Pickett, D. R. Stanley, *J. Chem. Soc. Dalton Trans.* **1980**, 121
49. G. A. Heath, R. Mason, K. M. Thomas, *J. Am. Chem. Soc.* **1974**, *96*, 254
50. S. Kahlal, J. V. Saillard, J. R. Hamon, C. Manzur, D. Carillo, *J. Chem. Soc. Dalton Trans.* **1998**, 1229
51. R. Henderson, *J. Chem. Soc. Dalton Trans.* **1982**, 917
52. R. Henderson, *J. Chem. Soc. Dalton Trans.* **1984**, 2259
53. Y. G. Borodko, A. E. Shilov, *Russ. Chem. Revs.* **1969**, *38*, 355
54. R. W. F. Hardy, R. C. Burns, G. W. Parshall, *Adv. Chem. Ser.* **1971**, *100*, 219
55. C. J. Pickett, G. J. Leigh, *J. Chem. Soc. Chem. Commun.* **1981**, 1033
56. P. C. Bevan, J. Chatt, G. J. Leigh, E. G Leelamini, *J. Organomet. Chem.* **1977**, *139*, C59
57. C. J. Pickett, *JBIC*, **1996**, *1*, 601
58. M. Kol, R. R. Schrock, R. Kempe, W. M. Davis, *J. Am. Chem. Soc.* **1994**, *116*, 4832

59. D. V. Yandulov, R. R. Schrock, *Science*, **2003**, *301*, 76
60. J. S. Anderson, J. Rittle, J. C. Peters, *Nature*, **2013**, *501*, 84
61. T. I. Al-Salih, C. J. Pickett, *J. Chem. Soc. Dalton Trans.* **1985**, 1255
62. C. J. Pickett, J. Talarmin, *Nature*, **1985**, *317*, 652
63. N. R. Dhar, *J. Chem. Phys.* **1958**, *55*, 983
64. F. Khan, P. Yue, L. Rizzuti, V. Augugliaro, M. Schiavello, *J. Chem. Soc. Chem. Commun.* **1981**, 1049
65. H. Miyama, N. Juji, Y. Nagae, *Chem. Phys. Lett.* **1983**, *74*, 523
66. Q. Li, K. Domen, S. Naito, T. Onishi, K. Tamaru, *Chem. Lett.* **1983**, 331
67. E. Endoh, J. K. Leland, A. J. Bard, *J. Phys. Chem.* **1986**, *90*, 6223
68. G. N. Schrauzer, T. D. Guth, *J. Am. Chem. Soc.* **1977**, *99*, 7189
69. W. Hussain, G. J. Leigh, C. J. Pickett, *J. Chem. Soc. Chem. Commun.* **1982**, 747
70. G. Butler, J. Chatt, G. J. Leigh, C. J. Pickett, *J. Chem. Soc. Dalton Trans.* **1979**, 113
71. J. D. Lane, R. A. Henderson, *J. Chem. Soc. Dalton Trans.* **1987**, 197
72. D. G. Gorenstein, *Phosphorus-31 NMR Principles and Applications*, Academic Press, **1984**, p 328
73. It has been shown that *weak* acids protonate *trans*-[W(N₂)₂(dppe)₂] at the metal centre to give the stable hydride *trans*-[WH(N₂)₂(dppe)₂]⁺.^{51, 52} rearrangement of the solvated diazenide and replacement of THF by molecular dinitrogen could also lead to this species although such an intermediate would be expected to have a more complex (AA'XX')³¹P{¹H} NMR spectrum which is not observed.
74. W. Hussain, G. J. Leigh, H. M. Ali, C. J. Pickett, D. A. Rankin, *J. Chem. Soc. Dalton Trans.* **1984**, 1703
75. C. J. Pickett, *Unpublished data*, **2013**
76. C. J. Pickett, *J. Chem. Soc. Chem. Commun.* **1985**, 323
77. T. Tatsumi, H. Tominaga, M. Hidai, Y. Uchida, *Chem. Lett.* **1977**, 37
78. T. Ishida, Y. Mizobi, M. Hidai, *Chem. Lett.* **1989**, 2077

Chapter 6

Experimental

6.1 General materials and techniques

Unless otherwise stated chemicals, solvents (Aldrich, VWR, Fisher) and high-purity gases (BOC) were obtained from commercial sources and used without further purification.

All manipulations of solutions used in synthesis and analytical measurements were carried out under a nitrogen or argon atmosphere using standard Schlenk techniques or in an M Braun glovebox.

Tetrahydrofuran was distilled from sodium-benzophenone. Acetonitrile was distilled over calcium hydride. Dichloromethane was distilled over phosphorus pentoxide-sodium carbonate.

The supporting electrolyte, tetra n-butylammonium tetrafluoroborate, $[Bu_4N][BF_4]$, was prepared by the standard laboratory procedure and dried by heating to 120 °C under vacuum.¹

Complexes $[MH_2(\eta^2-O_2CR)(dppe)_2][BPh_4]$ ($M = Mo$ or W , $R = CH_3$ or H)² ($M = Mo$ or W ; $R = CF_3$),³ $[W(N_2H_2)(TsO)(dppe)_2][TsO \cdot H_2O]$,⁴ $[Mo(CO)_2(S_2C_2Ph_2)_2]$ ⁵ and $[W(CO)_2(S_2C_2Ph_2)_2]$ ⁶ were all synthesised according to literature methods.

UV-visible data was collected using a Perkin Elmer Lambda 25 UV/visible spectrometer using Perkin-Elmer software.

Gas chromatography for measurement of dihydrogen was carried out using a Perkin-Elmer Clarius 500 instrument fitted with a 5 Å molecular sieve column (800/100 mesh, 6' x 1/8") and thermal conductivity detector using Clarity software. An external standard of 39.44 μ moles L⁻¹ of dihydrogen was used which was measured before and after experimental measurements. Dihydrogen yields were manually calculated from the ratio of the integrated peak areas.

NMR measurements were carried out on a Brüker 300 MHz UltrashieldTM NMR machine with Topspin software.

6.2 Experimental techniques

6.2.1 Electrochemical experiments and materials

Cyclic voltammetry experiments were controlled using an Autolab PGSTAT30 potentiostat controlled by GPES software and were carried out in three compartment glass cells separated by glass frits, using a three electrode system. The working electrodes used were vitreous carbon (area = 0.071 cm²), platinum or gold (0.02 cm²), gold-mercury amalgam (0.35 cm²), mercury pool (in excess of 2 cm²) or p-type silicon (*ca* 1 cm²) working electrodes. Vitreous carbon, platinum and gold electrodes were prepared by polishing in alumina, followed by rinsing with distilled water and then the solvent used in the electrolyte. Counter electrodes used were platinum gauze or foil and these were prepared by flaming. The reference electrodes employed were either a silver wire *pseudo* reference in conjunction with ferrocene as an internal standard or Ag/AgCl in 0.45 M [Bu₄N][BF₄] + 0.05 M [Bu₄N][Cl]-DCM; this has a value of + 0.42 V vs Fc⁺/Fc in 0.1 M [Bu₄N][BF₄]-MeCN. SCE (saturated calomel electrode) was also employed as a reference electrode in MeCN and this has a value of + 0.40 V vs Fc⁺/Fc in 0.1 M [Bu₄N][BF₄]-MeCN. All cyclic voltammetric experiments were performed at the ambient laboratory temperature of 25 °C unless otherwise stated.

The yield of the electrolysis product $[W(N_2)_2(dppe)_2]$ was determined by either IR or CV using calibration curves determined for these species in THF.

6.2.2 Photoelectrochemistry

The silicon is received as bulk material, supplied by Silicon Materials, in the form of large wafers so needs to be fabricated into electrodes. The silicon electrode fabrication procedure is as follows:

The bulk silicon wafer is approximately cut into 1 cm x 2 cm pieces, and then the unpolished side is etched with 40 % hydrofluoric acid (HF) for around 2 mins.⁷ The HF is removed by washing with degassed reagent-grade water, followed by degassed acetone, and then dried in a stream of inert gas. The etched area is scratched and a gallium-indium conductive eutectic is applied. A copper wire is attached and glued in place with conducting silver epoxy and left to dry.⁸ The whole back surface is then covered with an insulating, solvent resistive epoxy, Figure 1.

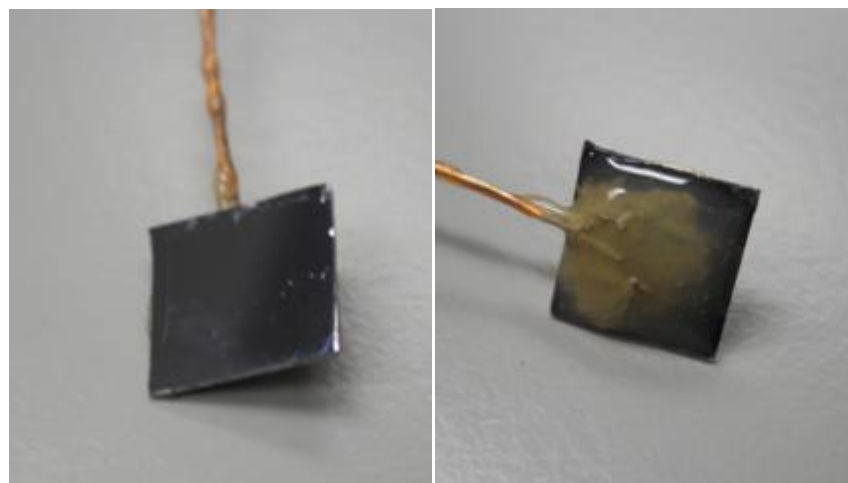


Figure 1 Front and back of silicon electrodes to show fabrication.

Prior to use, the silicon electrodes are required to be etched to become conductive. The electrodes are sonicated in dichloromethane to remove any grease from the surface. Next, the polished side is then etched with 40 % HF solution (in ethanol) for 2 mins and then washed with reagent grade water and acetone. Finally, the electrode is dried under vacuum and kept under inert gas until it is used.

6.2.3 Spectroelectrochemistry

Infrared spectroelectrochemical measurements were carried out in a Spectroelectrochemistry Partners SP-02 cell mounted on a Pike MIRacle ATR fitted with single-bounce silicon top plate. The ATR was fitted with a Northumbria Optical Coatings filter (pass band 4.76 μm to 5.60 μm). Spectra were recorded on a Bruker Vertex 80 spectrometer equipped with a mercury cadmium telluride (MCT) detector. Data was collected at 4 cm^{-1} resolution. Typically, 80 time points were recorded for each experiment. The SP-02 cell was fitted with a glassy carbon working electrode (area = 0.071 cm^2), a platinum counter electrode and a silver wire pseudo-reference electrode. These were attached to a Princeton Applied Research VersaSTAT 3 potentiostat controlled by v³ Studio software. Data collection was controlled by the Bruker Opus package, interfaced to the potentiostat using a custom Opus3D script and TTL connection. IR data was processed and analysed using Fit_3D.⁹

In a typical run, the cell was purged with nitrogen for some minutes before introduction of the solution for analysis. With the working electrode moved some distance from the ATR crystal (several 100 μm), CV data were acquired to estimate the $E_{\frac{1}{2}}$ value. A series of SEC runs were then carried out, moving the working electrode to within 10 μm of the ATR crystal. After each SEC run, the solution in the cell was allowed to equilibrate with unreacted material.

6.2.4 Indophenol test

The indophenol test is a chemical test that employs two separate reagents to calculate the yields of ammonia achieved. These are a mixture of phenol and sodium nitroprusside in water, Reagent **A**, and a solution of sodium hydroxide and sodium hypochlorite, Reagent **B**. The reagents are added in the order **A** then **B** to an ammonia test sample and left to develop for at least two hours.¹⁰ On a positive test the colour of the solution changed from colourless to a shade of blue, the deeper the more ammonia. To quantitatively calculate the concentration of ammonia UV-visible spectroscopy was used to measure the absorption of light in the blue region (632 nm). A calibration curve was created by measuring the absorbances of known

concentrations of ammonia. The absorbances of samples were then measured and the concentration was calculated from the calibration curve.

6.2.5 Electron paramagnetic resonance (EPR)

EPR spectra were undertaken with Dr. Vasily Oganesyan and measured using an X-band (9.5 GHz) Bruker EMX spectrometer at room temperature. The EPR tube was loaded into the cavity containing an almost saturated solution (*ca* 30 mM) of $[\text{MoX}_2(\eta^2\text{-O}_2\text{CCH}_3)(\text{dppe})_2][\text{BPh}_4]$ ($\text{X} = \text{H}$ or D) and a three electrode electrochemical setup of platinum working and secondary electrodes and a silver reference electrode connected to a HI-TEK DT 2101 potentiostat/galvanostat. The EPR active species was generated *in situ* by steadily increasing the potential until the cathodic peak current for the first reduction was reached.

6.3 Computational techniques

6.3.1 Digital simulation

Digital simulation of cyclic voltammetric data was carried out using *DigiElch 4.0*. Diffusion coefficients for the complexes being simulated were obtained from chemically related and similar molecular weight complexes that exhibited fully reversible redox behaviour. Simulations were fitted to the experimental I/V data either by user trial and error, or by computerised iterations using the commercial software.

6.3.2 Density functional theory (DFT)

DFT calculations were performed by Dr. Joseph Wright and Ms. Aušra Jablonskytė using the Gaussian 09 software package¹¹ using the Becke3LYP (B3LYP) hybrid GGA functional.¹²⁻¹⁴ The Stuttgart/Dresden basis set with effective core potential was employed to describe molybdenum;¹⁵ the 6-31++G** basis set was used for other atoms.¹⁶⁻²⁰ Structures were geometrically optimised in the gas phase and then with allowance for the effect of solvent using the integral equation formalism polarisable continuum model (IEFPCM)²¹ in MeCN in combination with the united atom

topological model for the radii setting (RADII = UAHF). Optimisations were carried out using the default convergence criteria and minima were confirmed through frequency calculation. Enthalpies are reported for the solvent-optimised structures.

The initial geometry for $[\text{MoH}_2(\eta^2\text{-O}_2\text{CCH}_3)(\text{dmpe})_2]^{+0/-}$ was derived from the crystal structure of $[\text{MoH}_2(\eta^2\text{-O}_2\text{CCH}_3)(\text{dppe})_2]^+$, with the phenyl groups replaced by methyls, with an adjustment of charge and multiplicity as required. For the 'closed' forms of $[\text{MoH}_2(\eta^2\text{-O}_2\text{CCH}_3)(\text{dmpe})_2]^{+0}$, the starting geometry was taken from the optimised structure of $[\text{MoH}_2(\eta^2\text{-O}_2\text{CCH}_3)(\text{dmpe})_2]^+$ with removal of a proton, whilst for the 'open' forms the initial geometry was taken from $[\text{MoH}_2(\eta^2\text{-O}_2\text{CCH}_3)(\text{dmpe})_2]^-$, again with removal of a proton. Optimisation of the geometries for all forms of $[\text{MoH}_2(\eta^2\text{-O}_2\text{CCH}_3)(\text{dmpe})_2]^+$ were carried out using a polarisability continuum model with MeCN as the solvent.

6.4 References

1. S. K. Ibrahim, *New electrochemical reactions of some metallo-sulphur compounds including the activation of NO and NHR ligands at Mo-S centres*, **1992**, Ph. D. Thesis
2. T. Ito, A. Takahashi, S. Tamura, *Bull. Chem. Soc. Jpn.* **1986**, 59, 3489
3. T. Ito, A. Yamamoto, *J. Chem. Soc. Dalton Trans.* **1975**, 1398
4. C. J. Pickett, K. S. Ryder, J. Talarmin, *J. Chem. Soc. Dalton Trans.* **1986**, 1453
5. B. S. Lim, J. P. Donahue, R. H. Holm, *Inorg. Chem.* **2000**, 39, 263
6. C. A. Goddard, R. H. Holm, *Inorg. Chem.* **1999**, 38, 5389
7. S. Watanabe, N. Nakayama, T. Ito, *Appl. Phys. Lett.* **1991**, 59, 1458
8. R. N. Dominey, N. S. Lewis, J. A. Bruce, D. C. Bookbinder, M. S. Wrighton, *J. Am. Chem. Soc.* **1982**, 104, 467
9. S. J. George, Lawrence Berkeley National Laboratory, USA,
http://abex.lbl.gov/~simon/Instrument_Development.html.
10. M. W. Weatherburn, *Anal. Chem.* **1967**, 39, 971
11. http://www.gaussian.com/g_tech/g_ur/m_citation.html
12. A. D. Becke, *J. Chem. Phys.* **1993**, 98, 5648
13. C. Lee, W. Yang, R. G. Parr, *Phys. Rev.* **1988**, 37, 785
14. B. Miehlich, A. Savin, H. Stoll, H. Preuss, *Chem. Phys. Lett.* **1989**, 157, 200
15. D. Andrae, U. Haeussermann, M. Dolg, H. Stoll, H. Preuss, *Theor. Chem. Acc.* **1990**, 77, 123
16. W. J. Hehre, R. Ditchfield, J. A. Pople, *J. Chem. Phys.* **1972**, 56, 2257
17. M. M. Franci, W. J. Petro, W. J. Hehre, J. S. Binkley, M. S. Gordon, D. J. DeFrees, J. A. Pople, *J. Chem. Phys.* **1982**, 77, 3654
18. T. Clark, J. Chandrasekhar, P. v. R. Schleyer, *J. Comp. Chem.* **1983**, 4, 294
19. R. Krishnam, J. S. Binkley, R. Seeger, J. A. Pople, *J. Chem. Phys.* **1980**, 72, 650
20. P. M. W. Gill, B. G. Johnson, J. A. Pople, M. J. Frisch, *Chem. Phys. Lett.* **1992**, 197, 499
21. J. Tomasi, B. Mennucci, R. Cammi, *Chem. Rev.* **2005**, 105, 2999 and references cited therein